SPECTRAL INVESTIGATIONS OF LUMINESCENCE

IN FELDSPARS

by

Marc René Baril

B.Sc., University of Toronto, 1994

M.Sc., Simon Fraser University, 1997

THESIS SUBMITTED IN PARTIAL FULFILLMENT

OF THE REQUIREMENTS FOR THE DEGREE OF

DOCTOR OF PHILOSOPHY

IN THE DEPARTMENT

OF

PHYSICS

© Marc René Baril 2002

SIMON FRASER UNIVERSITY

December 2002

APPROVAL

Name: Marc René Baril

Degree: Doctor of Philosophy

Title of thesis: Spectral Investigations of Luminescence in Feldspars

Examining Committee: Dr. Howard Trottier
           Professor, Department of Physics (Chair)

           _____

           Dr. David J. Huntley
           Professor, Department of Physics (Supervisor)

           _____

           Dr. George Kirczenow
           Professor, Department of Physics

           _____

           Dr. Robert Frindt
           Professor, Department of Physics

           _____

           Dr. Michael X. Chen
           Senior Lecturer, Department of Physics (Internal
           Examiner)

           _____

           Dr. Peter D. Townsend
           Professor, School of Engineering and Information
           Technology, University of Sussex, Brighton, U.K.
           (External Examiner)

Date Approved: _____

Abstract

Optical dating is a tool for dating the last exposure of minerals to sunlight. The technique relies on the optically stimulated luminescence of irradiated minerals, particularly quartz and feldspar. Despite the widespread use of feldspar in dating, very little is known about the defects that give rise to the luminescence in this mineral.

A new high-sensitivity spectrometer was constructed for measurement of the emission spectra of the infra-red stimulated luminescence (IRSL) for a wide range of feldspars, and an attempt made to correlate specific spectral features with feldspar type or elemental content. Comparison of the IRSL spectra with spectra of phosphorescence following γ-irradiation and the spectra of phosphorescence after illumination indicates that the emission spectra are highly dependent on the type of excitation. This is a clear indication that certain traps are connected to particular luminescence centers. This conflicts with the standard model involving recombination via the conduction band.

Excitation spectra were also measured and these indicated that the IRSL excitation resonance near 1.45 eV sometimes exhibits a strong Lorentzian character. The excitation spectrum was generally similar for both the violet (3.1 eV) and yellow-green (2.2 eV) emission bands, was unaffected by the polarization of the excitation light, and was best described by a Voigt profile near the 1.45 eV resonance.

The luminescence decay with time was found to follow Becquerel's equation, $I(t) = I_0/(1+t/t_0)^\alpha$. In terms of the time-integrated applied excitation energy E, this decay law may be expressed as, $I(E) = I_0/(1+E/E_0)^\alpha$. The parameters E_0 and α, were found to vary strongly with excitation photon energy. α was found to increase with applied γ dose, but both α and E_0 were relatively unaffected by sample temperature.

Measurement of the initial rate of decrease of intensity with time, $S_0 = -\frac{dI}{dt}$, versus initial intensity I_0, for a wide range of excitation photon energies from 1.2 eV to 2.54 eV

indicated that the scaling $S_0 \propto I_0^2$ holds for excitation photon energies from the infrared excitation resonance well into the visible band. This provides strong evidence that a single trap is involved in the luminescence.

Some emission and excitation spectra for inclusions in quartz are suggestive of these being feldspars.

To Jennifer, who taught me the beauty of nature's smaller details.

Acknowledgments

I would like to express my deepest gratitude to Dr. David Huntley who never wavered in offering me the greatest freedom in my research, yet always steered me along fruitful paths. His assistance in editing and providing suggestions for this text cannot be overstated.

The directions taken in this thesis have been greatly influenced by my colleague Michael Short. Many of the ideas presented in this work are the result of frequent discussions comparing our individual lines of research. He was indispensable in providing samples and equipment during my stay; for his collaboration and friendship, I raise a glass.

The following are thanked for provision of samples, or assistance with collecting them: W. Blake Jr., J.J. Clague, S.R. Dallimore, R.J. Fulton, L. Groat, H. Jungner, D.S. Lemmen, O.B. Lian, Yu.A. Mochanov, J. Ollerhead, M. Roy, P.A. Shane, P. Solovyeev, T.K. Rockwell, E. Thibault, S. van Heteren, J.F. Wehmiller and S.A. Wolfe.

I would like to extend special thanks to Dr. Dan Marshall of the Department of Earth Sciences at S.F.U. for his assistance with the S.E.M. imaging. The technical staff in the Department of Physics frequently provided invaluable assistance; Scott Wilson and Jeff Rudd deserve particular mention. I am also grateful to our graduate secretary Candida Mazza who has an unfailing memory for deadlines, and provided assistance in obtaining financial support during my research.

Finally, I would like to thank all of my past and present colleagues in the Department of Physics, for their friendship and support during my research. To them, and all others deserving but not mentioned, I raise another glass!

Contents

List of Tables

List of Figures

Chapter 1

Introduction

1.1 Optically Stimulated Luminescence of Feldspars

In 1985, optical dating was introduced as a method for dating the time since the mineral fraction of a sediment was last exposed to sunlight (Huntley *et al.*, 1985). The technique relies on the optically stimulated luminescence produced in quartz and feldspars once they have been subjected to ionizing radiation. The energies of the luminescence photons may exceed those of the excitation light. In feldspars the luminescence bands of particular interest extend from the near UV (300 nm) to the near IR (700 nm) and a resonant peak in the luminescence efficiency occurs for excitation in the IR (860 nm or 1.44 eV). The luminescence arises from trapped electrons being optically excited out of the traps followed by recombination at luminescence centers. The luminescence centers consist either of ionic impurities or structural defects in the lattice. Since the electron traps lie well above the valence band, whereas the acceptor levels lie close to the valence band, the electron requires less energy to be evicted from the trap than the energy released upon recombination at the luminescence center.

Electrons fall into traps when the crystal is subjected to ionizing radiation. Excited electrons in the lattice gain sufficient energy to travel through the crystal, thermalize and eventually fall into traps or recombine at acceptor sites in the lattice. The electrons of interest are those that fall into trap states in which they are thermally stable at room-temperature. The electrons may remain trapped for periods of time exceeding 10^5 years. This observation provided the basis for the development of thermoluminescence dating in the late 1960's,

and more recently optical dating. Thermoluminescence dating differs from optical dating in that the luminescence excitation in the first case is provided by heating and in the latter case, by light.

One should emphasize that the phenomena of optically and thermally stimulated luminescence is not restricted to feldspars, it is observed in many dielectric solids. However, most dating work has been devoted to the study of quartz and feldspars due to the ubiquity of these minerals in sediments suitable for optical dating. This dissertation focuses on the luminescence properties of feldspars with the ultimate goal of identifying the recombination center and trap defects, and elucidating the recombination and trapping mechanisms.

1.2 Optical Dating

Although this work will not specifically deal with the improvement of optical dating techniques, a cursory understanding of the optical dating process is required to appreciate some of the issues discussed in this thesis. Reviews of optical dating techniques have been compiled by Aitken (1998), Huntley and Lian (1999) and Berger (1995).

In the simplest model, the electron trap states lie relatively close to the conduction band, as shown in Figure 1.1. The trapped electrons remain in the traps over geological time scales; the thermal lifetime of the trap is not known but is believed to exceed 10^6 years. The recombination centers lie somewhere above the valence band, which is separated by several eV from the conduction band[1]. Although this model is incorrect (for reasons that will be evident shortly) it is sufficient for the purpose of describing the basic dating process.

In any dating technique, a resetting mechanism is required to set the dating clock to zero time. In optical dating the "zeroing" mechanism is provided by sunlight, in thermoluminescence dating the mechanism is heating. During deposition, a sediment containing feldspars or quartz may be exposed to sunlight. The sunlight excites electrons out of the "optical traps"[2] in the material; these traps are therefore largely empty after deposition. Eventually the sediment is buried and shielded from sunlight. At this point, electrons begin to slowly

---

[1]Although band structures have not been measured or calculated for feldspar, we can expect that the smallest band gap is over 6 eV, from band calculations for quartz (Xu and Ching, 1991).

[2]This term is used to distinguish the traps that are readily emptied by light from those that are only emptied by heating.

Figure 1.1: *The principle of optical dating. Sunlight empties a large fraction of the electron traps. Natural sources of ionizing radiation excite electrons out of the valence band and a number of these become localized in thermally stable traps. Undisturbed by light, the electrons may remain trapped for over 10^6 years unless the trap is emptied by ionizing radiation. Exposure of the excavated mineral to a lab light source ejects electrons from the traps. The recombination luminescence produced is proportional to the radiation dose acquired by the mineral at moderate to low doses.*
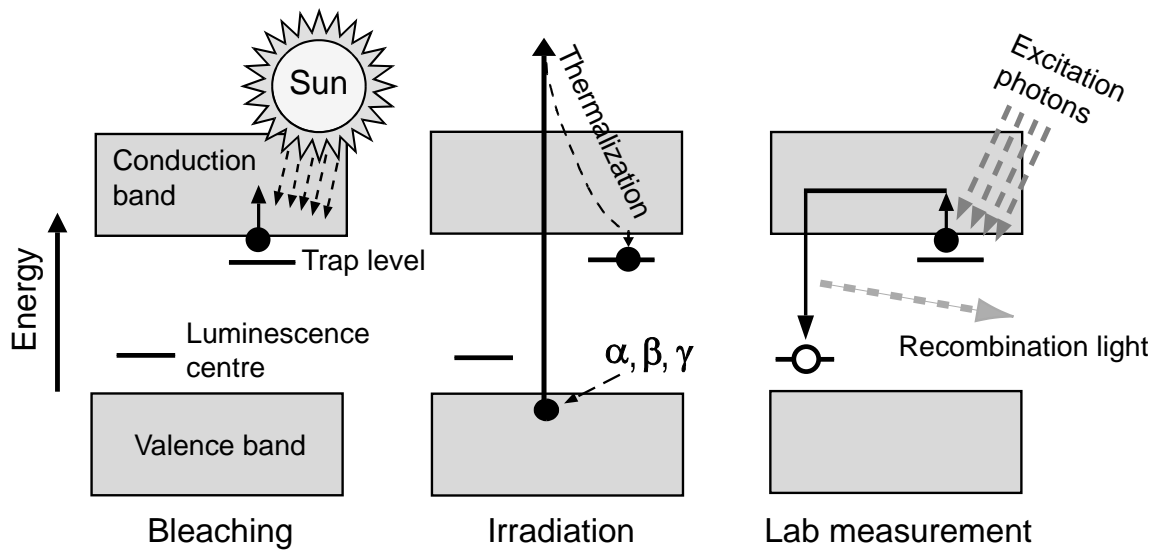
re-populate the traps as ambient sources of ionizing radiation excite electrons out of the valence band and some of these thermalize into the stable traps. As long as the number of occupied traps is well below saturation, the number of trapped electrons in the mineral will vary linearly with the radiation dose acquired since the sediment was deposited. The dose is defined as the total energy absorbed by the sample from sources of ionizing radiation both internal and external to the mineral grain.

If the buried sediment is excavated and brought to the lab (without light exposure), the optically stimulated luminescence in the separated mineral grains may be used to determine the dose accrued. The dose-rate is determined from the sum of all sources of ambient radiation to which the sample is exposed and will generally vary over the burial period. In general it is necessary to analyze the radioisotope contents in the measured mineral grains

and the neighbouring sediments as well as producing an estimate of the past cosmic ray dose. In the simplest case, where the dose rate is constant, the time since the sediment was last exposed to sunlight is given by the acquired dose divided by the dose-rate. In most situations however, one must apply corrections for variations in the dose-rate over the burial period. For example, the contribution of cosmic rays to the dose-rate decreases with depth of the sediment below the surface.

In order to determine the past dose, the luminescence response of the sample to radiation must be measured. This is done by subjecting a number of sample aliquots to ionizing radiation. The applied dose adds to the natural dose acquired by the mineral grains. If the curve describing luminescence intensity versus applied radiation dose, or "growth curve", is extrapolated back to zero luminescence intensity, the intercept with the dose axis provides the past dose acquired by the sample. Many variations on this dating procedure exist, each with its own merits, but all depend on a dose response curve obtained using laboratory radiation doses to the aliquots. Invariably, the hope is that the laboratory dose reflects the manner in which the dose accumulated in the natural environment, in the sense that the radiation flux is sufficiently low that an insignificant number of thermally shallow traps are filled at any given time.

It is clear that this last situation can never hold. The laboratory radiation flux is so much greater than the natural flux, typically by a factor of 10^8–10^9, that once the mineral is removed from the irradiation source, the distribution of trapped electrons in the mineral is in great disequilibrium. A significant amount of charge (*i.e.* electrons and holes) reside in thermally unstable traps, this charge is gradually redistributed in the crystal as the traps empty due to thermal excitation at room temperature. This process is usually accelerated in the lab by heating the sample, typically for several hours above 110 °C; this procedure is referred to as "preheating". In general the luminescence excited immediately after a long irradiation is significantly brighter than that after the preheat (often exceeding a factor of 2).

There is an additional fading of the luminescence signal with time that is not temperature dependent and has been observed on time scales of hours to years; this is referred to as "anomalous fading". Anomalous fading is attributed to the tunnelling of electrons out of otherwise stable traps. In feldspars, anomalous fading places a limit on the maximum age obtainable for a sediment. Anomalous fading is not known to occur in quartz.

Although quartz is much more abundant than feldspar and does not suffer from anomalous fading, feldspars have the advantage of having much brighter luminescence. This means that feldspars can be used to date much younger sediments than quartz. In addition, the luminescence in feldspars saturates at doses that are typically an order of magnitude greater than in quartz. This implies that, at least in principle, older samples can be dated using feldspars.

The problem of anomalous fading remains the greatest obstacle to the widespread use of feldspars in dating. The measurement of anomalous fading rates is time consuming due to the necessity of monitoring the luminescence of the sample aliquots over several months in order to obtain an accurate decay rate. Neglecting to correct the ages obtained by optical dating for anomalous fading can lead to an underestimate of the age approaching a factor of 2 in samples as young as 20 ka (see for example, Huntley and Lamothe, 2001).

It should be noted that some of the charge removed from shallow traps during the preheat is transferred into the deeper traps that are sampled by the excitation light. In young samples the amount of charge transferred from the shallow traps into the deep optical traps can be significant. Unless a correction is made for this "thermal transfer" of charge, erroneously large ages will result in samples less than ~ 1000 years old.

Another difficulty with optical dating is the problem of determining the level of light exposure, or "bleaching"[3], that the dated sediment received prior to deposition. If the sediment only received exposure sufficient to either partially empty the traps, or empty the traps in a few of the grains, then the optical ages obtained will be erroneously large. One must have an accurate picture of the geological context to determine whether the conditions for sufficient bleaching were present during deposition. Even in situations where sufficient light exposure appears likely, one occasionally finds that the individual feldspar grains did not acquire a sufficient bleach prior to sedimentation. The scatter of aliquot luminescence intensities on the growth curve may serve as an indication that the grains were not sufficiently bleached during deposition (Huntley and Berger, 1995; Lamothe, 1996).

---

[3]The term "bleaching" is used to describe a prolonged exposure of the sample to light leading to a significant reduction in the optically stimulated luminescence.

1.3 Feldspar structure and composition

1.3.1 Nomenclature of the feldspars

Feldspars are one of the most abundant rock-forming mineral groups, in this respect their importance ranks second only to quartz. The feldspars are framework alumino-silicates with a wide compositional range and are classified according to the content of their principal substitutional elements; potassium, sodium and calcium. The relatively large Na, Ca and K atoms are incorporated in the interstices of the silicate framework. The potassium and sodium bearing feldspars, or alkali feldspars are generally more abundant than the sodium and calcium bearing members, or plagioclases. The nominal composition for these minerals is,

Alkali feldspars: $(K,Na)[AlSi_3O_8]$
Plagioclase: $Na[AlSi_3O_8]... Ca[Al_2Si_2O_8]$

In each of these broad categories, one distinguishes a number of minerals with similar stoichiometry but differing structural states. The structural state of the mineral depends primarily on the temperature at which it crystallized. Thus a high temperature feldspar refers to a feldspar that has been rapidly cooled from a high temperature (or "quenched") so that the high temperature structural state has been frozen into the mineral. A low temperature feldspar is formed through slow cooling of the mineral during its crystallization (annealing).

The interrelation between the various feldspars is best shown on a compositional ternary diagram with the end members being potassium, sodium and calcium feldspar, Figure 1.2. The highest temperature phase of potassium rich feldspars is sanidine (or high-sanidine) which consists of a perfect solid solution of albite (Ab) and orthoclase (Or). The terms orthoclase and albite are often used to mean K-rich and Na-rich feldspar, however they more properly refer to a particular structural state of K and Na feldspar. Below ~40% Or, high-temperature alkali feldspars have a triclinic symmetry whereas at lower concentrations of Ab the symmetry is monoclinic (sanidine). The triclinic members of the low-temperature alkali feldspar series are termed anorthoclase (which is not to be confused with the calcium rich feldspar anorthite).

Figure 1.2: *Ternary diagram explaining feldspar nomenclature. The end members are orthoclase (high potassium, "Or"), albite (high sodium, "Ab") and anorthite (high calcium, "An").*
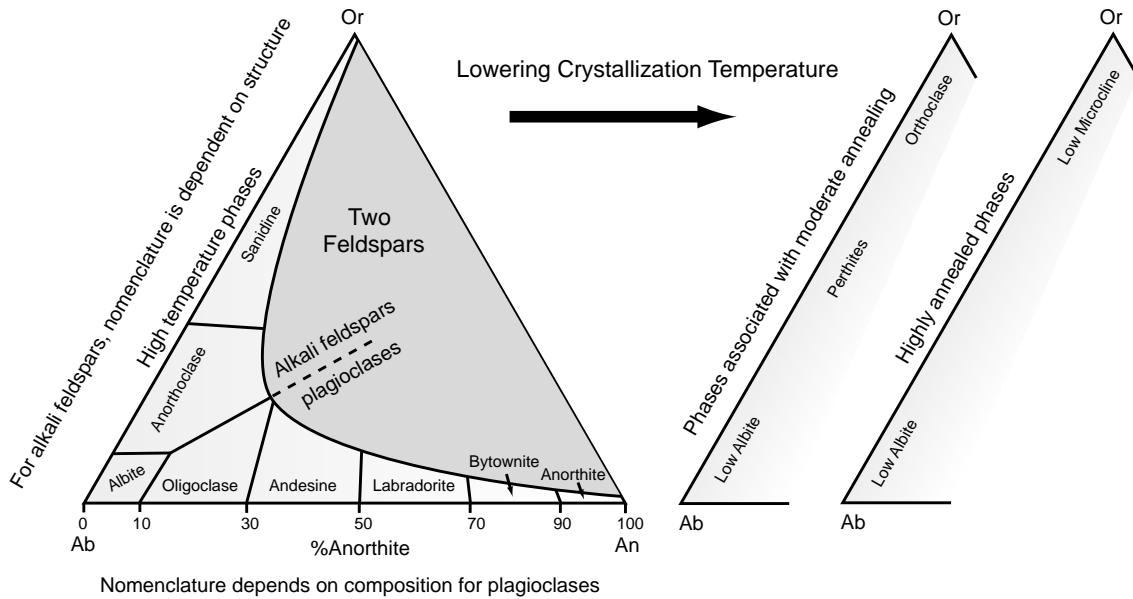
In the lower temperature alkali feldspar series we have orthoclase and microcline. For these, the solid solution of Or and Ab is not perfect as it is in sanidine and a varying amount of phase separation occurs, often in the form of lamellar inter-growths of Or and Ab. Or/Ab inter-growths of macroscopic scale are named perthites whereas microscopically scaled inter-growths are termed microperthites.

Orthoclase proper refers to a moderately low-temperature K-feldspar with monoclinic symmetry. The lowest temperature K-feldspar, microcline, has triclinic symmetry. In many microclines the degree of departure from monoclinic symmetry, or "obliquity" can be very small. Twinning is almost always present in microclines, so that the growth habit is rarely a good indication of the unit cell parameters. The twinning can lead to a bulk crystal with monoclinic habit, whilst the unit cell is triclinic.

Plagioclase is triclinic at all temperatures so that there is no distinct nomenclature for high and low temperature varieties. In some intermediate plagioclases (*e.g.* labradorite) lamellar exsolution of the Ab and An phases occurs at a very fine scale, leading to an

iridescent play of light. A similar effect is observed in perthites, *e.g.* moonstone, however the term labradorescence is reserved for plagioclases.

In the following chapters "orthoclase" and "albite" will occasionally be used to mean high-potassium and high-sodium bearing feldspars without making specific reference to the crystal structure. Use of these terms to refer to the actual crystal structure should be clear from the context.

1.3.2 Feldspar structure

Sanidine's unit cell is monoclinic, space group C2/m, with four $KAlSi_3O_8$ per cell. The idealized sanidine structure was first described by W.H. Taylor (1933). Its cell parameters are $a = 8.6$ Å, $b = 13.0$ Å, $c = 7.2$ Å, and $\beta = 116^o$. The structure consists of linkages of $(Si,Al)O_4$ tetrahedra joined through shared oxygen atoms. The K cations lie in the interstices of the framework of linked tetrahedra.

The structure is most easily visualized by first considering the chain of linked tetrahedra as seen looking down the b-axis, as shown in Figure 1.3(b) (for clarity, the K ions are not shown). This idealized chain linkage is identical to that in the orthorhombic silicate mineral β-tridymite. If one looks down the idealized chain (*i.e.* down the a-axis) then one would see the four membered ring of tetrahedra shown in Figure 1.3(c). Tetrahedra pointing upwards are labeled "U", whereas "D" denotes tetrahedra pointing downwards. This can be simplified even further if we represent the ring of tetrahedra as in Figure 1.3(d), where the "U" tetrahedra have been replaced by filled circles and the "D" tetrahedra replaced with open circles. The only oxygens shown are those that are not linked within the chain. In the actual feldspar chain, adjacent stacked rings do not exactly lie atop one another as viewed down the chain axis but are rotated with respect to one another, as shown in Figure 1.3(e). In addition, none of the crystal axes lie exactly within the plane of the rings (*i.e.* in the idealized model (010) lies within the plane of the ring).

Figure 1.4 shows how the chains are linked in the feldspar structure to form a "sheet" viewed down the (100) axis. Each ring of tetrahedra is joined to the underlying sheet by two oxygens as shown in Figure 1.3(e), but omitted in Figure 1.4. The potassium ions lie on the planes of mirror symmetry, M.

It is important to note that two distinct Si/Al tetrahedral sites exist in the sanidine struc-

Figure 1.3: *An ideal representation of the "double crankshaft" chain in feldspar, adapted from Deer et al. (1966). (a) The Si,AlO₄ tetrahedron. (b) View of the idealized feldspar chain along its length, i.e. down the b-axis. (c) View down the axis of the chain showing the ring of tetrahedra. The chain has been tilted forward slightly so that all the atoms are visible. (d) Simplified view of the ring replacing tetrahedra pointing upwards with small filled circles and tetrahedra pointing downwards with small open circles. (e) Actual orientation of adjacent stacked rings in the feldspar chain.*
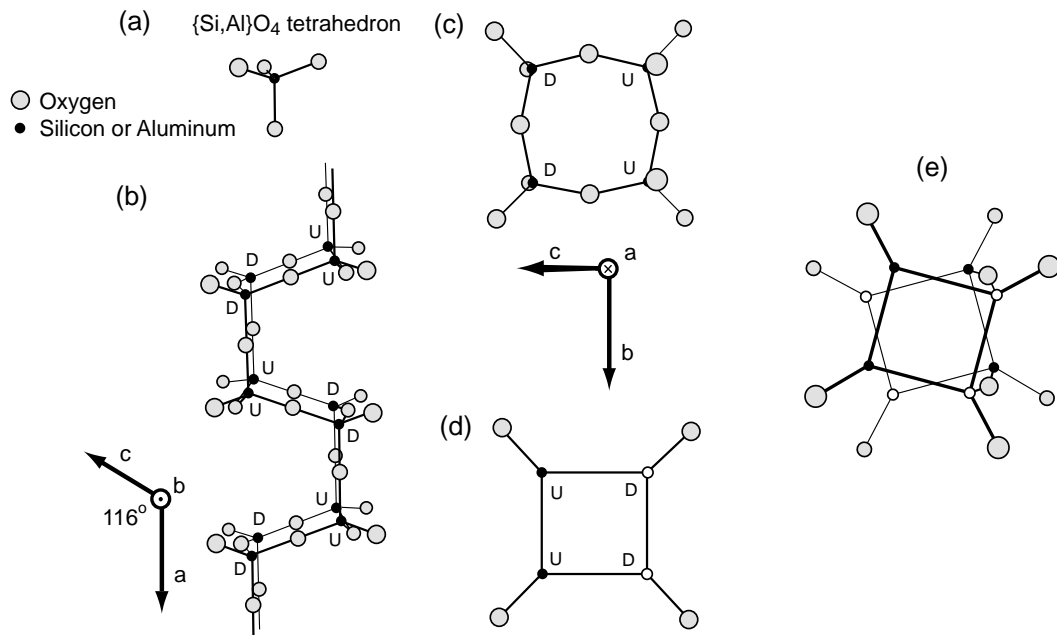
ture, these are labeled T^1 and T^2 in Figure 1.4. Similarly, the O^1 and O^2 are distinct oxygen sites, with the former lying on the same special mirror planes as the K ions. The T^1 sites are distinguished from the T^2 sites by being linked to O^1 oxygens, the T^2 sites are linked to O^2 oxygens.

In the highest temperature form of K-feldspar, sanidine, one finds that the aluminum atoms are randomly distributed among the T^1 and T^2 sites. In the lower temperature orthoclase, there is partial ordering of the Al atoms at these sites, with a preference for Al in the T^1 sites. Microcline is the lowest temperature phase of K-feldspar and its unit cell is generally triclinic. In the triclinic feldspars (microcline, albite and plagioclase) the loss of

Figure 1.4: *Linkage of the feldspar chains to form "sheets" in sanidine as viewed down (100). Oxygens linking the sheets have been omitted for clarity. Note that the c-axis does not lie within the plane of the page. After Deer et al. (1966).*
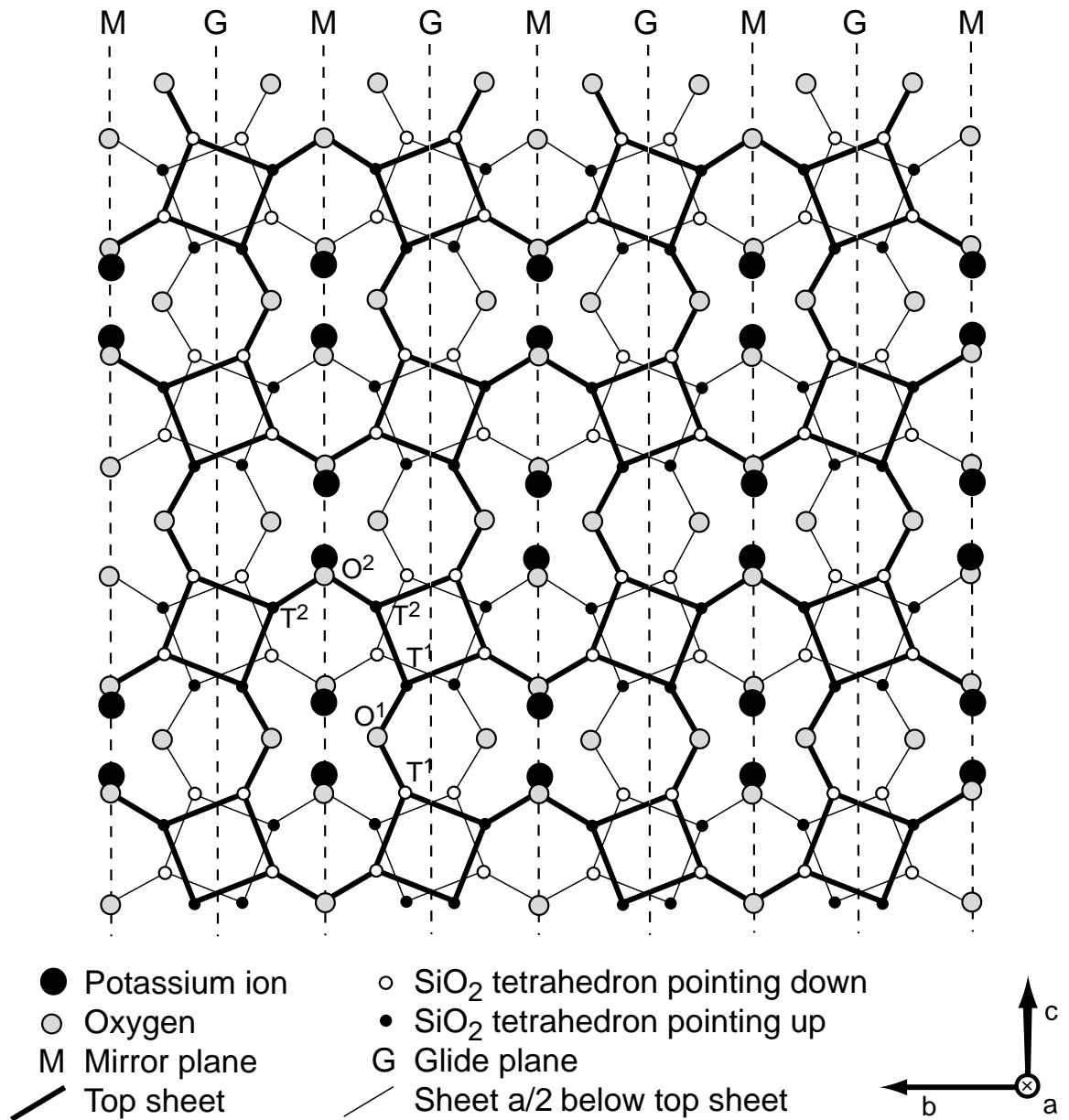
Figure 1.5: *Comparison of monoclinic (left) and triclinic (right) structures viewed down (001); sanidine and albite respectively. Grey circles represent oxygens, small black circles represent tetrahedrally coordinated (T) sites (Si and Al), large black circles are the M-cation sites (K, Na, Ca). Nomenclature for the distinct atomic positions follows that of Megaw (1956).*
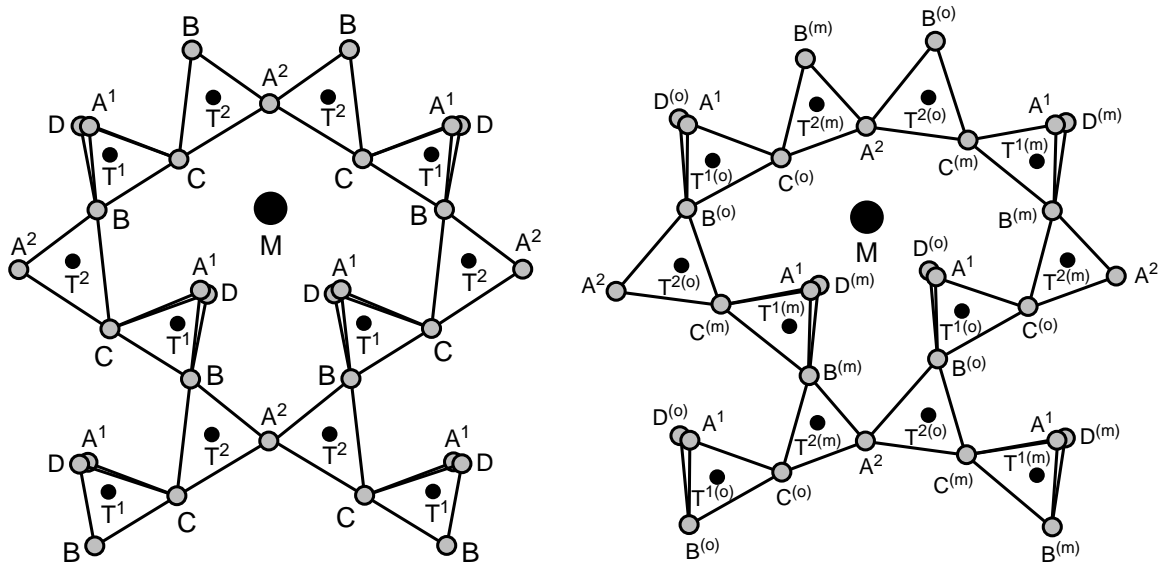
symmetry means that there are four distinguishable tetrahedral sites; these are designated $T^1(o)$ $T^1(m)$, $T^2(o)$ and $T^2(m)$ (Figure 1.5).

In microcline the "obliquity", or departure from the monoclinic symmetry, depends on the ordering of Al and Si atoms on the tetrahedral sites. Upon heating microcline above 1000 °C, maximum disorder between the Si-Al positions is attained and a sanidine is produced.

It should be noted that even in the case of perfect disorder of the Al and Si atomic positions, the positions of the Al atoms is not completely random. If two tetrahedra are adjoined by a common oxygen, then only one of the tetrahedra may be occupied by Al. This rule was observed to hold in many alumino-silicates, including feldspars ("Loewenstein's rule": Loewenstein, 1954).

1.3.3 Common impurities and defects

Substitutions in the lattice occur on the sites normally occupied by the monovalent or divalent cations (K, Na, Ca and rarely, Ba) called "M-sites", and the tetrahedrally coordinated Si/Al sites, said "T-sites". Large atoms exclusively occupy the large interstices provided at the M-sites whereas smaller atoms occupy the T-sites. The elements Mg, B, Al, Ga, Fe^{3+}, Ge, and P readily substitute for Si or Al in the T-sites, whereas Na, K, Rb, NH_4, Fe^{2+}, Ca, Sr, Pb, Ba, Eu^{2+} have been found to incorporate into the M-sites (Smith and Brown, 1988, with references therein). Many of these atoms (*e.g.* Ba, B and Ga) can substitute in large quantity for the more common feldspar constituents (Smith and Brown, 1988). Some of the ions which substitute into the lattice in smaller quantity are: Ti^{4+} (probably T-site), Mn (M-site), Sn^{4+} (possibly T-site), Cr, Rb, Cs, Be and several rare-earth elements (*e.g.* Eu^{2+}, Eu^{3+}, Sm^{3+}, Dy^{3+} and Ce^{3+}). Manganese contents in anorthite (Na-rich feldspar) are substantially greater than those found in the K-rich feldspars. This is significant in the context of feldspar luminescence because the bright 2.1–2.2 eV (570–590 nm) emission band that dominates Na-rich feldspars is thought to be due to Mn^{2+}.

Substitution of Si^{4+} for Al^{3+} on a T^1 site results in a net positive local charge imbalance so that one of the Si atoms becomes a donor (electron trap). Conversely, replacement of Si^{4+} by Al^{3+} on a T^2 site results in the Al atom becoming an acceptor (hole trap). Visocekas *et al.* (1994) suggested that such donor-acceptor pairs may be responsible for the infrared thermoluminescence (TL) emission in feldspars.

Oxygen charge defects are ubiquitous in silicate minerals. A comprehensive study of these centers in albite has been undertaken by Petrov *et al.* (1989). Six centers were identified, four due to Al–O^{1-}–Al bridges (violation of Loewenstein's rule, see Section 1.3.2), one from an Si–O^{1-}–Al(2Na) center and one due to an Si–O^{1-}–X^{2+} center. The positions of these centers are shown in Figure 1.6. The Al–O^{1-}–Al centers occur on the C^o, D^o, C^m and D^m oxygens and are destroyed upon heating above 520 K for three hours. The Si–O^{1-}–Al(2Na) center is found on an A^1 oxygen (the nearest oxygen to a Na atom) and probably occurs upon substitution of Si for Al on the nearest $T^{1(o)}$ site and Al for Si on the $T^{1(m)}$ site. This center is destroyed by heating above 490 K for 3 hours. The Si–O^{1-}–X^{2+} center is located on the D^m oxygen with X^{2+} (X = Mg^{2+}, Be^{2+} or Zn^{2+}) substituting for Al/Si at the $T^{1(m)}$ site. This center is removed upon heating above 620 K for 3h.

Figure 1.6: *Top: View of the albite lattice perpendicular to (201), notation is due to Megaw (1956). Dashed lines indicate tetrahedra pointing downwards. In perfectly ordered albite, Al atoms occupy T sites represented by the grey tetrahedra. Bottom: Location of the oxygen defect centers in the albite structure. Designations d_m, d_o, c_m and c_o are Petrov et al.'s notation for the four Al–O^{1-}–Al centers. After Petrov et al. (1989).*
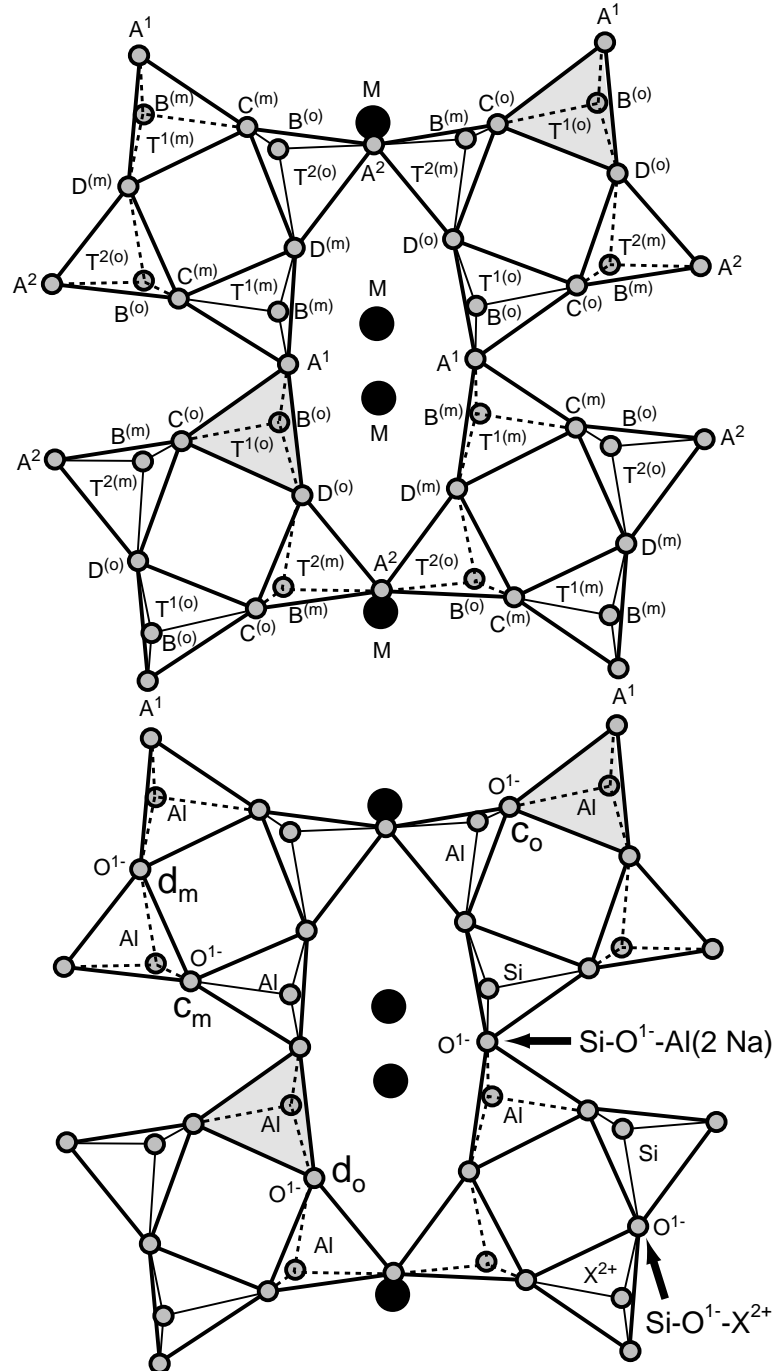
All six defects can be restored by subjecting the sample to ionizing radiation. The centers Al–O^{1-}–Al and Si–O^{1-}–X^{2+} have also been observed in microcline and plagioclase by Speit and Lehmann (1982).

1.4   A Review of Luminescence of Feldspars

It is a fair statement to say that very little is known about the physical processes governing luminescence in feldspars. Although the impurities acting as the recombination centers are known in a few cases, the nature of the defects that act as the electron traps are unknown as yet. The identification of these defects is the ultimate goal because it would lead to the development of an accurate model for the luminescence behaviour.

1.4.1   Luminescence spectra

Luminescence can be induced in feldspars by a number of excitation mechanisms. Since the emission bands are generally dependent on the mode of excitation it is important at the outset to distinguish between the types of excitation mechanisms that have been studied;

- *Optically stimulated luminescence, OSL*: In an irradiated sample, excitation of trapped charges by light. IRSL is reserved to denote excitation by photons near the 1.44 eV excitation resonance of feldspars.

- *Thermoluminescence, TL*: In an irradiated sample, excitation of trapped charges through thermal activation.

- *Cathodoluminescence, CL*: Excitation of electrons by a low energy (keV) electron beam.

- *Radioluminescence, RL*: Excitation of electrons by a radioactive source, typically a β emitter.

- *Photoluminescence, PL*: Photo-excitation of a centre.

The following will concentrate on the TL and OSL emissions because these are more directly applicable to our line of investigations. A comprehensive review of feldspar luminescence can be found in Krbetschek *et al.* (1997).

TL emission spectra

Huntley *et al.* (1988) measured TL emission spectra for a wide range of natural feldspar rock samples between 1.65–4.1 eV (300–750 nm). Prescott and Fox's (1993) study extended the bandwidth measured to 1–5 eV (250-1200 nm) and included some synthetic feldspar samples. Both investigations identified three "type spectra" that are representative of high potassium, high sodium and plagioclase (calcium bearing) feldspars.

At temperatures above 200 ºC the high potassium feldspars are characterized by a bright TL emission band centered at 3.1 eV (400 nm). A weaker band at 2.17 eV (570 nm) is characteristic of high-sodium feldspars and may be due to exsolved Na-feldspar phases in the crystal. At low temperatures a broad band is observed at 2.6 eV (480 nm), and is brightest in laboratory irradiated samples.

In the high sodium plagioclases (oligoclase/anorthite) the principal emission is at 2.17 eV (570 nm) with a weaker band centered in the near UV at 4.45 eV (275 nm) (Prescott and Fox, 1993). Garcia *et al.* (1996) suggest a correlation between Na-rich phases in alkali feldspars and the UV emission which they find at 4.27 eV (290 nm). Their results are inconclusive due to the difficulty in determining the level of Na/K feldspar exsolution in the sample, and their inability to separate out the luminescence arising from the individual phases and the bulk luminescence that is measured. On the high-Na end of the alkali feldspar axis, the dominant emission is found at 1.75 eV (710 nm). The 3.1 eV band that is prominent in K-feldspar is either exceedingly weak or not present in the high sodium plagioclases.

The high anorthite plagioclases are characterized by a much weaker emission intensity than the Na-rich plagioclases and, especially, the alkali feldspars. Prescott and Fox (1993) report a bright TL emission at 1.95 eV (635 nm) and 300 ºC with a small emission near 3.1 eV (400 nm), they suggest that this emission may correspond to the violet emission observed in K-feldspar. In andesine (30-40% An) Huntley *et al.* (1998) observed a bright TL emission at 2.2 eV with a weaker band at 3.1 eV, similar to the Ab spectrum.

OSL emission spectra

In what follows, optically stimulated luminescence (OSL) refers to luminescence excited by light in general in irradiated samples, whereas infra-red stimulated luminescence (IRSL)

refers to emission specifically excited by near-infrared light (typically near 1.44 eV, or 860 nm). Huntley *et al.* (1991) produced OSL spectra for five potassium feldspar sediment extracts, a plagioclase and one orthoclase sample (K3). Three bands were observed, at 3.76 eV (330 nm), 3.1 eV and 2.2 eV, with relative intensities apparently correlated to K/Na content in a similar manner to that described for the TL emission. Measurements of almost pure K-feldspar extracts under 1.96 eV (632.8 nm) excitation by Jungner and Huntley (1991) indicate a 3.1 eV OSL emission band similar to that observed in the TL of such samples. The bands observed by Junger and Huntley at 3.87 eV (320 nm) and 3.64 eV (340 nm) in the OSL emission do not appear in the TL emission of alkali feldspars but are prominent in CL and may be due to Pb^{2+} (Marfunin, 1979b).

Rendell *et al.* (1995) measured TL and IRSL (1.41 eV excitation) for potassium-feldspar rich sediment extracts and found that the 4.27 eV emission was absent in the "natural"[4] IRSL, but present in laboratory irradiated samples. Clarke and Rendell (1997a) found that a 5 minute preheat at 220 °C would remove the 4.27 eV IRSL emission present in laboratory irradiated samples immediately after irradiation. Clarke and Rendell (1997b) report that the decrease of the emission in the 4.27 eV band subsequent to a short preheat or prolonged room temperature storage is accompanied by an absolute increase in the intensity of the other emission bands.

Rieser *et al.* (1997) found that the rise of the IRSL intensity with temperature was highly dependent on the emission band measured. For the yellow-green emission band (near 2.2 eV), the intensity drops near 380 K; this is in contrast to the rise of the violet emission with temperature following the Arrhenius factor. Rieser's data clearly indicates two thermal activation energies E_{th} for this Arrhenius dependence; E_{th}=0.15 eV above 220 K, and E_{th}=0.05 eV at lower temperatures. They also noted a marked shift of the yellow-green emission to higher energy as the temperature increased.

Cathodoluminescence and radioluminescence

Much of what is known concerning the centers giving rise to the luminescence in feldspars has been inferred from cathodoluminescence CL spectra and its correlation to electron paramagnetic resonance (EPR) studies. The CL technique consists in aiming an accelerated

---

[4]That is, the luminescence acquired from a slowly accumulated dose, as occurs in nature, as opposed to a laboratory dose.

electron beam at the sample and measuring the excited luminescence. The method is relatively indiscriminate because the beam energy, typically exceeding 10 keV is sufficiently large that most luminescence centers in the mineral are excited. Three broad CL emission bands appear near 2.88 eV (430 nm), 2.1 eV (590 nm) and 1.91 eV (650 nm); it is generally presumed that these are the same bands that are present in the TL and OSL (*e.g.* Rendell and Clarke, 1997). On these bands may be superimposed narrower emission peaks due to rare-earth elements, notably Eu^{2+}, Eu^{3+}, Sm^{3+}, Dy^{3+} and Ce^{3+} (*e.g.* Krbetschek *et al.*, 1997, and references therein). The red (1.91 eV) CL appears to be absent in cryptoperthites (that is, perthites with exsolution lamella spacings less than $\sim$0.5 μm.) but is found in microperthites (lamellar spacings between $\sim$0.5 μm and 0.05 mm), Finch and Klein (1999).

The red CL has been attributed to Fe^{3+} activation. Petrov and Hafner (1988) proposed that the EPR peak at $g_{eff} = 4.3$ is due to Fe^{3+} on T_1 feldspar sites whereas the peak at $g_{eff} = 3.7$ represents Fe^{3+} on T_2 sites. Assuming this last interpretation to be correct, Finch and Klein (1999) found a strong correlation between the Fe^{3+} tetrahedral order (as indicated by the relative heights of the 3.7 and 4.3 g_{eff} peaks in EPR) and the intensity of the red CL; specifically, greater ordering on the T_1 site was correlated with brighter red CL. They suggested that the red CL arose from Fe^{3+} on the T_1 sites, whereas Fe^{3+} on T_2 sites would produce an emission in the IR.

In general, manganese contents increase by a factor of ten from K-feldspar to anorthite (Smith and Brown, 1988). Telfer and Walker (1978) and, Mora and Ramseyer (1992) have shown clear correlations between the yellow-green (2.1 eV) CL emission and Mn contents in synthetic anorthites and plagioclases.

The 3.1 eV (400 nm) band has been attributed to activation by Eu^{2+} (Mariano and Ring, 1975), Ti^{4+} (Mariano, 1988), Ga^{3+} (De St Jorre and Smith, 1988) or a paramagnetic oxygen defect (Geake *et al.*, 1973, Finch and Klein, 1999). At present, this last defect which consists of a hole centered on an Al–O–Al bridge (Al^{3+}–O^-–Al^{3+}), appears to be the most compelling possibility. This defect is present in feldspar fractions that demonstrate predominantly violet CL but is absent in fractions that display only red CL (Finch and Klein, 1999).

A recent development has been the possibility of dating using the radioluminescence (RL) in feldspars (Trautmann *et al.*, 1999). The excitation source in RL consists of a source of ionizing radiation (α, β or γ) so that the excitation energies are generally much greater

than those used in CL (∼10 keV). Rendell and Clarke (1997) find broadly similar emission bands independently of the method of excitation (RL, CL or TL) although the relative intensities of the emissions vary greatly for the three modes of excitation. The RL spectra of Trautmann *et al.* (1999) indicate a strong emission at 1.44 eV, the intensity of which decreases with the applied radiation dose. The opposite is seen for the yellow-green and violet emission bands, that is, the RL intensity increases with applied dose. The coincidence of the RL emission band with the OSL excitation resonance at 1.44 eV (described in the next section), has led Trautmann *et al.* to suggest that the 1.44 eV RL arises from the recombination of electrons into the "principal trap" responsible for the IRSL. As dose increases, the number of electrons occupying the principal trap increases. This reduces the number of traps available for recombination, so that the 1.44 eV RL intensity decreases with irradiation time. Eventually the recombination rate into the principal trap equals the eviction rate, at which time the 1.44 eV RL intensity reaches a limit.

1.4.2   The 1.44 eV resonance: luminescence models

As mentioned in the last section, there exists an excitation resonance for the OSL in the infra-red, centered at 1.44 eV. The observation of this resonance was first reported by Hütt *et al.* (1988), and has been studied by several others since then (Bailiff and Barnett, 1994; Godfrey-Smith and Cada, 1996; Barnett and Bailiff, 1997; Hütt *et al.*, 1999). The work of Ditlefsen and Huntley (1994) indicates that at high excitation energies, the luminescence is roughly exponentially dependent on the excitation energy. A more thorough discussion of these studies is found in Chapter 5, it suffices here to re-state the main features of the excitation luminescence response: a resonance at 1.44 eV with an exponential rise at high energies.

The existence of a resonance implies that the electron must be excited to a meta-stable level before proceeding to the recombination center. The simplest mechanism has the electron proceeding to the recombination center via the conduction band by thermal excitation out of the meta-stable state; this will be hereafter referred to as "Hütt's model". Hütt's model is most easily explained in terms of the semi-classical configuration curve diagram for the trap state. A number of possibilities exist; here a version of Hütt's model is shown in which the intermediate state is simply an excited state of the trap state, Figure 1.7. The

purpose of this model is to illustrate the concept of a configuration coordinates, its details are fictitious.

Figure 1.7: *The standard configuration model for the electron traps giving rise to the optically stimulated luminescence in feldspars. (a) Example of how the levels may vary with the local crystal field. (b) Effect of the configuration coordinate on the level energies. (1) Photo-ionization from the excited level to the conduction band. (2) Thermal excitation into the conduction band.*
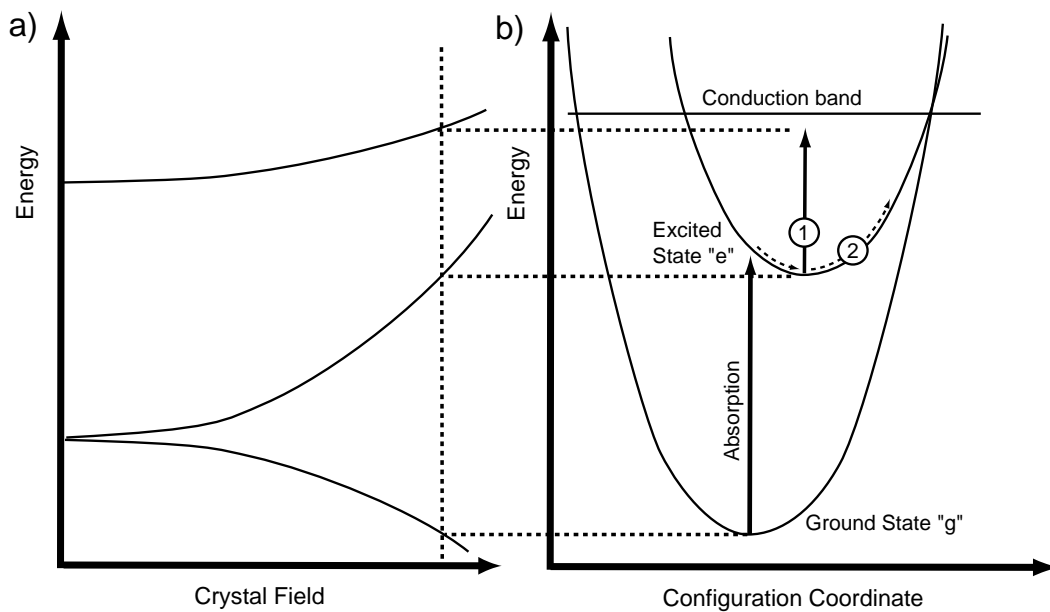
The intermediate state in this particular model is brought about by an increase in the crystal field strength that splits the trap's ground state (Figure 1.7a). Since the crystal field strength is a function of the atomic positions in the crystal, one expects that the splitting of the levels will in general be a function of the atomic positions in the vicinity of the defect.

In Figure 1.7b the crystal field splitting is a function of a one-dimensional "configuration coordinate" which represents the deviation of the atomic positions from the average configuration. In general, the crystal field splitting depends on several inter-atomic distances and angles so that the potential energy surface is multi-dimensional. Nevertheless, the one-dimensional model shown here can be used to qualitatively describe some of the more general luminescence effects.

For example, the configuration coordinate model can explain why the energy required to excite the state into the upper level optically (optical activation energy) is always larger than or equal to the energy required to effect the transition thermally (thermal activation energy). During an optical transition from the ground to the excited state, the electron proceeds vertically to the excited level in the configuration coordinate diagram. This occurs because the optical transition occurs over a time that is much shorter than the thermal relaxation time. During a thermal transition to the upper level, the electron must await a phonon interaction that places it at a point on the ground-state potential curve where it is at the same potential (or higher) as the excited level. The electron may then proceed to the excited level by tunnelling. Thus the minimum excitation energy for the thermal transition, or thermal activation energy, is the potential difference between the minima of the excited and ground state levels in configuration space. The optical activation energy is therefore seen to always be larger than the thermal activation energy. The configuration coordinate model can also be used to explain the shift (usually to shorter wavelength) of the excitation spectrum with respect to the emission spectrum, by considering a model in which the minima of the ground and excited states do not coincide in configuration space.

It should also be noted that the potential curves in the configuration coordinate model cannot intersect as drawn in Figure 1.7b; rather the two bands interact as shown in Figure 1.8. As the electron approaches the minimum gap between the bands, there exists a very high probability of tunnelling between the two bands.

In Hütt's model, the fate of the electron in the meta-stable state depends on the detailed structure of the potential curves in configuration space, the possibilities are:

- Case where the *e* and *g* levels "overlap" at a relatively low energy - In this case the electron in *e* may return to *g* by a radiationless transition, or it may absorb a photon and be excited into the conduction band, or it may be excited into the conduction band by absorption of a phonon, if the thermal energy gap is sufficiently small.

- Case where the *e* and *g* overlap at high energy, if at all - Now return to *g* through a radiationless transition is unlikely but excitation into the conduction band is still possible via either direct photo-ionization or by absorption of a phonon.

- Case where the *e* lies well below the conduction band - In this case the only possibility for excitation into the conduction band is through photo-ionization.

Figure 1.8: *Overlap of potential curves in configuration space; the potential curves never intersect. When an electron is near the gap between the two bands its wave-function strongly overlaps both states so that a transition to either state is likely.*
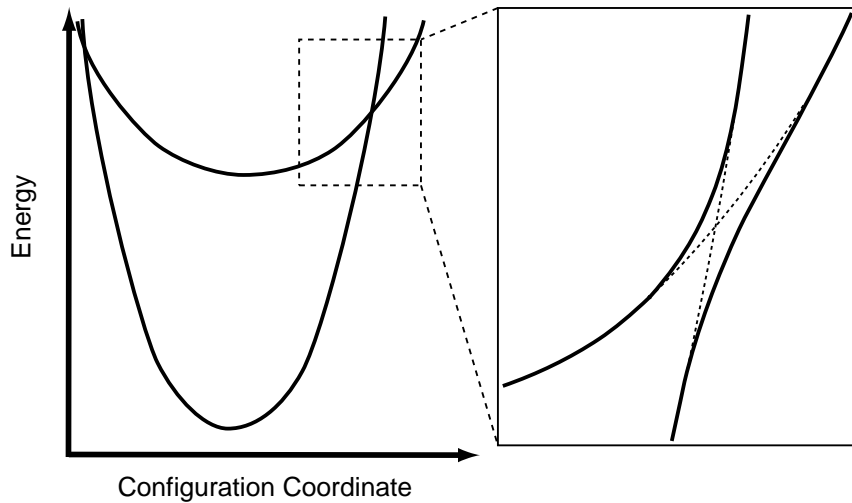
In any given case, the question as to which of the competing thermal or direct recombination and ionization processes is dominant depends on the relative rates of radiative or thermal decay of the excited state *e*. If the electron is to be excited into the conduction band, so that it may recombine at a luminescence center, then the lifetime in the excited state (that is, the inverse decay rate of *e* into *g*) must be sufficiently long to allow either thermal excitation or photo-ionization into the conduction band.

In our context, the mechanism by which the charge is excited from the intermediate level into the conduction band through absorption of a phonon is referred to as "thermally-assisted" charge transfer, whereas excitation from the intermediate level into the conduction band through absorption of a second photon is referred to as the "two-photon" process (Figure 1.9).

The two-photon process is considered unlikely for the following reason. The individual excitation rates for the two photo-excitation processes are assumed to be proportional to the excitation beam power. In the case where the lifetime in the excited state is relatively long compared to the average time taken for photo-excitation out of the excited state, the rate is entirely determined by the photo-excitation from the ground to the excited level of

the trap. The luminescence in this case would be observed to increase in proportion with the excitation beam power. However, if the lifetime in the excited state is relatively short, then both photo-excitation processes contribute to the overall recombination rate so that a dependence on the square of the excitation power is observed. This second possibility may be dismissed because the OSL intensity is in fact observed to vary in proportion to the excitation power. The first possibility seems unlikely on the basis that one would expect to see a transition from the dependence of the intensity on the square of the beam power at very low beam powers (where in effect the second case above holds) to a linear dependence at high beam powers; here again, there is no evidence for such behaviour.

Figure 1.9: *Example of a two-photon recombination process. Excitation into the meta-stable and conduction band states occurs by independent optical transitions (1) and (2).*
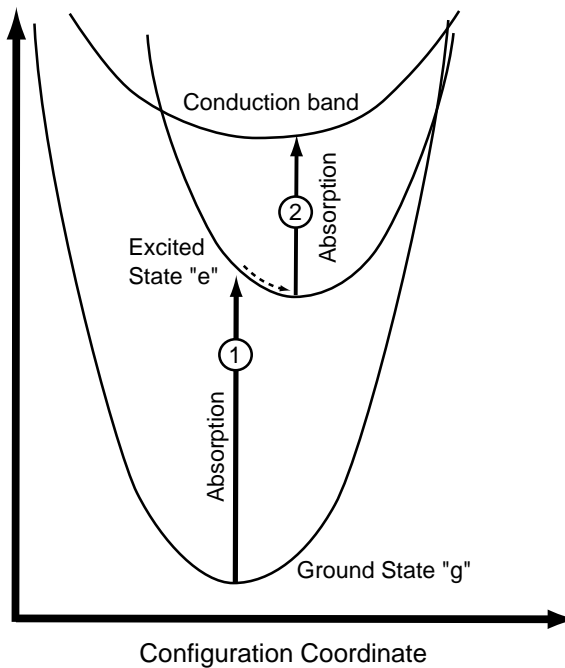
The original objection to Hütt's model centers on the thermal stability of the trap state. The energy required to thermally excite the electron out of the trap into the conduction band (thermal activation energy) may be estimated from the simple model due to Mott and Gurney (1948). According to this model the ratio of the optical to thermal activation

energies is given by the ratio of the optical to static dielectric constants in the material. The static dielectric constant of microcline is $\sim$5.6 at 50 Hz, whereas in orthoclase it is $\sim$4.5 at 100 Hz (Parkhomenko, 1967). The optical dielectric constant of alkali feldspars is close to 2.31 (Deer *et al.*, 1973) so that the ratio of the static to optical dielectric constants is roughly $\sim$2.2. The optical activation energy may be estimated from the onset of the direct-absorption regime in Spooner's (1993) bleaching spectra as being between 1.6–1.7 eV, whence a thermal activation energy of $\sim$0.75 eV. In general, the thermal lifetime τ of a lattice state is given by,

$$\tau = s^{-1} e^{E_t/k_b T} \tag{1.1}$$

where E_t is the thermal activation energy and s is the frequency factor, which is generally material dependent and may be thought of as an "average" phonon frequency. One expects s to be of the order of a typical lattice vibration frequency, that is $\sim 10^{13}$ s^{-1} (Aitken, 1985). Using our estimate of 0.75 eV for E_t, one finds a lifetime of the order 1 s at room temperature which is almost 11 orders of magnitude smaller than the observed thermal lifetime of $\geq 10^6$ years. The expected thermal activation energy should in fact be approximately >1.4 eV (which is almost the same as the optical activation energy) to obtain the required thermal stability. Clearly, the expectation from Mott and Gurney's model cannot be reconciled with Hütt's model for the traps.

Whether this is an indication of the failure of Hütt's model depends on how much trust is placed in Mott and Gurney's somewhat heuristic argument. Thomas and Houston (1964) obtained good agreement between the optical and thermal activation energies of Cr^{3+} transitions in MgO determined using Mott and Gurney's theory and experimental values. Similar agreement with Mott and Gurney's model was found by Chao (1971) for the V_1 center in Mg0.

The OSL depends strongly on temperature, the intensity increasing with temperature in proportion to the Boltzmann factor, $e^{-E_a/k_b T}$, where E_a is a thermal activation energy[5]. E_a is generally found to reach a local minimum near the 1.44 eV resonance (Bøtter-Jensen *et al.*, 1994; Poolton *et al.*, 1994; Poolton *et al.*, 1995). At least one other minimum in E_a was observed at excitation photon energies of 2.0 eV.

Poolton *et al.*'s (1994) explanation for the increase in E_a at lower energies is incorrect. They expect that E_a is simply the difference between the depth of the trap below the con-

---

[5]E_a should not to be confused with the thermal activation energy E_t for the deep trap discussed earlier.

duction band and the photon energy, so that E_a is linearly related to the photon energy at low energies. However, direct excitation from the excited state into the conduction band by absorption of a phonon is highly unlikely. It is much more probable that the electron relaxes into the equilibrium position of the excited state by emission of a phonon(s) before it is excited into the conduction band. Therefore, the effect of the excitation energy on E_a is likely much less (and certainly more complicated) than that anticipated by these authors. It is difficult to reconcile these results with Hütt's model because it does not provide an explanation as to why E_a reaches a minimum value near the excitation resonance.

It is known that the time decay of the OSL in feldspars during excitation follows an inverse power law of the form, $A/(1+t/t_0)^\alpha$ (Bailiff and Poolton, 1991; Bailiff and Barnett, 1994). Poolton *et al.* (1994) found that the shape of the initial portion of the IRSL decay curve can be modified by arresting the luminescence decay (*i.e.* blocking the excitation source), letting the sample rest for some time and then turning on the excitation so that the subsequent decay can be measured. Somewhat non-intuitively, the luminescence following the initial illumination period starts off at a slightly higher intensity than the final intensity of the initial decay curve. Instead of decreasing, the luminescence intensity increases to a maximum before the decay is observed. The time (after the beginning of the second illumination) at which the luminescence maximum was reached was found to increase as the length of the initial illumination period increased.

McKeever *et al.* (1997) further studied this effect and found that the appearance of the "peak" in the decay curve was dependent on the excitation energy as well the intensity of the illumination; for green excitation the peak only appeared at low illumination intensities. Poolton *et al.* (1994) and McKeever *et al.* (1997) suggested that this may be evidence for a donor-acceptor pair recombination mechanism in feldspar IRSL. The idea is that the recombination rate is highly dependent on the average donor-acceptor pair distances in the material. During illumination, the distribution of donor-acceptor pair distances changes since the closely separated pairs are the first to recombine. Since the recombination time-constant for the more distant pairs is much longer than for the close pairs, a delay is introduced between the time the illumination begins and the time at which the luminescence intensity reaches a maximum. These ideas are illustrated in Figure 1.10.

The few alternatives to Hütt's model that have been proposed concentrate on explaining the apparent thermal activation of the recombination process; the three models of note are,

Figure 1.10: *Left: Schematic diagram showing the effect of the illumination time on the shape of the decay curve. Curve 1 is the initial IRSL decay curve. If the illumination is halted and the sample is left for some time (or heated at low temperature for a short time) then the luminescence intensity once the illumination is turned back on (curve 2) is slightly higher than at the end of the initial decay curve. The sign of the initial slope of the decay curve changes with increased illumination time (curves 3 and 4). Right: Interpretation of this effect in terms of the change in the donor-acceptor pair distance distribution G(r) with increased illumination time. As illumination time increases, the average donor-acceptor distance increases due to depletion of the closely separated pairs.*
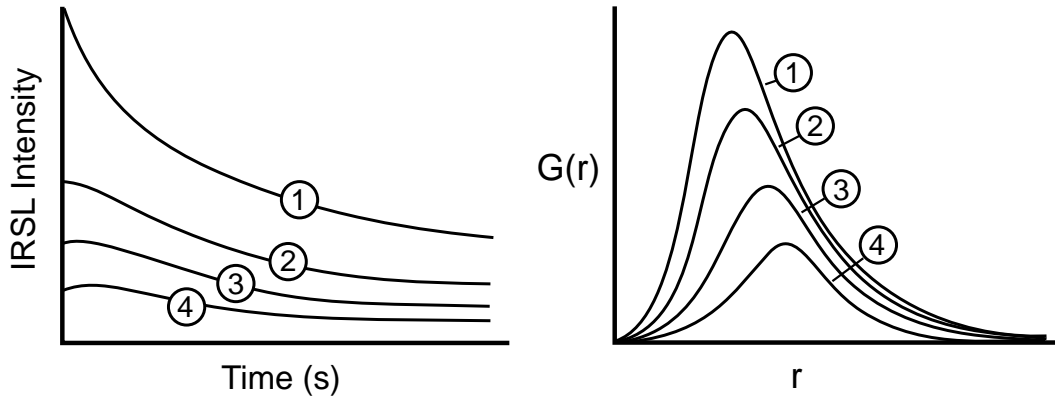
- Hopping among localized conduction-band tail states.

- Model with significant re-trapping probability into thermally shallow traps.

- Donor-acceptor recombination with hopping among the acceptor states.

Schematic energy-band diagrams for these models are shown in Figure 1.11. The first mechanisms is due to Poolton *et al.* (1995) and is a refinement of Hütt's model to explain the presence of a thermal activation energy at high excitation photon energies. According to this view, a thermal activation energy exists even for direct photo-excitation into the conduction band due to the presence of localized states on the edge of the conduction band. The electron is transported to the recombination center by hopping between these shallow localized states. Since the hopping is thermally activated, the recombination rate will necessarily have a strong temperature dependence.

Figure 1.11: *Models proposed to explain the temperature dependence of the IRSL recombination: (a) Hütt's thermally assisted excitation into the conduction band (Hütt et al., 1988), (b) conduction band "tail-state" hopping (Poolton et al., 1995), (c) hopping through shallow traps (Markey et al., 1995), (d) donor-acceptor state hopping (Poolton et al., 1994).*
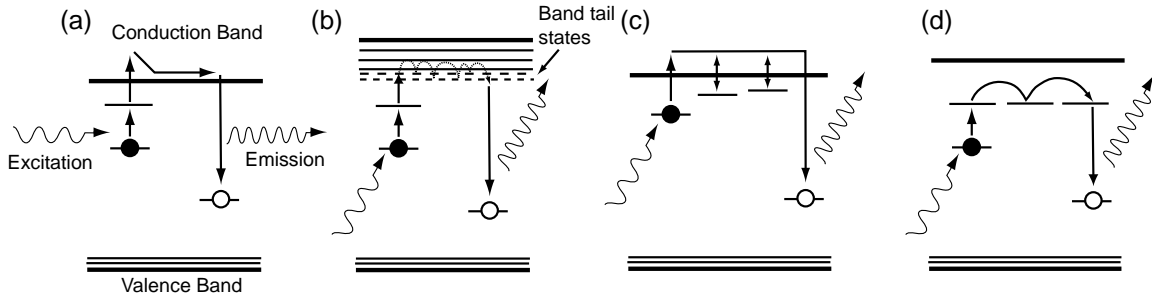
The second model is due to Markey *et al.* (1995), here the thermal activation energy arises from the energy required to excite the electrons out of shallow traps into the conduction band. Here again, the shallow traps must contribute to the conduction of the electrons from the optical trap to the recombination centers for a temperature dependence to arise. Note that Markey's model as shown in Figure 1.11 cannot account for the excitation resonance. If this model is combined with Hütt's model (to explain the resonance) then the temperature dependence would arise both from hopping between the shallow traps as well as the thermal eviction out of the excited state of the trap.

Poolton *et al.* (1994) introduced the third model to explain the influence of the illumination time on the shape of the decay curve (discussed above). The donor-acceptor recombination itself is not thermally activated (the recombination occurs by tunnelling), so that a thermally activated hopping motion between acceptor states was postulated to explain the temperature dependence.

The principal difficulty with these models is that although they successfully explain the increase of the luminescence with temperature, they entirely fail to explain the increase of *the total integrated luminescence* with temperature. In fact, temperature has little effect on the kinetics of the decay, as will be discussed in the later chapters of this thesis.

1.5   Overview

The measurement of feldspar luminescence spectra, excitation spectra and the lumines-cence decay kinetics are the three core topics in this work. Luminescence emission spectra principally provide information about the recombination centers in the mineral. Few com-parative studies of infrared stimulated luminescence (IRSL) spectra exist and these have generally not involved measurements below 1.9 eV. A new high-throughput/low-resolution CCD-based spectrometer was designed to achieve good sensitivity over the 250–1000 nm band (Chapter 2). This instrument permitted spectral measurements of an IRSL emission band at 1.76 eV that has not been previously achieved. In addition, spectral measurements of the faint phosphorescence following irradiation and infrared optical excitation of the sample were possible. The term phosphorescence is used here to mean luminescence in the absence of an excitation source other than thermal excitation[6]. As will be seen in Chapter 4, the emission spectra differ significantly for the different modes of luminescence excitation (*i.e.* IRSL, post-irradiation phosphorescence and post-illumination phosphorescence).

Whereas luminescence spectra provide information about the luminescence centers, and their possible connection to particular traps, excitation response spectra provide informa-tion about the traps themselves. Precious few comparative studies of excitation spectra for feldspars of differing composition have been produced, and these have always involved measurement of the violet emission band of K-feldspar. The excitation spectra in this study involve an extensive range of samples derived both from rocks and sediments and have been performed for both the violet and yellow-green (Na-feldspar) emission bands, as well as the UV band in one sample (K3). In addition, the effect of the polarization of the exci-tation light on the excitation response spectrum was investigated in an oriented microcline crystal (K7). The excitation spectra were fit to a more physically meaningful model which accounts for departures from the Gaussian line-shape assumed previously.

Chapter 7 describes an experiment in which the slope of the luminescence decay curve upon "shine-down"[7] as a function of the initial intensity was measured. The particular scaling of the slope with the initial intensity observed in such an experiment imposes re-

---

[6]In this sense thermoluminescence would be classified as phosphorescence.

[7]"Shinedown" refers to the decay of the optically stimulated luminescence intensity during illumination by excitation photons.

strictions on the possible models for the electron traps.

The necessity for a thorough investigation of the luminescence decay kinetics became apparent from our measurements of the change in the IRSL spectrum upon "shine-down" decay of the luminescence. The term shine-down is used to describe the time decay of the luminescence when a sample is exposed to excitation light. In general, the shape of the decay curve alone provides little information as to the mechanism of the excitation–recombination process (see Chapter 10). Nevertheless, important information can be derived from the change in the decay curve as a function of the possible physical parameters affecting the luminescence (*e.g.* temperature, excitation energy and radiation dose). Chapter 6 involves a detailed investigation of the decay kinetics in a K-feldspar sample. In Chapter 10 an empirical model to explain the behaviour of the decay parameters is presented.

Two additional studies are included that do not have direct bearing on the principal goal of this dissertation. False colour images of the IRSL of a few bright samples were produced, showing the spatial distribution of the violet and yellow-green emission bands in the specimen; these are discussed in Chapter 8. A spectral study of the IRSL produced by feldspar inclusions in quartz is presented in Chapter 9.

Chapter 2

The Luminescence Spectrometer

2.1 Review of TL/OSL spectrometers

Several methods have been used to measure the spectral emission of the dim TL and OSL in minerals, these are summarized in Table 2.1. The simplest input optics for a spectrometer employs lenses to transfer the light from the sample to the spectrometer input slit. An example of a system with refractive input optics is that of Luff and Townsend (1992). This system employed two entirely separate f/2 spectrometers, one to measure the short wavelength range (200–450 nm) and the second to cover longer wavelengths (400–800 nm). This configuration was necessary to compensate for the narrow spectral responses of the multi-anode photomultiplier tubes used in the detection systems.

An f/4 charge-coupled detector (CCD) based system employing refractive optics was constructed by Rieser *et al.* (1994). The use of a CCD detector allowed for a much wider spectral response, obviating the need for two detection systems to cover the 200–800 nm range. Rieser *et al.* (1999) built an improved CCD based system in which the input optics consisted of a combination of a condenser lens and a fast ellipsoidal mirror. The first CCD based thermoluminescence spectrometer was developed by Bakas (1984). The main drawbacks of Bakas's system was the the limited numerical aperture of the optics due to his use of a prism dispersion element. CCD based systems did not come into common usage until the 1990's due to the poor quantum efficiency of CCD sensors in the violet and UV.

Optically stimulated luminescence spectra were first measured by Huntley *et al.* (1991) using an f/4 spectrometer fitted with a microchannel plate (MCP) detector with long-wavelength

response to 550 nm. Martini *et al.*'s (1996) system employed a microchannel plate with greater spectral range, however the principal improvement was his use of efficient off-axis parabolic mirrors as input optics. The only disadvantage of Martini's system is the cost of the input optics, and its relatively small spectral range (200–700 nm) as compared to CCD's.

A more unusual approach is Brovetto *et al.*'s (1990) use of a continuous, rotating inter- ference filter to separate out the spectrum. It is worthy of mention because it has, at least in principle, the possibility of a very high detection efficiency, albeit at a significantly reduced resolution. One must ensure in such a design that one limits the numerical aperture of the input beam, otherwise the interference filter's band-pass will broaden for rays that are not at a normal incidence to the filter. Bailiff *et al.* (1977) used interference filters to measure TL in the 340–640 nm range. Glass absorption filters have been used by Short (2003) and, Jungner and Huntley (1991) to obtain low resolution spectra with little expense. The prin- cipal limitation of such systems is the loss of wavelength multiplexing which means that several samples (or measurements) are required to obtain a single spectrum.

The instrument with the highest throughput is the Fourier transform spectrometer. The sample is placed at the input of a Twyman-Green Michelson interferometer. With the in- terferometer mirrors aligned and a monochromatic source on the input, the output of the interferometer should vary sinusoidally with intensity as one of the interferometer mirrors is moved along the optical axis. Thus, the output intensity as a function of mirror position is the Fourier transform of the input spectrum. The spectral distribution is recovered by taking the inverse Fourier transform of the intensity versus mirror position data.

An example of such a system is that developed by Prescott *et al.* (1988) for use in mea- suring thermoluminescence spectra. At short wavelengths, the instrument is principally limited by the difficulty in maintaining alignment of the mirrors. Otherwise, the sensitivity is only limited by the desired resolution (controlled by the input collection angle) and the detector response. The maximum étendue of Prescott's instrument as defined by the prod- uct of the maximum accepted beam area and the solid angle is approximately 180π mm^2, with a resolution of 20 nm. This assumes a sample of diameter equivalent to the limiting aperture ($\sim$5 cm). In practice the sample is much smaller than this (1 cm in diameter), so the effective étendue is actually $\sim$7π mm^2. For comparison, the diffraction grating spec- trometer presently to be described has an étendue of 0.74π mm^2 at a resolution of 25 nm, barely 1/10 the throughput of Prescott's instrument.

Type	Optics	Sensor	f#	$\Delta\lambda$ (nm)	Advantages	Disadvantages	Reference
Grating	lenses	MCP (two)	2	200–800	High detection sensitivity	Chromatic aberration, low resolution, high cost.	Luff and Townsend (1992)
Grating	lenses	CCD	4	200–800	High resolution.	Chromatic aberration, low light collection.	Rieser et al. (1994)
Grating	lens & mirror	CCD	4	200–800	High resolution, moderate light collection.	Awkward sample placement.	Rieser et al. (1999)
Grating	mirrors	MCP	6	300–750	High detection sensitivity, no chromatism.	Poor IR sensitivity, poor light collection.	Huntley et al. (1991)
Grating	mirrors	MCP	2	200–700	High detection sensitivity, no chromatism, good light collection.	Poor IR sensitivity.	Martini et al. (1996)
Grating	fiber optic	PDA	3.8	250–800	Fair UV response	Poor IR response, low light collection.	Piters et al. (1993)
Grating	**mirrors**	**CCD**	**2**	**250–1000**	**Wide bandwidth, no chromatism, versatile geometry.**	**Moderate detection sensitivity.**	**Present study.**
Prism	lenses	CCD	~7	380–880	Moderate cost.	Chromatism in the optics, low resolution, poor light collection.	Bakas (1984)
Interference filters	lenses	PMT	n.a.	375–730 340–640	Low-cost, good throughput.	No wavelength multiplexing. Poor resolution.	Brovetto et al. (1990) Bailiff et al. (1977)
Absorption filters	mirror(s)	PMT	n.a.	380–600	Low-cost, good throughput.	No wavelength multiplexing. Poor resolution.	Short (2003), Jungner and Huntley (1991)
Fourier transform	lenses	PMT	1.75	350–600	Excellent throughput.	Poor time resolution, high cost and long development time.	Prescott et al. (1988)

Table 2.1: Comparison of TL/OSL spectrometers. PMT: photomultiplier tube, CCD: charge coupled device, MCP: microchannel plate, PDA: photodiode array. Design described in this study is in bold typeface.

The principal limitation of the Fourier transform spectrometer is that, since it is a scanning instrument, it does not acquire the spectral information in parallel. Artifacts may arise from the variation of the sample intensity with time. It is essential that the excitation source be very stable to avoid the introduction of spurious short wavelength artifacts when measuring optically stimulated luminescence. Long-term variations, for example the decay of the sample luminescence with time, must be corrected for before the Fourier spectrum is inverted.

2.2 Input collection optics

2.2.1 Refractive vs. reflective optics

The calibration of the spectral sensitivity of a system that employs refracting input optics is nontrivial where large bandwidths are involved. In general, this calibration must be done whenever any change is made in the system; either a shift in the position of the lenses or a change of slit width. This is due to the displacement of the focal point for different coloured rays at the input slit. Over the visible near-IR band (200 nm to 1000 nm) it is not possible to produce fast lenses (*i.e.* f/3 or less) with sufficient chromatic correction to avoid this problem.

As a first example, consider using a single lens to transfer the light to the slit. For the ray-tracing analysis an f/2 biconvex lens made of BK7[1] is selected. A symmetric biconvex lens is the optimal choice in this case because it minimizes spherical aberration and field curvature. The lens diameter and focal length, F, has been set to 5 cm so that the effective focal ratio is f/2 when the source and image distances are equal.

The spot diagrams in Figure 2.1 represent the intersection of randomly oriented rays departing from the point source (approximately $2F$ away from the lens) at the image plane. The image plane of course is ill-defined due to geometric aberrations so the best focus plane for 590 nm light has been selected as the reference. The spot diagrams show that geometric aberrations[2] outweigh chromatic aberration in the simple biconvex lens, that is, the focus spot diameters are roughly the same at each of the three wavelengths calculated.

---

[1]The most commonly used low-dispersion crown glass; n_{590nm}=1.517.
[2]Principally spherical aberration and field curvature.

Figure 2.1: *Ray tracing spot diagrams for a biconvex lens (standard low-dispersion crown glass, BK7) and an infinity corrected achromat. Both series of spot diagrams are in the plane of best focus of 590 nm light. Geometric aberrations predominate over chromatic aberration in both cases.*
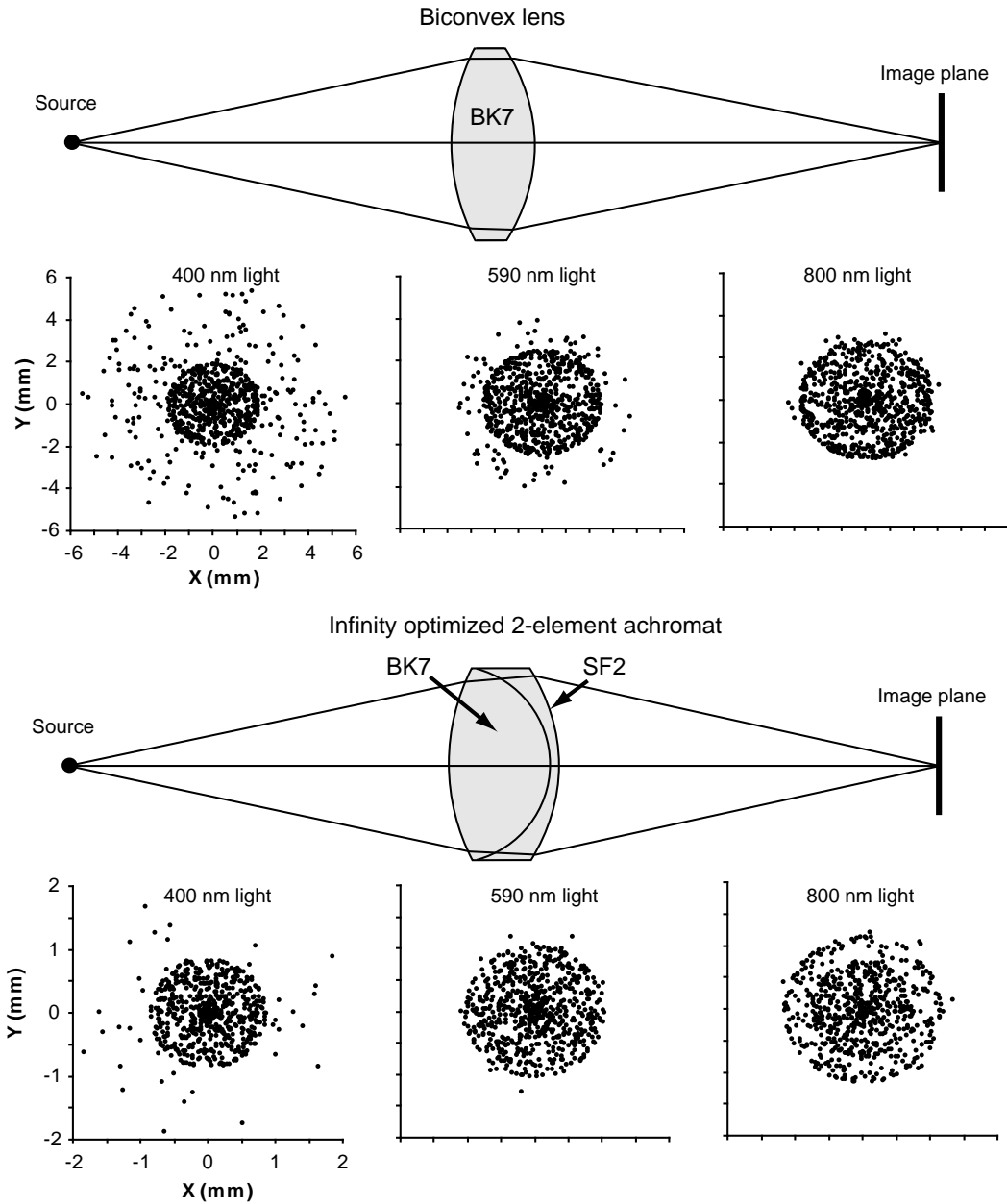
If a "standard" achromat[3] is selected instead, a similar result is found; spherical aberration (S.A.) is the dominant aberration (see lower half of Figure 2.1. However, both spherical and chromatic aberration have been reduced by roughly a factor of 3 over the single lens design[4]. Neither the achromat nor the biconvex lens are optimal for the present purpose since the focus spot in both cases is wider than our maximum spectrometer slit size of 1.24 mm. On the other hand, the effects of chromatism mentioned earlier would not significantly affect these lenses since they are so severely limited by spherical aberration.

A preferable transfer system is a pair of plano-convex lenses with the convex surfaces almost touching as used by Luff and Townsend (1992), Figure 2.2. This is the simplest two element projection system; its principal improvement over the single lens is a reduction in spherical aberration. In the analysis of this system lenses made of BK-7 glass have been selected, however the curvature of all four surfaces has been allowed to vary to minimize S.A. The optimized system nevertheless remains very close to a system with two equal focal length plano-convex lenses.

As can be seen in Figure 2.2 aberrations are considerably reduced in the dual lens condenser as compared to the single element design. The spot size is comparable to the infinity corrected achromat and chromatic aberration is now limiting aberration. It is clear from the spot diagram that chromatism is by no means negligible over the wavelength range of interest in our application. Note that the spot diagram is only shown at the best focus of 590 nm light; were the image plane shifted slightly along the optical axis (z-axis) towards the lens, the focus for 400 nm rays would be optimized. Similarly, a shift away from the lens would cause the 800 nm light cone to come into better focus. A shift of the image plane between experiments would cause a significant change in the spectral response of the spectrometer.

If response is required below 350 nm, the use of quartz or fused silica lenses is necessary. These materials will produce slightly less chromatism than typical crown-glass since the dispersion index (Abbe number, V_d) of fused silica is 67.7, whereas in BK-7 it is 64.2.

The simple two-lens condenser can be improved by replacing the plano-convex lenses

---

[3]By "standard" is meant an achromat that has been corrected for use in the visible band and optimized for a source at infinity.

[4]The reason S.A. is reduced in this case is that the positive S.A. of the crown lens partially cancels the negative S.A. of the flint element.

Figure 2.2: *Ray tracing spot diagrams for a simple two element condenser (low-dispersion crown glass, BK7). Shown are the spot diagrams at the plane of best focus of 590 nm light, for a source on the optical axis (top) and +5mm above the optical axis (bottom). Chromatic aberration is dominant.*
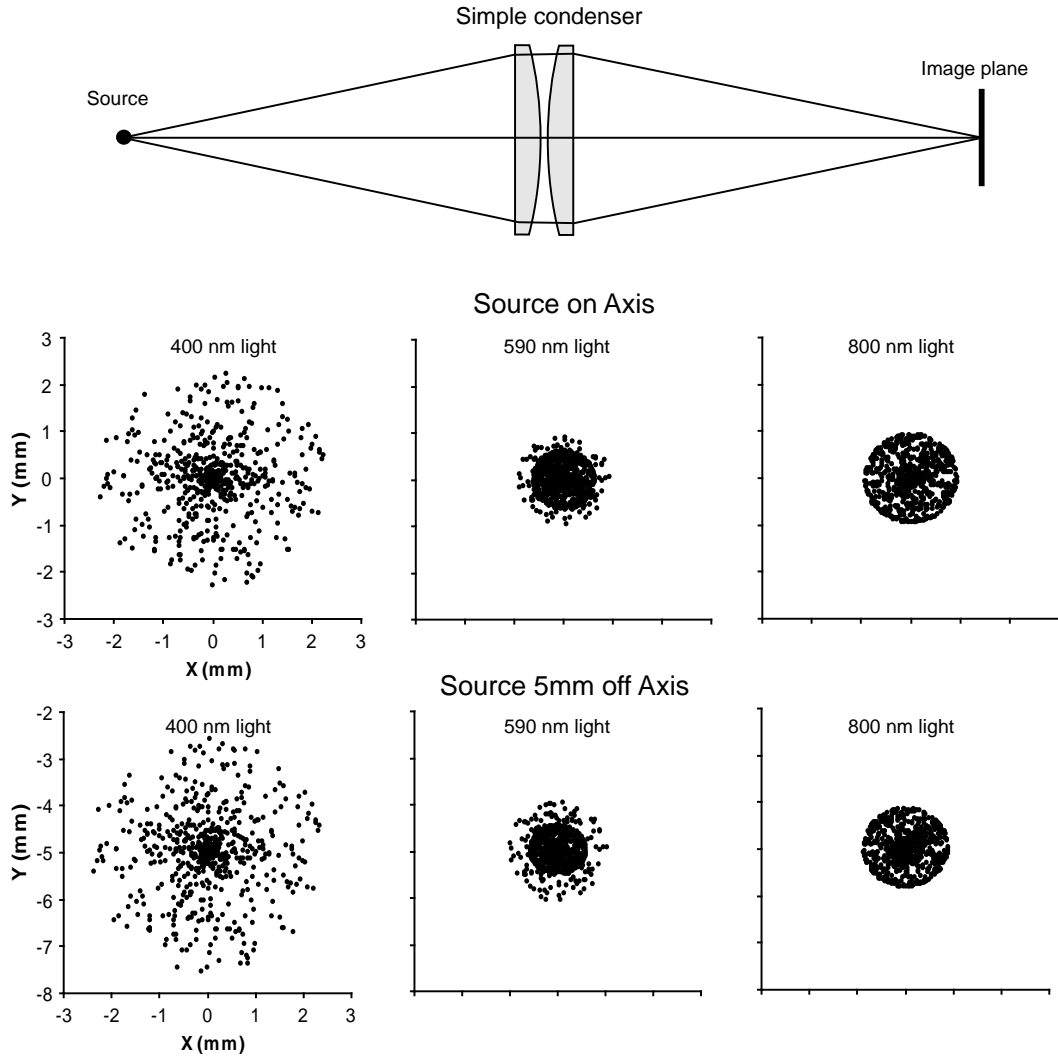
with two standard f/2 achromats. As can be seen in Figure 2.3 chromatic aberration is sufficiently corrected in this system that the problem of a focus-dependent spectral throughput is minimal. In addition, the additional 2 surfaces allows spherical aberration to be reduced

to acceptable levels. Unfortunately, the correction for chromatic aberration is only good over a limited range, in this case from 400–700 nm. Other disadvantages of this system are the slight astigmatism, and the loss of throughput in the UV due to absorption in the glass.

Figure 2.3: *Ray tracing spot diagrams for an achromatic four element condenser (crown BK7 glass, flint SF2 glass) optimized for use between 400 nm and 700 nm. Shown are the spot diagrams at the plane of best focus of 590 nm light, for a source on the optical axis (top) and +5mm above the optical axis (bottom). Chromatic aberration is dominant, astigmatism is slight.*
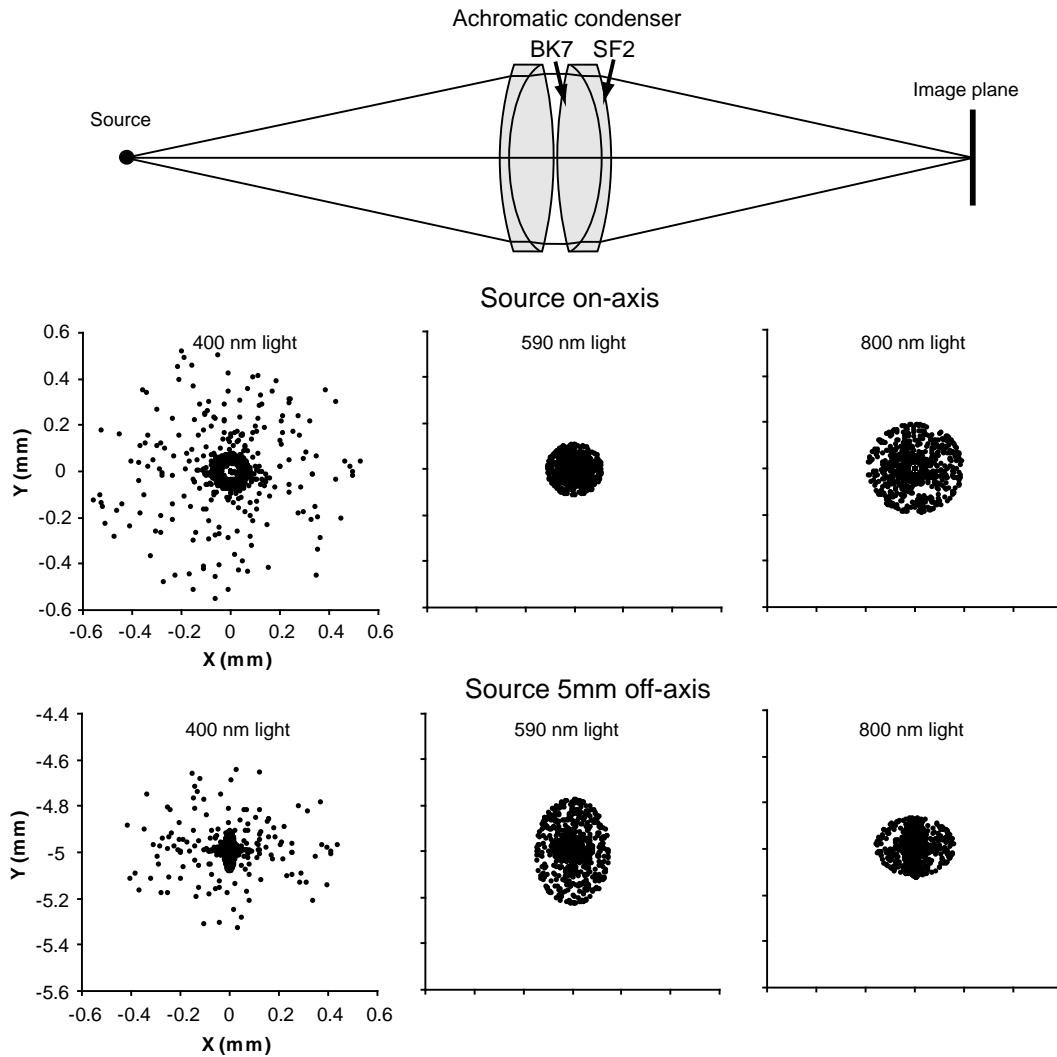
It should be apparent from the above discussion that the use of lens optics for the present application is fraught with difficulty. In addition to the problems of chromatism and geometric aberrations, a lens transfer system leaves very little space between the sample and the lens for the insertion of additional instrumentation. The use of large, short-focus achromats is a costly solution to this problem.

2.2.2 Spherical mirror optics

Mirrors are easily produced in large diameters and do not suffer from chromatic aberration. Although mirror optics suffer from geometric aberrations, a careful choice of geometry can make use of these aberrations to the benefit of light collection efficiency.

The difficulty in using mirrors for input optics is that at high numerical apertures an off-axis configuration must be used to avoid blocking of the reflected beam by the sample. One solution to this problem is to use two identical off-axis paraboloidal mirrors to transfer the light from the sample to the spectrometer input, as was done by Martini *et al.* (1996). The only optical shortfall of this arrangement is the presence of serious comatic aberration for sources slightly off the optical axis. The only other prohibitive factor in implementing such a system is cost.

Short focus spherical mirrors are relatively easily produced by standard simple optical fabrication techniques. Spherical mirrors have the useful property that spherical aberration is absent as long as the object and image lies at the radius of curvature of the mirror. This is easily understood if one considers that the tangent plane of any point on a sphere is always perpendicular to the line from this point to the center of curvature. Thus, any light ray originating at the center of curvature of the mirror is reflected back to its origin.

If the collection mirror is tilted so that the sample does not lie on the optical axis, then the reflected cone can be picked up with a small relay mirror and directed to the spectrometer slit. This off-axis configuration introduces a large amount of astigmatism into the system, however the astigmatism can be used to the benefit of light collection if the focus is adjusted appropriately.

When a beam of light is obliquely incident on a mirror or lens then the image of the source becomes a pair of focal lines (Kingslake, 1978). The *sagittal* focus line is oriented radially in the field of view whereas the other focal line is oriented tangentially in the field

(*tangential* focus line). In the case of a concave mirror, the tangential focus is located slightly closer to the mirror than the sagittal focus (as measured along the optical axis). The best "average" focus is located mid-way between the sagittal and tangential foci.

Figure 2.4: *Ray tracing spot diagrams for a 25 cm diameter f/1 mirror (i.e. 50 cm radius of curvature). Image of a point source shifted 2.5 cm along the x-axis away from the center of curvature at z = 50 cm (z is measured along the optical axis, with z=0 at the mirror surface). The image plane for the tangential focus is at Δz = -1.22 mm (far left). The sagittal focus occurs at Δz = +1.22 mm (far right).*
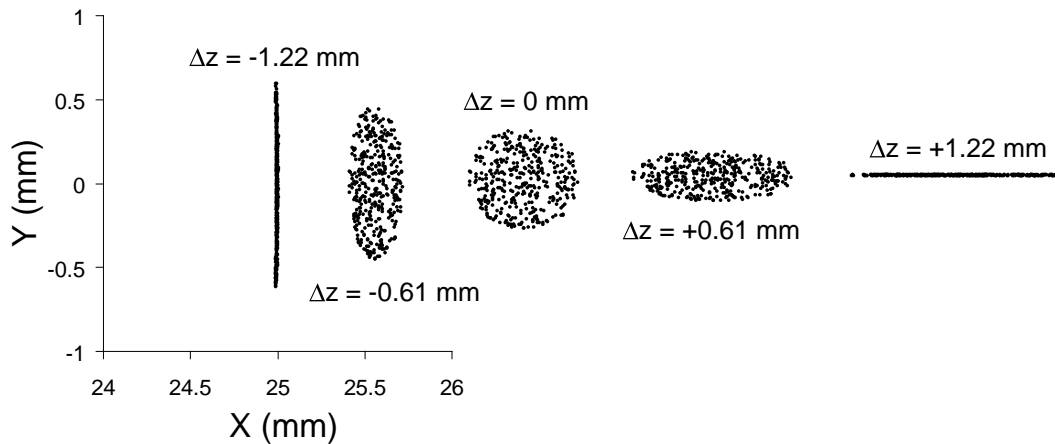
One may adjust the position of the spectrometer input slit along the optical axis so that it is parallel to one of the astigmatic focus lines. In this way resolution in the direction of the slit length is traded off for greater concentration of light along the slit width. The spot diagrams in Figure 2.4 demonstrate this effect in a 25 cm diameter f/1 mirror with the source shifted along the x axis by 2.5 cm from the center of curvature (the optical axis is along z).

2.2.3   Fabrication of the collection mirror

The selected diffraction gratings were f/2 and f/2.5 concave holographic gratings with nominal bandwidths of 190–800 nm and 500–1200 nm respectively. A 28 cm diameter f/0.8 spherical mirror was custom fabricated to match the focal ratio of these gratings (note that

the sample sits at the radius of curvature of this mirror, not its focus, hence the need for an ~f/1 mirror). A large collection mirror was required to provide clearance for the relay mirror (used to direct the collected beam into the spectrometer slit) while minimizing the distance of the sample off-axis.

The mirror was fabricated by slumping 1/2" plate glass into an approximately shaped spherical mold at 600 °C. The glass blank was annealed and then allowed to cool slowly to room temperature over 7 hours. A convex tool of hard ceramic tiles embedded in plaster was made to match the curvature of the slumped glass blank. By using successively finer grades of abrasives this tool was used to grind the glass blank so that the surface was spherical. The glass was polished using a honeycomb foundation wax lap (cemented to the grinding tool) and cerium-oxide polishing compound. Additional details on the fabrication of the glass blank are provided in Appendix A.

Optical testing was not performed because this optical generation technique usually yields optics that are spherical to within several wavelengths of sodium D-light. Such accuracy is perfectly acceptable for the present application. The mirror was coated with bare evaporated aluminum to ensure high reflectivity over a broad wavelength band[5].

2.2.4   Spectrometer throughput and resolution

The spectrometer throughput is characterized by the geometric étendue, *G*, which is loosely defined as the product of the accepted solid angle with the area of the source. More exactly, the étendue is defined as,

$$G = \oint \int_0^{4\pi} dS \, dQ \tag{2.1}$$

where the integral is over the source area dS and the solid angle dQ. For a conical beam of half angle Ω whose axis is perpendicular to the source of area S this becomes,

$$G = 4\pi \, S \, \sin^2 \frac{\Omega}{2} \tag{2.2}$$

The bandpass for a given slit width may be calculated as follows. The grating equation is,

$$d(\sin\alpha + \sin\beta) = k\lambda \tag{2.3}$$

---

[5]The reflectivity of aluminum is relatively flat for wavelengths longer than 190 nm

where d is the grating spacing, k is the grating order, and α and β are the angles of the incident and diffracted beams with respect to the normal to the grating. If the detector plane is perpendicular to the diffracted beam, then the linear dispersion at the detector plane is the product of the angular dispersion with the focal length of the imaging optic f_2,

$$\frac{\partial x}{\partial \lambda} = \frac{\partial \beta}{\partial \lambda} \qquad (2.4)$$

where x is the distance on the detector plane. The resolution of the spectrometer is determined from the width of the image of the slit at the detector, w'. Since w' is small one may approximate the spectral width $\delta \lambda$ corresponding to w' from the last equation as,

$$\delta \lambda = \frac{w'}{f_2} \left(\frac{\partial \beta}{\partial \lambda} \right)^{-1} \qquad (2.5)$$

Differentiating the grating equation while taking α as fixed yields,

$$\frac{\partial \beta}{\partial \lambda} = \frac{k}{d \cos \beta} \qquad (2.6)$$

Combining the above with Equation 2.5 one finds,

$$\delta \lambda = \frac{w' d \cos \beta}{f_2 k} \qquad (2.7)$$

The width of the image of the slit, w' relative to the slit width itself, w is determined by the magnification of the instrument and is generally given by (Hutley, 1982),

$$w' = w \frac{f_2}{f_1} \frac{\cos \alpha}{\cos \beta} \qquad (2.8)$$

where f_1 is the focal length of the optic collimating the beam from the slit. For a concave imaging grating the grating itself acts as the imaging optic so that $f_1 \simeq f_2 = f$. Combining the previous two equations one finds,

$$\delta \lambda = \frac{w d \cos \alpha}{k f} \qquad (2.9)$$

For the first order of the 190–800 nm blaze holographic grating and a 20 nm bandpass; $d = 3.51 \ \mu$m, $f = 137$ mm and $\alpha = 5.73^{\rm o}$, whence a slit width of $w = 0.78$ mm.

In practice it was found that the 632.8 nm He-Ne emission produced a line of spectral width ~ 25 nm using a slit width of 1.24 mm. This line width is somewhat smaller than

the 32 nm line width expected for a 1.24 mm slit, this may be explained by the presence of other factors that effectively limit the width of the beam accepted into the spectrometer (*e.g.* spatial non-uniformity of the illumination at the slit). At a bandpass of 25 nm, a slit width of 1.24 mm, a slit height of 10 mm and $\Omega = 14.04^\circ$ for f/2 input optics, the étendue of the system is, $G = 0.74\pi$. Of course, this assumes that the sample is shaped in a manner that makes optimal use of the slit. For this reason, samples were prepared on long narrow planchets not significantly wider than the maximum slit width (1.24 mm).

2.3   Optical and mechanical layout

2.3.1   Input optics

The optical layout is shown in Figure 2.5. The sample rests on a gimbal mounting that can be rotated through three axes and shifted vertically to achieve focus. One of the rotational axes of the gimbal mounting ensures that the sample plane is perpendicular to the optical axis, another axis aligns the planchet slot so that its image is parallel to the slit. This mounting was interchangeable with a heating strip to investigate thermal effects.

The collection mirror mount is fitted with horizontal and vertical tilt adjustments to allow simple centering of the sample image on the slit. Sliding filter holders were placed between the adjustable slit and main relay mirror, and in front of the excitation illumination port.

2.3.2   The Spectrometer

The spectrometer proper was designed as a separate unit so that it could be removed from the sample chamber and used in other experiments. The use of concave holographic gratings considerably simplified the optical layout; a single relay mirror and a diffraction grating constitute all of the optical elements. A top-view of the instrument is shown in Figure 2.6. An electronic shutter on the input of the spectrometer allows computer control of the CCD detector exposure time to times as short as 50 ms. During use, dry nitrogen gas is blown into the chamber to prevent frosting of the cooled CCD sensor.

Figure 2.5: *Layout of the spectrometer input optics. The spectrometer proper has been rotated 90° about the optical axis to show the complete optical path through the instrument.*
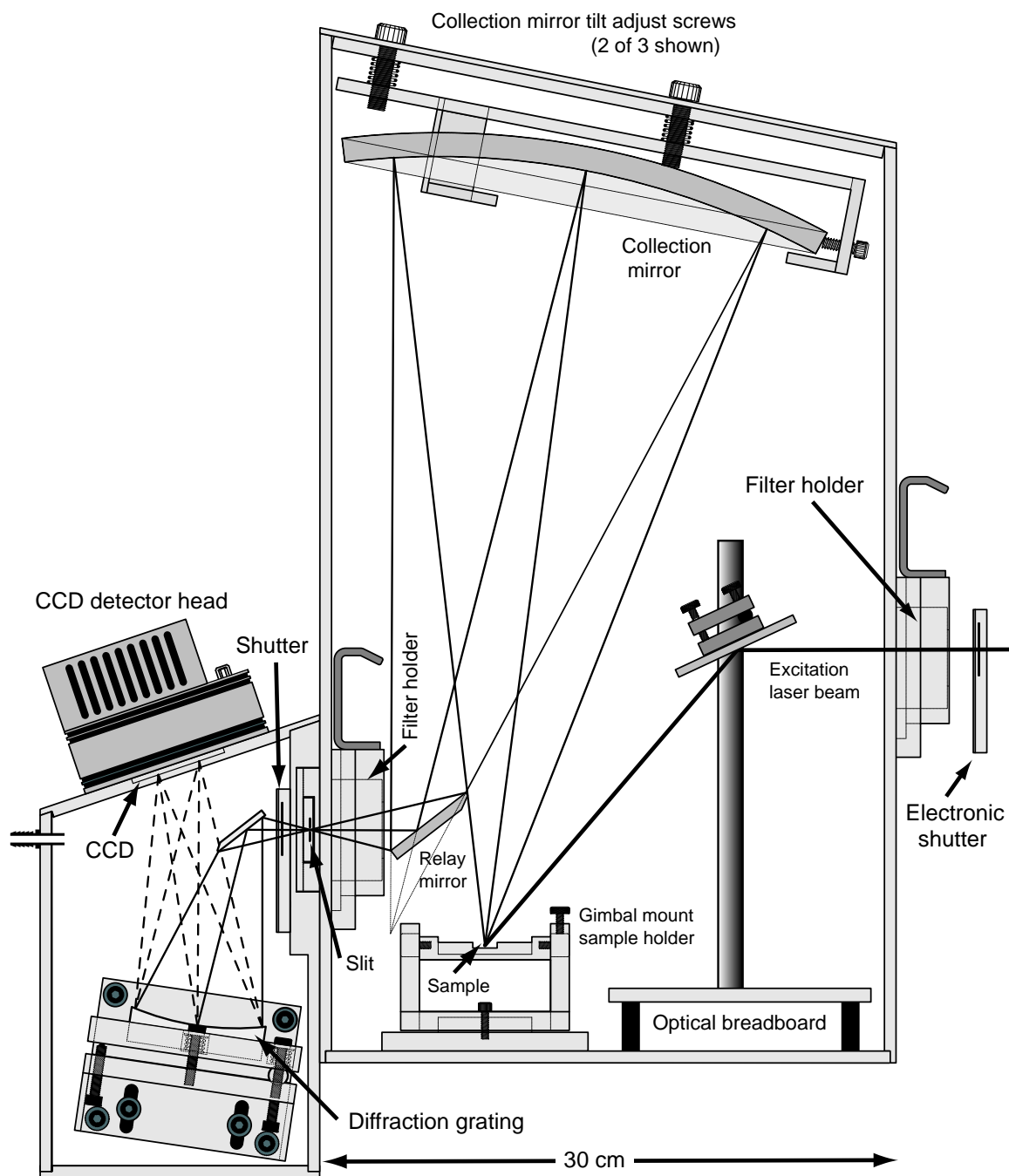
Figure 2.6: *Optical layout of the f/2 spectrometer. The entire grating mounting assembly is removed to interchange gratings so that minimal alignment of the optics is necessary. The cooling block shown is the air cooled unit provided with the Hamamatsu C7041 detector head.*
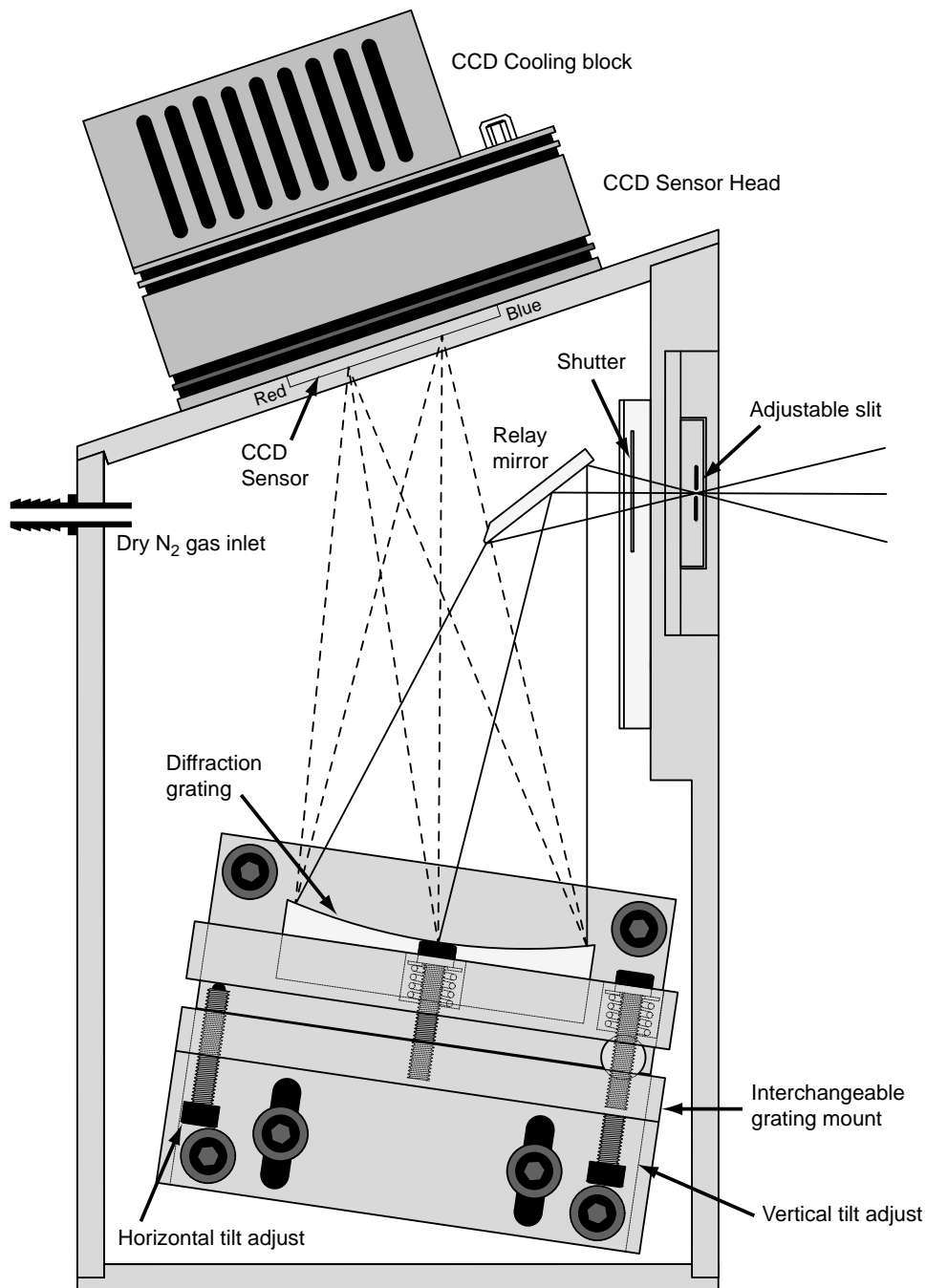
The diffraction gratings are mounted on separate dovetail slide assemblies to allow quick interchange of the gratings. Unlike ruled concave gratings, the focal plane of concave holographic gratings is flat so that electronic imaging sensors may be used (*i.e.* as opposed to film).

A Jobin Yvon-Spex[6] 523.02.100, f/2 concave holographic grating was used to cover the 190–800 nm wavelength range. The wavelength range 500–1200 nm was covered using a Jobin Yvon-Spex 523.01.090, f/2.5 concave holographic grating. Filters were used in instances where there was a possibility of overlap of the first and second order spectra. For example, a strong emission at 400 nm (as is often the case in feldspars) would produce a weak second order peak at 800 nm. Due to the wide angle of the light cone entering the spectrometer (15° half angle) and the level of rejection required for the excitation light ($>10^5$ attenuation), absorption filters proved the most practical means of isolating separate regions of the spectrum. The exception was the 750-650 nm bandpass region for which no convenient absorption filters exist; in this band several thin-film interference filters were used to achieve the necessary attenuation of the excitation beam. Further details on the filter-defined pass bands is given in the experimental sections.

2.3.3 Spectral response calibration

The spectral response of the entire system, including the input optics was determined using a tungsten/halogen light source, the black-body temperature of which was determined using an optical pyrometer. The tungsten source directly illuminated a MgO powder coated disk placed at the sample position. The spectral reflectivity of the MgO powder is sufficiently flat that it does not significantly change the spectrum from that of the tungsten source.

In order to test the validity of the model of the source as a black-body emitter, the spectrum was recorded at several different filament temperatures. The spectral responses measured at different filament temperatures were consistent with the black-body model. In order to avoid the effect of the second-order and third-order spectra, glass absorption filters were used to separate out the long-wavelength and short-wavelength bands. Below 300 nm the tungsten source did not provide sufficient light to achieve an adequate calibration. Since the CCD response is relatively flat from 200-300 nm (as is the reflectivity of bare aluminum)

---

[6]Jobin Yvon Inc. (USA), 3880 Park Avenue, Edison, N.J., 08820-3097.

Figure 2.7: *Spectral response of the spectrometer (including input optics) with the 190–800 nm grating installed (a), and the 500–1200 nm grating installed (b). Each curve is normalized to its maximum response, except for curve (c) which represents the quantum efficiency of the CCD sensor.*
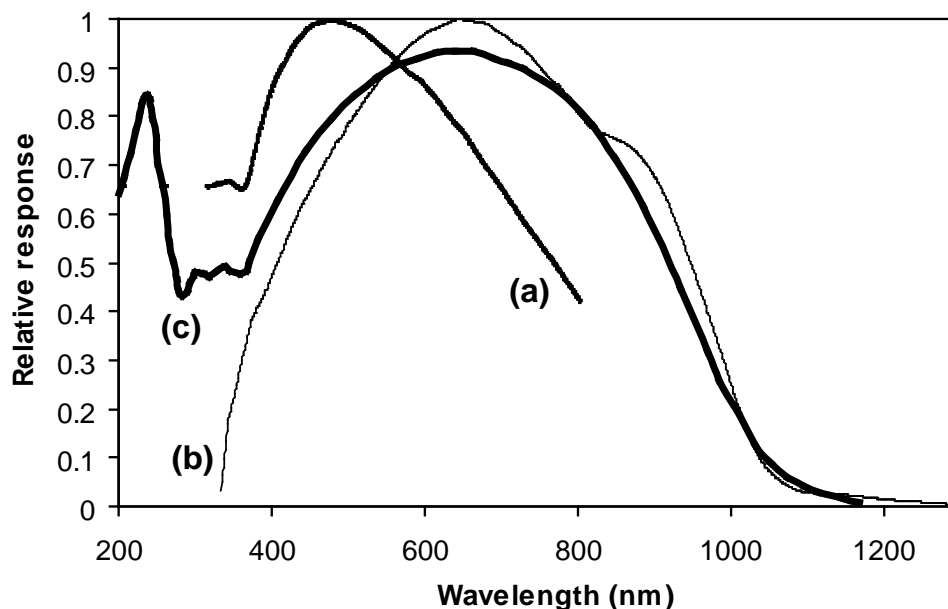
the system response was arbitrarily set to a flat value over this range. The spectral response curves with the 190–800 nm grating and the 500–1200 nm grating installed are shown in Figure 2.7.

2.4 The CCD Acquisition System

2.4.1 Electronics

The Hamamatsu C7041 detector head was interfaced to an IBM PC using hardware and software designed and built by the author. It suffices here to summarize the design architecture (Figure 2.8), detailed electronic schematics are provided in Appendix B. The detector head is fitted with a 1044x256 pixel S7031-1008 back thinned full frame transfer CCD. The interface is simple because the C7041 detector head provides most of the driving circuitry for the CCD chip, including the preprocessing necessary to perform correlated double sam-

pling of CCD video output[7].

The interface consists of the following modules,

- *The interface card*: Provides a simple means of communicating with the control electronics from the PC.

- *The CCD power supply*: Provides well-regulated voltage levels to the detector head.

- *The signal processor*: Consisting primarily of a digital to analog converter; this converts the 1V analog video level from the detector head to its digital representation for input into the PC.

- *The cooling power supply*: Delivers power to the thermoelectric Peltier element. It also provides a modest level of temperature control through feedback from a thermistor mounted near the CCD.

To this might be added the shutter controllers, the schematics of which are provided in Appendix B. Two shutters are used; one to prevent light from entering the spectrometer during readout (which would cause blurring of the image) and a second to switch the excitation beam on and off the sample.

A custom interface card was built to provide three 8-bit bidirectional parallel ports through one of the 8-bit ISA slots in a PC. Two of these ports are used exclusively in read mode to input 14 bit video data words from the camera. The third port is used in output mode to send control signals to the camera, including signals to control opening and closing of the spectrometer shutters.

The signal processing unit consists of some operational amplifiers to rescale the 4.5–9 V video signal from the detector head and subtract any constant offset that may be present in the signal. The signal is scaled to the 0–10 V input range of the Datel ADS-917, 14-bit, 1MHz sampling analog to digital (A/D) converter. The amplifier gain is adjustable by a factor of 2 to compensate for the reduced dynamic range of the CCD when operated in binning mode (*i.e.* a larger gain is necessary in vertical binning mode). In either vertical binning or imaging modes the gain was set so that the saturation level of the CCD corresponded

---

[7]See Appendix C for an explanation of this noise reduction technique.

Figure 2.8: *Architecture of the spectrometer acquisition hardware.*
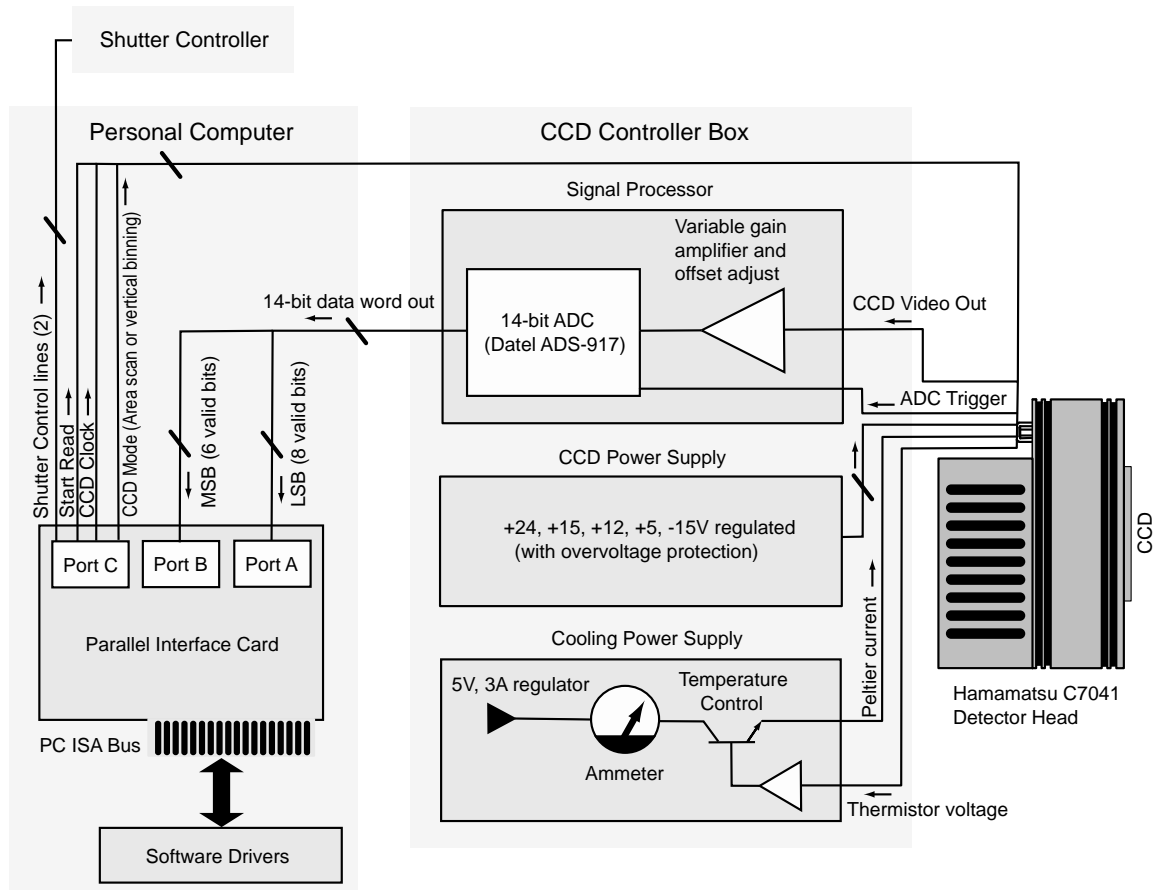
to maximum input of the A/D converter; that is, close to 16384 ADU at the output of the converter.

The camera transfer constant, that is, the number of CCD photo-electrons per ADU, is best determined using the noise measurement method described in Appendix C. The electronic camera noise was not measured for this system, however it may be estimated from the manufacturer's data sheets. In vertical binning mode (the most commonly used mode) the full-well capacity is 300 000 e$^-$. If the output is scaled so that this maximum capacity corresponds to the 10 V input of the ADC, then the transfer constant is, 300 000 e$^-$/16384 ADU = 18.3 e$^-$/ADU.

2.4.2   CCD cooling

Due to the high level of thermal noise present in a CCD sensor operated at room temperature, cooling of the CCD chip was necessary. The factory shipped Hamamatsu C7041 CCD detector head was fitted with a fan cooled thermoelectric (TE) cooler set for -10 °C operation. It became abundantly clear that this cooling level was not sufficient for our experiments in most cases. The forced air heat-exchanger was therefore replaced with a water jacket allowing the detector head to be set for -20 °C operation. Unfortunately, the -20 °C setting on the Hamamatsu temperature controller did not operate correctly; operation near -20 °C would trip the safety shut-down of the Peltier current. The simple feedback circuit shown in Figure B.5 was built to circumvent this problem and provide temperature control between room-temperature and -20 °C.

The cooling level provided by this arrangement proved adequate for bright samples

Figure 2.9: *Nominal dark signal versus temperature for Hamamatsu's S7031-1008 CCD. After Hamamatsu's preliminary datasheet, November 1997, for S7030/S7031 series CCD area image sensors.*
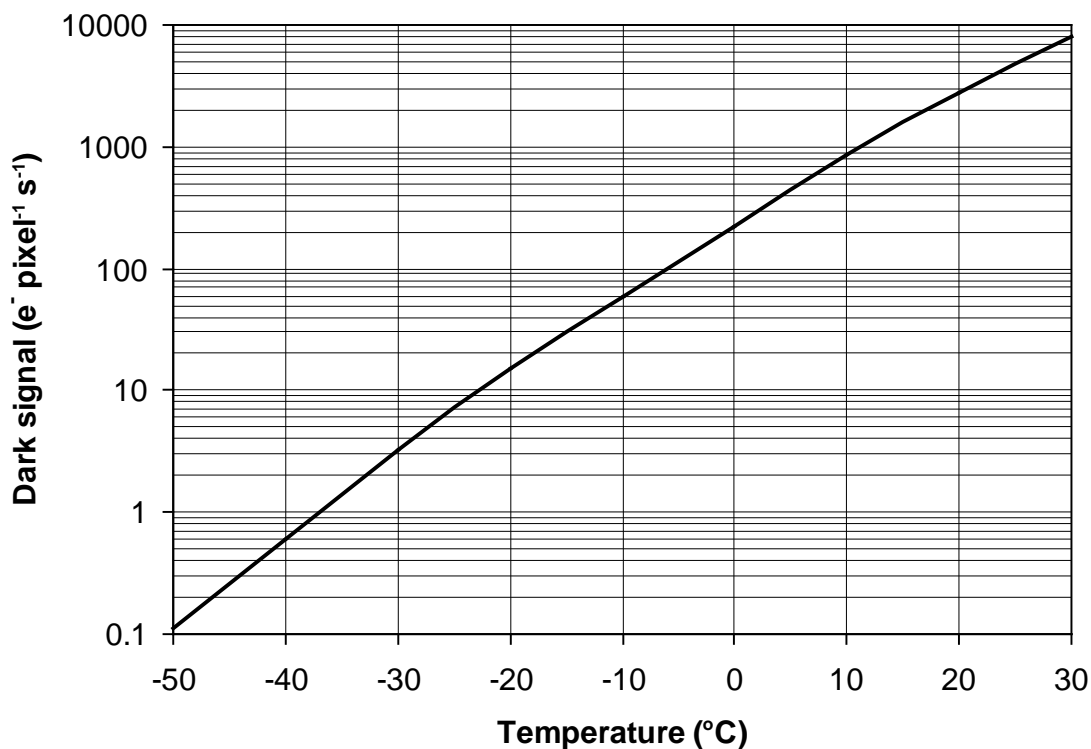
in integrations up to 15 seconds. However, the dark count at -20 $^\circ$C was inadequate in many measurements, in particular with experiments requiring integration times several minutes long (*e.g.* room-temperature phosphorescence measurements). In these cases the water jacket was replaced with a cooling block connected to a reservoir containing a mixture of dry ice and ethyl alcohol. This arrangement provided a pixel dark count of 0.023 ADU/pixel·s or 0.42 e$^-$/pixel·s; in vertical binning mode this corresponds to 6 ADU/channel·s or 110 e$^-$/channel·s. From this, and Hamamatsu's nominal dark-signal versus temperature curve (see Figure 2.9) for the S7031-1008 CCD, one can estimate a CCD temperature of $\sim$-42 $^\circ$C using dry-ice cooling.

2.4.3 Software

Hardware drivers were written using Borland's in-line C assembler. The experiment interface was developed for a Windows$_{TM}$ 98 platform using Borland's C++ Builder$_{TM}$ visual programming environment. This allowed for efficient interface of the equipment in a manner that was best suited to our particular application with a minimal amount of development time. Spectrum files are stored in a custom binary format that can be converted to ASCII format for entry into other programs.

Chapter 3

Samples

3.1 Provenance

The spectrometer described in Chapter 2 allowed the measurement of infra-red stimulated luminescence (IRSL) emission spectra for twelve granular K-feldspar separate samples. In addition, the emission spectra of twelve feldspar rock samples were measured; these included five (nominally) Na-rich feldspars, six K-rich feldspars and one intermediate plagioclase. IRSL emission spectra were also obtained for three quartz grain separates. The nominal composition and provenance of the samples is given in Tables 3.2–3.4. The study codes are provided as a cross-reference to the different studies performed on a given sample in this work. The study codes are defined in Table 3.1.

Granular K-feldspar samples were prepared from sediments by standard density separation. Typically, the sediment was first treated with dilute HCl to dissolve the calcareous fraction, then with H_2O_2 to remove any organic material if necessary. The sediment was dried at low temperature and then sieved to select a grain size. The grains were centrifuged in a sodium-polytungstate solution of density slightly larger than the nominal density of pure K-feldspar ($\sim$2.58 g/cm^3). In such a solution, quartz and most of the plagioclase sinks while the K-feldspar fraction floats. This procedure was usually repeated to ensure a good separation. The separated "K-feldspar" grains were etched in dilute HF to remove the outer layer of the grains[1] and to break up any remaining clusters of grains. The grains were sieved

---

[1]This step is necessary in dating because of the higher dose rate acquired in the $\sim 10 \mu m$ thick outer layer

again to remove any sub-size grains and the magnetic fraction removed using a magnetic separator.

Sample OKA-4 consisted of unseparated sediment grains primarily containing quartz, plagioclase feldspar and clay minerals. The K-feldspar fraction was dissolved *in situ* in this sediment due to its deposition in an acidic environment [2].

The rock samples consisted mostly of rocks obtained from Ward's supply house[3], cut into approximately 6 x 6 x 1 mm slices. Sample K3 was obtained from a collection at the University of British Columbia[4] and has been the focus of extensive studies by M. A. Short (Short and Huntley, 2000; Short, 2003).

Table 3.1: *Study codes used in the sample descriptions.*

Code	*Definition*	*Section reference*
Ex-f	Near infrared excitation spectra, feldspar samples	Chapter 5
Ex-q	Near infrared excitation spectra, inclusions in quartz	Section 9.3
IRSL-f	Infra-red stimulated luminescence emission spectra, feldspar samples	Section 4.2
IRSL-q	Infra-red stimulated luminescence emission spectra, inclusions in quartz	Section 9.2
PP	"Prompt" phosphorescence – phosphorescence spectra measured a short time after cessation of gamma irradiation.	Section 4.5
PI	"Post-illumination" phosphorescence – phosphorescence spectra measured immediately after cessation of illumination by 1.44 eV excitation photons.	Section 4.6

---

of the grain from external α-rays.

[2]Olav Lian, 2001, personal communication.

[3]Ward's Natural Science Ltd., 397 Vansickle Road, St. Catherines, Ontario.

[4]The author wishes to thank Michael A. Short for obtaining this sample which was generously provided by Dr. Lee A. Groat of the University of British Columbia, Vancouver, B.C.

Table 3.2: *Cut rock sample descriptions.*

Sample	Nominal composition	Appearance	Provenance	Studies
A1	Albite Ward #46E 0234	white with clear patches	Bancroft, Ontario, Canada	IRSL-f, Ex-f
A2	Albite Ward #49E 5851	white	Amelia Courthouse, Virginia, U.S.A.	Ex-f
A3	Oligoclase Ward #46E 5804	white with black specks	Mitchell County, North Carolina, U.S.A.	IRSL-f, Ex-f
A4	Anorthoclase Ward #46E 0579	brownish black, irridescent	Larvik, Norway	Ex-f
A5	Albite Ward set #45E 2941	white with black specks	Bancroft, Ontario, Canada	IRSL-f, Ex-f
A6	Albite (cleavlandite) Ward #46E 0240	white	Keystone, South Dakota, U.S.A.	IRSL-f, Ex-f, PP, PI
K3	Orthoclase	transparent, slightly yellow	Red Lodge, Montana, U.S.A.	IRSL-f, Ex-f, PP, PI
K7	Microcline Ward set #45E 2941	light pink	Crystal peak, Colorado, U.S.A.	IRSL-f, Ex-f
K8	Microcline Ward #46E 0514	pink, brown and white striped	Perth, Ontario, Canada	IRSL-f, Ex-f, PP, PI
K9	Microcline (amazonite) Ward #46E 5164	light turquoise with white stripes	Kola Peninsula, Murmansk, Russia	IRSL-f, Ex-f, PP, PI
K10	Microcline Ward #46E 5125	translucent white with clear layers	Keystone, South Dakota, U.S.A.	IRSL-f, Ex-f, PP, PI
K11	Orthoclase Carlsbad twin, Ward #49E 3080	orange brown, brittle	Gothic, Colorado, U.S.A.	IRSL-f, Ex-f
P9	Anorthite in pyroxene Ward #46E 0559	grey mottled black	Grass Valley, California, U.S.A.	Ex-f
P10	Labradorite Ward #46E 4510	dark grey with blue irridescence	Nain, Labrador, Canada	IRSL-f, Ex-f
P11	Andesine Ward #46E 0024	black	Essex County, New York	Ex-f
P12	Bytownite Ward #46E 1384	greenish white, translucent	Crystal Bay, Minnesota, U.S.A.	Ex-f

Table 3.3: *Granular feldspar separate samples (continued on next page).*

Sample	*Sediment composition*	*Provenance*	*Reference*	*Studies*
AKHC	Marine silty sand, 150-180 μm	Akpatok Island, Quebec, Canada	Huntley & Lamothe 2001	IRSL-f, Ex-f, PP
BIDS	Sand dunes, 150-300 μm	Bruneau Dunes State Natural Park, Idaho, U.S.A.	Huntley & Lamothe 2001	IRSL-f
CBSS	Eocene or Oligocene sandstone, 180-250 μm	China Beach, Vancouver Island, British Columbia, Canada	Huntley & Lamothe 2001	IRSL-f
CES-5	Glaciomarine sandy clay and silt, 125-250 μm	Saint-Césaire, Québec, Canada	Lamothe 1996, Lamothe & Auclair 1997, Huntley & Lamothe 2001	IRSL-f
CKDS	Dune sand, 180-250 μm	Cape Kidnappers, New Zealand	Shane *et al.* 1996, Huntley & Lamothe 2001	IRSL-f
CTL2	Fluvial sand, 180-250 μm	Coutlee sediments, Lily Lake Road, Merritt, British Columbia, Canada	Fulton *et al.* 1992, Huntley & Lamothe 2001	IRSL-f
DY-23	180-250 μm	Stratum 3, Diring Yuriakh archaeological site, Lena River, Yakutia, Russia	Mochanov 1988; Waters *et al.* 1999, Huntley & Lamothe 2001	IRSL-f
EIDS	Delta sand, 180-250 μm	Near Cape Herschel, Ellesmere Island, Nunavut Terr., Canada	Blake 1992, Huntley & Lamothe 2001	IRSL-f, Ex-f, PP
GP1	Fluvial sediments, 150-250 μm	Gomez Pit, Virginia, U.S.A.	Lamothe and Auclair 1999, Huntley & Lamothe 2001	IRSL-f, PP

Table 3.3: *(Continued) Granular feldspar separate samples.*

Sample	Sediment composition	Provenance	Reference	Studies
IV.1	Late Pleistocene sediment	Ostrobothnia, Finland	Huntley *et al.* 1991, Jungner and Huntley, 1991	IRSL-f, Ex-f, PP
LP-D	Dune sand	Long Point, Ontario, Canada	Huntley & Lamothe 2001	IRSL-f
OKA-4	Fine fluvial clay, <90 μm	Okarito, South Island, New Zealand	Almond *et al.* 2001	IRSL-f, Ex-f
RHIS	Intertidal sand, 150-250 μm	Rewa Hill, New Zealand	Huntley & Lamothe 2001	IRSL-f
SAW 95-09	Dune sand	Sandy Lake, Northwest Territories, Canada	Huntley & Lamothe 2001	IRSL-f, PP
SAW 97-08	Dune sand, 250-350 μm	Brandon Sand Hills, Manitoba, Canada	Wolfe *et al.* 2000, Huntley & Lamothe 2001	IRSL-f
SN-27	Beach dunes, 180-250 μm	Sandy Neck, Cape Cod, Massachusetts, U.S.A.	van Heteren *et al.* 2000, Huntley & Lamothe 2001	IRSL-f, PP
SUN	Lodgement till, 125-250 μm	Sundance section, Nelson River, Manitoba, Canada	Lamothe & Auclair 1999, Huntley & Lamothe 2001	IRSL-f
SW5-01	Dune sand, 90-125 μm	(Northern) Great Sand Hills, Saskatchewan, Canada	Wolfe *et al.* 2001	IRSL-f
TAG-8	Fluvial sand, 180-250 μm	TAGLU core, Mackenzie River, N.W.T., Canada	Wang and Evans (1997), Huntley & Lamothe 2001	IRSL-f
TTS	Tsunami-laid sand, 90-125 μm	Tofino, Vancouver Island, British Columbia, Canada	Huntley & Clague 1996, Huntley & Lamothe 2001	IRSL-f

Table 3.4: *Granular quartz samples.*

Sample	Sediment composition	Provenance	Reference	Studies
CBSS	Eocene or Oligocene sandstone, 180–250 μm	China Beach, Vancouver Island, Canada	CBBS: Huntley *et al.* 1988	Ex-q
DY-23	180–250μm	Stratum 3, Diring Yuriakh archaeological site, Lena River, Yakutia, Russia	Mochanov (1988), Waters *et al.* 1999, Huntley & Lamothe 2001	Ex-q
NL-1	Ancient beach sand dune, 180–250 μm	Nhill, County Lowan, West Wimmera, Australia		IRSL-q, Ex-q
SESA-63	Ancient beach sand dune, 180–250 μm	East Naracoorte Range, south-east South Australia	Huntley *et al.* 1993a, Ditlefsen and Huntley 1994, Huntley *et al.* 1995, Huntley *et al.* 1996	IRSL-q, Ex-q
SESA-71	Ancient beach sand dune, 180–250 μm	Woakwine I Range, south-east South Australia	Huntley *et al.* 1994	Ex-q
SESA-101	Ancient beach sand dune, 180–250 μm	Black Range, south-east South Australia	Huntley and Prescott 2001	IRSL-q, Ex-q
SESA-121	Ancient beach sand dune, 180–250 μm	Coorong, south-east South Australia	Huntley and Prescott 2001	IRSL-q, Ex-q
TAG-8	Fluvial sand, 180-250 μm	TAGLU core, Mackenzie River estuary, Northwest Territories, Canada	Wang and Evans 1997, Huntley & Lamothe 2001	Ex-q

3.2 Elemental analyses

Since the luminescence spectra were expected to be dependent on the bulk feldspar compo-sition (*i.e.* Na vs. Ca or K-feldspar) as well as certain trace element contents (*e.g.* Mn and Pb), elemental analyses were performed for the rock samples. Major element analyses (Si, Al, K, Na, and Ca) were performed by inductively coupled plasma emission spectroscopy (ICP-ES) whereas trace element analyses were obtained from inductively coupled plasma mass-spectrometry (ICP-MS)[5].

Table 3.5 gives the expected elemental contents for pure K, Na and Ca feldspars. The elemental contents (by weight) for the major feldspar constituents and some of the minor elements from the analyses are listed in Table 3.2. Contents for the lanthanide elements are given in Table 3.7. The minor elements shown are those that are known to substitute in feldspars (see for example, Smith and Brown, 1988) or that have been suggested as possible luminescence centers (Krebetschek *et al.*, 1997). The mole percentage contents of "orthoclase", "albite", and "anorthoclase" are plotted on a ternary diagram in Figure 3.1.

It is evident from the position of K11 on this diagram that either it consists of a mixture of minerals or that the Ca contents are erroneously large. The Al and Si contents in K11 are close to the 9.7–10.3% and 30–32% expected for pure alkali feldspar, respectively. However, this is inconsistent with the mole percentage plagioclase implied from the Ca content relative to K and Na; one may only conclude that the Ca in this sample is associated with a Ca rich mineral, perhaps calcite. The large Mn content in this sample is consistent with the presence of calcite, in which Mn readily substitutes.

Table 3.5: *Elemental contents for pure end-member feldspars (by weight).*

Mineral	Si (%)	Al (%)	K (%)	Na (%)	Ca (%)
K-AlSi$_3$O$_8$	30.2	9.7	14.0	–	–
Na-AlSi$_3$O$_8$	32.1	10.3	–	8.8	–
Ca-Al$_2$Si$_2$O$_8$	20.1	19.4	–	–	14.4

---

[5]Analyses were performed by Acme Analytical Laboratories Ltd., 852 East Hastings St., Vancouver, B.C., V6A-1R6.

Sample	Si %, ±0.01	Al %, ±0.02	K %, ±0.03	Na %, ±0.01	Ca %, ±0.01	Ba ppm, ±1	B ppm, ±3	Fe %,±0.01	Mg %,±0.01	Mn ppm, ±1	Tl ppm, ±0.1	Pb ppm, ±0.1	Cu ppm, ±0.1	Ga ppm, ±1	Ti %, ±0.001	Total, %
A1	29.14	12.24	1.02	5.55	3.29	15	7	0.17	0.07	26	<0.1	5.0	2.2	2	<0.001	99.2
A2	32.20	10.30	0.15	7.85	0.19	1	6	0.06	<0.01	5	<0.1	21.8	1.9	3	<0.001	99.5
A3	32.79	9.68	0.13	4.54	2.99	9	5	0.22	0.02	21	<0.1	3.8	1.3	1	0.005	99.4
A4	28.42	9.71	3.14	4.41	2.38	62	9	1.98	0.33	414	<0.1	1.8	5.1	4	0.118	98.8
A5	30.23	10.38	6.46	4.38	0.29	30	9	0.24	0.02	53	0.2	16	0.8	2	0.011	99.8
A6	32.20	10.15	0.18	7.67	0.19	1	9	0.06	<0.01	35	<0.1	7.6	1.2	1	<0.001	99.3
K3	30.94	9.56	9.38	1.79	0.16	75	4	0.05	<0.01	4	0.1	5.5	2.6	1	<0.001	99.3
K7	32.50	8.94	6.93	2.97	0.01	11	4	0.21	<0.01	10	0.1	9.8	1.3	3	<0.001	99.1
K8	31.11	9.67	9.50	1.76	0.10	14	4	0.17	0.01	13	0.1	11.9	1.4	1	<0.001	99.1
K9	31.14	9.64	9.88	1.77	0.01	48	4	0.03	<0.01	4	1	57.6	1.0	7	<0.001	99.3
K10	31.18	9.60	10.06	1.73	0.05	3	3	0.03	<0.01	5	0.3	7.9	1.0	2	<0.001	99.4
K11	28.64	9.30	8.08	1.45	2.27	141	3	0.58	0.12	397	<0.1	11.6	1.3	1	0.001	95.2
P9	20.30	10.96	0.03	0.39	8.48	31	5	6.15	6.94	1071	<0.1	0.5	17.8	13	0.003	99.3
P10	26.25	13.98	0.37	3.47	7.33	45	4	0.30	0.02	23	<0.1	0.9	2.7	4	0.042	99.3
P11	24.78	12.53	1.00	3.18	7.44	28	5	1.68	0.13	83	<0.1	1.5	3.6	5	0.054	98.5
P12	23.27	15.65	0.07	1.84	10.48	45	3	0.36	0.11	47	<0.1	0.5	3.9	17	0.007	98.8

Table 3.6: *Results of ICP-ES and ICP-MS elemental analyses (weight %). Lanthanides are listed in Table 3.7*

Figure 3.1: *Ternary diagram indicating the composition of the feldspar rock samples. Axes represent mol% KAlSi₃O₈, NaAlSi₃O₈ and Ca₂Al₂Si₂O₈.*
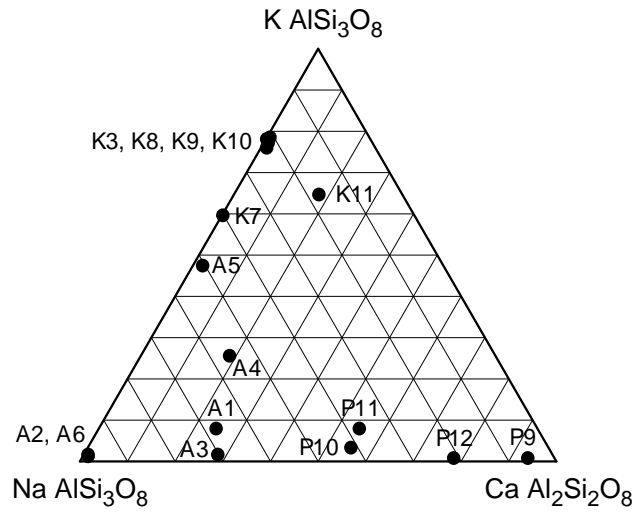
Table 3.7: *Results of ICP-ES and ICP-MS analyses for lanthanides.*

Sample	Ce ppm ±0.5	Nd ppm ±0.4	Sm ppm ±0.1	Eu ppm ±0.05	Tb ppm ±0.01	Dy ppm ±0.05
A1	1.0	<0.4	<0.1	0.35	0.01	0.05
A2	<0.5	<0.4	<0.1	<0.05	<0.01	<0.05
A3	2.7	1.2	0.4	0.37	0.19	1.57
A4	208.9	83.2	13.7	5.12	1.35	7.58
A5	1.4	<0.4	<0.1	0.20	<0.01	<0.05
A6	<0.5	<0.4	<0.1	<0.05	<0.01	<0.05
K3	4.6	1.5	0.2	1.08	0.01	0.07
K7	1.7	1.2	0.3	<0.05	0.09	0.51
K8	<0.5	<0.4	<0.1	0.56	0.01	0.1
K9	<0.5	0.4	0.1	<0.05	<0.01	0.11
K10	0.9	<0.4	<0.1	0.09	0.01	0.13
K11	26.9	14.5	3.1	0.55	0.33	1.61
P9	1.7	0.5	0.3	0.21	0.02	0.13
P10	12.6	5.0	0.9	0.95	0.06	0.34
P11	36.2	28.8	6.5	1.75	0.82	4.4
P12	1.4	0.5	0.1	0.46	0.01	<0.05

Chapter 4

Emission Spectra

4.1 Overview

The spectrometer described in Chapter 2 enabled the measurement of emission spectra for a number of feldspar sediment extracts that had been previously studied in the context of dating work. Of particular interest was the emission stimulated by 1.44 eV light (infra-red stimulated luminescence, or IRSL) of the cut-rock feldspar samples for which excitation energy spectra were obtained (Chapter 5). In all cases the emission studied was the consequence of an applied gamma radiation dose. The following spectral investigations were performed;

- IRSL spectral characterization of a wide range of feldspars.

- IRSL spectra of inclusions in quartz thought to be feldspars (Chapter 9).

- Effect of 120 $^{\text{o}}$C preheat for $\sim$16 hours on the IRSL spectrum (1.44 eV excitation).

- Variation of the emission spectrum during "shinedown" decay of the IRSL.

- Effect of the excitation energy on the emission spectrum.

- Phosphorescence following illumination of a dosed sample by 1.44 eV light.

- Room temperature TL (phosphorescence).

Most of these studies were motivated primarily on the basis of a search for "effects"; only two of these effects having been investigated by other authors. The effect of a short pre-heat on the IRSL spectrum has been investigated by Clarke and Rendell (1997a), (1997b). The emission spectra described in this study exhibit a significant feature not reported by these authors, specifically the presence of an emission band near 1.76 eV (700 nm) that vanishes on heating the sample at 120 $^{\circ}$C.

The thermal stability of the 1.76 eV TL emission band has been studied in depth, for example by Visocekas *et al.* (1994) and Zink *et al.* (1995), but these studies strictly involve TL and CL measurements and the results do not translate in a straightforward manner to the IRSL behaviour. Room temperature TL (phosphorescence) has been previously observed by many authors (*e.g.* Prescott and Fox, 1993). In the present work, both phosphorescence and IRSL spectra have been measured so that new information may be inferred.

4.2 Feldspar IRSL spectra

The excitation source consisted of a Ti-Sapphire laser tuned to 1.43 eV (865 nm), with a beam power in the range of $\sim$10–50 mW/cm^2 at the sample. An RG-780 filter was placed in the beam path to absorb any short-wavelength light from the laser. In order to avoid problems with the overlap of the first and second-order diffraction spectra, as well as to remove the excitation light, filters were used on the input of the spectrometer. Three pass bands were defined; the "red" band (700–600 nm), the "visible" band (600–350 nm) and the "UV" band (350–275 nm). The filter combinations used to define these bands were,

"Red"	Two CVI[1] 500–750 nm bandpass filters,
	875 nm & 830 nm Raman notch filters[2].
"Visible"	Schott BG-39 (2.2 mm thick)
"UV"	Schott UG-11 (3.0 mm thick)

The bandpasses of these filter combinations are shown in Figure 4.1. The excitation was selected as 865 nm to make effective use of the available 875 nm notch filter while

---

[1]CVI Laser Corp., 200 Dorado Place S.E., Albuquerque, N.M. 87123. Filter: SPF-800-1.00

[2]Physical Optics Corp., Filters: #848 (λ=875 nm) and #703 (λ=830 nm).

Figure 4.1: *Filter defined pass bands for the IRSL spectra.*
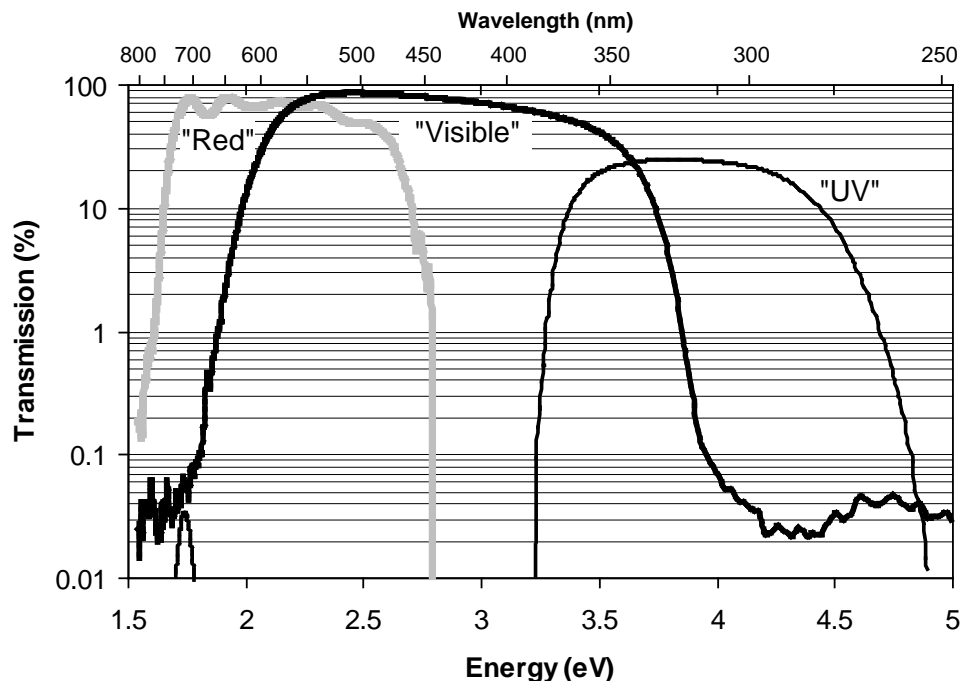
remaining close to the excitation resonance of feldspars at 1.44 eV. The 830 nm notch filter proved useful because it blocked portions of the scattered 865 nm excitation that were not at normal incidence to the filter.

The spectra for each defined pass-band were measured separately on the same sample aliquot, integrating for 10–20 seconds of illumination. Since each measurement necessarily drained the luminescence, the samples were first bleached under a sun-lamp and then given a 750 Gy dose using a Co^{60} γ-source between measurements. The spectra were corrected for CCD thermal dark count and normalized for the spectrometer response (including the filters). The "UV" and "Red" band data was then scaled to match the overlap with the "visible" pass-band data. The spectral intensities were then scaled for display on an energy scale.

The measurements immediately following irradiation were performed within 5 hours of removal from the γ-source. Spectral measurements were repeated on the same aliquots after they had been re-irradiated and then heated at 120 ℃ for 16–20 hours. Generally, a

0.6 mm or smaller slit was used whenever possible, providing an effective bandwidth of 15 nm at 500 nm. Aliquots were illuminated for an additional 60 s after measurement, then the measurement was repeated. The prolonged illumination effectively reduced the IRSL to a negligible level so that an accurate background level could be measured for each aliquot[1]. The CCD was operated in vertical binning mode to reduce the readout noise. The data were smoothed by resampling, averaging over groups of 5 CCD columns. This last step did not reduce the resolution since the resolution bandwidth of 25 nm corresponded to ∼10 CCD columns[2].

IRSL emission spectra in the 250–700 nm band for the feldspar samples are shown in Figures 4.2–4.17. In these figures the spectra for the unpreheated samples are drawn in bold black and the spectra for the preheated samples are drawn in bold grey. Unless otherwise noted, the preheated sample spectra have been scaled so that the 3.1 eV emission band has the same intensity as that in the unpreheated sample spectrum. The values shown on the ordinate axes are an approximate guide as to the relative intensities of the samples, but otherwise have no meaning. Spectra for sediment mineral extract samples are shown in Section 4.2.1 and spectra for cut-rock samples are in Section 4.2.2.

Bandwidths are reported in the caption of each figure using the format, (unpreheated sample data) {1.7–2.1 eV, 2.1–3.5 eV, 3.5–4.5 eV}, (preheated sample data) {1.7–2.1 eV, 2.1–3.5 eV, 3.5–4.5 eV}. For example, {25,15,15},{25,25,25} indicates that in the unpreheated sample data a 25 nm bandwidth applies to the red band, and a 15 nm bandwidth applies to the violet and UV bands, whereas a 25 nm bandwidth was used for all of the preheated sample bands.

---

[1]Note that the red and UV filter combinations allowed a significant amount of excitation light into the spectrometer. The background from this was highly sensitive to the reflectivity of the particular aliquot being measured.

[2]Ideally it would be best to perform this binning before readout of the CCD to reduce readout noise. Unfortunately the Hamamatsu detector head did not allow for horizontal binning operation.

4.2.1 Sediment mineral extract emission spectra

Figure 4.2: *AKHC and BIDS IRSL spectra. Preheated sample data in grey, unpreheated sample data in black. Bandwidths (nm): AKHC {15,15,15},{25,25,25} BIDS {25,25,25},{-,-,-} (Code explained in text).*
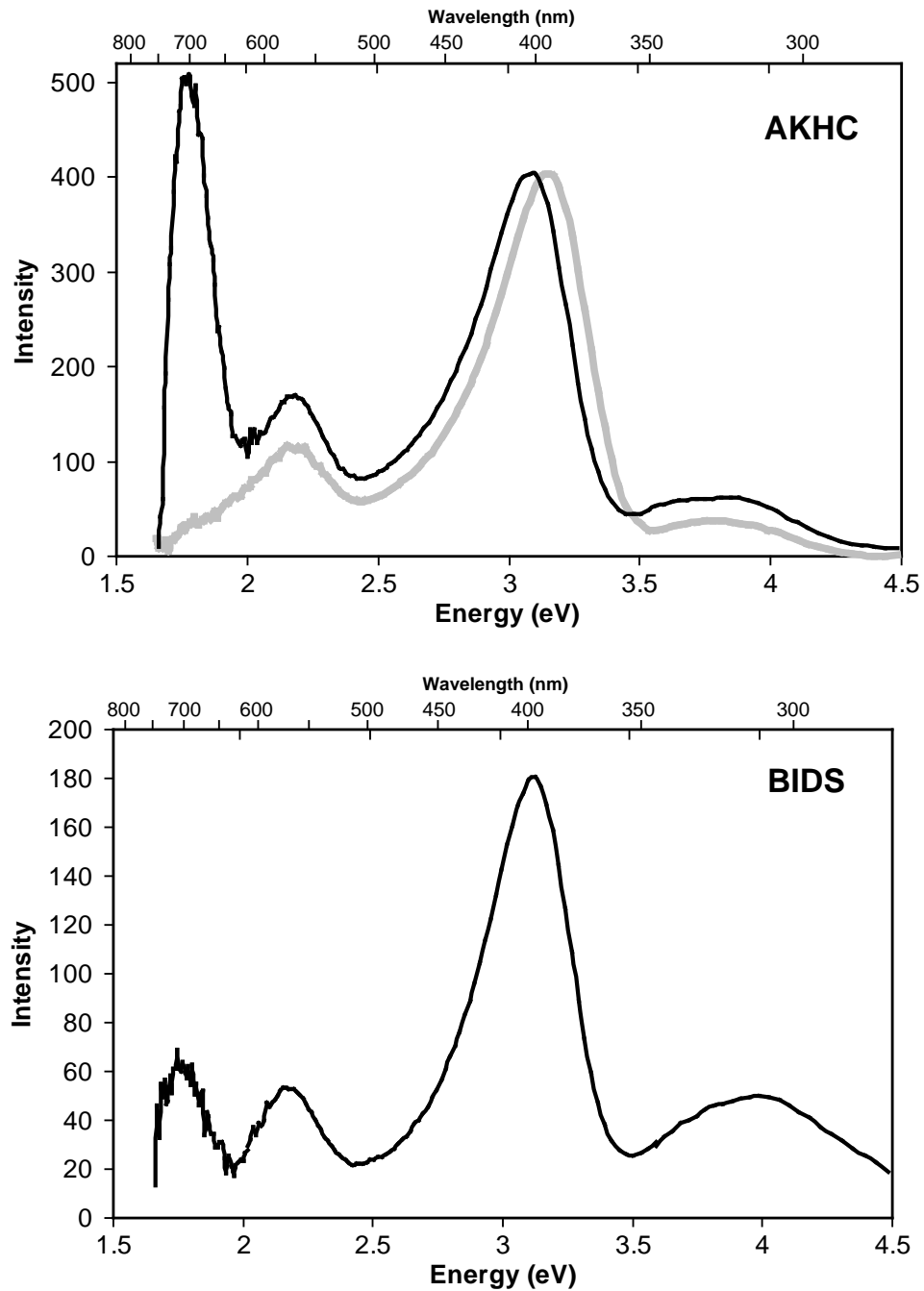
Figure 4.3: *CBSS and CES-5 IRSL spectra. Preheated sample data in grey, unpreheated sample data in black. Bandwidths (nm): 15,15,15,25,25,25 (Code explained in text).*
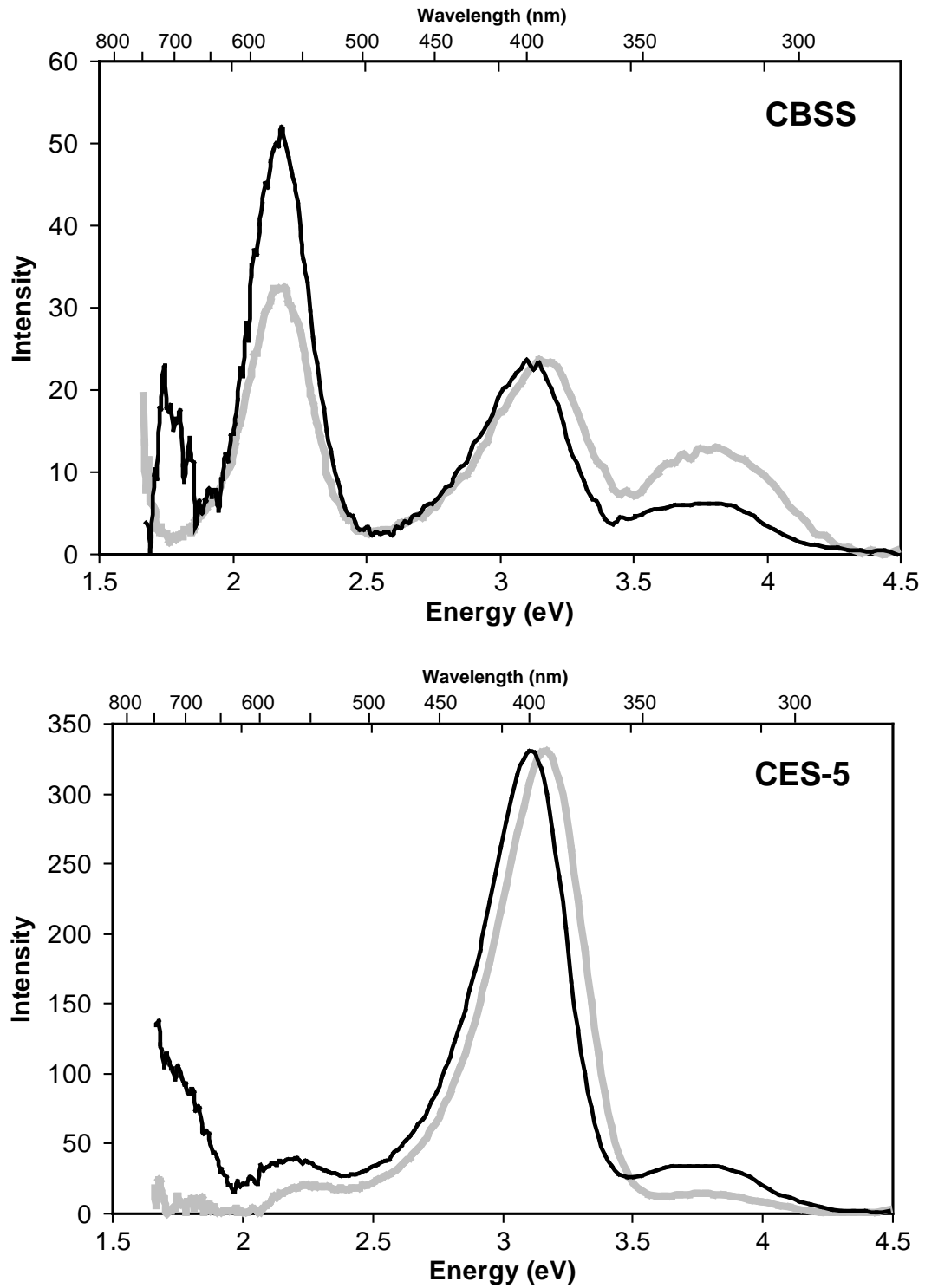
Figure 4.4: *CKDS and CTL-2 IRSL spectra. Bandwidths (nm): {-,25,15},{-,-,-} (Code explained in text).*
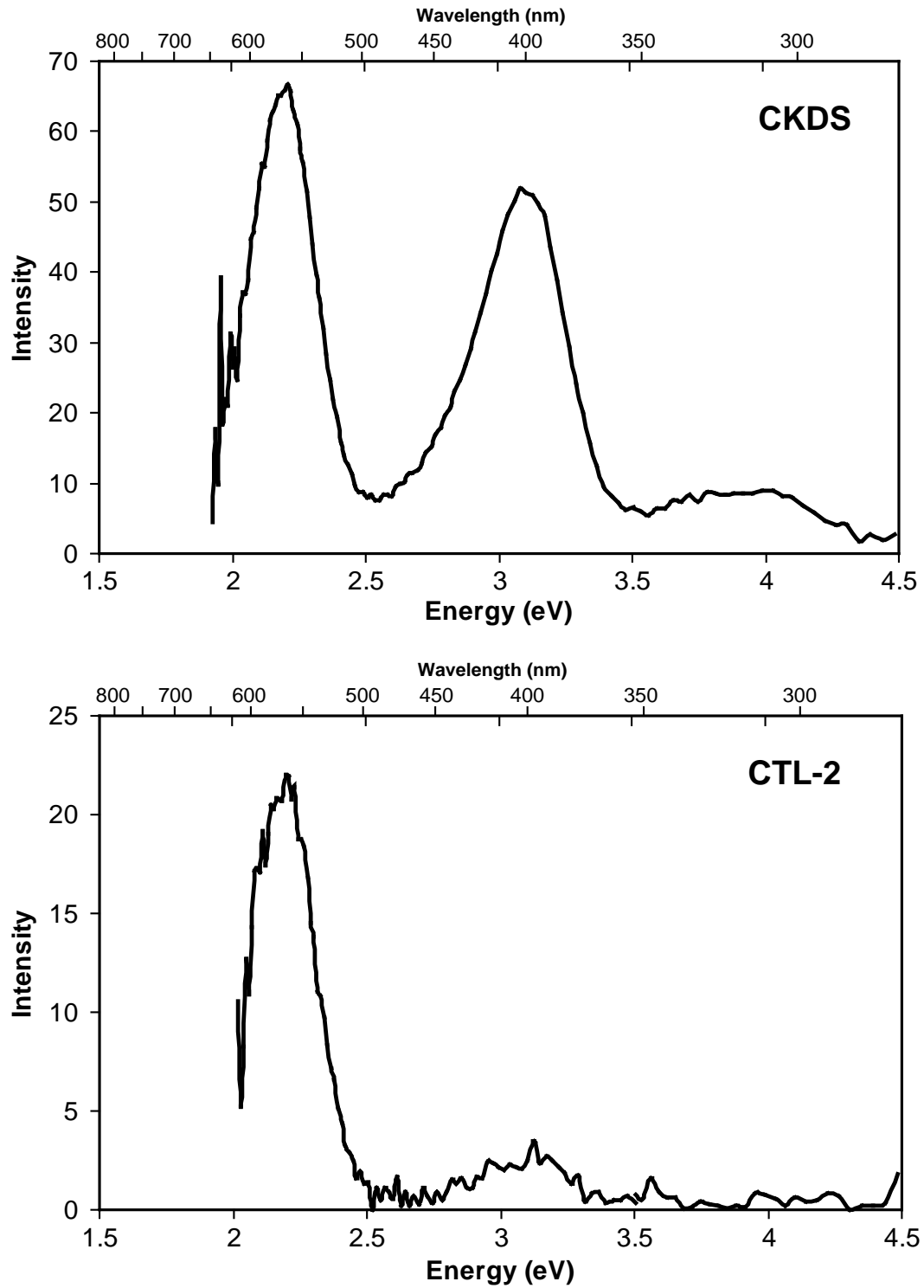
Figure 4.5: *DY-23 and EIDS IRSL spectra. Preheated sample data in grey, unpreheated sample data in black. Bandwidths (nm): DY-23 {15,15,15},{25,25,25} EIDS {15,15,15},{25,15,15} (Code explained in text).*
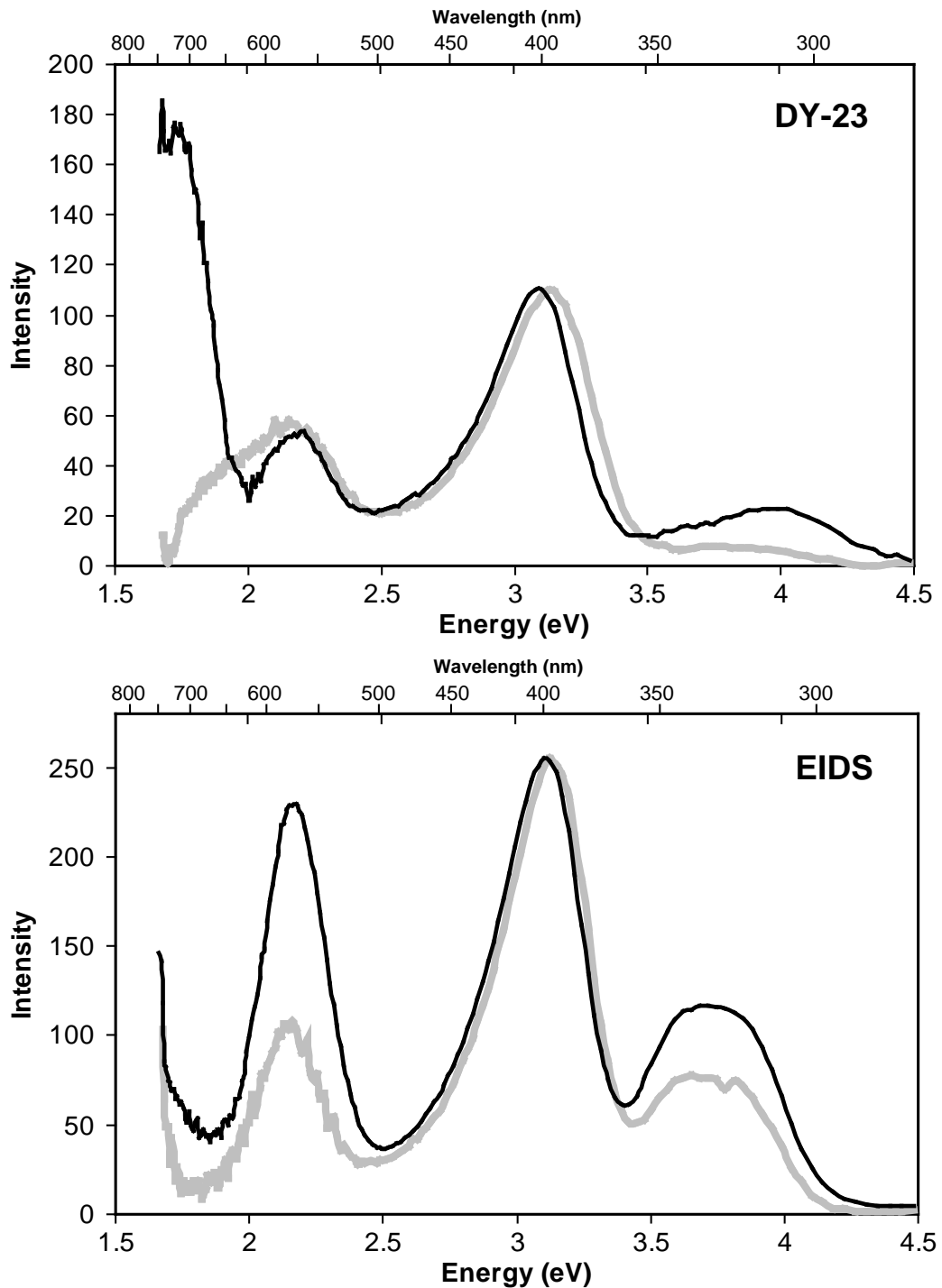
Figure 4.6: *GP-1 and IV.1 IRSL spectra. Preheated sample data in grey, unpreheated sample data in black. Bandwidths (nm): GP-1 {15,15,15},{25,25,25}*
IV.1 {15,7.5,15},{-,15,15} (Code explained in text).
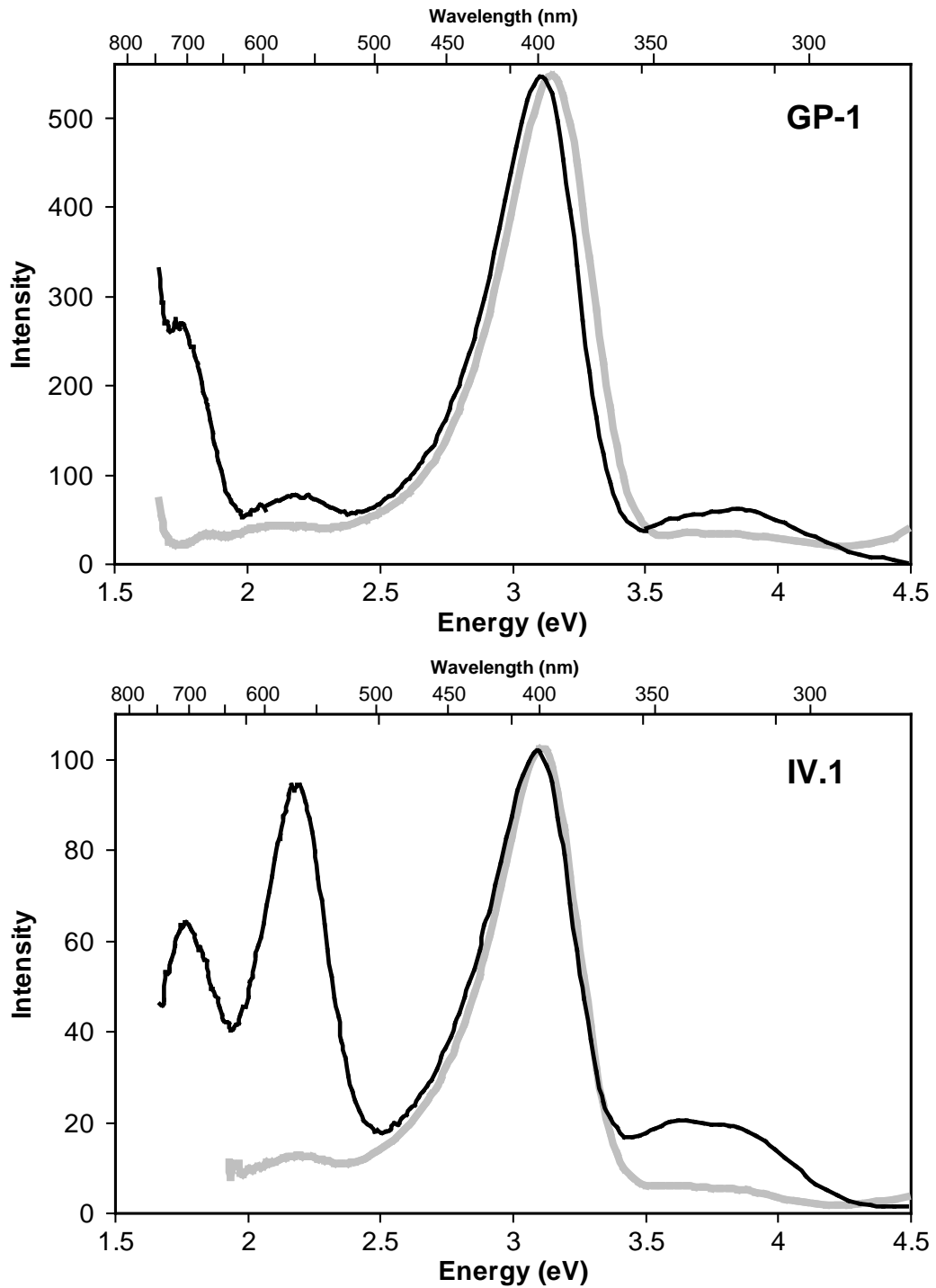
Figure 4.7: *LPD and OKA-4 IRSL spectra. Preheated sample data in grey, unpreheated sample data in black. Bandwidths (nm): LPD {15,15,15},{25,25,25} OKA-4 {25,25,25},{-,-,-} (Code explained in text).*
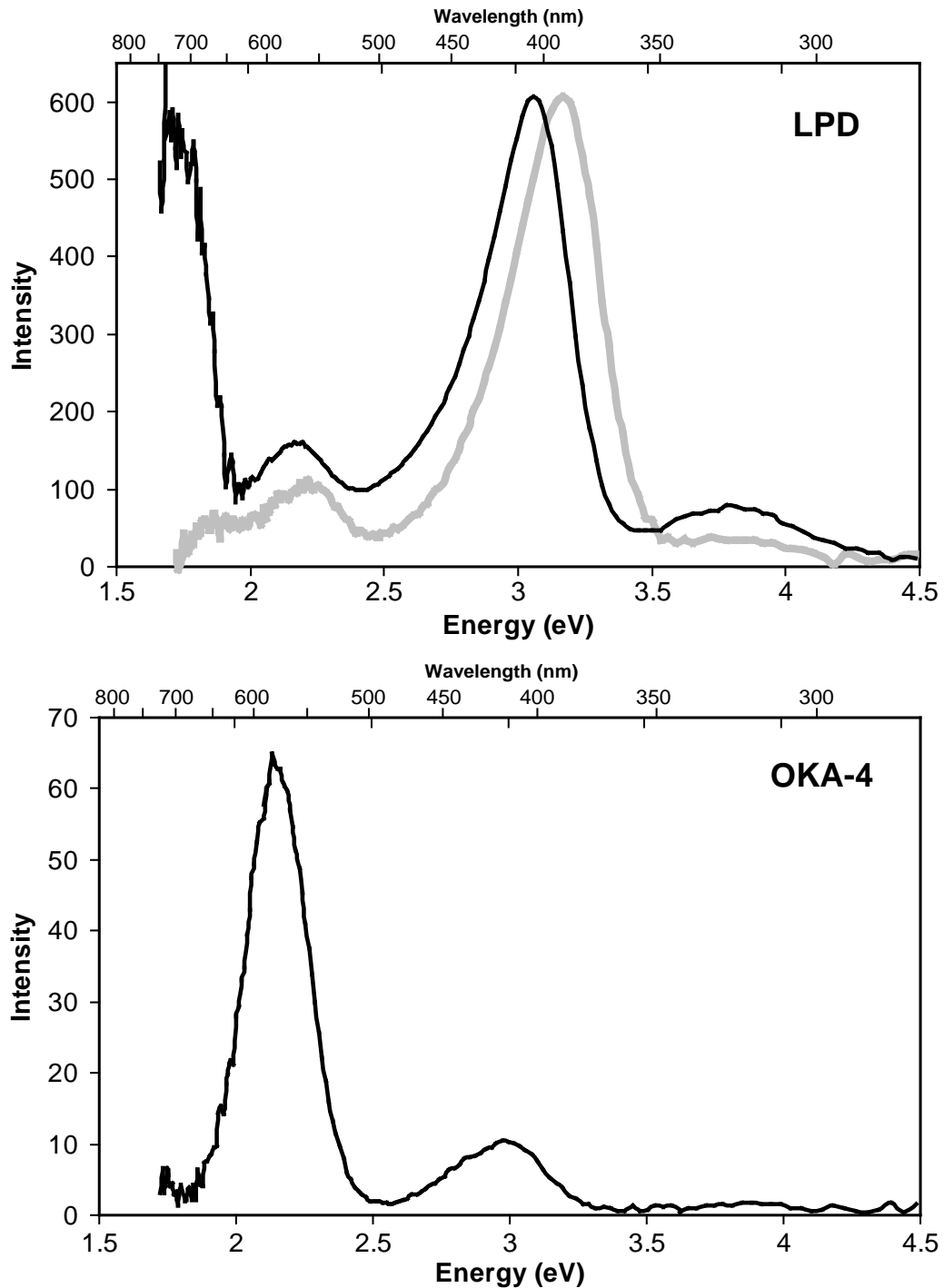
Figure 4.8: *RHIS and SAW-95-09 IRSL spectra. Preheated sample data in grey, unpre-heated sample data in black. Bandwidths (nm): RHIS {15,15,15},{25,25,25} SAW-95-09 {15,15,15},{25,15,15} (Code explained in text).*
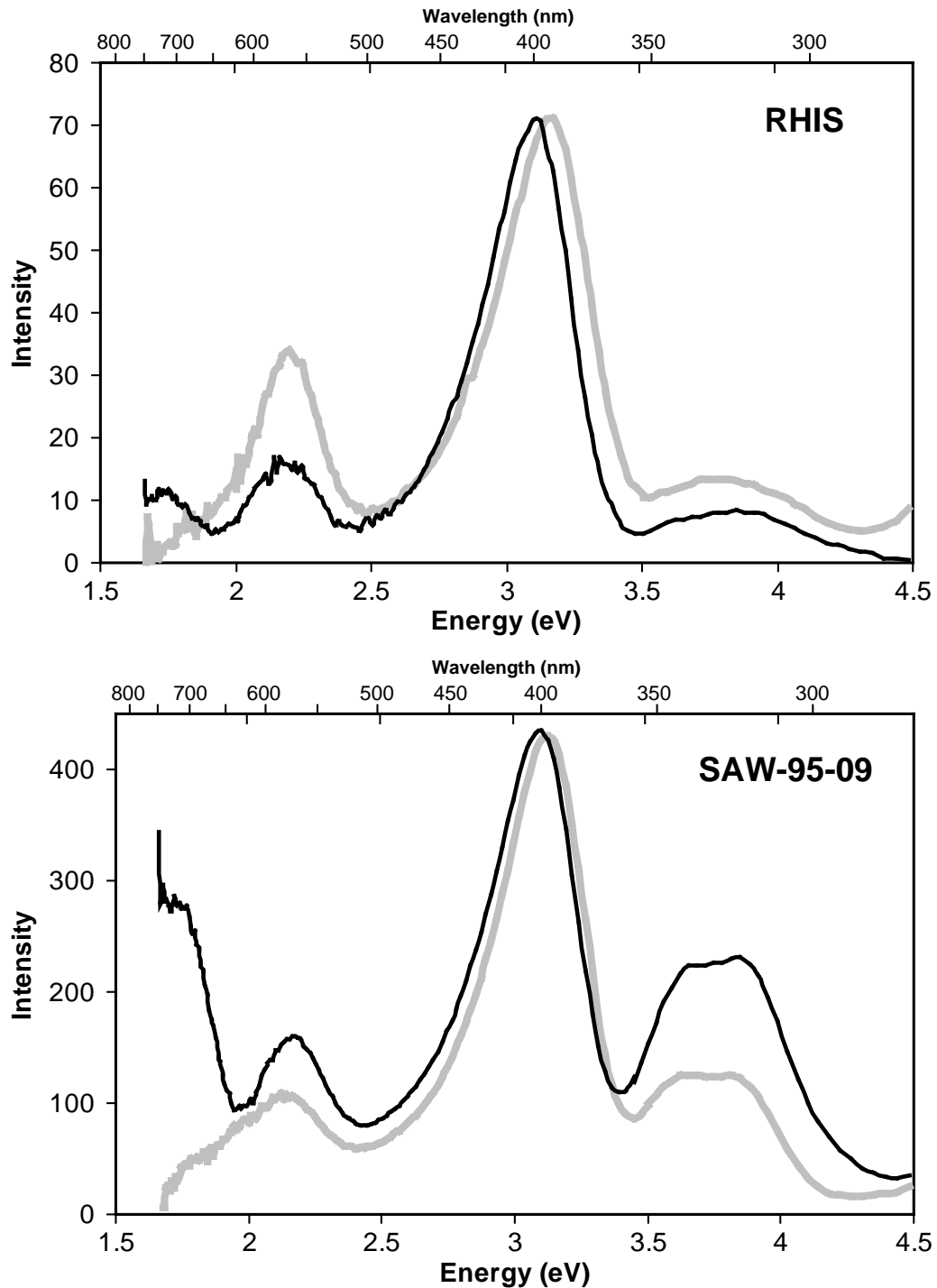
Figure 4.9: *SAW-97-08 and SN-27 IRSL spectra. Preheated sample data in grey, unpre-heated sample data in black. Bandwidths (nm): {15,15,15},{25,25,25} (Code explained in text).*
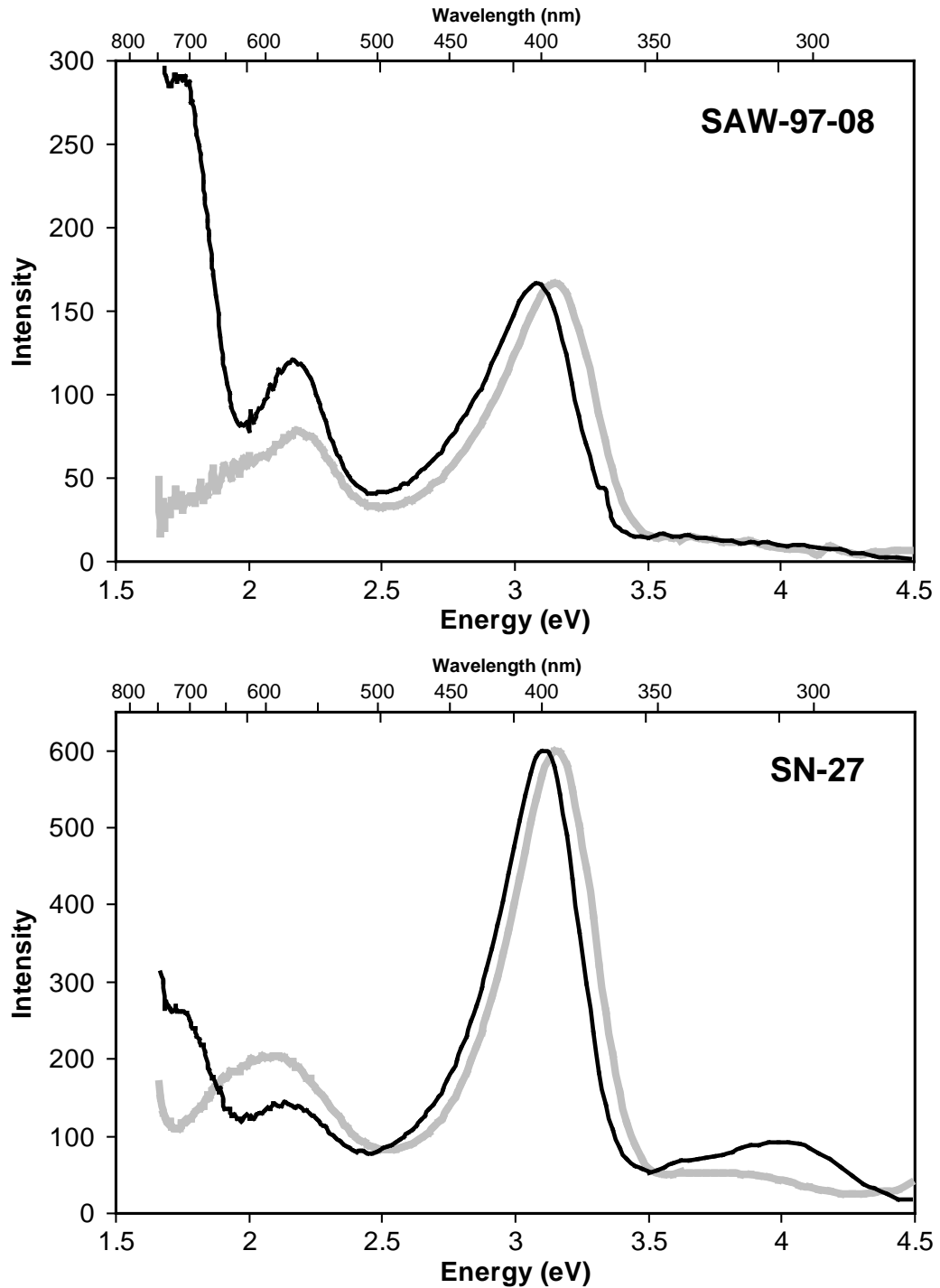
Figure 4.10: *SUN and SW5-01 IRSL spectra. Preheated sample data in grey, unpreheated sample data in black. Bandwidths (nm): {15,15,15},{25,25,25} (Code explained in text).*
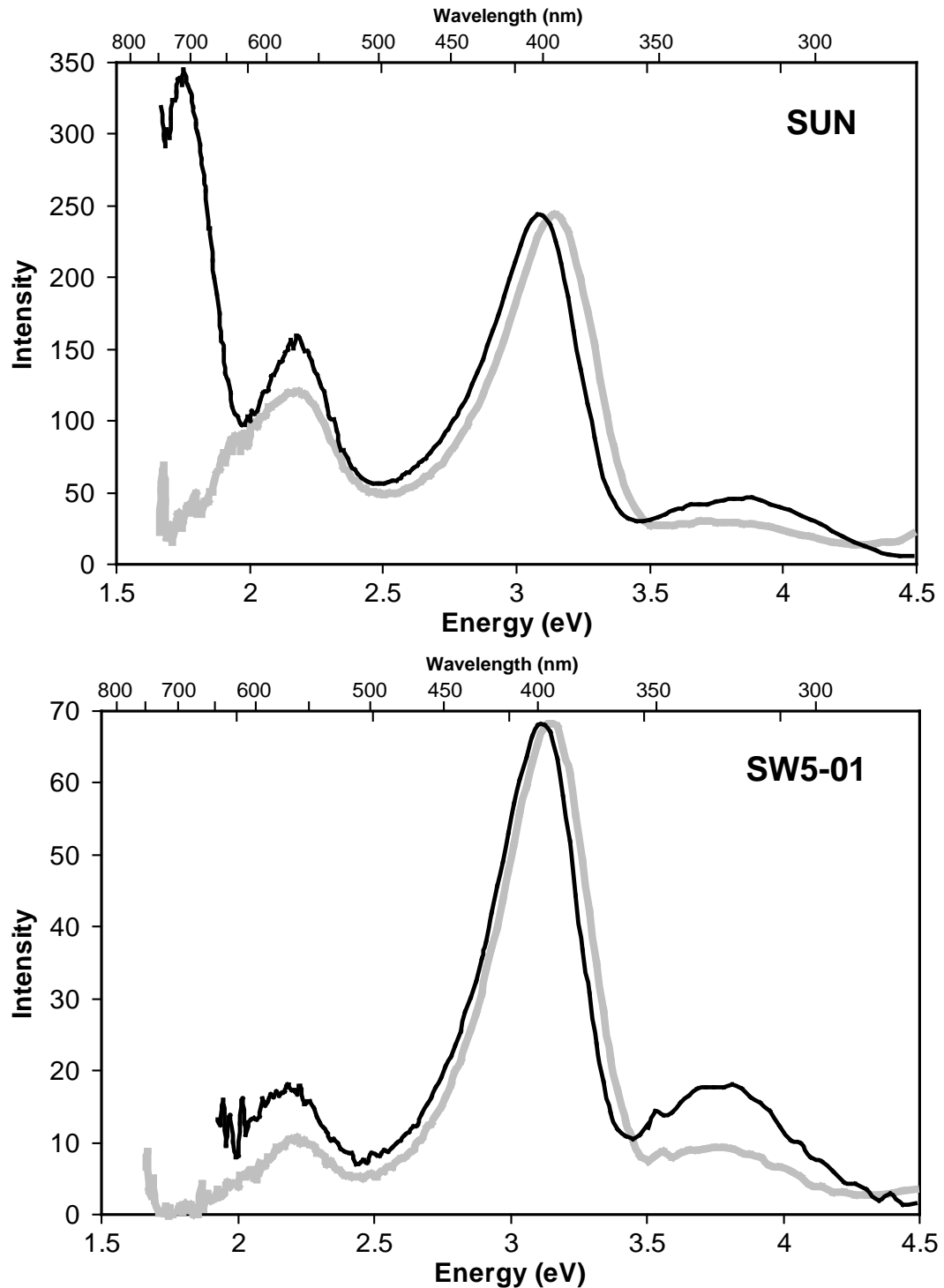
Figure 4.11: *TAG-8 and TTS IRSL spectra. Bandwidths (nm): TAG-8 {-,25,25},{-,-,-}*
TTS {15,15,15},{25,25,25} (Code explained in text).
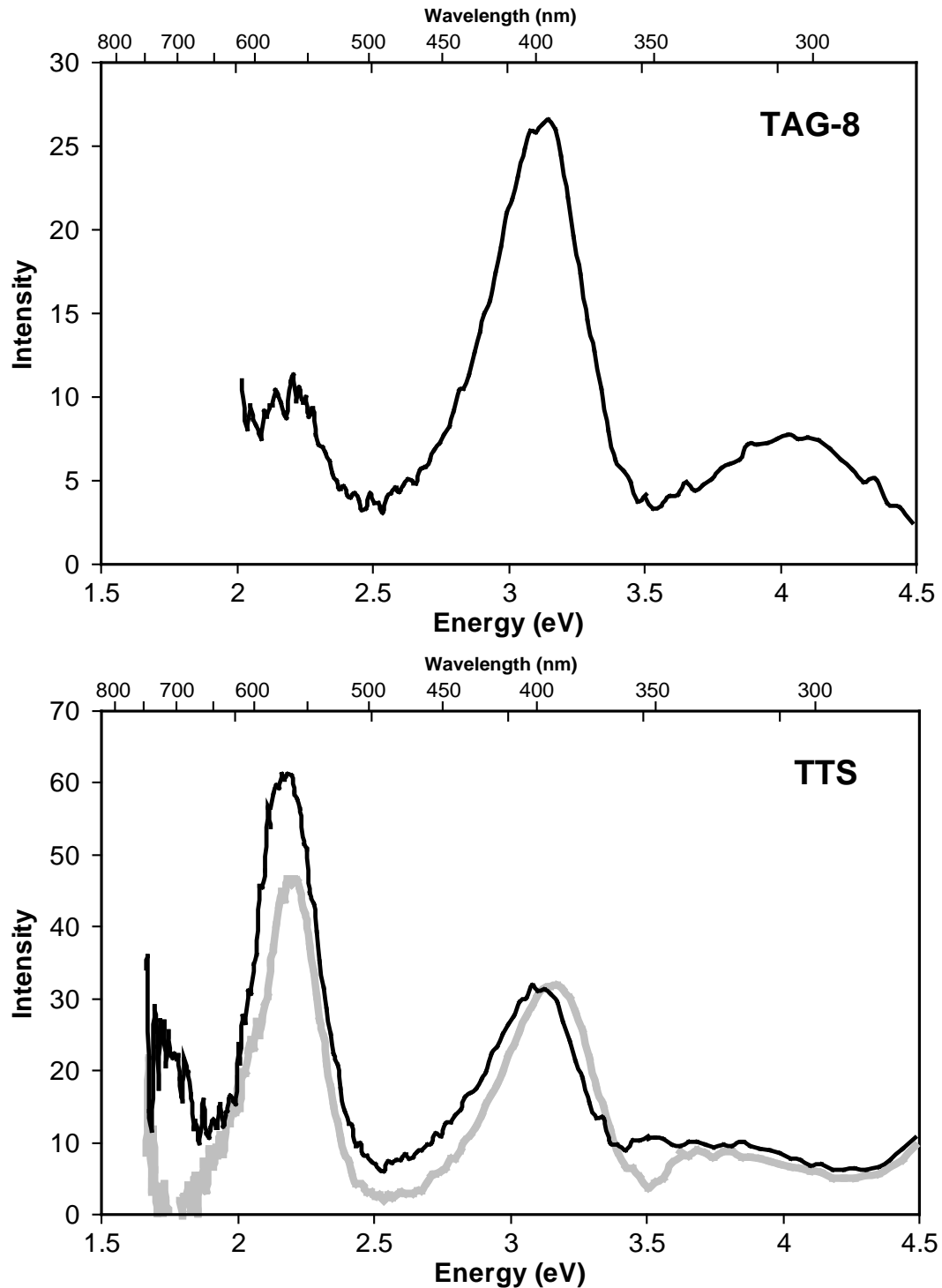
4.2.2   Emission spectra for cut rock samples

Figure 4.12: *A1 and A3 IRSL spectra. Preheated sample data in grey, unpreheated sample data in black. Bandwidths (nm): A1 {7.5,4.5,7.5},{15,15,15}, A3 {7.5,3.5,15},{15,4.5,15} (Code explained in text).*
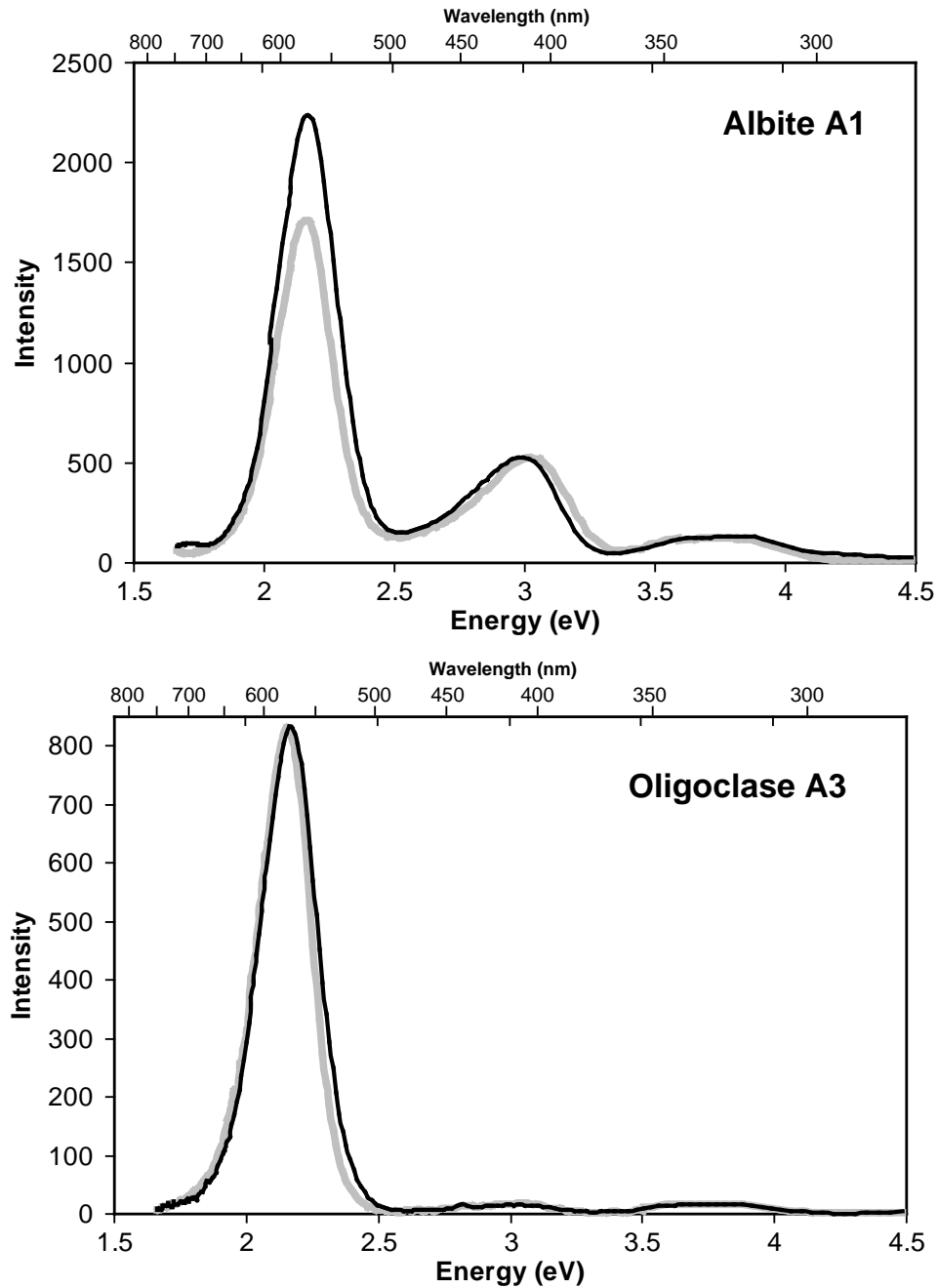
Figure 4.13: *A4 and A5 IRSL spectra. Preheated sample data in grey, unpreheated sample data in black. Bandwidths (nm): A4 {-,25,25},{-,-,-}, A5 {15,15,15},{25,25,15} (Code explained in text).*
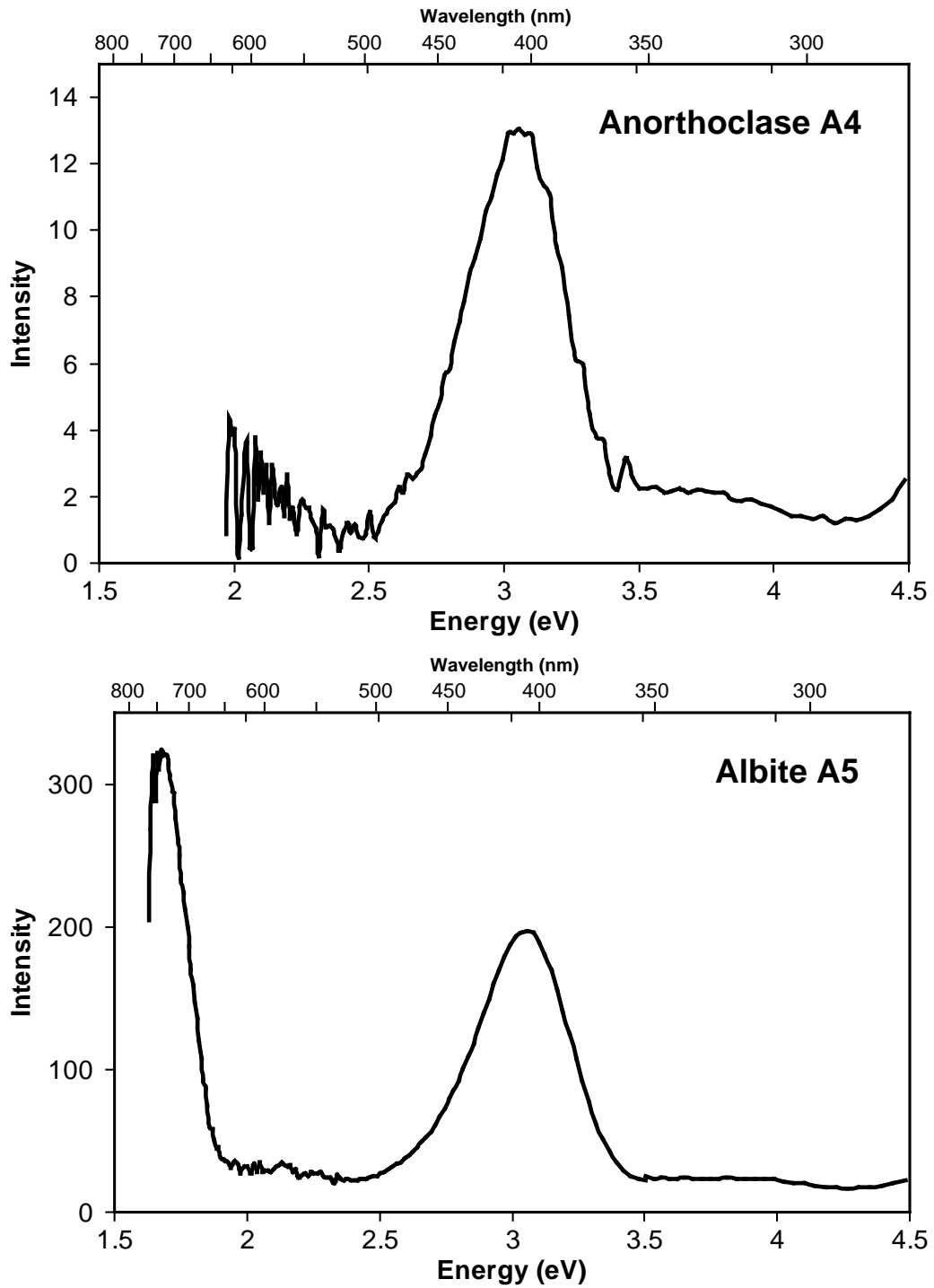
Figure 4.14: *A6 and K3 IRSL spectra. Preheated sample data in grey, unpreheated sample data in black. Bandwidths (nm): A6 {15,15,15},{25,25,15}, K3 {15,7.5,7.5},{15,15,15} (Code explained in text).*
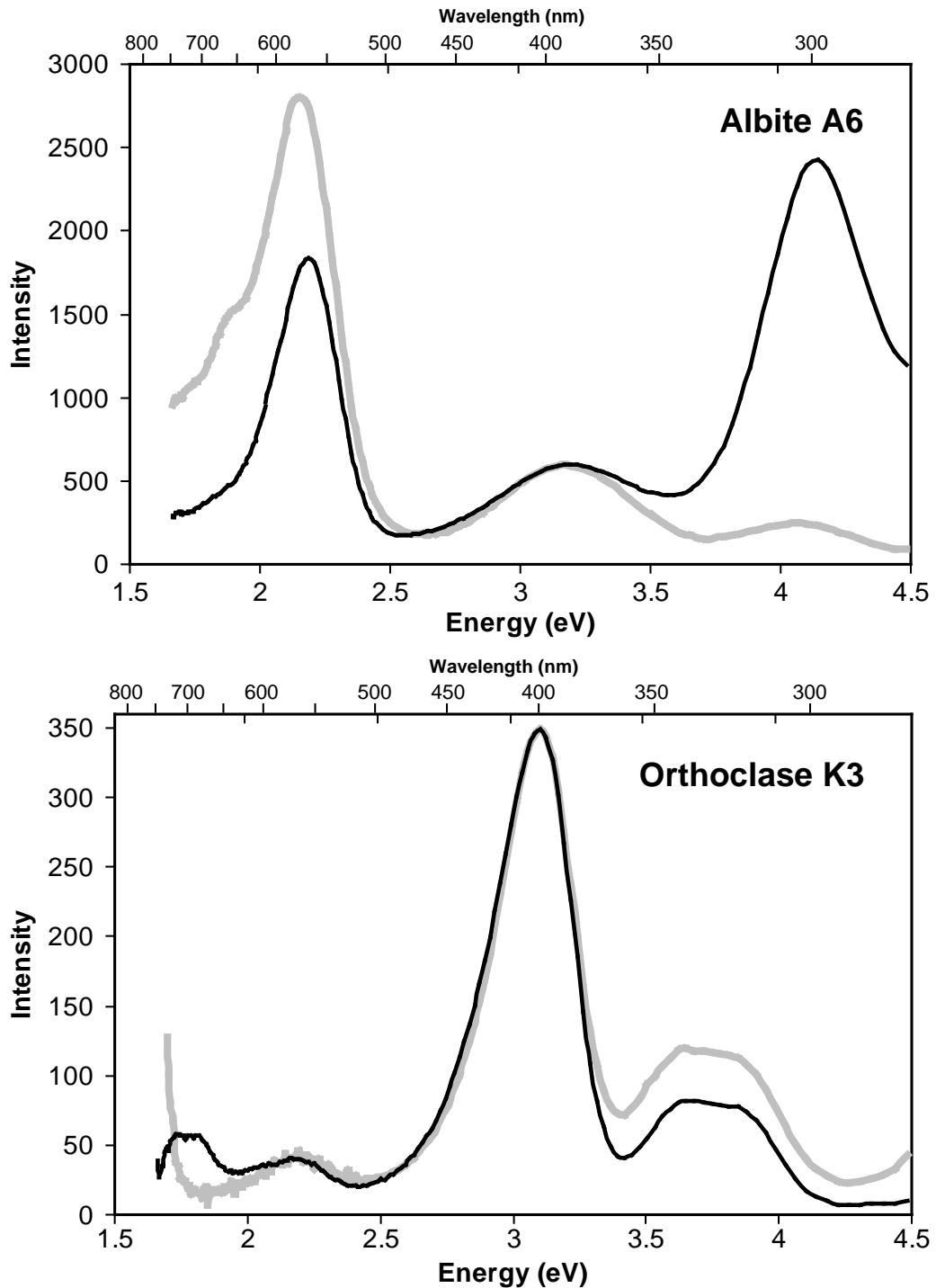
Figure 4.15: *K7 and K8 IRSL spectra. Preheated sample data in grey, unpreheated sample data in black. Bandwidths (nm): K7 {15,15,7.5},{15,25,15}, K8 {15,15,7.5},{15,15,15} (Code explained in text).*
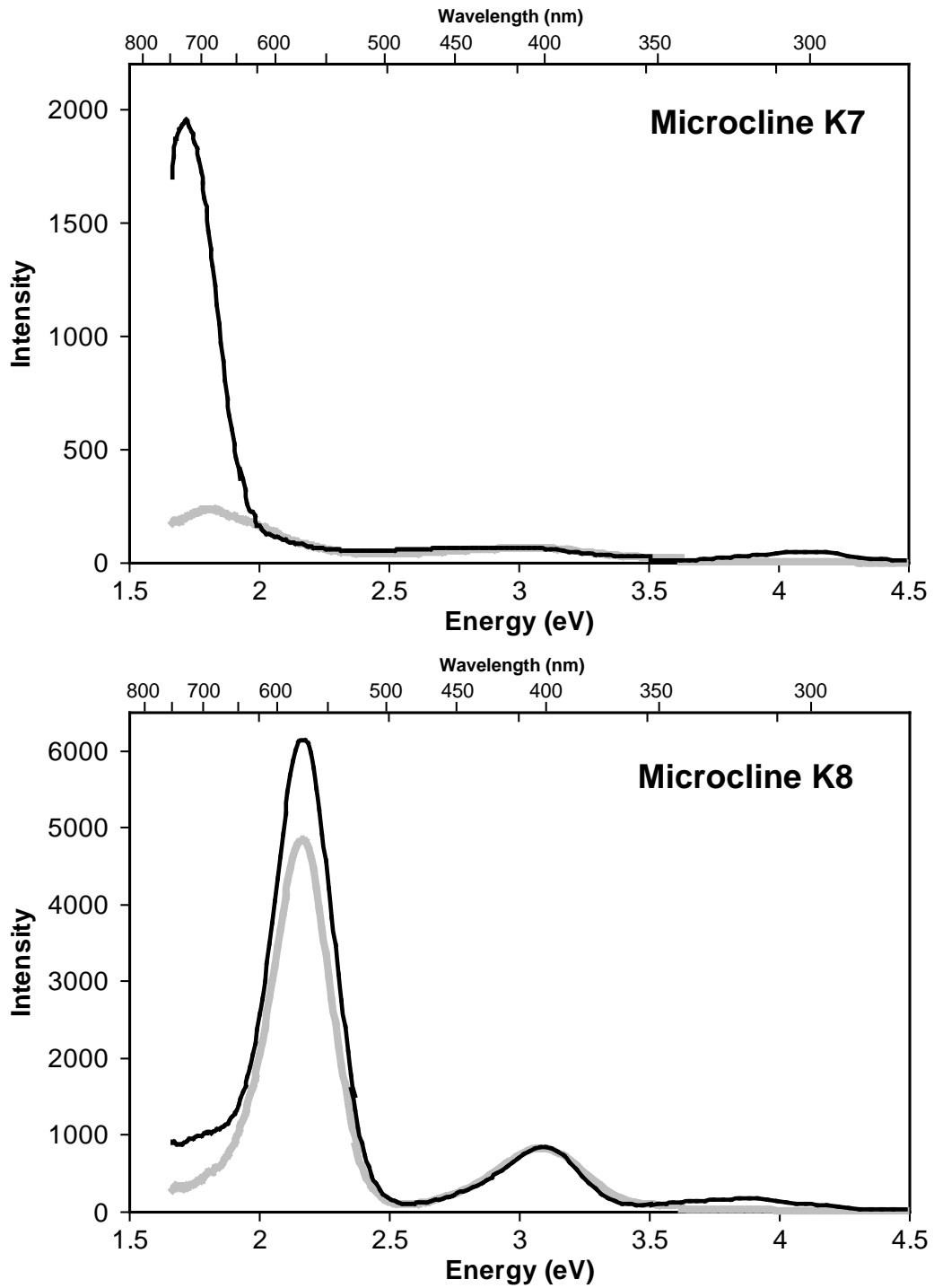
Figure 4.16: *K9 and K10 IRSL spectra. Preheated sample data in grey, unpreheated sample data in black. Bandwidths (nm): {15,7.5,7.5},{15,15,15} (Code explained in text).*
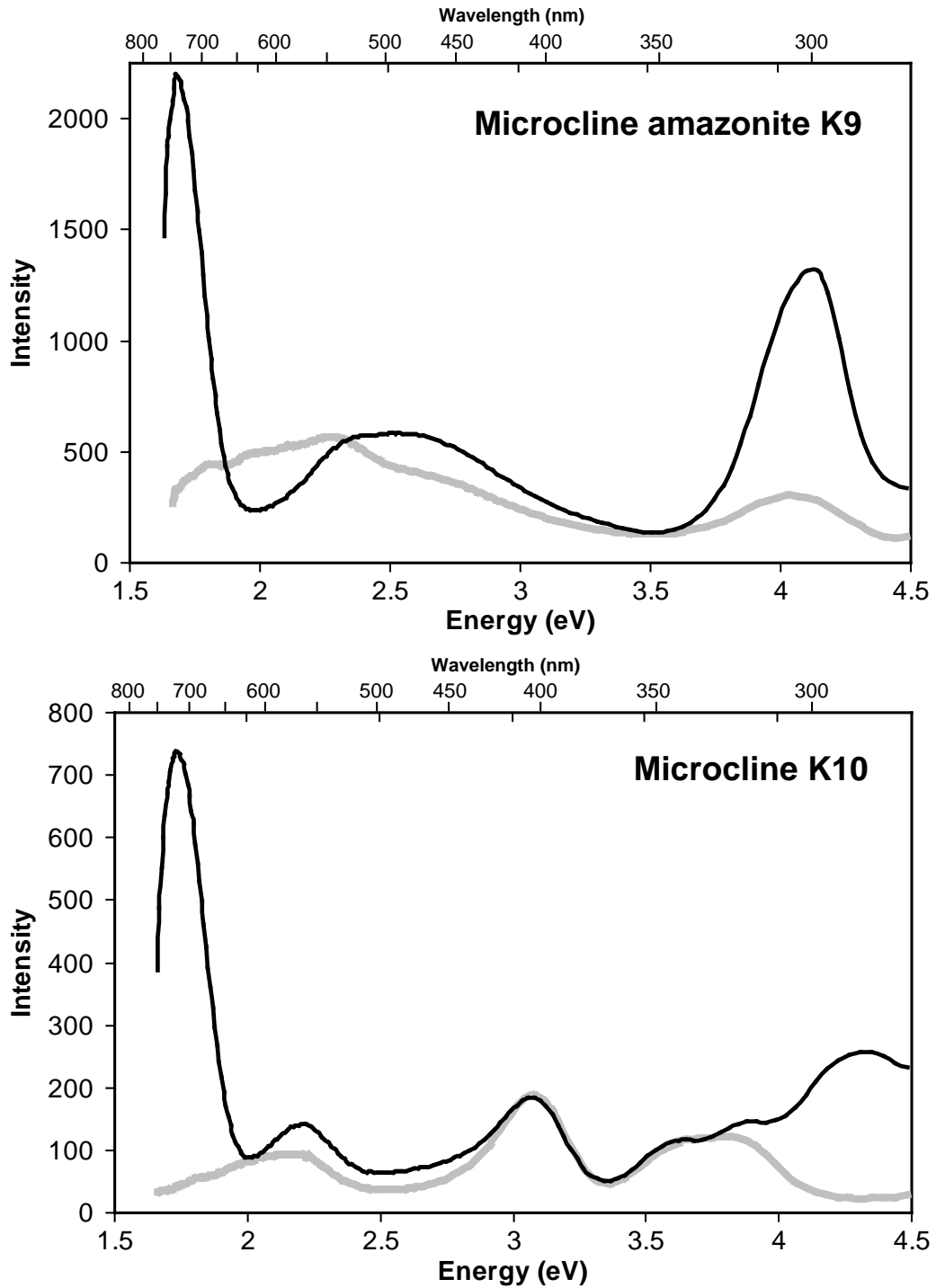
Figure 4.17: *K11 and P10 IRSL spectra for unpreheated samples. Bandwidths (nm): K11 {25,25,25},{-,-,-}, P10 {-,25,25},{-,-,-} (Code explained in text).*
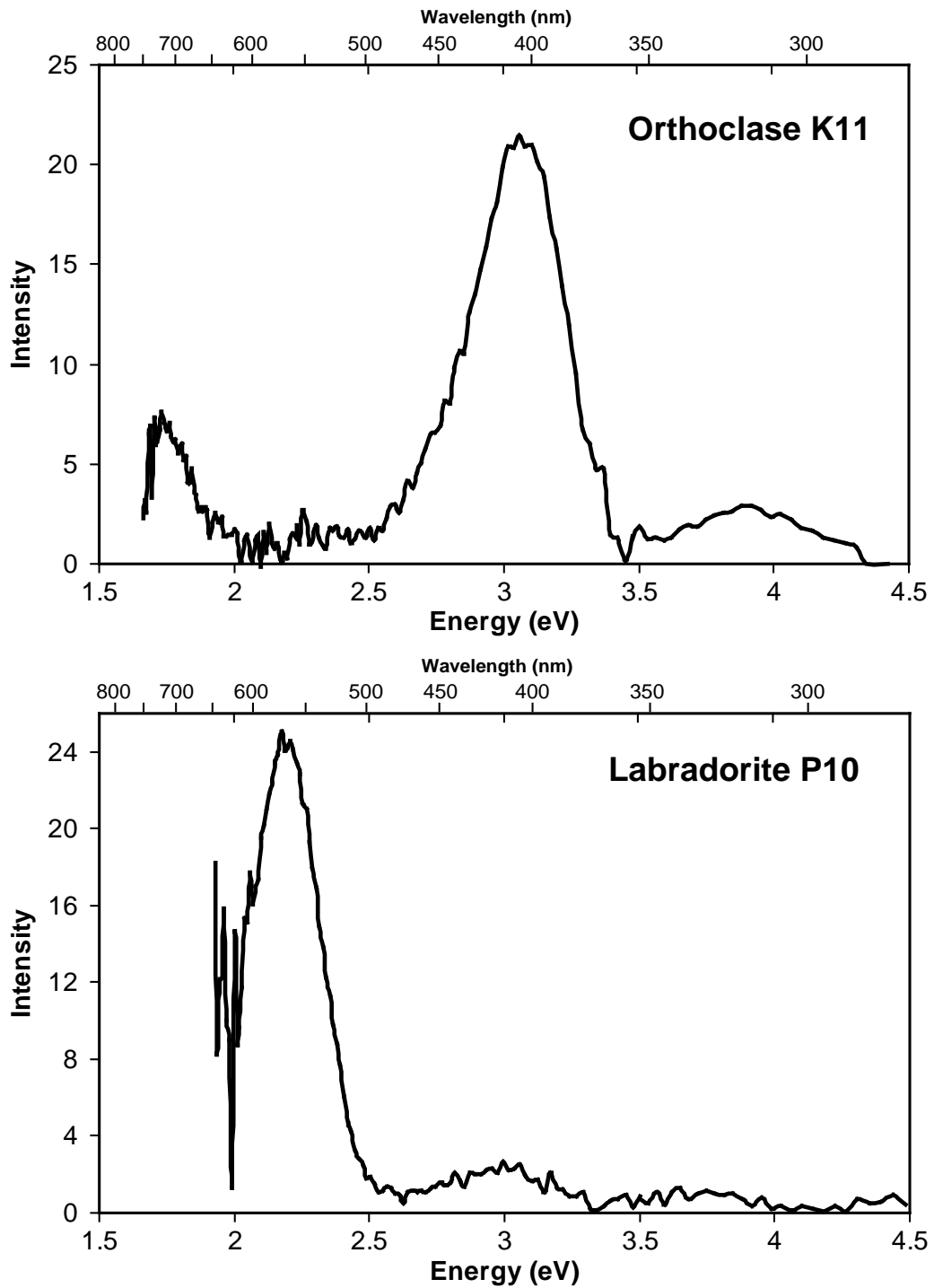
4.2.3 Principal features of the spectra

The relative IRSL peak intensities and positions are reported in Table 4.1. Most of the granular K-feldspar separate samples exhibit a strong IRSL emission band centered at 3.1 eV (400 nm) as well as bands at 2.2 eV (570 nm) and 3.6–3.8 eV (340–326 nm). The UV emission band was occasionally well resolved into two components near 3.65 and 3.85 eV (*e.g.* IV.1, SAW-95-09, SN-27, K3, K10). An additional broad UV band at 4.28 eV (290 nm) was prominent in sample K10. This emission band disappeared upon preheating the sample. Clarke and Rendell (1997) also report disappearance of the 4.28 eV emission band upon heating. The bright UV emission in amazonite K9 correlates well with Marfunin (1979) who notes bright UV emission in amazonites and other high Pb content feldspars. In some samples, *i.e.* TTS, CBSS, CKDS and CTL-2 the 2.2 eV emission is the dominant emission, whereas in others, *i.e.* IV.1 and SAW-97-08 this emission band is of comparable intensity to the violet emission. This suggests that for many of the K-feldspar separates a considerable amount of Na-feldspar is also present.

In addition to the well-known yellow-green, violet and UV emission bands many samples exhibited a strong red emission near 1.76 eV (700 nm). The 1.76 eV emission band is well known from TL emission spectra (*e.g.* Prescott and Fox, 1993; Visocekas and Zink, 1999) where it predominates in low potassium feldspars, but this emission has never been reported in IRSL spectra. This emission band has been attributed to Fe^{3+}, which substitutes for Al^{3+} in the center of the SiO_4 tetrahedron, by various authors (Telfer and Walker, 1978; Short, 2003). The 1.76 eV emission disappears upon heating the sample at 120 $^{\circ}$C for 16 hours. This appears somewhat paradoxical because the TL glow curve for the 1.76 eV emission peaks around 250–300 $^{\circ}$C, whereas very little emission is observed below 100 $^{\circ}$C. If the 1.76 eV emission arises from a separate population of traps, then one would expect from the TL data that these traps should be thermally stable at 120 $^{\circ}$C.

Another peculiar feature of the spectra is a shift of the violet emission band towards the UV following the preheat. The amount of this shift varies between samples, ranging from no shift to a 0.11 eV shift. The shift was almost ubiquitous in the feldspar separate samples (the exception being sample IV.1) but was not observed as clearly in the cut rock samples. In particular, K3 exhibited no shift of the violet peak whatsoever. At first this appeared to be explained by the fact that a wide band pass (25 nm) was used for the preheated sample

data compared to the 15 nm bandpass used in the unpreheated sample measurements for the granular samples. However, an earlier experiment in which spectra were measured using a 1.24 mm slit throughout led to similar results, leaving no doubt as to the existence of this effect.

Rieser *et al.* (1997) have previously reported a shift of the violet and yellow-green IRSL peaks with increasing measurement temperature, however the shift was observed to be greatest for the yellow-green peak; there is no clear evidence of a shift of this peak in our data. In addition, the physical situation investigated by Rieser *et al.* differs significantly from that under discussion here; namely, they have measured the IRSL spectra as a function of temperature for samples that had been allowed several weeks to several months of storage after irradiation and a short preheat at 220 °C. Clarke and Rendell (1997a) did not observe this shift of the violet emission band upon preheating at 220 °C for 5 minutes. Clarke's data appears to suggest a strong shift in one sample[3] but was not remarked upon.

Upon preheating, the intensity of the yellow-green emission and UV bands usually decreases by a relatively larger amount than the decrease in the violet emission. However a sufficient number of samples depart from this behaviour that it cannot be established as a rule. In particular the UV peak(s) were observed to increase relative to the violet in K3, CBSS and RHIS, whereas the yellow-green emission increased relative to the violet in A6, DY-23, RHIS and SN-27.

---

[3]The "Cat Dune" sample.

Table 4.1: *IRSL emission bands for the granular samples. Unpreheated sample data in bold and preheated sample data in regular typeface. Columns E and I are the peak positions (in eV) and intensities relative to the brightest peak in the sample, respectively. I$_{intr.}$ indicates roughly the intrinsic brightness of the sample; it is the intensity of the brightest peak divided by the intensity of the violet peak in the unpreheated sample spectrum of K3. Where the UV emission band is unresolved into two components, the emission for the UV band is quoted in column "UV 1".*

Sample	Red		Yellow-green		Violet		UV 1		UV 2		I$_{intr.}$
	E	I	E	I	E	I	E	I	E	I	
AKHC	**1.76**	**1.00**	**2.18**	**0.34**	**3.08**	**0.80**	**3.65**	**0.12**	**3.84**	**0.12**	**0.6**
	–	–	2.18	0.28	3.14	1.00	3.77	0.094	–	–	0.4
BIDS	**1.76**	**0.35**	**2.18**	**0.29**	**3.11**	**1.00**	**3.98**	**0.27**	**–**	**–**	**0.1**
CBSS	**1.76**	**0.36**	**2.17**	**1.00**	**3.13**	**0.46**	**3.75**	**0.12**	**–**	**–**	**0.07**
	–	–	2.19	1.00	3.18	0.73	3.75	0.40	–	–	0.04
CES-5	**1.76**	**0.32**	**2.17**	**0.12**	**3.09**	**1.00**	**3.75**	**0.10**	**–**	**–**	**0.4**
	–	–	2.23	0.062	3.16	1.00	3.75	0.046	–	–	0.3
CKDS	**–**	**–**	**2.20**	**1.00**	**3.10**	**0.78**	**3.91**	**0.13**	**–**	**–**	**0.04**
CTL-2	**–**	**–**	**2.2**	**1.00**	**3.09**	**0.12**	**–**	**–**	**–**	**–**	**0.015**
DY-23	**1.76**	**1.00**	**2.19**	**0.27**	**3.09**	**0.57**	**3.97**	**0.12**	**–**	**–**	**0.2**
	–	–	2.14	0.51	3.14	1.00	3.84	0.071	–	–	0.15
EIDS	**–**	**–**	**2.17**	**0.90**	**3.11**	**1.00**	**3.66**	**0.45**	**4.00**	**0.45**	**0.4**
	–	–	2.15	0.42	3.13	1.00	3.71	0.30	–	–	0.2
GP-1	**1.76**	**0.49**	**2.21**	**0.14**	**3.10**	**1.00**	**3.69**	**0.10**	**3.85**	**0.11**	**0.7**
	–	–	2.13	0.08	3.16	1.00	3.85	0.06	–	–	0.6
IV.1	**1.77**	**0.63**	**2.20**	**0.92**	**3.10**	**1.00**	**3.62**	**0.20**	**3.80**	**0.19**	**0.3**
	–	–	2.20	0.12	3.13	1.00	3.71	0.06	–	–	0.3

Table 4.2: *IRSL emission bands for the granular samples (continued from Table 4.1).*

Sample	Red		Yellow-green		Violet		UV 1		UV 2		$I_{intr.}$
	E	I	E	I	E	I	E	I	E	I	
LPD	**1.74**	**0.94**	**2.18**	**0.26**	**3.06**	**1.00**	**3.79**	**0.13**	**–**	**–**	**0.8**
	–	–	2.22	0.17	3.19	1.00	3.79	0.056	–	–	0.06
OKA-4	**–**	**–**	**2.15**	**1.00**	**3.00**	**0.16**	**3.89**	**0.03**	**–**	**–**	**0.09**
RHIS	**1.75**	**0.16**	**2.20**	**0.22**	**3.10**	**1.00**	**3.81**	**0.12**	**–**	**–**	**0.1**
	–	–	2.20	0.48	3.15	1.00	3.76	0.19	–	–	0.07
SAW-95-09	**1.75**	**0.64**	**2.18**	**0.37**	**3.10**	**1.00**	**3.68**	**0.51**	**3.85**	**0.53**	**0.6**
	–	–	2.15	0.24	3.13	1.00	3.76	0.19	–	–	0.3
SAW-97-08	**1.75**	**1.00**	**2.18**	**0.41**	**3.09**	**0.57**	**–**	**–**	**–**	**–**	**0.4**
	–	–	2.20	0.46	3.16	1.00	–	–	–	–	0.3
SN-27	**1.76**	**0.44**	**2.14**	**0.24**	**3.12**	**1.00**	**3.67**	**0.11**	**4.02**	**0.16**	**0.8**
	–	–	2.10	0.34	3.17	1.00	3.75	0.09	–	–	0.3
SUN	**1.76**	**1.00**	**2.18**	**0.47**	**3.10**	**0.72**	**3.84**	**0.14**	**–**	**–**	**0.5**
	–	–	2.18	0.48	3.16	1.00	3.84	0.12	–	–	0.3
SW5-01	**–**	**–**	**2.19**	**0.25**	**3.12**	**1.00**	**3.77**	**0.26**	**–**	**–**	**0.09**
	–	–	2.22	0.15	3.16	1.00	3.77	0.13	–	–	0.07
TAG-8	**–**	**–**	**2.22**	**0.38**	**3.14**	**1.00**	**3.91**	**0.29**	**–**	**–**	**0.02**
TTS	**1.76**	**0.39**	**2.19**	**1.00**	**3.11**	**0.51**	**3.75**	**0.16**	**–**	**–**	**0.09**
	–	–	2.21	1.00	3.17	0.68	3.75	0.19	–	–	0.04

Table 4.3: *IRSL emission bands for the cut-rock samples. See Table 4.1 for detailed explanation. Notes: †The 2.4 eV and 2.6 eV emission bands in K9 may not correspond to the "yellow-green" emission in other samples. ✠K10 has an additional UV emission band at 4.28 eV (I=0.35). ‡Data for sample A2 were estimated from the emission spectra of Short (2003).*

Sample	Red		Yellow-green		Violet		UV 1		UV 2		$I_{intr.}$
	E	I	E	I	E	I	E	I	E	I	
A1	–	–	**2.19**	**1.00**	**3.00**	**0.23**	**3.63**	**0.05**	**3.82**	**0.06**	**15**
	–	–	2.19	1.00	3.03	0.30	3.72	0.7	–	–	3
A2‡	?	?	**2.25**	**1.00**	**3.00**	**0.04**	**3.3**	**0.05**	?	?	**6**
A3	–	–	**2.18**	**1.00**	**3.01**	**0.02**	**3.74**	**0.02**	–	–	**13**
	–	–	2.17	1.00	3.01	0.02	3.74	0.02	–	–	3
A4	–	–	**2.1**	**0.2**	**3.08**	**1.00**	**3.78**	**0.16**	–	–	**0.008**
A5	**1.98**	**1.00**	**2.2**	**0.15**	**3.07**	**0.61**	**3.89**	**0.08**	–	–	**0.5**
A6	–	–	**2.20**	**0.76**	**3.21**	**0.25**	**4.14**	**1.00**	–	–	**4**
	–	–	2.17	1.00	3.21	0.22	4.09	0.09	–	–	2
K3	**1.78**	**0.16**	**2.18**	**0.12**	**3.11**	**1.00**	**3.65**	**0.23**	**3.87**	**0.22**	**1**
	–	–	2.18	0.12	3.11	1.00	3.65	0.34	3.87	0.32	1
K7	**1.73**	**1.00**	–	–	**3.01**	**0.03**	**4.13**	**0.03**	–	–	**3**
	1.82	1.00	–	–	3.01	0.03	–	–	–	–	2
K8	–	–	**2.18**	**1.00**	**3.11**	**0.14**	**3.89**	**0.03**	–	–	**8**
	–	–	2.18	1.00	3.11	0.17	–	–	–	–	8
K9 †	**1.71**	**1.00**	**2.38**	**0.26**	**2.62**	**0.26**	**4.12**	**0.61**	–	–	**7**
	–	–	2.26	1.00	2.70	0.66	4.04	0.54	–	–	6
K10 ✠	**1.76**	**1.00**	**2.21**	**0.19**	**3.08**	**0.25**	**3.63**	**0.16**	**3.89**	**0.20**	**2**
	–	–	2.15	0.50	3.10	1.00	3.63	0.63	3.82	0.66	2
K11	**1.75**	**0.26**	–	–	**3.08**	**1.00**	**3.89**	**0.14**	–	–	**0.01**
P10	–	–	**2.21**	**1.00**	**3.02**	**0.10**	**3.74**	**0.05**	–	–	**0.01**

4.2.4   Correlation of IRSL with sample composition

As can be seen from a plot of the fraction of the violet relative to the yellow-green + violet intensity versus the ratio of the K molar content to the combined K and Na molar content, [K]/([K]+[Na]), there is a strong correlation between K-rich samples and samples where the violet predominates over yellow-green luminescence (Figure 4.18, left). Sample K8 exhibits the greatest departure from this rule; the analyses suggest a K-feldspar yet the yellow-green emission predominates in this sample. The position of samples A4 and A5 in this diagram suggest that these are perhaps better classified as microclines rather than anorthoclase and albite respectively, although X-ray diffraction measurements would be required to confirm this.

Figure 4.18: *Left: Correlation of the K molar content [K] relative to the Na molar content [Na] with the intensity of the violet emission band relative to the yellow-green lumines-cence. Right: Correlation of the Ca content (weight percent) with the intrinsic intensity, $I_{intrinsic}$ (see text for definition).*
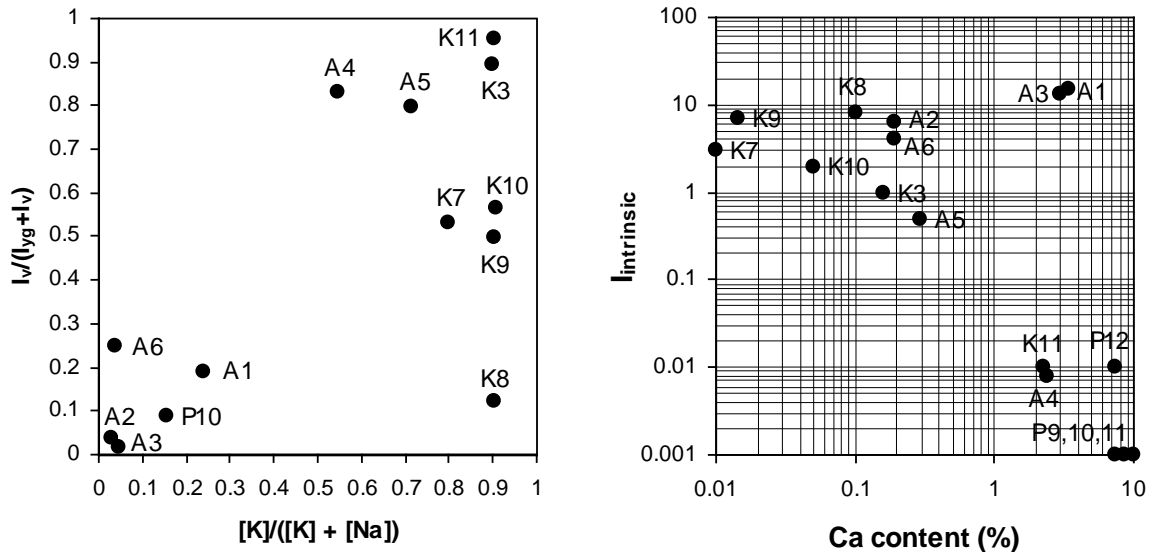
The intrinsic intensity was dimmest in the Ca bearing samples, particularly the plagio-clases (Figure 4.18, right). The intrinsic intensity is defined here as the intensity of the brightest emission band in the sample relative to violet emission band in sample K3. This quantity is useful because the variation in intensity between different samples is often much

larger than the variation in the relative intensity of emission bands in a single sample. For example, if one plots the absolute intensity of the violet or yellow-green emission vs. Ca content, the same general trend towards lower intensity at higher Ca content is observed for both emission bands.

Correlations were sought between the individual absolute peak intensities (and intrinsic intensity) and all of the minor elements listed earlier in Tables 3.2 and 3.7. Few correlations were found; trends were noticed only for Mn, Fe, Pb and perhaps some of the lanthanide element contents.

The correlation between Pb content and the UV emission bands is not straightforward, if it exists. As expected, the amazonite microcline K9 had the largest Pb content and also the brightest UV emission. High Pb contents are not unusual in amazonites which derive their bright green colour from Pb^{2+} centers (Smith and Brown, 1988). However, the Pb content appeared to be positively correlated with the intrinsic intensity rather than being specifically connected to the intensity of the UV band(s); see Figure 4.19.

Figure 4.19: *Plots of the absolute intensity of the brightest UV band (left) and the intrinsic intensity (right) vs. the Pb contents.*
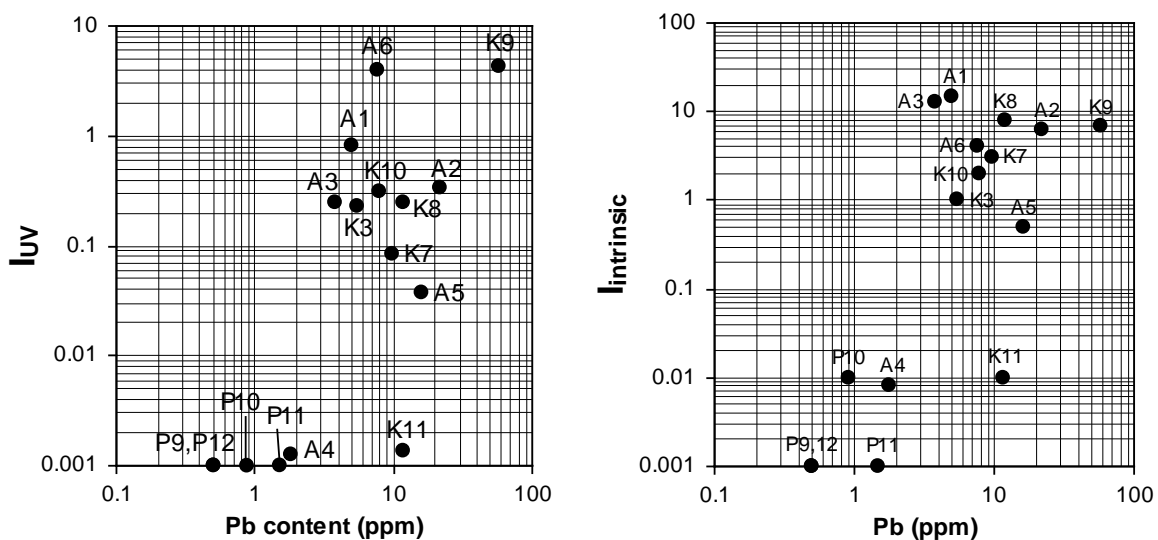
A weak anti-correlation was noted between the contents of Sm, Tb, Nd, Ce and the intrinsic intensity of the samples, Figure 4.20. It is impossible to say which of these elements is responsible for this effect because the individual abundances of these elements are

strongly correlated (*e.g.* if Ce is abundant in one sample, then Sm, Tb, and Nd are also likely to be abundant). It should be noted that it is known that the incorporation of rare-earth elements in certain materials (*e.g.* CaF_2 can cause lattice strains that affect the luminescence properties (Townsend *et al.*, 2001).

Figure 4.20: *Plots of the intrinsic intensity versus the contents of Sm, Tb, Nd and Ce.*
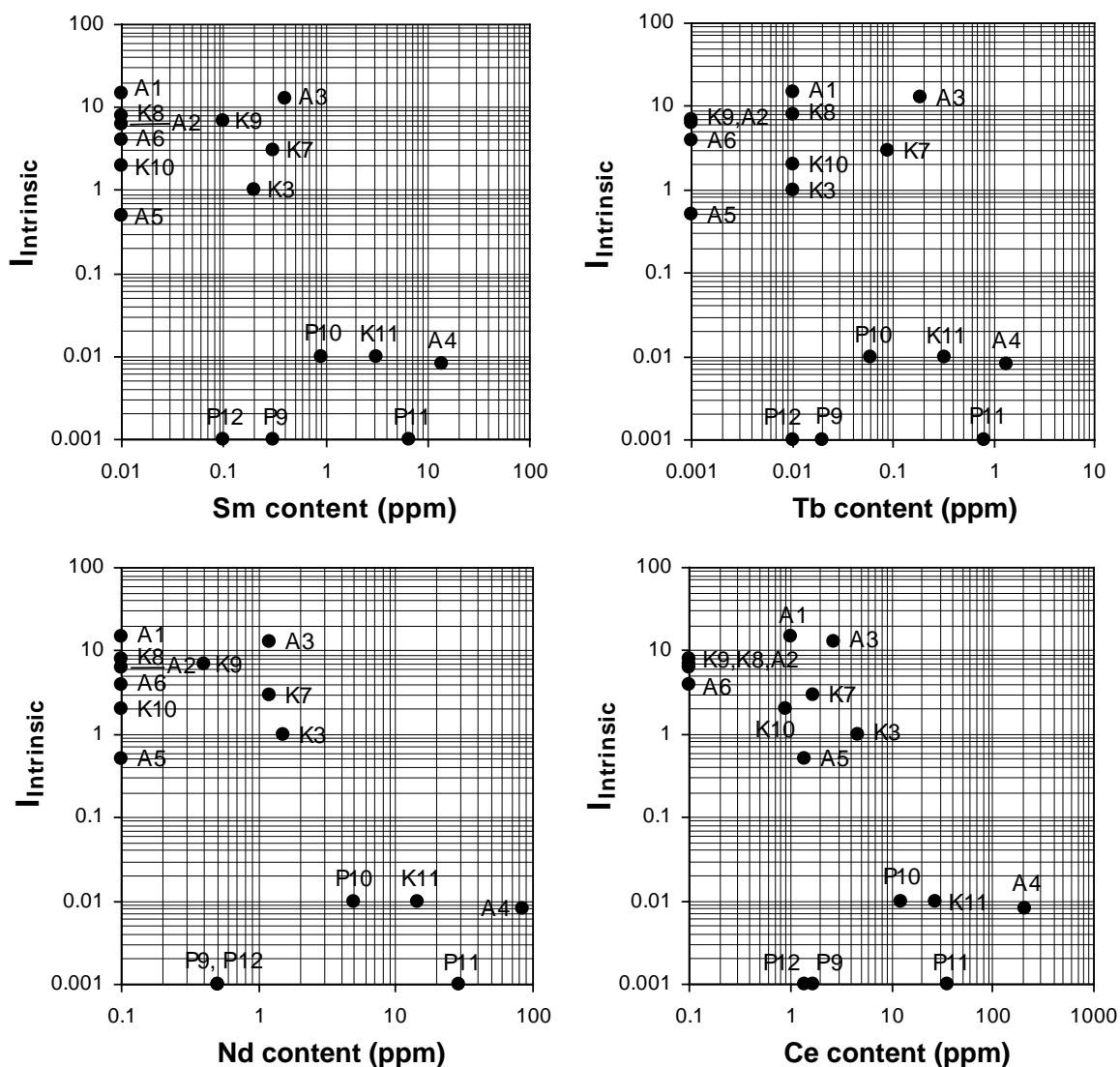
The correlation suggested by previous authors (see Section 1.4) between Mn and Fe content and the intensity of the yellow-green and red emission bands respectively, is not

supported by our data. In fact, there appears to be an *anti-correlation* between the presence of Mn and/or Fe and the intensities of all emission bands. It is impossible to tell whether this is due to the presence of Mn, Fe or both, because there is a very strong positive correlation between the Mn and Fe contents (Figure 4.21).

Further investigations correlating elemental contents and luminescence behaviour should place more attention on the problem of obtaining absolute sample intensities. It should be emphasized that the intrinsic intensities given in this study are only approximate due to several factors. The slight sensitivity difference between different measurements due to changes in the spectrometer setup is probably the least significant problem and likely contributes less than a factor of 2 to the spread in intrinsic intensities. Likewise, the size of the sample is not a significant factor because the spectrometer slit was over-filled by the luminescence from the sample in all cases. The large variation in the transparency between samples is the most significant issue. Some plagioclase samples were almost opaque whereas other samples, such as K3, were almost transparent. This problem may be minimized in future work by thinning the samples to a uniform thickness, although this would be practically impossible for some brittle samples, such as K11. Once thinned, the transmissivity of the samples could be measured and corrections applied for the absorption of the excitation light and the IRSL. Milling the samples and mounting the powder in index matching fluid is another possibility, although the effect of milling the samples on the luminescence properties would require investigation.

4.3   Variation of the emission spectrum during "shinedown" decay of the IRSL.

In the brightest of the samples it was possible to measure the emission spectrum several times during a short excitation under 1.44 eV light. In this way, the relative rate of decay of the violet and yellow-green emission bands as a function of excitation time could be compared.

Each spectrum was integrated for 4 s using a beam power of $\sim$100–300 mW/cm^2, for a total of 80 s (20 time slices). A 2.2 mm thick Schott BG-39 filter allowed both the yellow-green and violet emissions to be measured while absorbing the scattered 1.44 eV

Figure 4.21: *Effect of the Fe content on the IRSL bands. Fe and Mn contents are strongly correlated (top-left), so that the trends observed for Fe may in fact be due to Mn.*
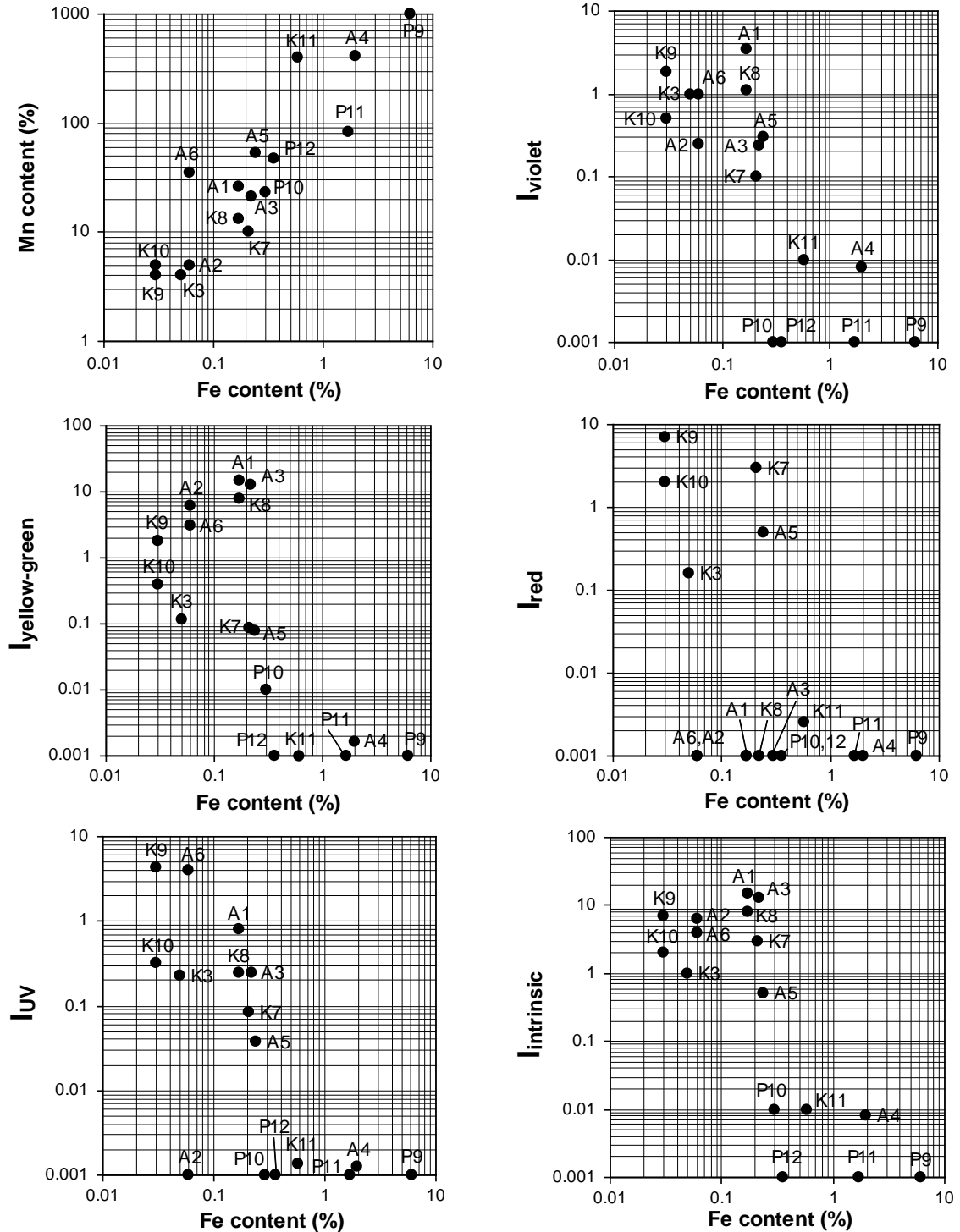
excitation. A spectrometer bandpass of 25 nm was used. The spectra were normalized for the response of the spectrometer and are shown in Figures 4.22- 4.29 for our 8 brightest granular samples and 7 rock samples. Also plotted are the violet and yellow-green peak intensities as a function of illumination time on double logarithmic axes.

Figure 4.22: *Left: K10 emission spectra as a function of illumination time. Each curve represents an increment of 4 seconds of illumination time. Right: Violet emission (solid circles) and yellow-green emission (open circles) peak intensity as a function of illumination time. The time shown corresponds to the endpoint of the measurement. Lines through the data are a fit to $I_0/(t-t_0)^\alpha$.*
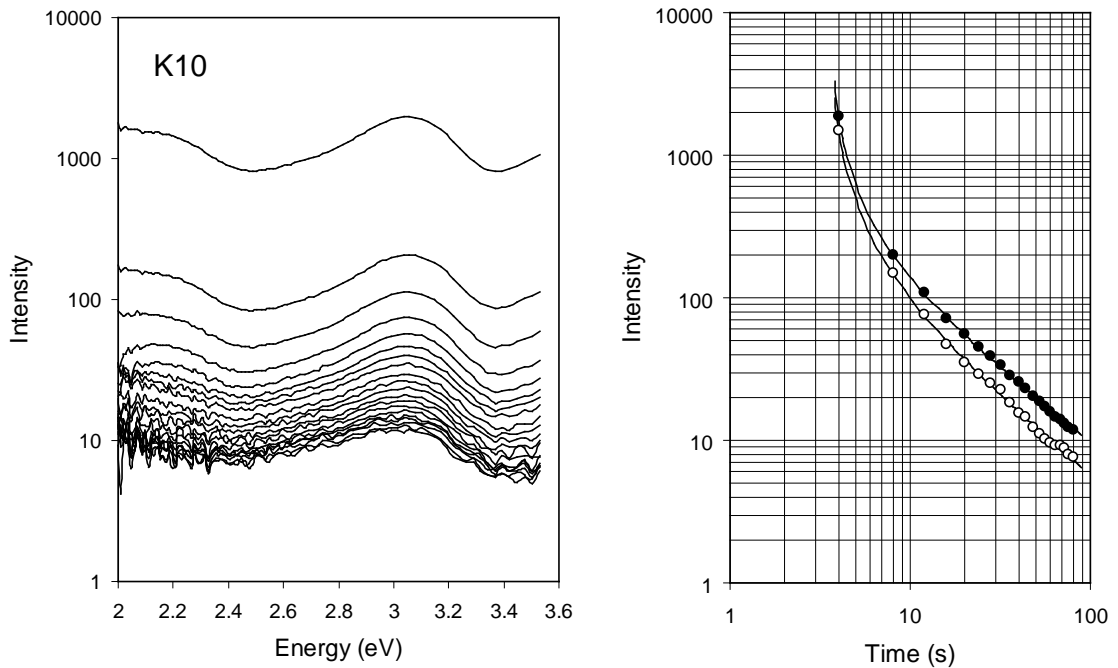
Figure 4.23: *Left: AKHC (top) and DY-23 (bottom) emission spectra as a function of illumination time. Each curve represents an increment of 4 seconds of illumination time. Right: Violet emission (solid circles) and yellow-green emission (open circles) peak intensity as a function of illumination time. The time shown corresponds to the endpoint of the measurement. Lines through the data are a fit to $I_0/(t - t_0)^{\alpha}$.*
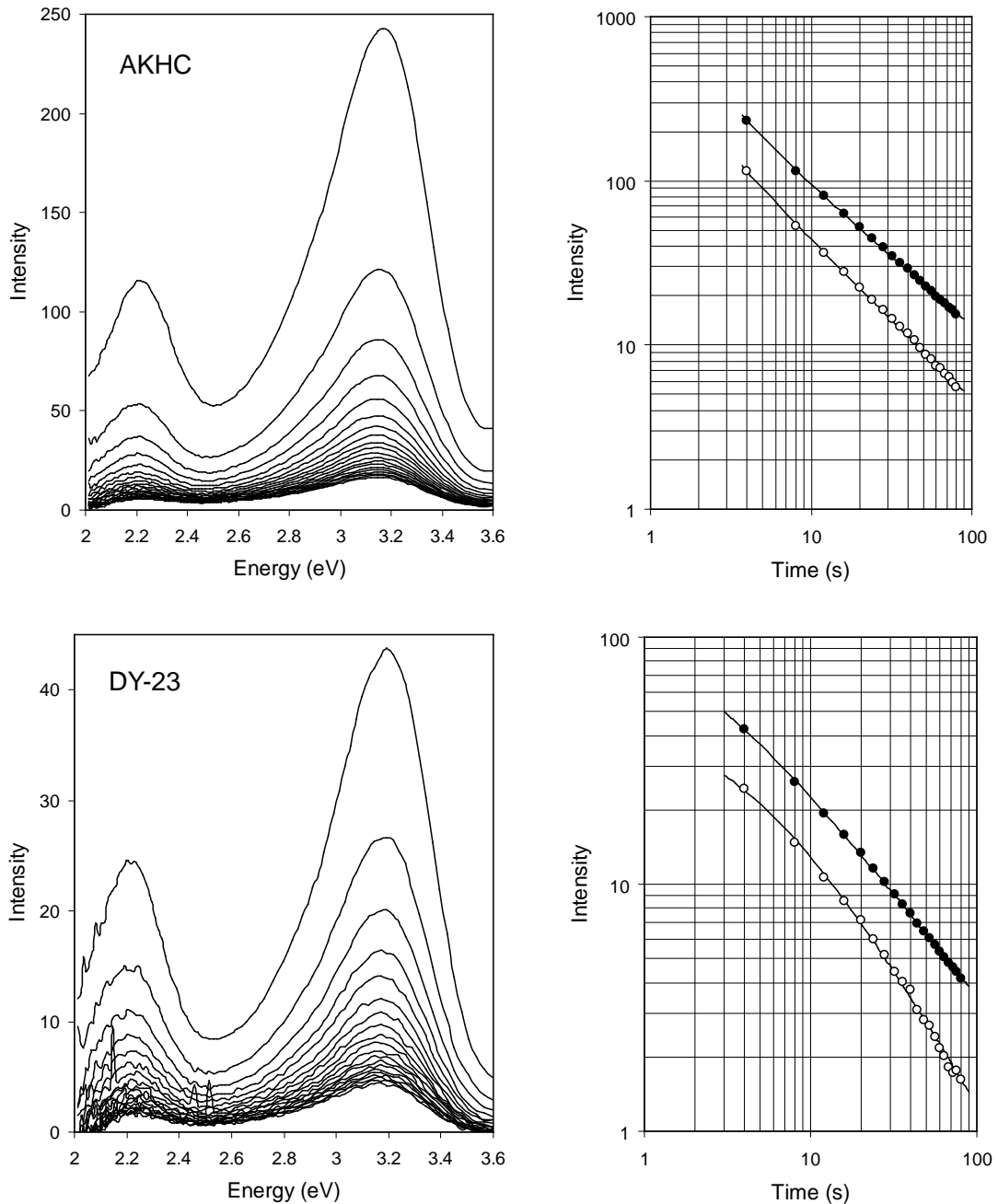
Figure 4.24: *Left: EIDS (top) and GP-1 (bottom) emission spectra as a function of illumination time. Each curve represents an increment of 4 seconds of illumination time. Right: Violet emission (solid circles) and yellow-green emission (open circles) peak intensity as a function of illumination time. The time shown corresponds to the endpoint of the measurement. Lines through the data are a fit to $I_0/(t-t_0)^\alpha$.*
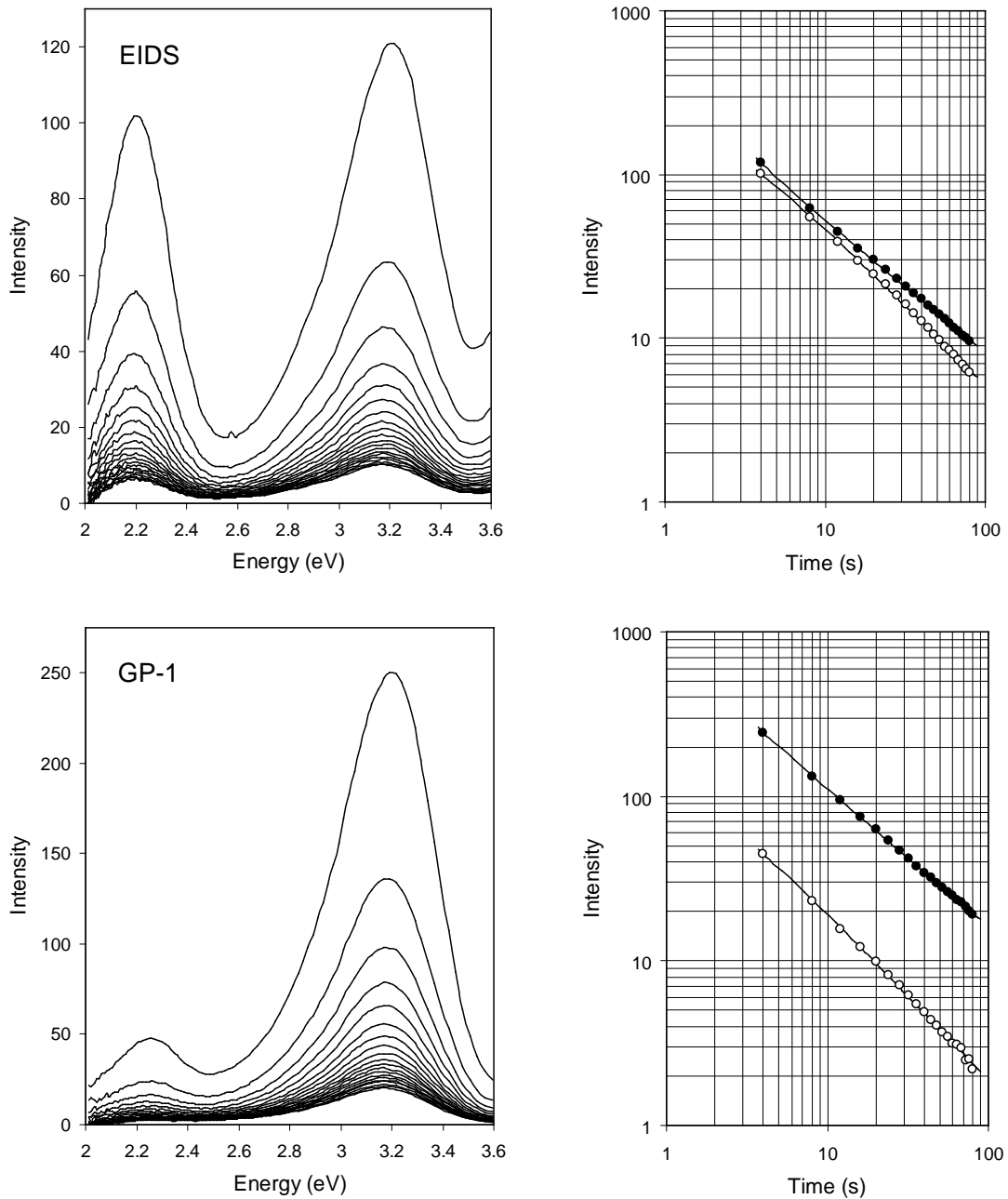
Figure 4.25: *Left: IV.1 (top) and SAW-95-09 (bottom) emission spectra as a function of illumination time. Each curve represents an increment of 4 seconds of illumination time. Right: Violet emission (solid circles) and yellow-green emission (open circles) peak intensity as a function of illumination time. The time shown corresponds to the endpoint of the measurement. Lines through the data are a fit to $I_0/(t - t_0)^\alpha$.*
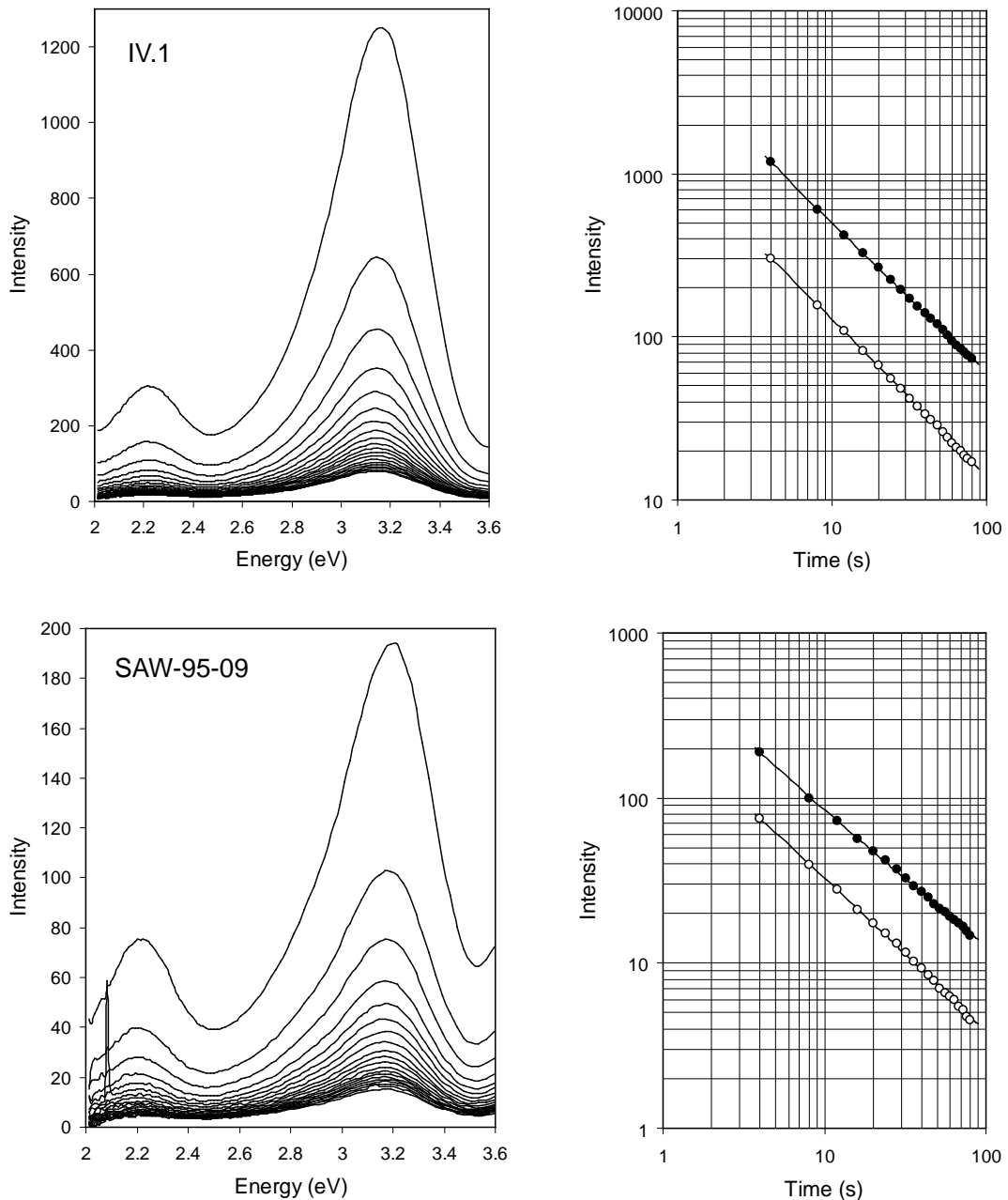
Figure 4.26: *Left: SN-27 (top) and SUN (bottom) emission spectra as a function of illumination time. Each curve represents an increment of 4 seconds of illumination time. Right: Violet emission (solid circles) and yellow-green emission (open circles) peak intensity as a function of illumination time. The time shown corresponds to the endpoint of the measurement. Lines through the data are a fit to $I_0/(t-t_0)^{\alpha}$.*
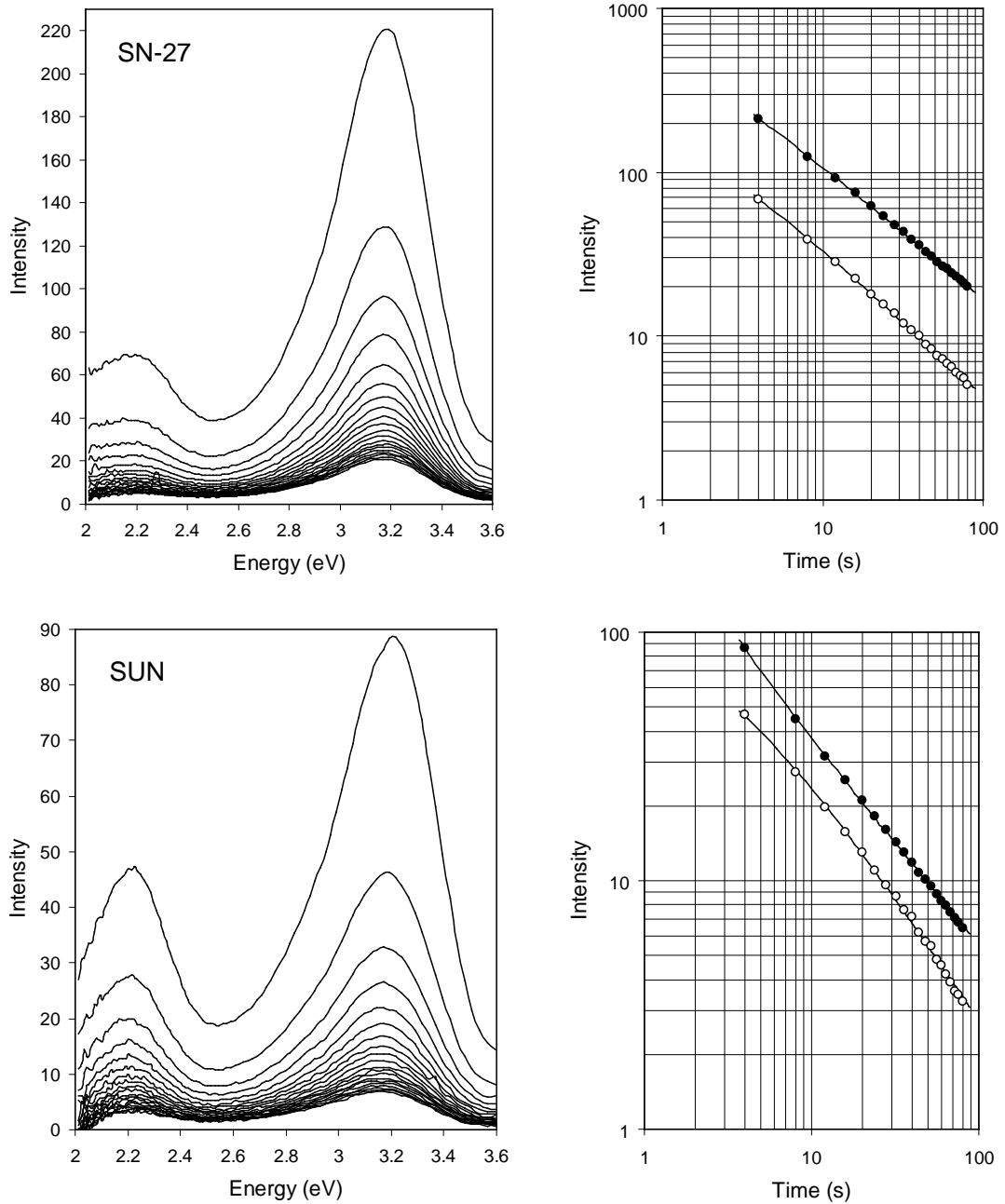
Figure 4.27: *Left: A1 (top) and A3 (bottom) emission spectra as a function of illumination time. Each curve represents an increment of 4 seconds of illumination time. Right: Violet emission (solid circles) and yellow-green emission (open circles) peak intensity as a function of illumination time. The time shown corresponds to the endpoint of the measurement. Lines through the data are a fit to $I_0/(t - t_0)^\alpha$.*
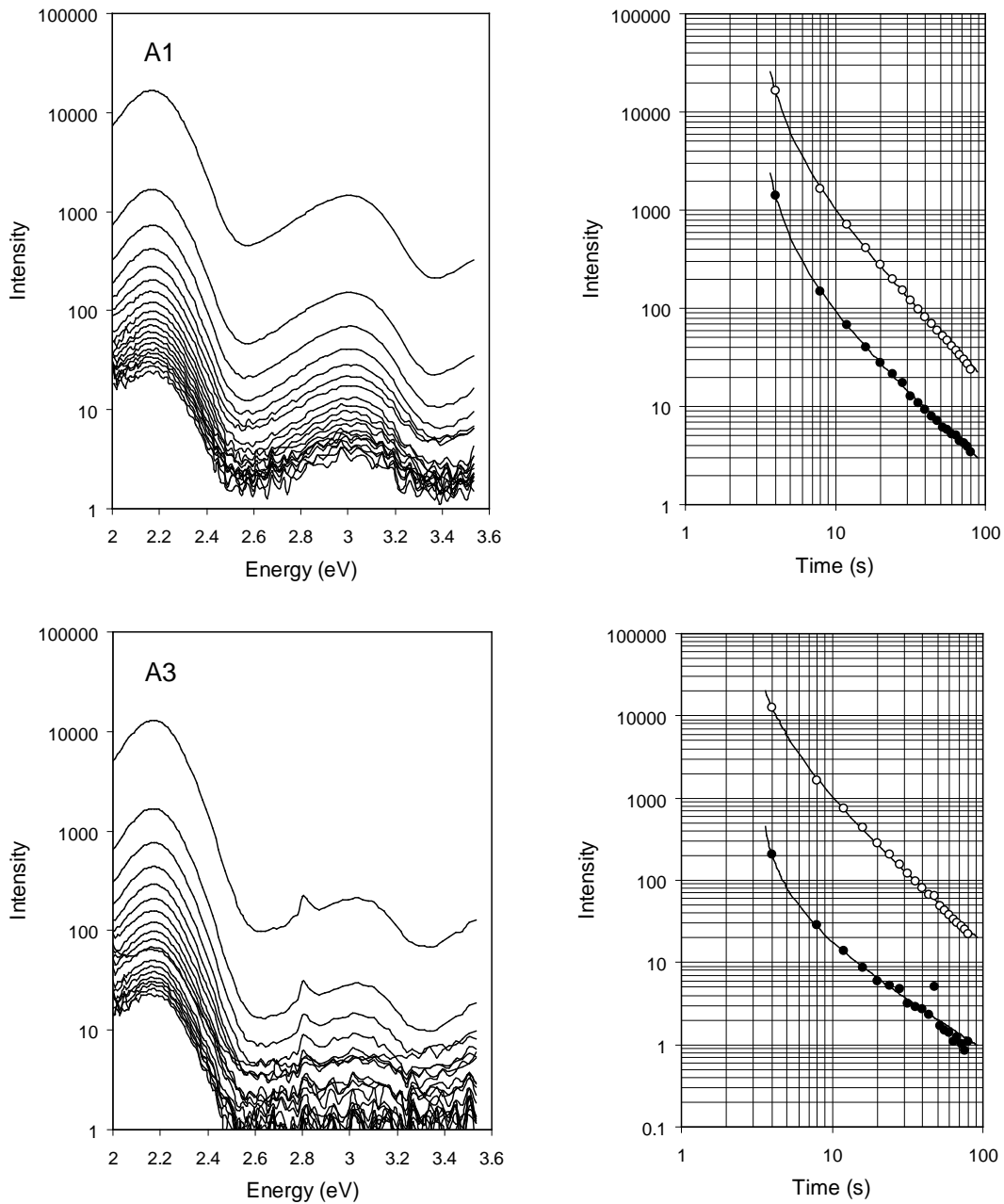
Figure 4.28: *Left: A6 (top) and K3 (bottom) emission spectra as a function of illumination time. Each curve represents an increment of 4 seconds of illumination time. Right: Violet emission (solid circles) and yellow-green emission (open circles) peak intensity as a function of illumination time. The time shown corresponds to the endpoint of the measurement. Lines through the data are a fit to* $I_0/(t - t_0)^{\alpha}$*.*
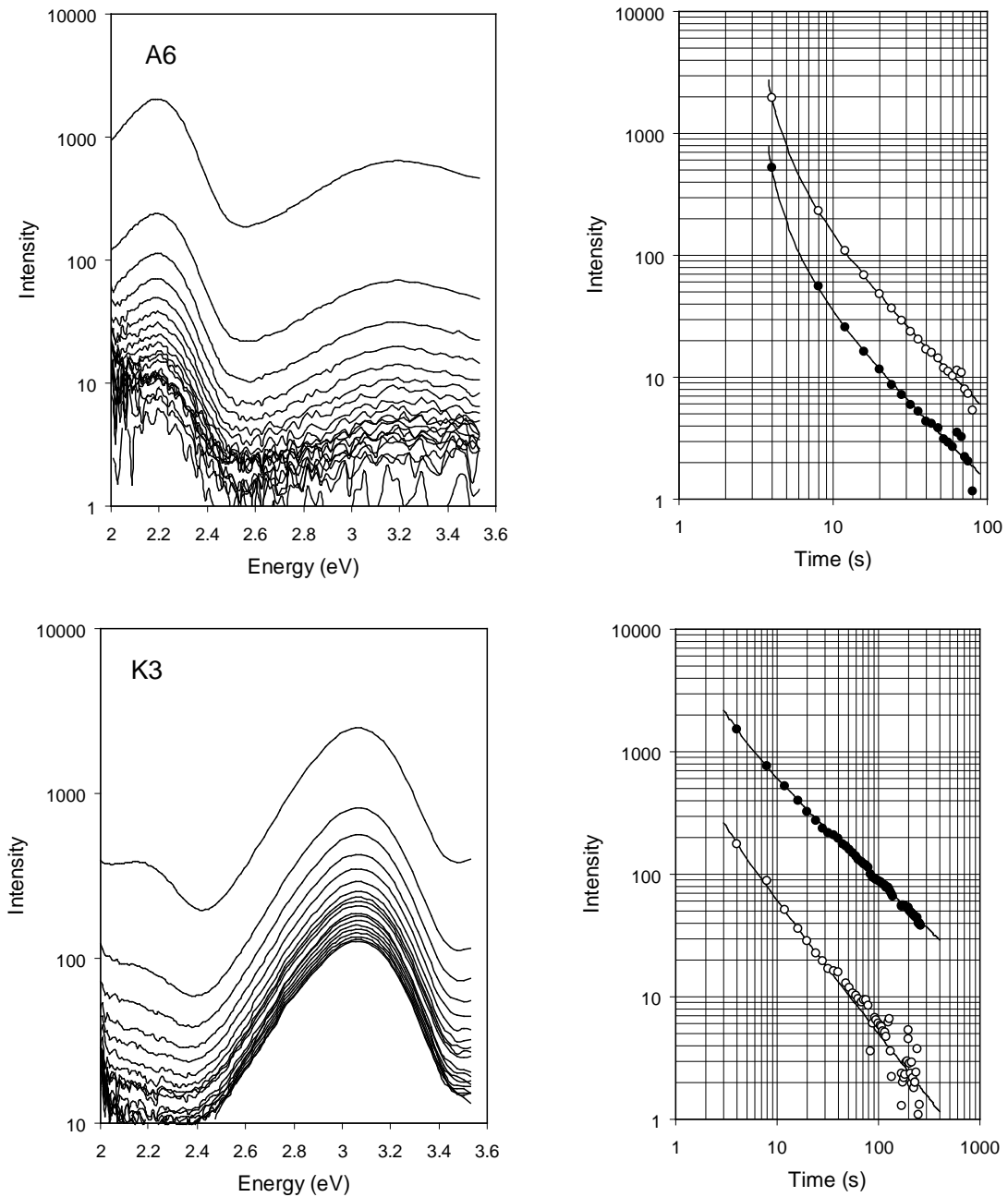
Figure 4.29: *Left: K8 (top) and K9 (bottom) emission spectra as a function of illumination time. Each curve represents an increment of 4 seconds of illumination time. Right: Violet emission (solid circles) and yellow-green emission (open circles) peak intensity as a function of illumination time. The time shown corresponds to the endpoint of the measurement. Lines through the data are a fit to $I_0/(t-t_0)^\alpha$.*
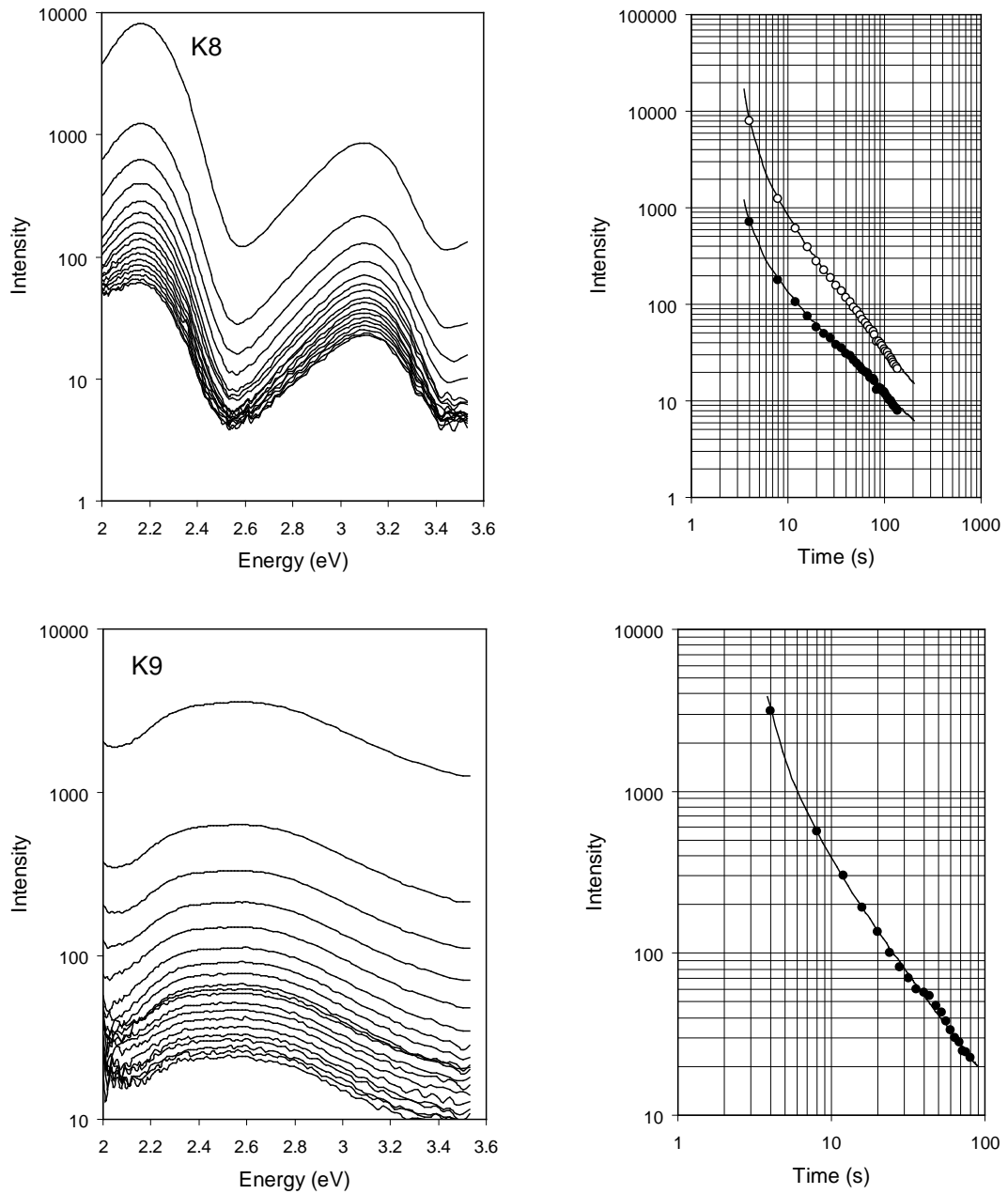
4.3.1   Discussion: $1/t^\alpha$ dependence of the shinedown curves

One can see that the rate of decay of the yellow-green emission in all of the samples is slightly higher than that for the violet emission. One may not have anticipated this result given what was seen earlier from the effect of the preheat. For example, samples DY-23 and SN-27 were observed to have a lower relative decrease in the yellow-green band upon preheat, however the relative rate of decrease of this band upon photo-excitation is greater than the violet band (as for all the samples measured). The only reasonable conclusion one may draw from this is that the thermal and photo-excitation processes are fundamentally different or that a different set of traps are being sampled in the two cases.

The most significant observation is that in all the samples measured, the intensity scales as a power law with illumination time, t. For several samples, the scaling of the decay curve approaches 1/t. Such a scaling has been reported by Bailiff and Poolton (1991) in the IRSL of sanidine immediately following laboratory irradiation and by Bailiff and Barnett (1994) in the IRSL of orthoclase at 160 K and 290 K. The scaling of intensity as an inverse power law with time according to,

$$I(t) \propto 1/t^\alpha \tag{4.1}$$

with α typically ranging between 0 and 2 was first interpreted by Debye and Edwards (1952) as arising from the diffusion of detrapped electrons towards a distribution of recombination centers in the material. Empirically, this law is observed to hold in many luminescent systems (Jonscher and Polignac, 1984 (review); Bazin *et al.*, 1977; Visocekas and Geoffroy, 1977; Cordier *et al.*, 1974; Debye and Edwards, 1952).

On this basis alone it may not appear surprising that the phenomenological Debye-Edwards law should arise in the context of IRSL. However, past analysis of OSL decay kinetics have concentrated on sums of decaying exponentials (or similar variants) which derive from kinetics that do not depend on a time-varying distribution of recombination centers (*e.g.* McKeever *et al.*, 1997, in feldspars, and Bailey *et al.*, 1997, in quartz). A thorough investigation of the power law scaling and its possible physical interpretation is clearly required; this is addressed in Chapter 6.

The time t, in Equation 4.1 represents the time since irradiation in the case of isothermal phosphorescence. In phosphorescent systems, the phosphorescence begins to decay rapidly after irradiation so that one cannot practically measure the phosphorescence at short times

after irradiation. For this reason an additional parameter t_0, representing the time since irradiation must be introduced,

$$I(t) = \frac{A}{(t+t_0)^\alpha} \tag{4.2}$$

where A/t_0^α is the intensity at time $t = 0$. This relation is known as Becquerel's equation; it is more conventionally written as, $I(t) = \frac{I_0}{1+b(t-t_0)^\alpha}$ so that I_0 is the intensity at t_0. However, since b has no physical significance (Hamill, 1979) and t_0 in the case of OSL cannot be straightforwardly interpreted as the time since irradiation, here the equation has been modified to contain only 3 free parameters; A, t_0 and α. A more easily interpreted empirical relation for the decay is introduced in Chapter 6.

In the case of OSL, the luminescence decay between irradiation and measurement is minimal; the parameter t_0 might then be thought of as the "equivalent illumination time" applicable to the sample between irradiation and measurement. One might expect t_0 to be non-zero a certain time after irradiation because recombination occurs in the absence of photonic excitation either by tunnelling (*i.e.* resulting in tunnelling afterglow) or by thermal excitation. As will be shown in Chapter 6, this interpretation is incorrect; nevertheless, this preliminary work is included to indicate the process that led to the later work.

It is relevant to note that the case where $\alpha=1$ is expected in systems where tunnelling provides the mechanism by which electrons exit the traps, but is not exclusively limited to tunnelling models. It is known that the isothermal afterglow[4] of feldspars in the infra-red follows a 1/t rate law. This was part of the evidence that suggested the interpretation of this afterglow as arising from tunnelling recombination. Extensive studies have correlated the infra-red afterglow with the "anomalous" fading of the violet luminescence in feldspars (Visocekas, 1985; Visocekas, 1993; Visocekas *et al.*, 1994; Zink *et al.*, 1995).

In our separated grain samples, $1/(t+t_0)$ often provides a good fit for the 2.2 eV emission, however the more general Becquerel equation always provides a better fit. For the rock samples and the violet emission in the granular samples, the only good fit is to the Becquerel equation, with the exponent α ranging between 0.8 and 1.6 (see Table 4.4). One will note that t_0 is negative in many of the measurements whereas this is unexpected on the physical basis explained previously. However, this situation is resolved if we consider that the intensity is integrated over a time in which significant decay of the luminescence

---

[4]The phosphorescence following irradiation of a material; in this case by ionizing radiation.

can occur. Any significant nonlinearity in the decay rate over the integration time will lead to an incorrect assessment of t_0 because the integrated intensity disproportionately reflects the initial portion of the decay. In fact, we find that in the samples in which the first 4 s of decay is greatest (notably, the rock samples for which the initial decay exceeds 90%) the estimated value of t_0 is always large and negative.

If our initial interpretation of t_0 is correct, then t_0 should increase significantly if the sample is heated prior to measurement. The spectral decay measurements were repeated for the rock samples after being subjected to a similar irradiation dose followed by a 20 hour preheat at 120 °C. As in the unpreheated aliquots, a power law scaling of the decay curve was observed, however the exponent α as well as the parameter t_0 differed from that observed in the unpreheated samples (see Table 4.5).

Since the decay in 4s of illumination is close to 90% and the decay due to the preheat is in the range 50–75%, we expect that the change in t_0 upon preheat to be of the order 1–2 s. Although t_0 generally decreased (i.e. became more negative) upon preheating, it was observed to increase in K3 and A3. Again, this may be due to the lack of data on the high decay portion of the shinedown curve which does not allow an accurate determination of t_0. Further work, presented in Chapter 6 indicates that preheating likely has a minimal effect on the decay kinetics.

4.4 Effect of the excitation energy on the IRSL emission spectrum.

According to the standard model (*i.e.* Hütt's model) in which electrons proceed from the traps to the recombination centers through the conduction band, one expects that luminescence spectrum should not be affected by the excitation energy. The excitation energy should only affect the rate at which traps are emptied, so that the shape of the emission spectrum should remain unchanged as long as the relative distribution of recombination centers is fixed. Since the shape of the luminescence excitation spectrum is not strongly affected by the emission band measured (see Chapter 5), a correlation is not expected between the trap(s) associated with the 1.44 eV resonance and a particular emission band. Therefore, the only manner in which the IRSL emission spectrum may be affected by the excitation

Table 4.4: *Fit of the shinedown curves to Becquerel's equation, $I_0/(t+t_0)^{\alpha}$. Data for 3.1 eV emission is in bold, 2.2 eV emission in regular typeface, except for K9 where the data is for the emission peak at 2.5 eV.*

Sample	α	t_0 (s)	A (arb. units)
AKHC	**0.835 ± 0.005**	**-0.8 ± 0.1**	**607 ± 9**
	0.948 ± 0.008	-0.5 ± 0.2	370 ± 10
DY-23	**0.854 ± 0.004**	**1.5 ± 0.2**	**181 ± 3**
	1.175 ± 0.009	4.6 ± 0.4	300 ± 10
EIDS	**0.785 ± 0.005**	**-0.6 ± 0.1**	**304 ± 6**
	0.991 ± 0.007	1.1 ± .2	500 ± 10
GP-1	**0.828 ± 0.003**	**-0.2 ± 0.1**	**732 ± 8**
	1.030 ± 0.008	0.68 ± 0.2	219 ± 6
IV.1	**0.907 ± 0.004**	**-0.2 ± 0.1**	**3930 ± 50**
	0.985 ± 0.003	0.38 ± 0.06	1290 ± 10
SAW-95-09	**0.811 ± 0.005**	**-0.4 ± 0.1**	**530 ± 10**
	0.943 ± 0.006	0.4 ± 0.2	300 ± 7
SN-27	**0.816 ± 0.004**	**0.5 ± 0.1**	**730 ± 9**
	0.917 ± 0.005	0.9 ± 0.1	294 ± 5
SUN	**0.810 ± 0.005**	**-0.7 ± 0.1**	**229 ± 3**
	1.019 ± 0.008	2.4 ± 0.3	306 ± 8
A1	**1.377 ± 0.007**	**-3.03 ± 0.007**	**1370 ± 10**
	1.53 ± 0.01	-2.84 ± 0.01	20700 ± 300
A3	**1.13 ± 0.06**	**-3.2 ± 0.1**	**160 ± 30**
	1.60 ± 0.02	-2.40 ± 0.02	26900 ± 600
A6	**1.21 ± 0.03**	**3.28 ± 0.03**	**350 ± 20**
	1.27 ± 0.02	-3.09 ± 0.02	1740 ± 60
K3	**0.796 ± 0.009**	**-1.2 ± 0.2**	**3400 ± 100**
	1.06 ± 0.04	-0.6 ± 1	650 ± 50
K8	**0.92 ± 0.01**	**-2.83 ± 0.08**	**830 ± 50**
	1.20 ± 0.01	-2.93 ± 0.03	8600 ± 200
K9	**1.19 ± 0.01**	**-2.74 ± 0.03**	**4150 ± 100**
K10	**0.989 ± 0.006**	**-3.538 ± 0.007**	**880 ± 10**
	1.06 ± 0.01	-3.49 ± 0.01	730 ± 20

Table 4.5: *Comparison of fits to the Debye-Edwards scaling, $I_0/(t+t_0)^\alpha$ for the unpre-heated and preheated aliquots. Data for 3.1 eV emission is in bold, 2.2 eV emission in regular typeface, except for K9 where the data is for the emission peak at 2.48 eV. $\Delta\alpha$ and Δt_0 are the changes observed in α and t_0 upon preheating the sample. Complete fitting parameters for the unpreheated aliquots are given in Table 4.4.*

Sample	α (unpreheated sample)	Δα (s)	Δt₀
A1	**1.377 ± 0.007**	**-0.23 ± 0.02**	**0.73 ± 0.02**
	1.53 ± 0.01	-0.18 ± 0.02	0.37 ± 0.03
A3	1.60 ± 0.02	0.01 ± 0.03	-0.18 ± 0.04
A6	**1.21 ± 0.03**	**-0.03 ± 0.04**	**0.14 ± 0.04**
	1.27 ± 0.02	-0.03 ± 0.02	0.09 ± 0.02
K3	**0.796 ± 0.009**	**-0.13 ± 0.02**	**-0.81 ± 0.02**
	1.06 ± 0.04	-0.46 ± 0.04	-3 ± 1
K8	**0.92 ± 0.01**	**-0.01 ± 0.02**	**0.29 ± 0.02**
	1.20 ± 0.01	-0.05 ± 0.02	0.00 ± 0.05
K9	**1.19 ± 0.01**	**0.08 ± 0.01**	**0.01 ± 0.05**
K10	**0.989 ± 0.006**	**-0.12 ± 0.03**	**0.17 ± 0.03**
	1.06 ± 0.01	-0.06 ± 0.04	0.11 ± 0.06

energy is if the sample consists of segregated mineral domains exhibiting different luminescence characteristics (or if Hütt's model is incorrect). Since this is often likely to be the case in natural feldspars, especially in microclines, an investigation of the effect of varying excitation energy on the emission spectrum is warranted.

The greatest difficulty in undertaking such a measurement is that the IRSL emission spectrum must be measured for a single aliquot at multiple excitation energies without introducing any decay in the luminescence. The use of a single aliquot is essential because the luminescence spectrum can vary greatly from aliquot to aliquot when using cut rock samples. K3 for example, was particularly problematic in this respect, with the 570 nm emission being prominent in some aliquots and almost absent in others. The requirement that little decay in the luminescence occur over the measurement is necessary to avoid the

effect of the differing draining rates of the different luminescence bands (see Section 4.3).

These restrictions meant that only the violet (3.1 eV) and yellow-green (2.2 eV) bands could be easily compared. Only three samples had sufficiently bright 3.1 eV and 2.2 eV bands to allow an accurate comparison to be made; albite A1, oligoclase A3 and microcline K8. The spectra were measured for excitation energies between 1.36 eV and 1.61 eV using a tunable Ti-Sapphire laser with a power of 3–6 mW on the sample. Each measurement produced a total decay in the luminescence of less than 2% in A1 and A3 and 24% in K8.

The emission spectra are shown in Figures 4.30–4.32. No effect was seen for oligoclase A3, but a large effect was found in microcline K8. Sample K8 shows the greatest departure from the ideal behaviour, with the yellow-green emission being relatively greater than the violet at smaller excitation energies. A similar, possible trend is also seen in the data for A1. The relatively large decay of the luminescence over the measurement period in K8 affected the ratio of the violet to yellow-green emission. However, the effect of the decay is in the opposite direction to that of the excitation energy so that this latter effect is probably underestimated.

The most satisfactory explanation for the large effect of the excitation energy on the emission spectrum of K8, and little if any effect on A1 and A3 is found in the morphology of K8. K8 is a classic perthitic microcline containing exsolved phases of orthoclase and albite. The segregation of the violet and yellow-green emissions to the regions containing orthoclase and albite respectively has been observed and is discussed in Chapter 8. In A3 and A1 on the other hand, the violet and yellow-green emission as well as the potassium and sodium content has been found to be evenly distributed throughout the rock chip; or more precisely, in those regions where IRSL emission is present. We therefore interpret the difference in the excitation response of the violet and yellow-green bands in K8 to be due to the existence of two minerals in the sample. This is consistent with the excitation response spectra measured for K8 – this sample produced the greatest variation between the excitation response measured for the violet and yellow green emission bands separately (see Chapter 5). Not surprisingly, A1 shows very little variation in the excitation response spectra for these two emission bands.

These results appear to support the hypothesis that no particular type of luminescence center is tied to trap(s) associated with the 1.44 eV excitation resonance. It is also evident that the comparison of effects on different emission bands should only be made in samples for which the separation into separate mineral phases is not present.

Figure 4.30: *Effect of varying the excitation photon energy on the visible emission spectrum of A1. Inset: Ratio of the violet to the yellow-green peak intensity as a function of excitation photon energy. Spectra normalized to the 3.1 eV intensity.*
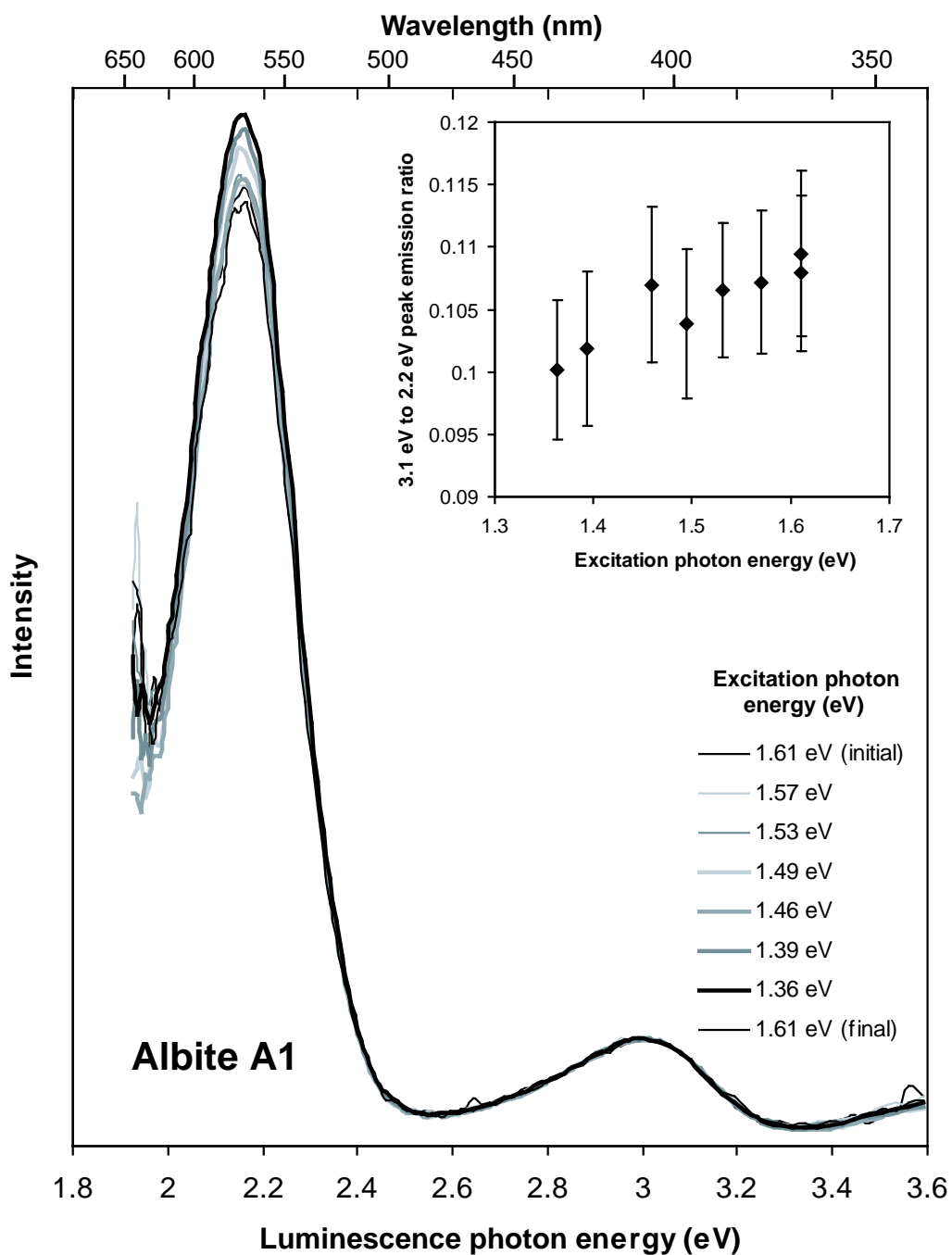
Figure 4.31: *Effect of varying the excitation photon energy on the visible emission spectrum of A3. Inset: Ratio of the violet to the yellow-green peak intensity as a function of excitation photon energy. Spectra normalized to the 3.1 eV intensity.*
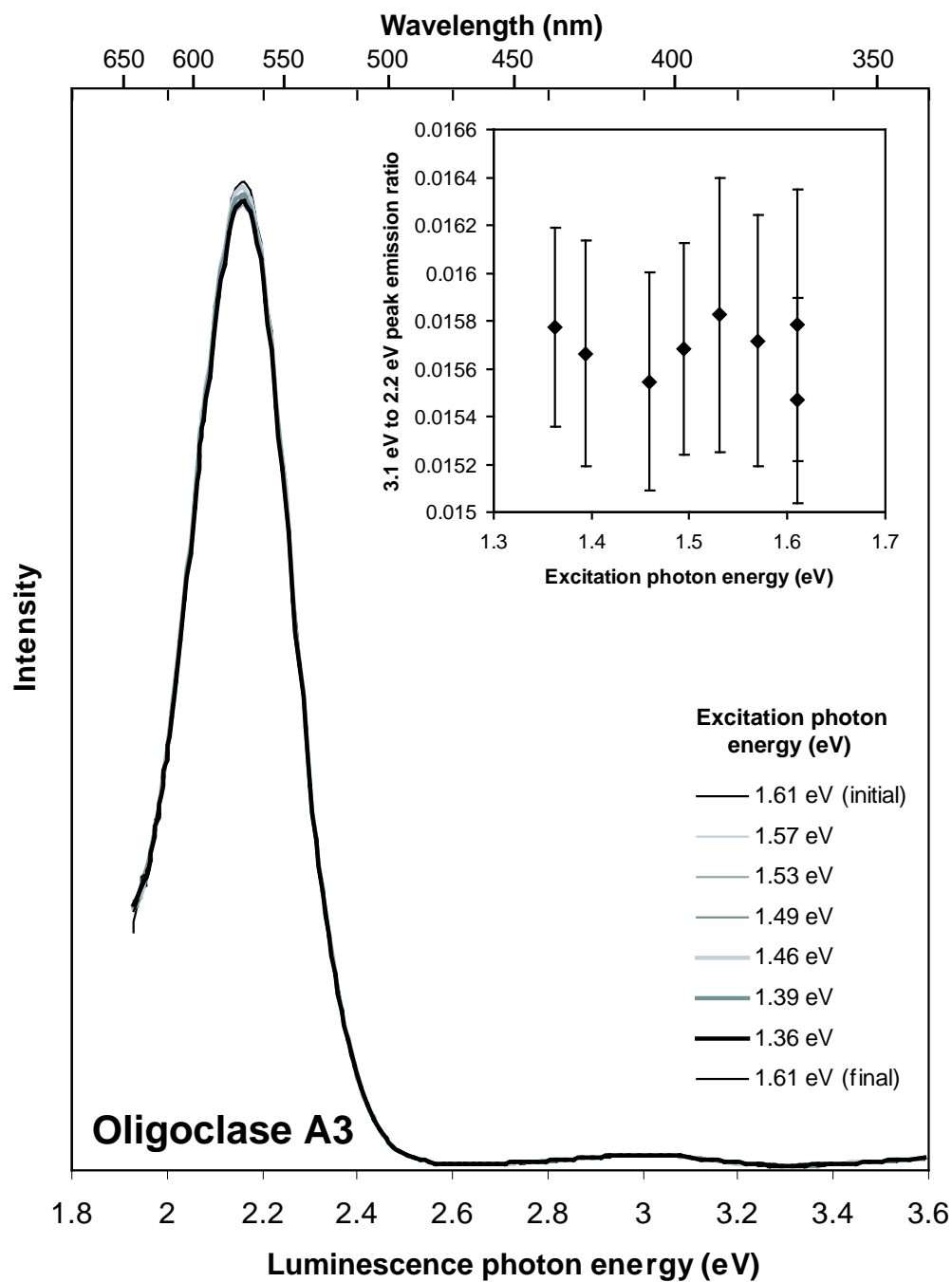
Figure 4.32: *Effect of varying the excitation photon energy on the visible emission spectrum of K8. Inset: Ratio of the violet to the yellow-green peak intensity as a function of excitation photon energy. Spectra normalized to the 3.1 eV intensity.*
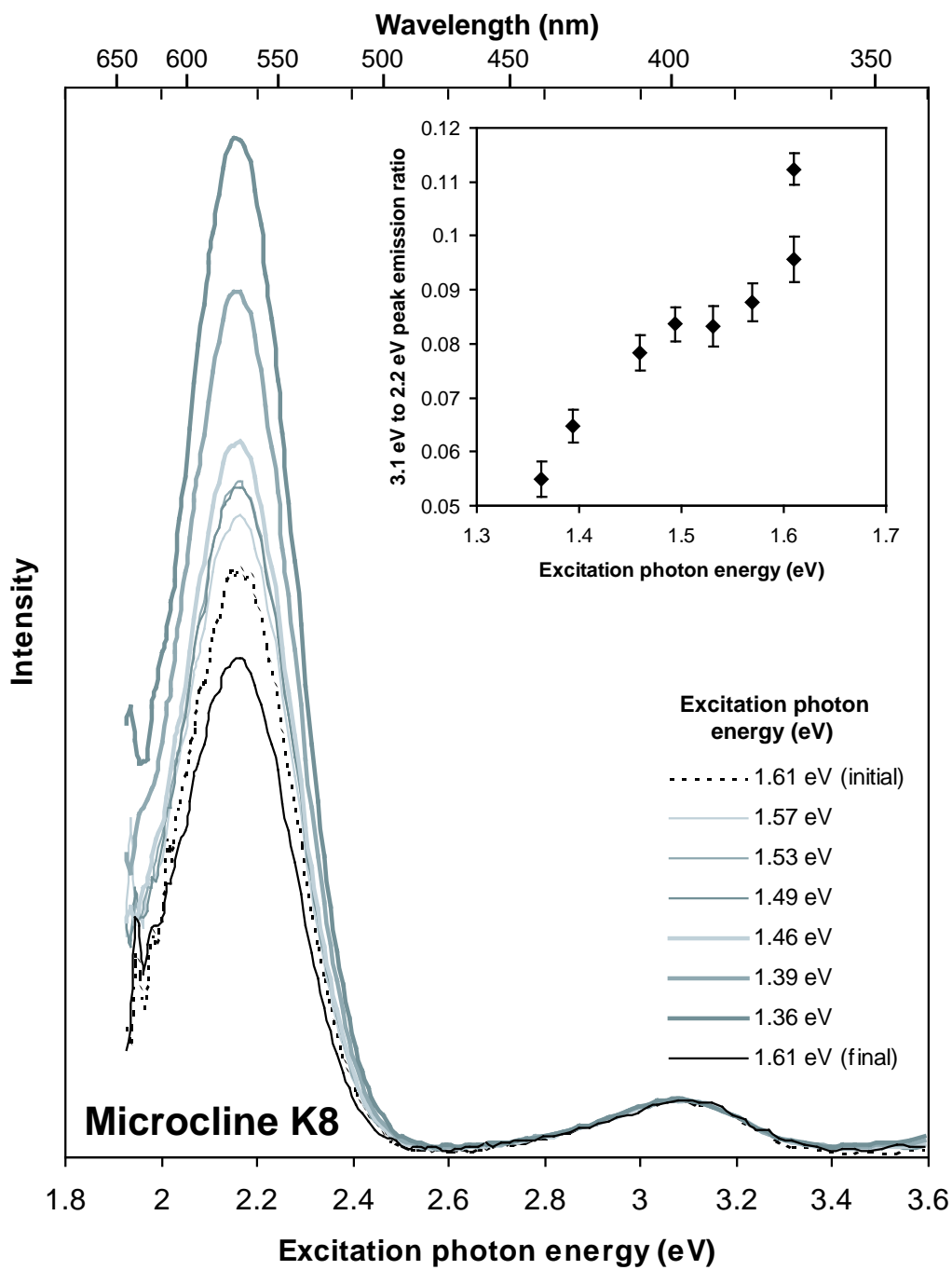
4.5   Post-irradiation phosphorescence

It is interesting to compare the IRSL with the phosphorescence produced after laboratory irradiation of a feldspar. The measurement of this phosphorescence amounts to measuring the prompt TL at room temperature; that is, the luminescence that arises from the thermal eviction of electrons from shallow traps. Although several authors have published TL spectra, the emphasis has been on high-temperature TL (*i.e.* thermally deep traps) usually in well thermalized samples (*i.e.* the shallow traps have been allowed to empty by long period storage). Of particular interest is the thermal stability of the 1.76 eV band which appears in the IRSL immediately after irradiation, but is not present in the samples preheated at 120 °C. Henceforth we will refer to the luminescence immediately following irradiation as "prompt" luminescence (*e.g.* prompt phosphorescence and prompt IRSL).

Three of the feldspar sediment extract samples were selected for study by virtue of their bright 700 nm emission in the prompt IRSL: AKHC, GP-1 and SAW-95-09. The phosphorescence was also measured for samples EIDS, IV.1 and SN-27 (Figure 4.33), but the temperature dependence of the phosphorescence was not measured for these samples. In addition, phosphorescence spectra were obtained for the bright rock samples; albite A6, orthoclase K3, and microclines K8, K9 and K10.

The samples were given a γ-dose of 2770 Gy over 11 days and measured within 2 hours of removal from the γ source. The 500–1200 nm grating was used with an effective bandpass of 25 nm. Integration times ranging between 1 and 5 minutes were used, depending on the brightness of the aliquot at a particular temperature. No filters were used to separate out the first and second diffraction orders, instead the data was corrected using the following method.

The relative system response for the second to the first order spectra was determined by making several measurements of the peak positions and heights for monochromatic light from 350–600 nm. A broad-band tunable source of monochromatic light was provided by a monochromator with a tungsten filament lamp.

In order to correct for the second order spectrum the measurement of two properties of the spectrometer were required. The position of the first-order wavelength λ_1 as a function of the second-order wavelength λ_2 was measured and modeled; to first order this may be approximated as, $\lambda_1 = f(\lambda_2) \simeq \frac{1}{2}\lambda_2$. Also required was the relative effective system

response for the two diffraction orders; $I(\lambda_2)/I(\lambda_1) \equiv k(\lambda_1)$. Using this information, the second order contribution to the spectrum due to the short wavelengths could be calculated and subtracted from the spectrum. The correction applied to the data was,

$$I_c(\lambda) \,=\, I_0(\lambda) \,-\, k(\lambda_{1/2}) \cdot I_0(\lambda_{1/2}), \qquad \lambda_{1/2} \,=\, f(\lambda) \,\simeq\, \frac{1}{2}\lambda \qquad (4.3)$$

where $I_0(\lambda)$ and $I_c(\lambda)$ are the measured and corrected intensities. Once this correction was applied, the intensity was normalized for the system response and scaled for display as a function of photon energy.

The phosphorescence spectra as a function of temperature are shown in Figures 4.33–4.41. The relative intensities of the spectra should be regarded as approximate due to the unknown and varying amount of decay in the phosphorescence between measurements at different temperatures. Nevertheless, it is clear that the phosphorescence intensity increases rapidly with temperature.

Several features stand out in these spectra, the first is the appearance of an emission band at 1.38 eV (900 nm) as the temperature increases. This emission band has not previously been reported in TL although it is hinted at by the TL spectra of Krbetschek and Rieser (1995). A bright band near 1.44 eV has been seen in the radioluminescence of K-feldspar (*e.g.* Trautmann *et al.*, 1999), but there is no trace of it in the present data.

Secondly, the 3.1 eV and 2.2 eV bands that dominated the IRSL are completely absent in the phosphorescence, whereas a broad band at 2.5 eV (500 nm) is dominant in all the samples measured. The 2.5 eV band was observed in the IRSL of only one sample (out of 33), the amazonite microcline K9; curiously the 2.5 eV phosphorescence in K9 is relatively dim. Krbetschek and Rieser (1995) found two well-resolved phosphorescence bands near 2.5 eV as well as a band near 2.75 eV. This band may be weakly present for samples "Cat Dune" and "Irkutsk orthoclase" in Clarke and Rendell's (1997a) IRSL spectra, but is otherwise not present in other published IRSL spectra[5]. Prescott and Fox (1993) found the broad 2.53 eV (490 nm) TL emission band to be typical of intermediate composition alkali-feldspars. Huntley *et al.* (1988) found that the 2.53 eV TL peak dominated at low temperatures but vanished at high temperatures, where only the 3.1 eV and 2.2 eV emissions were visible. The 2.53 eV phosphorescence band is virtually absent in microcline K8 and

---

[5]Duller and Bøtter-Jensen, 1997; Clarke and Rendell, 1997b; Rieser *et al.*, 1997; Huntley *et al.*, 1991; Jungner and Huntley, 1991.

albite A6. Instead, other bands are found between 2.1 eV and 3 eV; this is particularly obvious in sample A6.

The 2.53 eV emission appears to increase with temperature in proportion to the 1.38 eV IR band; the increase of the 1.67 eV (740 nm) band is proportionately lower. There does not appear to be an obvious shift of the peak positions with temperature for any of the three emission bands. It is tempting to say that the 1.76 eV emission that appears in the prompt IRSL is related to the band observed in the post-irradiation phosphorescence at 1.67 eV; both bands dim after storage of the sample at room temperature and have similar peak widths ($\sim$0.18 eV in both cases). Krbetschek and Rieser (1995) observe a band in the phosphorescence near 720 nm, so that the apparent shift of our peak to longer wavelength may be due to the relatively low resolution of our spectra ($\sim$25 nm).

In well thermalized samples the 1.76 eV TL emission peaks at 425 K (Zink *et al.*, 1995) and no significant emission is seen below 350 K. Similarly, the 1.76 eV emission is absent in thermalized samples under 1.44 eV excitation, as was shown earlier. However, the 1.76 eV band appears both in the prompt room temperature TL and prompt IRSL of the samples. These facts clearly indicate that the recombination center associated with the 1.76 eV band (*i.e.* Fe^{3+}) is available to at least two populations of traps; deep thermally activated traps that are not drained by 1.44 eV excitation photons, and shallow traps that may be emptied either thermally or by the IR excitation.

Figure 4.33: *Room temperature prompt phosphorescence in samples EIDS, IV.1 and SN-27. Relative intensities of the different samples is approximately correct.*
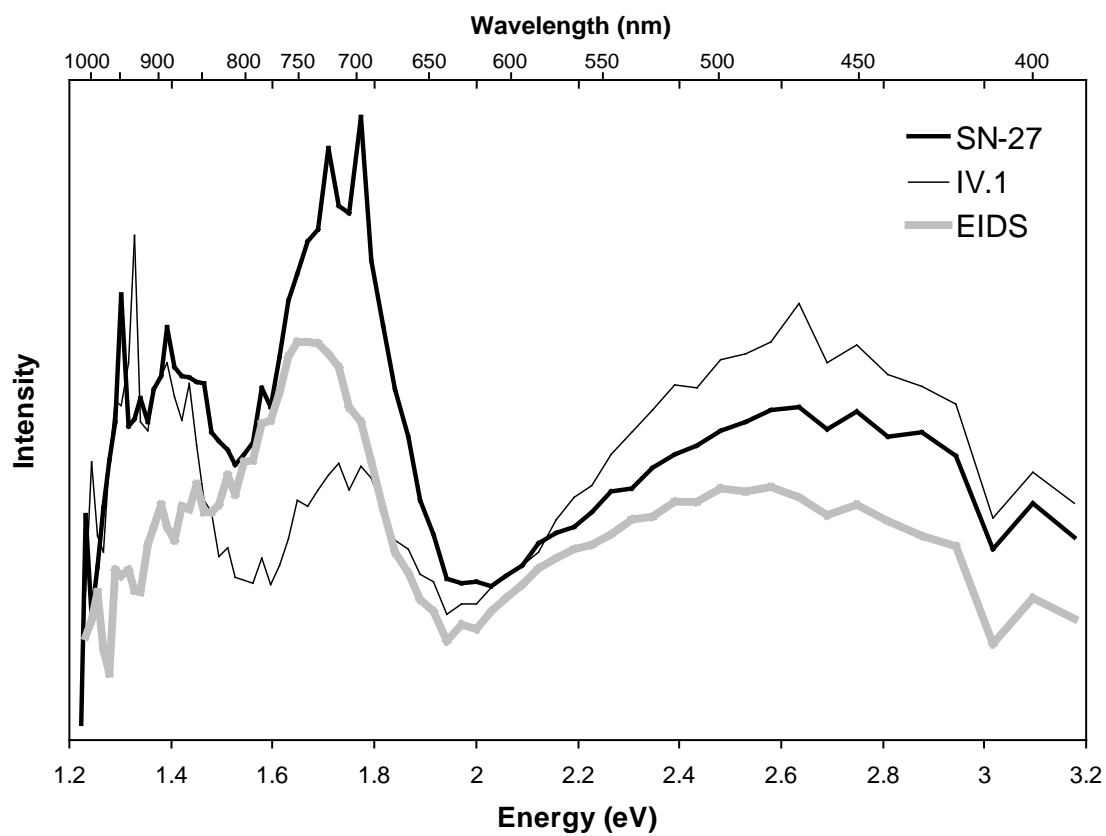
Figure 4.34: *Top: Temperature dependence of the prompt phosphorescence spectrum of AKHC. Relative intensities of the spectra at different temperatures are only approximate. Bottom: Spectra scaled to the intensity of the 1.67 eV emission peak.*
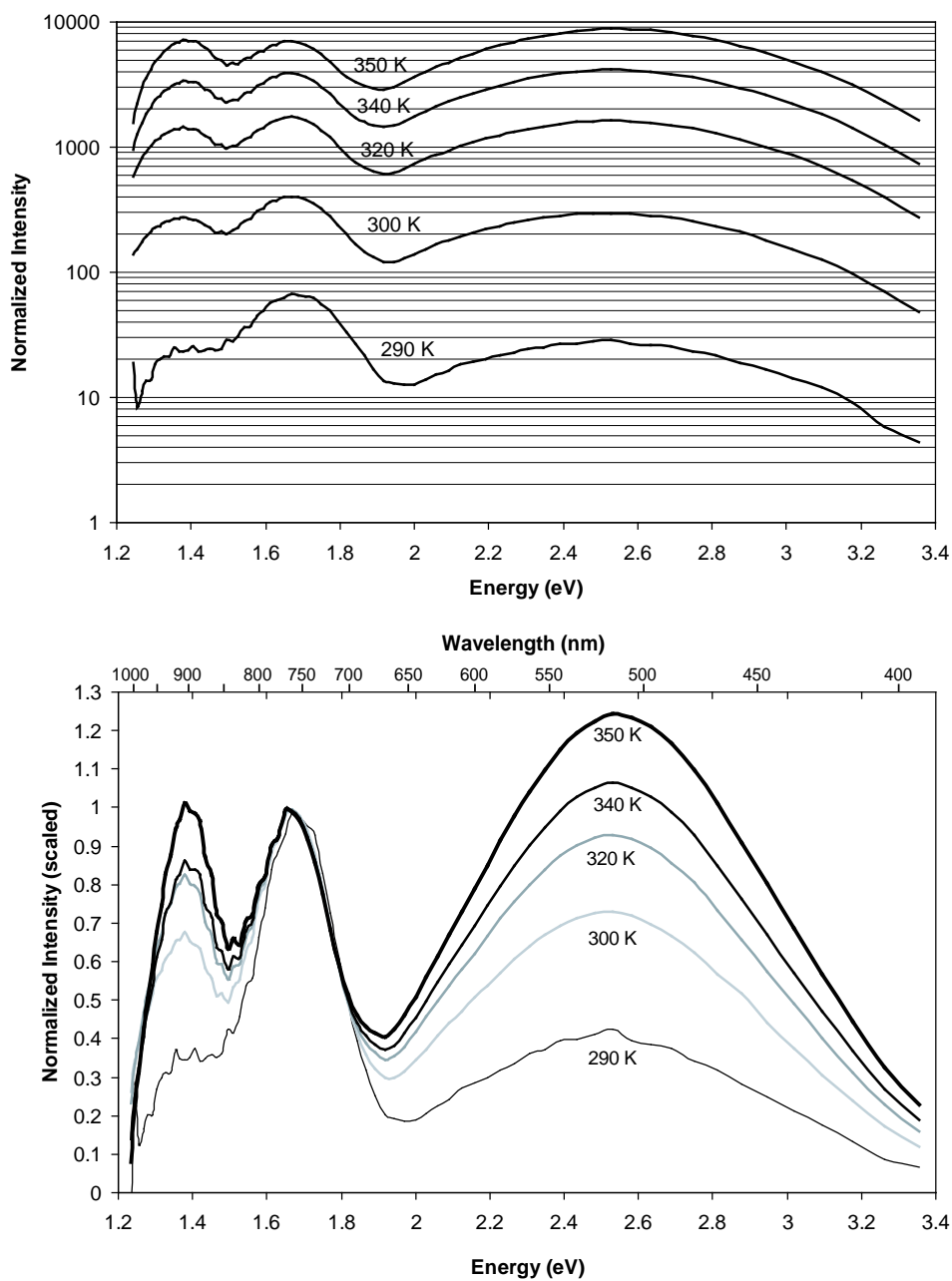
Figure 4.35: *Top: Temperature dependence of the prompt phosphorescence spectrum of GP-1. Relative intensities of the spectra at different temperatures are only approximate. Bottom: Spectra scaled to the intensity of the 1.67 eV emission peak. Feature indicated by arrow is an artifact.*
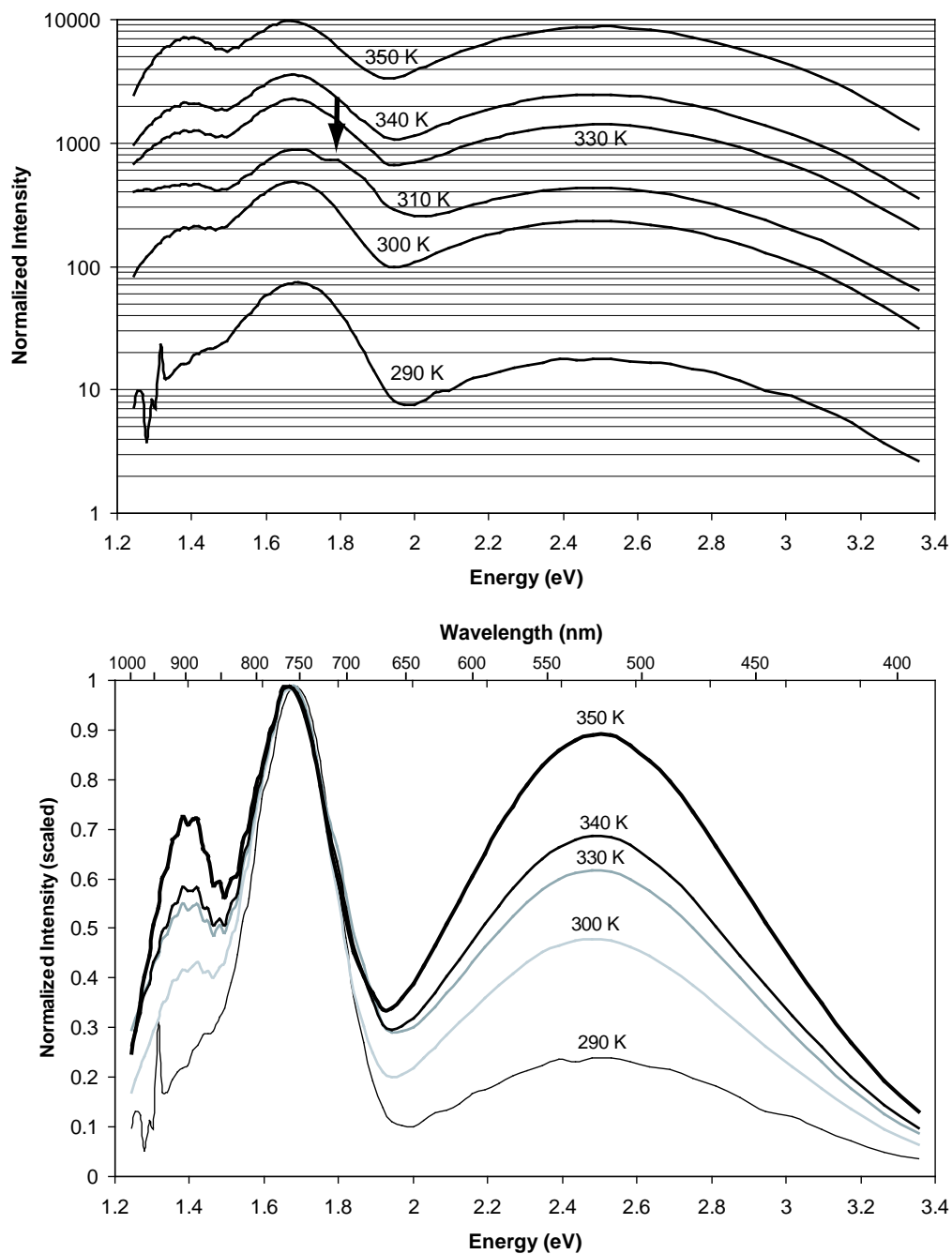
Figure 4.36: *Top: Temperature dependence of the prompt phosphorescence spectrum of SAW-95-09. Relative intensities of the spectra at different temperatures are only approximate. Bottom: Spectra scaled to the intensity of the 1.67 eV emission peak.*
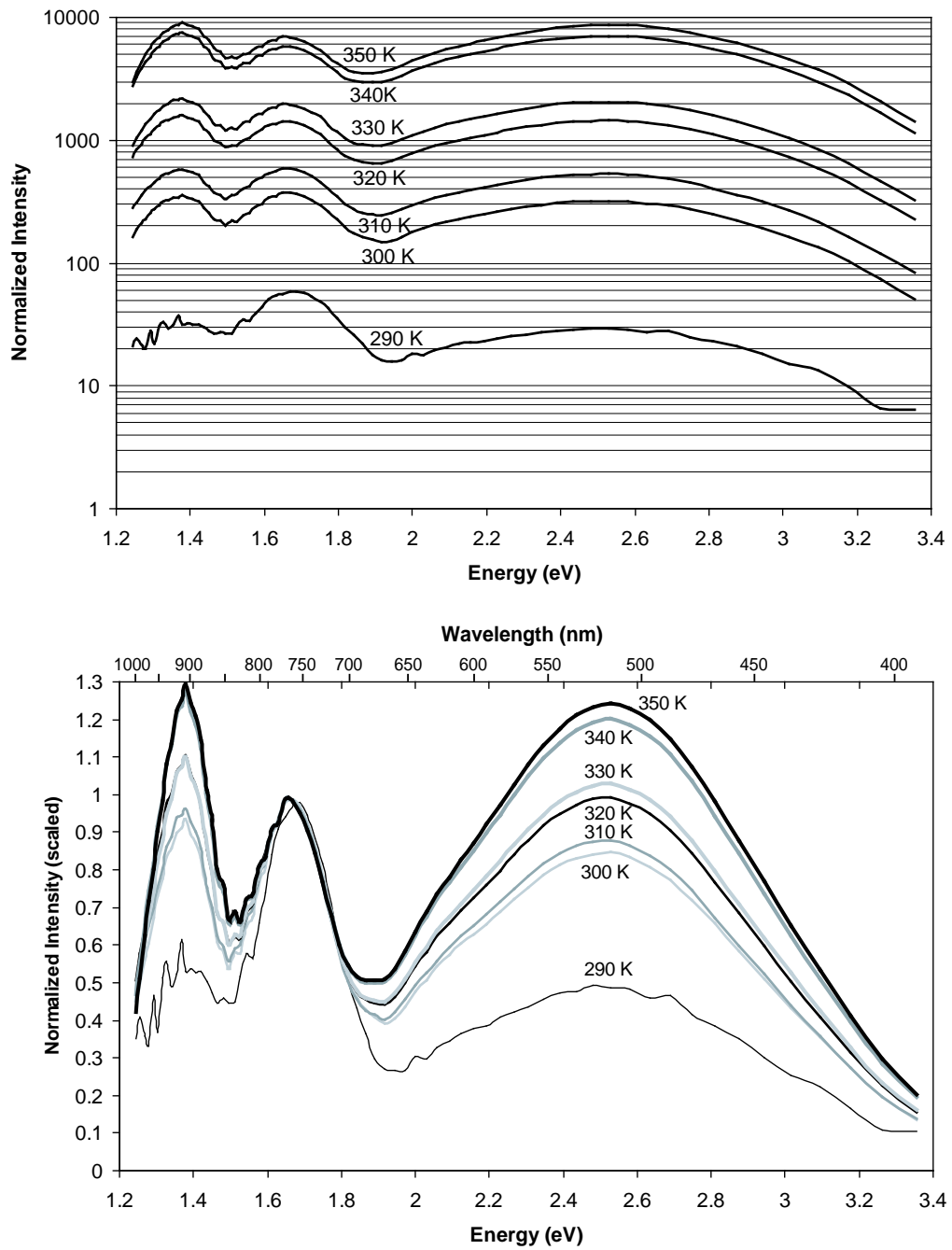
Figure 4.37: *Top: Temperature dependence of the prompt phosphorescence spectrum of albite A6. Relative intensities of the spectra at different temperatures are only approximate. Bottom: Spectra scaled to the intensity of the 1.67 eV emission peak.*
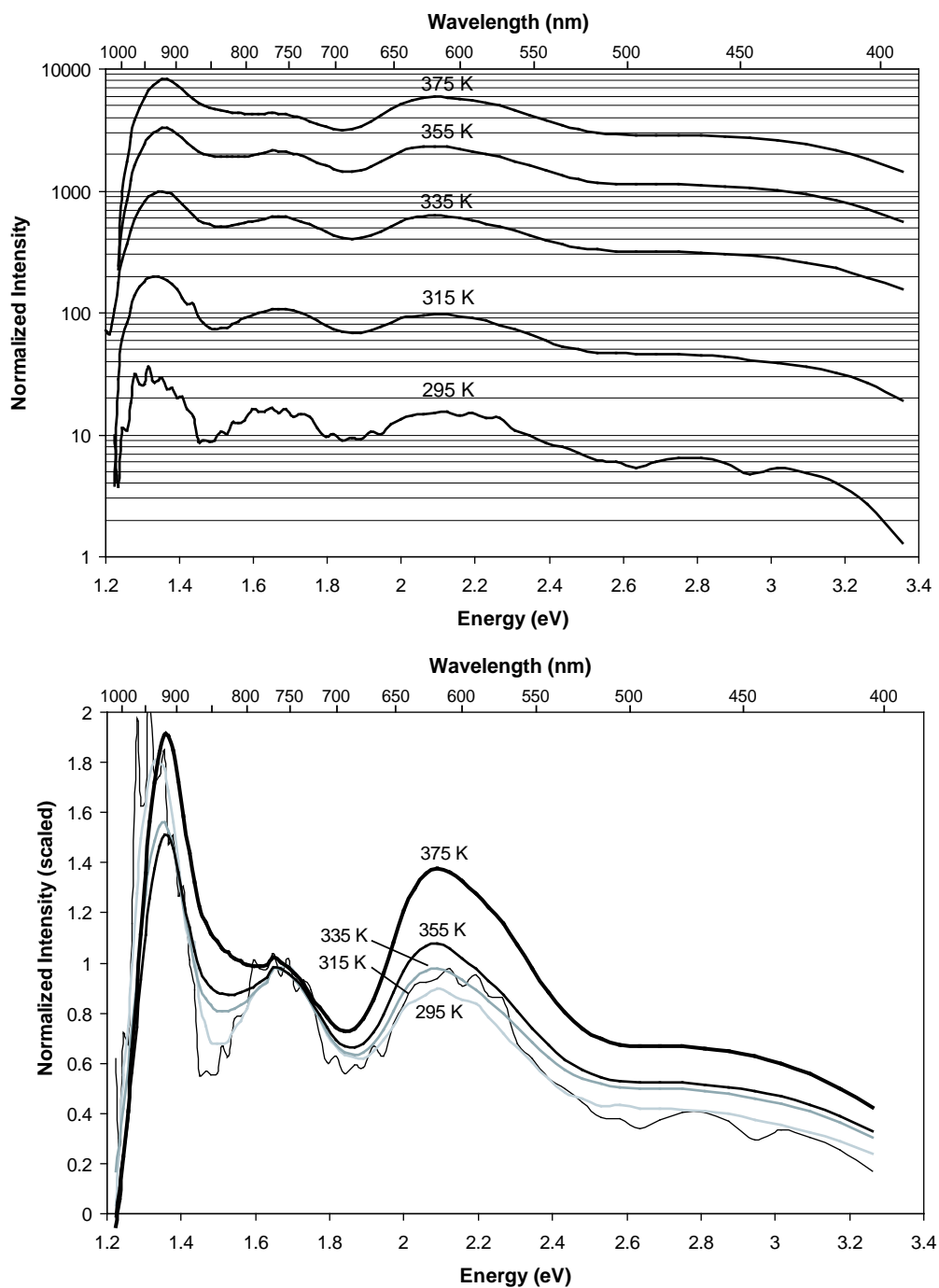
Figure 4.38: *Top: Temperature dependence of the prompt phosphorescence spectrum of orthoclase K3. Relative intensities of the spectra at different temperatures are only approximate. Bottom: Spectra scaled to the intensity of the 1.67 eV emission peak.*
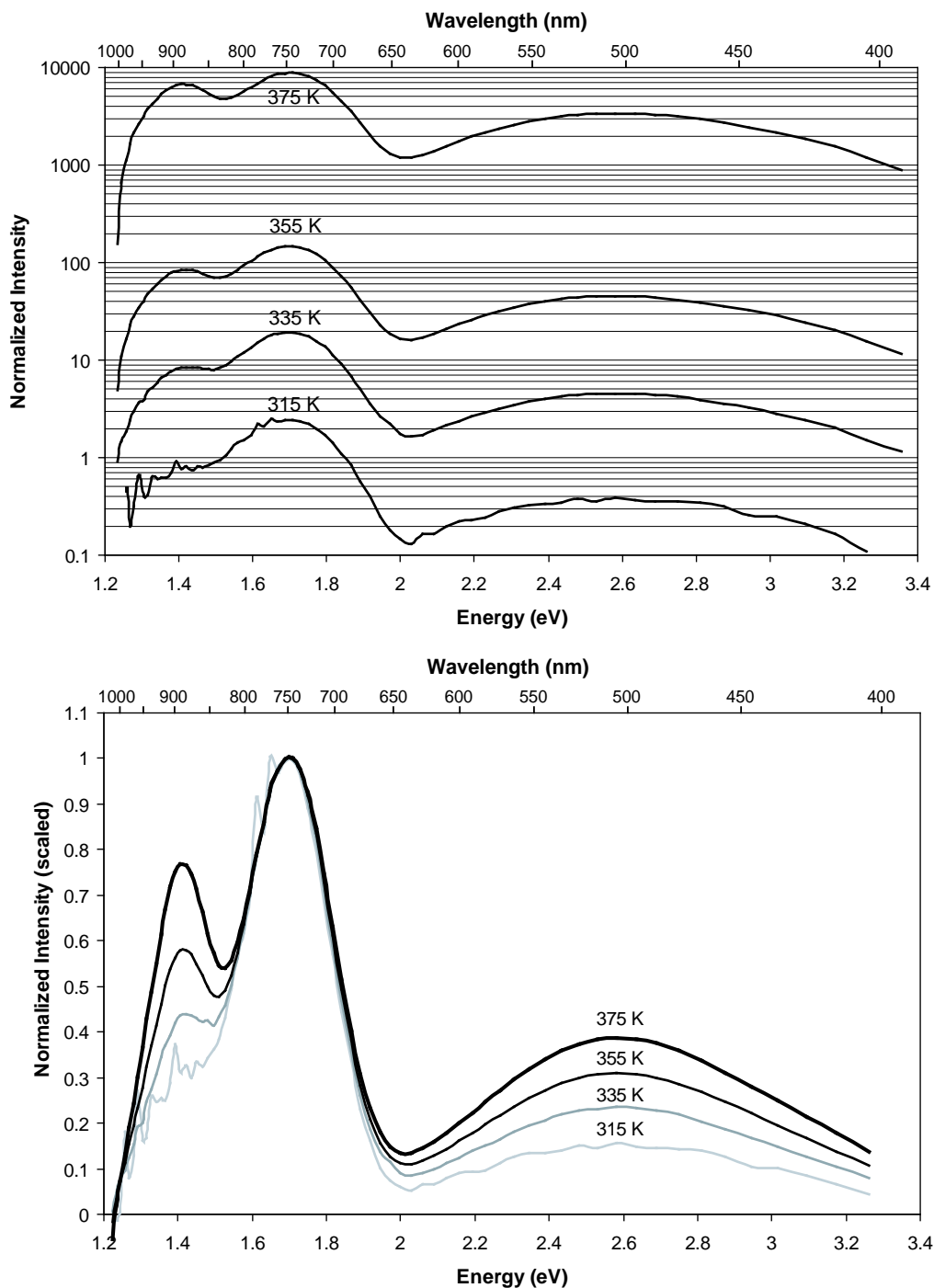
Figure 4.39: *Top: Temperature dependence of the prompt phosphorescence spectrum of microcline K8. Relative intensities of the spectra at different temperatures are only approximate. Bottom: Spectra scaled to the intensity of the 1.67 eV emission peak.*
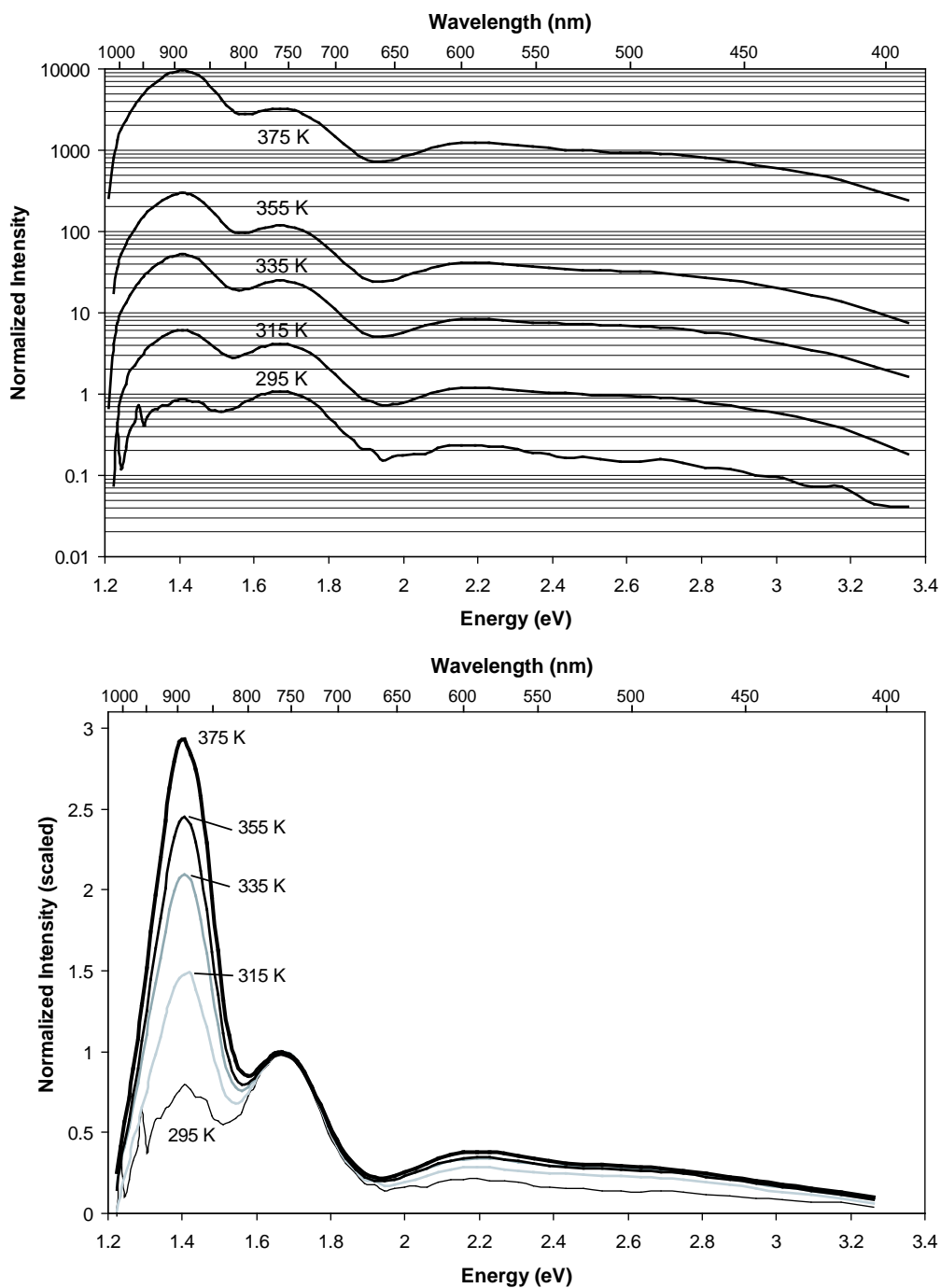
Figure 4.40: *Top: Temperature dependence of the prompt phosphorescence spectrum of microcline K9. Relative intensities of the spectra at different temperatures are only approximate. Bottom: Spectra scaled to the intensity of the 1.67 eV emission peak.*
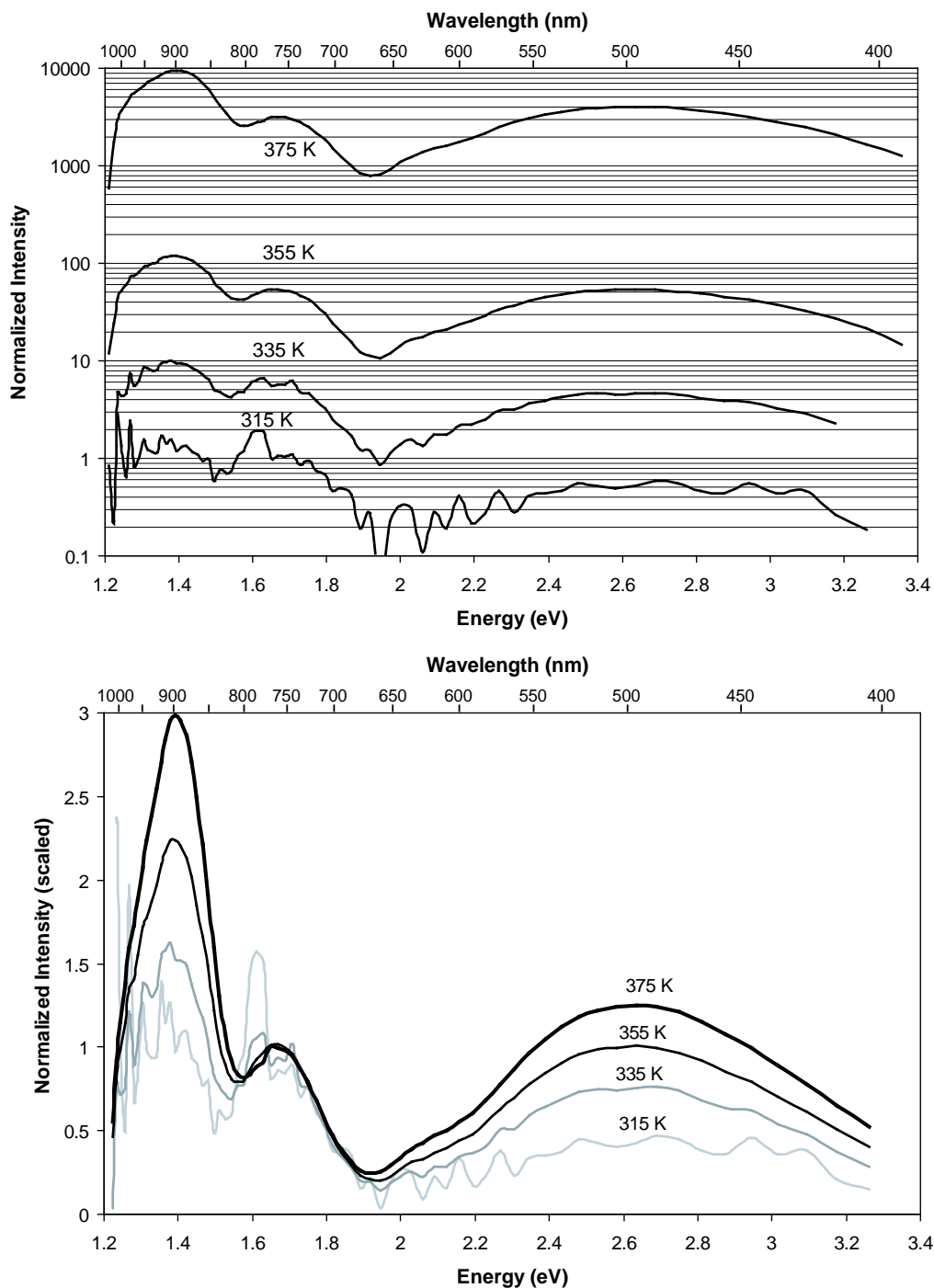
Figure 4.41: *Top: Temperature dependence of the prompt phosphorescence spectrum of microcline K10. Relative intensities of the spectra at different temperatures are only approximate. Bottom: Spectra scaled to the intensity of the 1.67 eV emission peak.*
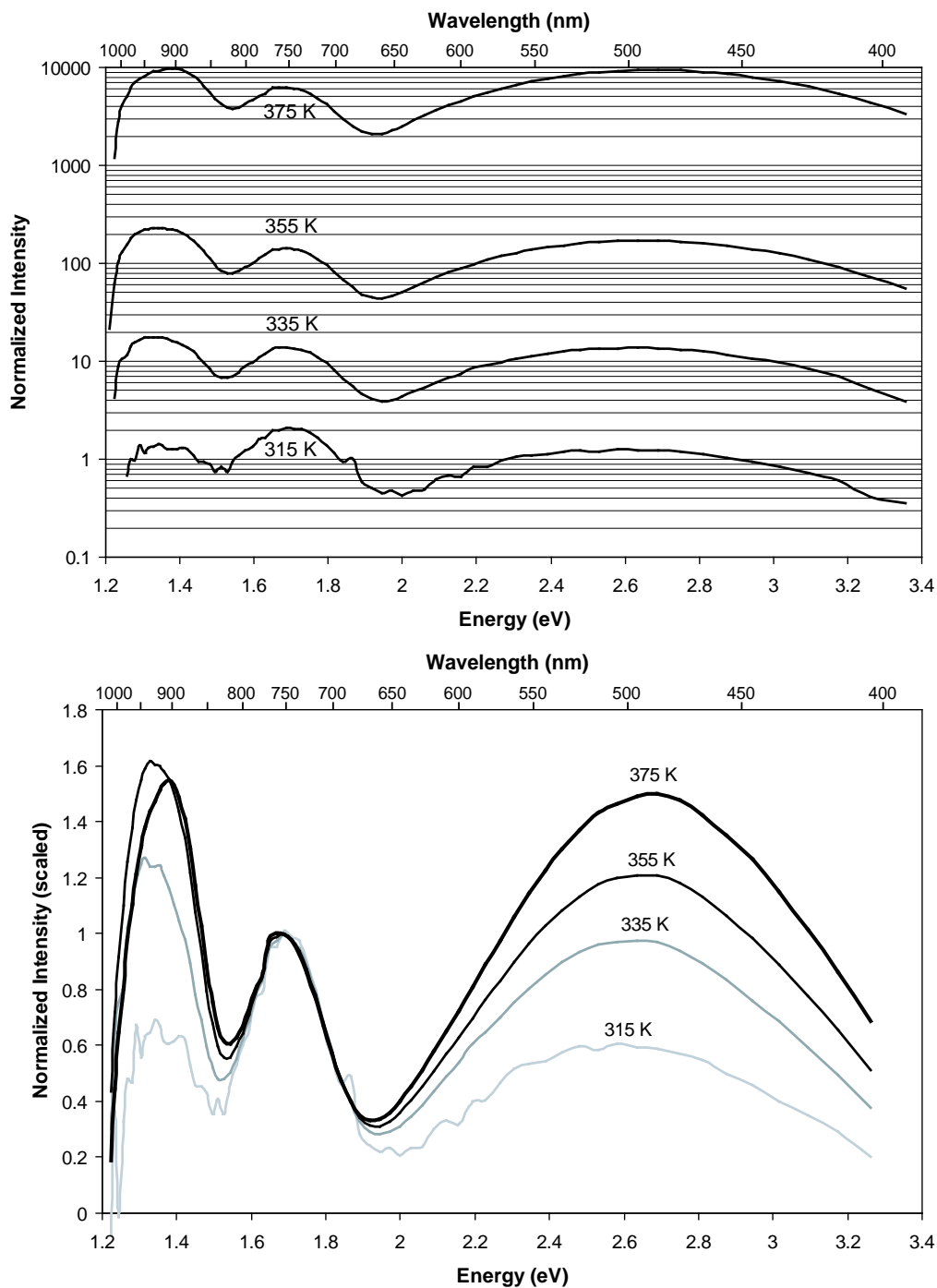
4.5.1 Time dependence of the phosphorescence

Figure 4.42 shows how the prompt phosphorescence intensity decreases with time for the three emission bands in our samples. Prior to measurement, the samples were given a 2770 Gy γ-dose over 11 days. The sample temperature was held at 120 $^{\circ}$C during the measurement.

The decay of the luminescence follows Becquerel's law with the power-law exponent close to unity in all cases; fitting parameters are given in Table 4.6. The exponent for 1.38 eV (900 nm) band is consistently lower, 0.95–1.05, than that for the 2.53 eV (490 nm) and 1.65 eV (750 nm) bands, both of which are close to 1.10–1.15 (this is most readily seen in the decay curves of Figure 4.42).

Table 4.6: *Fit of the phosphorescence decay to Becquerel's equation, $I_0/(t+t_0)^{\alpha}$.*

Sample	Emission	α	t_0 (s)
AKHC	1.38 eV	0.990 ± 0.006	54.7 ± 0.9
	1.65 eV	1.148 ± 0.006	64.1 ± 0.8
	2.53 eV	1.148 ± 0.005	56.9 ± 0.6
SAW-95-09	1.38 eV	0.948 ± 0.004	68.5 ± 0.5
	1.65 eV	1.128 ± 0.006	88.4 ± 0.8
	2.53 eV	1.083 ± 0.005	77.2 ± 0.6
GP-1	1.38 eV	1.045 ± 0.005	69.0 ± 0.5
	1.65 eV	1.148 ± 0.005	78.6 ± 0.6
	2.53 eV	1.137 ± 0.004	72.5 ± 0.5

4.6 Post-illumination phosphorescence

Comparison of the post-irradiation (or prompt) phosphorescence spectra with the IRSL spectra clearly indicates that the emission spectrum depends critically on the mode of excitation. In particular, the broad phosphorescence emission at 2.5 eV is entirely absent in IRSL, whereas the 3.1 eV and 2.2 eV IRSL emission bands are absent in the prompt phosphorescence. It would be useful to know if the post-irradiation phosphorescence spectrum

Figure 4.42: *Top: Phosphorescence emission spectrum as a function of time for sample AKHC; each curve represents a 10 second increment. Bottom: Phosphorescence decay with time for the three emission bands. Decay curves have been shifted on the time-axis to display adherence to Becquerel's law. Intensity has been corrected for the second-order spectrum and normalized for system response.*
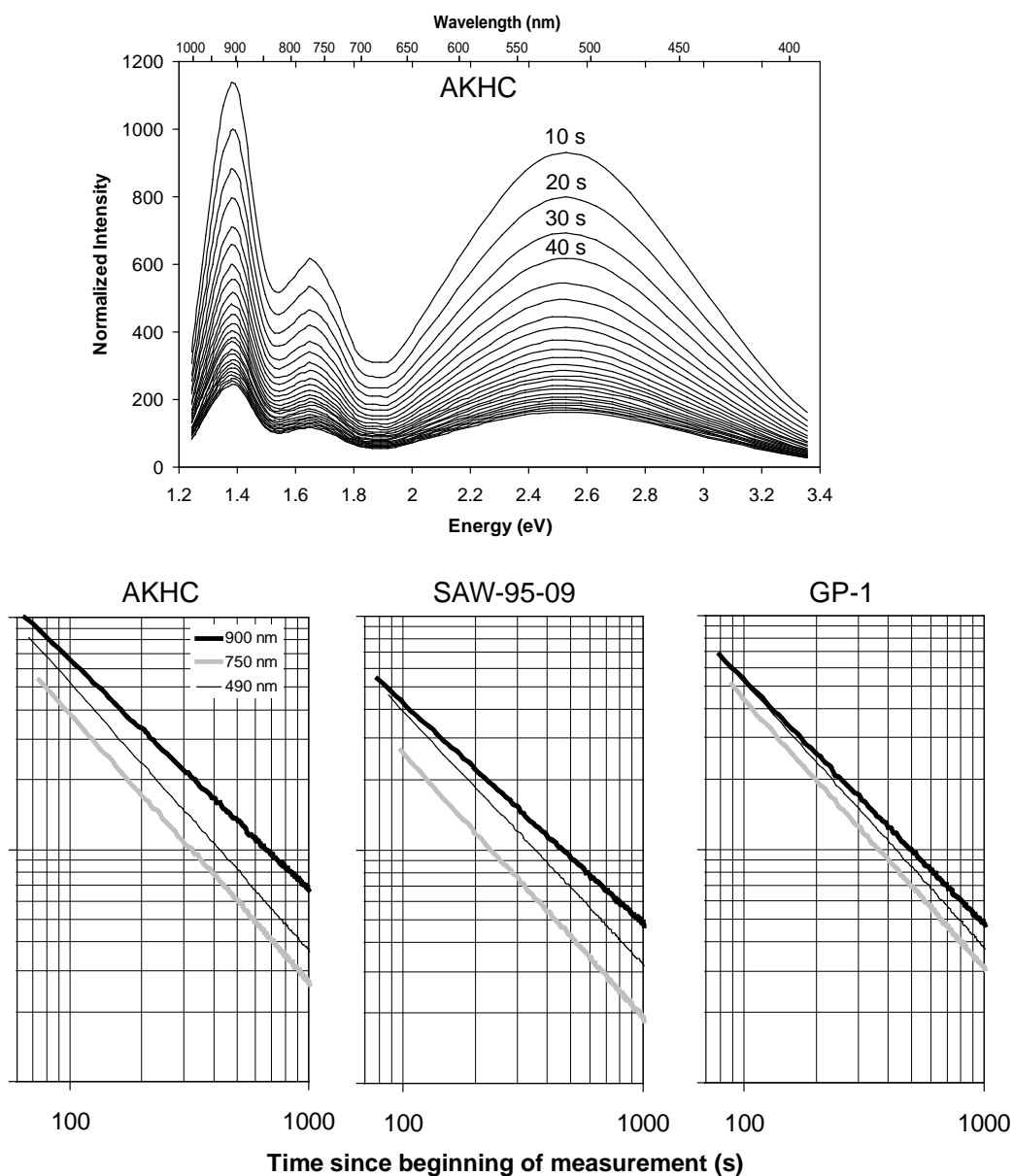
is similar to the phosphorescence spectrum of the sample following illumination. Although the distribution of trapped charges in the lattice is likely to be different for the two cases, one might expect that the emission bands would at least be similar.

The post-illumination phosphorescence appears to be particularly intense and long-lived (up to several 100 ms) in the Na-rich feldspars (*e.g.* A3 and A6). Spectra of the phosphorescence were obtained for five cut feldspar samples; albite A6, perthite K8, orthoclase K3 and microclines K9 and K10. The samples were given a 1450 Gy γ dose over 139 hours and measured within 4 hours of the end of irradiation. The samples were excited with 1.44 eV light for 1 s, then, once the illumination shutter closed, the latent phosphorescence was measured for 3 s. Over this integration period, the prompt phosphorescence (due to the use of unpreheated samples) contributed a negligible amount to the post-illumination phosphorescence[6]. The measurement was repeated 20 times so that the change of the phosphorescence as the IRSL decreased could be noted. The spectra and decay curves for the principal emission bands are shown in Figures 4.43–4.45.

The spectra obtained for the post-illumination phosphorescence differ in many respects from those observed for the post-irradiation phosphorescence. The dominant emission band is in the IR, centered between 1.265–1.38 eV (900–980 nm), whereas the broad 2.5 eV emission band that predominated in the post-irradiation phosphorescence is absent. The only significant emission in the visible is roughly centered at 2.1 eV (590 nm) and may be due to the same recombination center as the 570 nm "albite" IRSL (Mn^{2+}). The relative rate of decrease of the emission bands varies greatly between samples so that no generalization can be made in this regard.

---

[6]The prompt phosphorescence was barely detected in samples A6 and K8 over a 300s integration, and completely undetected in the remaining samples.

Figure 4.43: *Post-illumination phosphorescence from A6 (top) and K8 (bottom) as a function of IR illumination time. Each curve (in black) represents a 1 s increment in illumination time. The unpreheated IRSL spectrum is shown in grey for comparison. Inset: Decay curves of the phosphorescence for the three brightest emission peaks. The curves have been shifted along the illumination time axis by the amount necessary to obtain best agreement with Becquerel's equation.*
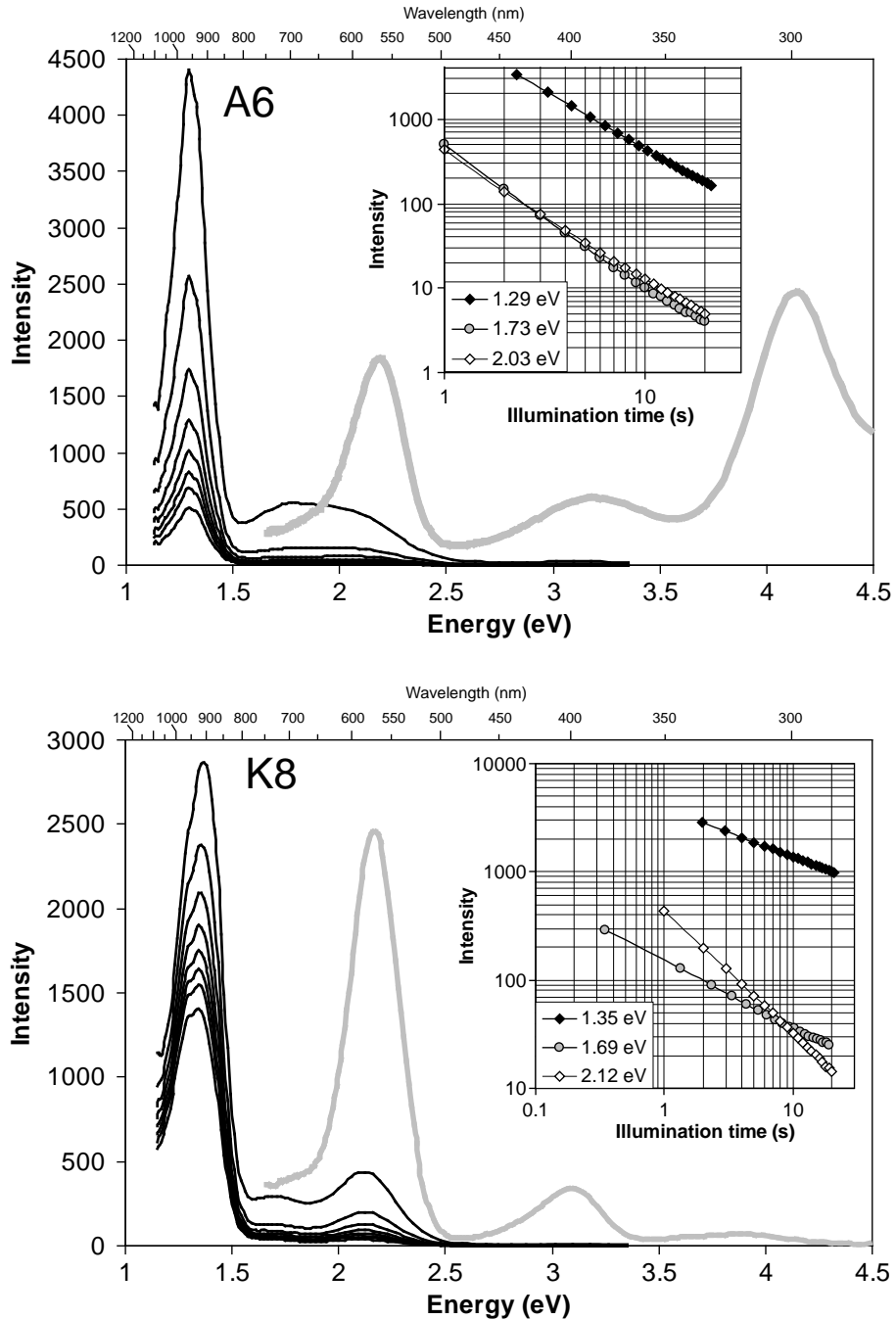
Figure 4.44: *Post-illumination phosphorescence from K9 (top) and K10 (bottom) as a function of IR illumination time. Each curve (in black) represents a 1 s increment in illumination time. The unpreheated IRSL spectrum is shown in grey for comparison. Inset: Decay curves of the phosphorescence for the three brightest emission peaks. The curves have been shifted along the illumination time axis by the amount necessary to obtain best agreement with Becquerel's equation.*
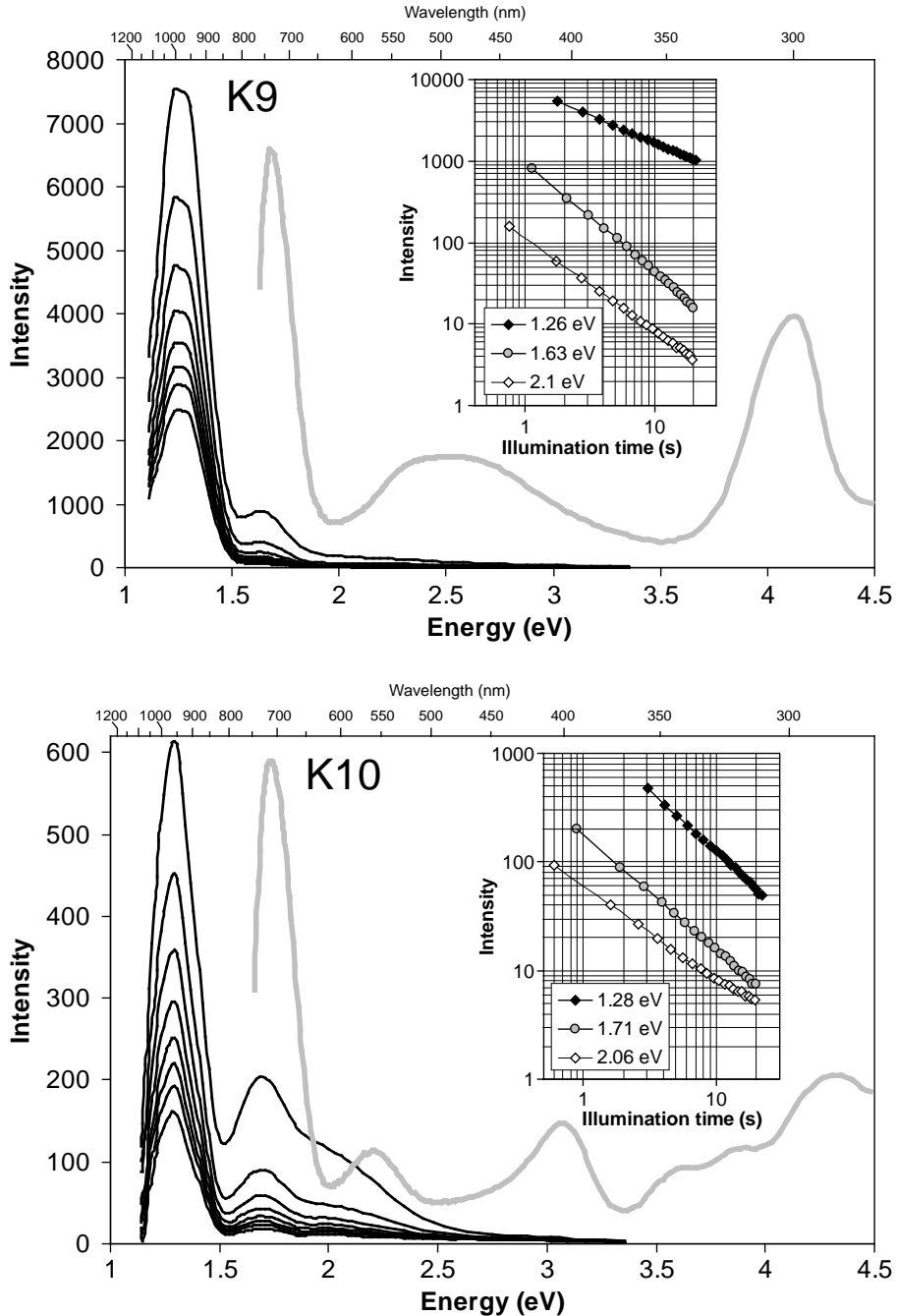
Figure 4.45: *Post-illumination phosphorescence from K3 as a function of IR illumination time. Each curve (in black) represents a 1 s increment in illumination time. The unpreheated IRSL spectrum is shown in grey for comparison. Inset: Decay curves of the phosphorescence for the three brightest emission peaks. The curves have been shifted along the illumination time axis by the amount necessary to obtain best agreement with Becquerel's equation.*
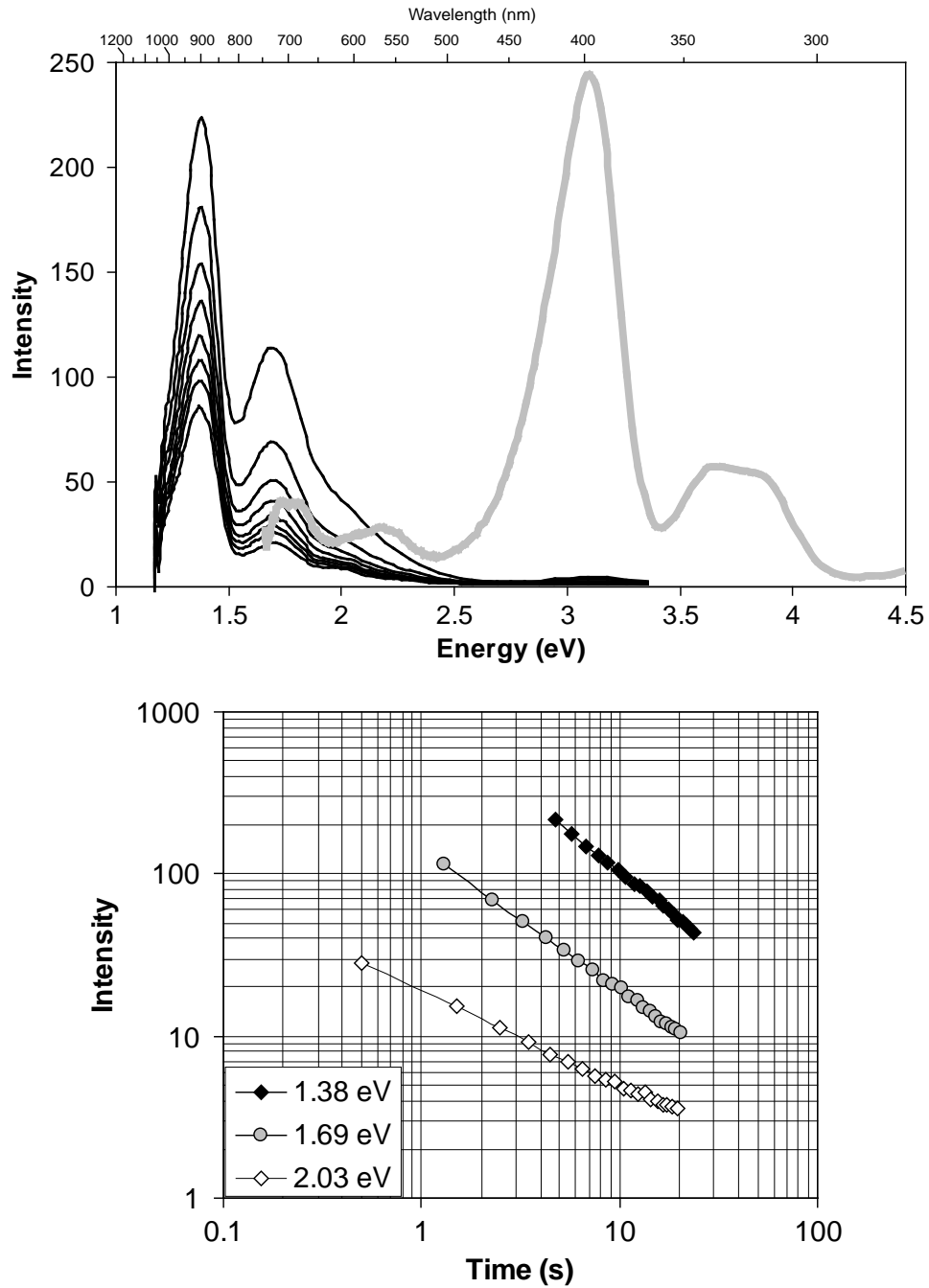
4.7 Summary

It is evident from comparisons of the phosphorescence, IRSL and TL spectra that the notion of the recombination centers being largely independent of the electron traps cannot be correct. If this were true, we would expect the spectra for each excitation mechanism to be generally similar; that is, any electron in the "conduction-band" would have access to all recombination centers. However, it appears that even when the excitation mechanisms are similar (*e.g.* post-illumination and post-irradiation phosphorescence) the emission spectra can differ considerably. The behaviour of the 1.76 eV emission is a case in point; it appears only in IRSL and room-temperature phosphorescence immediately following irradiation but can also appear in well thermalized samples upon heating above 350 K. It can only be concluded that certain recombination pathways are available only to specific traps.

This conclusion conflicts with the conventional view of the electrons proceeding to the recombination centers via the conduction band. Instead of recombination through the conduction band, it seems more likely that certain traps are connected to particular luminescence centers and that the distance traveled by the electrons in the crystal during recombination may be minimal. In such a case, a tunnelling recombination model may provide a better description of the emission. Clusters of defects as found in CaF_2 and other materials commonly used in dosimetry (Townsend *et al.*, 2001) may explain the close correlation between certain traps and the recombination centers. Another possibility is an energy transfer mechanism where the recombination energy is transferred to a neighbouring center which produces the luminescence.

The observation of 1.265–1.38 eV phosphorescence emission is a new development that has not been previously investigated. It is not possible to discern from our studies whether this is a "transient" phosphorescence emission akin to the the 700 nm band. An internal transition in Fe^{2+} ($^5T_2(^5D)$–$^5E(^5D)$) is known to be responsible for 1.265 eV luminescence in ZnS phosphors (Nelkowski, 1979). Another possibility is that the IR emission arises from re-trapping in the "principal" IRSL trap with resonance at 1.44 eV. Trautmann *et al.* (1999) attribute the 1.46 eV emission in their RL spectra to recombination in the principal IRSL trap; this recombination is at a substantially higher energy than our 1.265–1.38 eV phosphorescence. In our case, an explanation is required for the shift by 0.06–0.17 eV to lower energy in the phosphorescence relative to the excitation (*i.e.* emission vs. absorption). This energy shift is sufficiently small that it could easily be attributed to a classical Stokes shift.

Chapter 5

Excitation Spectra

5.1   Overview

Luminescence emission spectra provide limited information as to the nature of the electron traps in the material. Measuring the OSL intensity as a function of the energy of the excitation light provides information about the energetic separation of the trap state and its excited states. In addition, the shape of the excitation response of the luminescence provides insight into the nature of the trapping defects.

Excitation spectra were produced for several cut rock feldspars and a few feldspar sediment extracts with the goal of providing a better understanding of the dependence of the excitation spectrum on feldspar composition. The energy range of the excitation photons was between 1.24 eV to 1.77 eV (700 to 1000 nm)[1]. Excitation spectra were produced for both bright emission bands of alkali feldspars at 3.1 eV and 2.2 eV. The dependence of the excitation spectrum on the polarization of the exciting light was studied in microcline K7 (Section 5.7). In addition, the effect of sample temperature on the excitation spectrum was investigated for orthoclase K3 (Section 5.6).

---

[1]Measurements at higher excitation energies can be found in Chapter 7 for samples K3, K8, K9 and K10.

Figure 5.1: *Setup for measuring excitation spectra.*
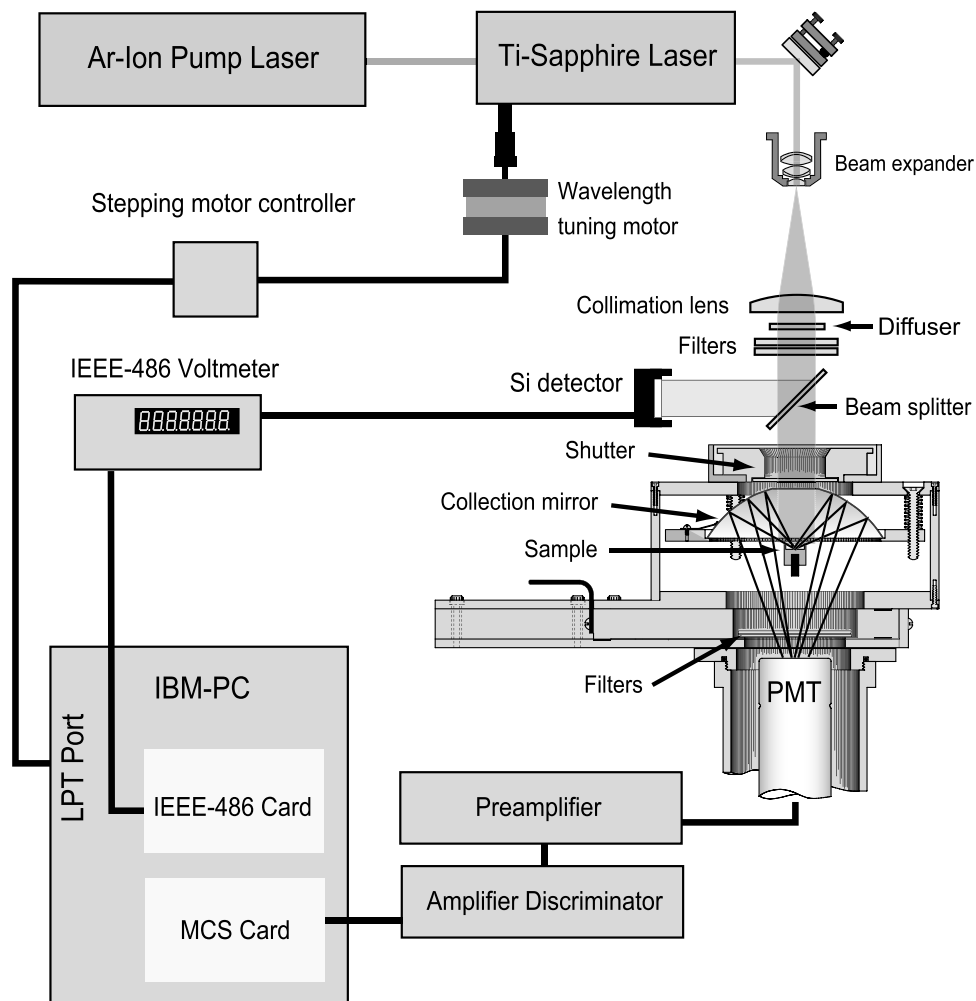
5.2 Experimental setup

The setup consisted of an excitation source, provided by a tunable Ti-Sapphire laser pumped by a 6W Argon-ion laser and a measurement chamber to collect and count the luminescence photons (Figure 5.1). Light collection was provided by an ellipsoidal mirror with the sample placed at one focus of the ellipsoid and a photomultiplier tube (PMT) placed at the second

Figure 5.2: *Product of the filter transmission coefficients with the quantum efficiency of the 9635Q PMT for the different filter combinations used.*
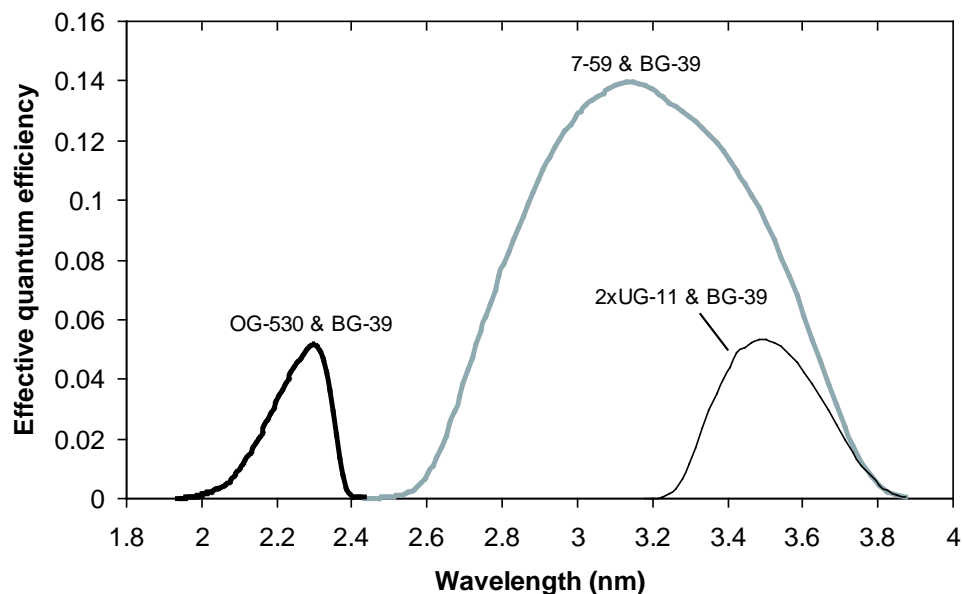
focus[2]. The excitation beam was admitted through a 3 cm diameter hole in the center of the ellipsoidal mirror. Filters placed before the PMT attenuated the scattered excitation photons while allowing the selected luminescence band to be measured. An EMI 9635Q PMT was employed. The 9635Q's bi-alkali photocathode has the advantage of having a poor response in the IR, so that only the short-wave (<600 nm) emission from the sample was detected. The violet emission band was selected using a 2.2 mm thick Schott BG-39 filter and a Kopp 7-59 filter. The yellow-green emission was selected using two BG-39's and one 3.1 mm thick Schott OG-530 filter. For sample K3, the UV band was selected using two 3.0 mm thick Schott UG-11's and a BG-39 filter. The combination of these filter bandpasses with the PMT response is shown in Figure 5.2.

The laser beam power was recorded during the experiment by monitoring the reflection of the beam off a thin glass beam splitter using a calibrated silicon photo-diode detector. The ratio of the intensity of the reflected beam to the transmitted beam (at the sample) was measured using a pair of calibrated silicon detectors. From this, it was found that the

---

[2]This apparatus is described in detail by Baril (1997).

variation in the beam splitter reflectivity with wavelength was sufficiently small over the excitation band that it could be neglected. Care was taken to ensure that the laser polarization always remained fixed relative to the beam-splitter orientation during measurement. The luminescence intensity was later divided by the average beam power recorded during the measurement.

A holographic diffuser was placed in the excitation beam, between the beam splitter and the collimation lens. The purpose of the diffuser was to avoid strong diffraction patterns from forming at the sample due to the interposed beam-splitter. The diffuser also ensured a broad, uniform illumination of the sample so that the the ratio of the power at the sample and at the beam-splitter was relatively unaffected by small shifts in the beam direction.

The wavelength of the Ti-Sapphire laser was tuned automatically using a stepping motor driven by the acquisition software. Fine manual adjustments to the Ti-Sapphire mirrors during the measurement ensured that the laser mode remained primarily in TEM-00.

A single aliquot was used for all excitation measurements. In order to check that a negligible decay of the luminescence occurred during the scan, a measurement at the initial excitation wavelength was repeated at the end of the scanning sequence. Generally, the level of decay was well below 10%, so that no attempt at correction for the decay was made[3]. The sample was typically illuminated for 3 seconds at each wavelength, with a laser beam power of the order ~ 0.1 μW/cm^2.

Acquisition of the full 1.24 eV to 1.77 eV (690 nm to 1000 nm) excitation band required the insertion of three separate optic sets into the Ti-Sapphire laser. Each excitation spectrum therefore represents the combination of three spectra for the ranges, 1.65–1.77 eV (700–750 nm), 1.35–1.65 eV (750–915 nm) and 1.24–1.35 (915–1000 nm). The short and long-wavelength tails were matched to the 1.34–1.65 eV spectrum by appropriate scaling of the intensities.

The excitation spectra for the yellow-green band were scaled to the maximum response of the violet emission and are shown along with the violet emission excitation spectra in Figures 5.3–5.12. The bold line in these diagrams represents the fit that best represents the data for the violet emission band; that is, either the fit using two Gaussians or the fit using a Lorentzian and a Gaussian. Where there is ambiguity between which fit is better, the fit with

---

[3]Note that for samples in which decay was significant, scatter in the data would have been as important as the decay correction.

the Lorentzian is shown. Preference was given to the fit that clearly distinguished between the 1.445 eV resonance and the feature at higher energy ($\sim$1.6 eV), although this was not always possible (*e.g.* K3 and K8). Where applicable, the data have been shifted upwards in intensity by the magnitude of the fitting parameter *B* (see Equations 5.1 and 5.2). In such cases the arrow marked "0" in the diagrams indicates zero on the intensity scale. The components of the fitting function are represented by the fine lines with the following letter designations;

- **L**: Primary Lorentzian component.

- **G**: Primary Gaussian component.

- **g**: Secondary Gaussian component.

- **e**: Exponential background.

5.3 Feldspar rock sample excitation spectra

Figure 5.3: *A1 and A2 excitation spectra (top and bottom respectively). Open diamonds are for the violet emission band, grey circles represent the yellow-green emission band. Bold solid line is a fit to the violet emission data. See text for details.*
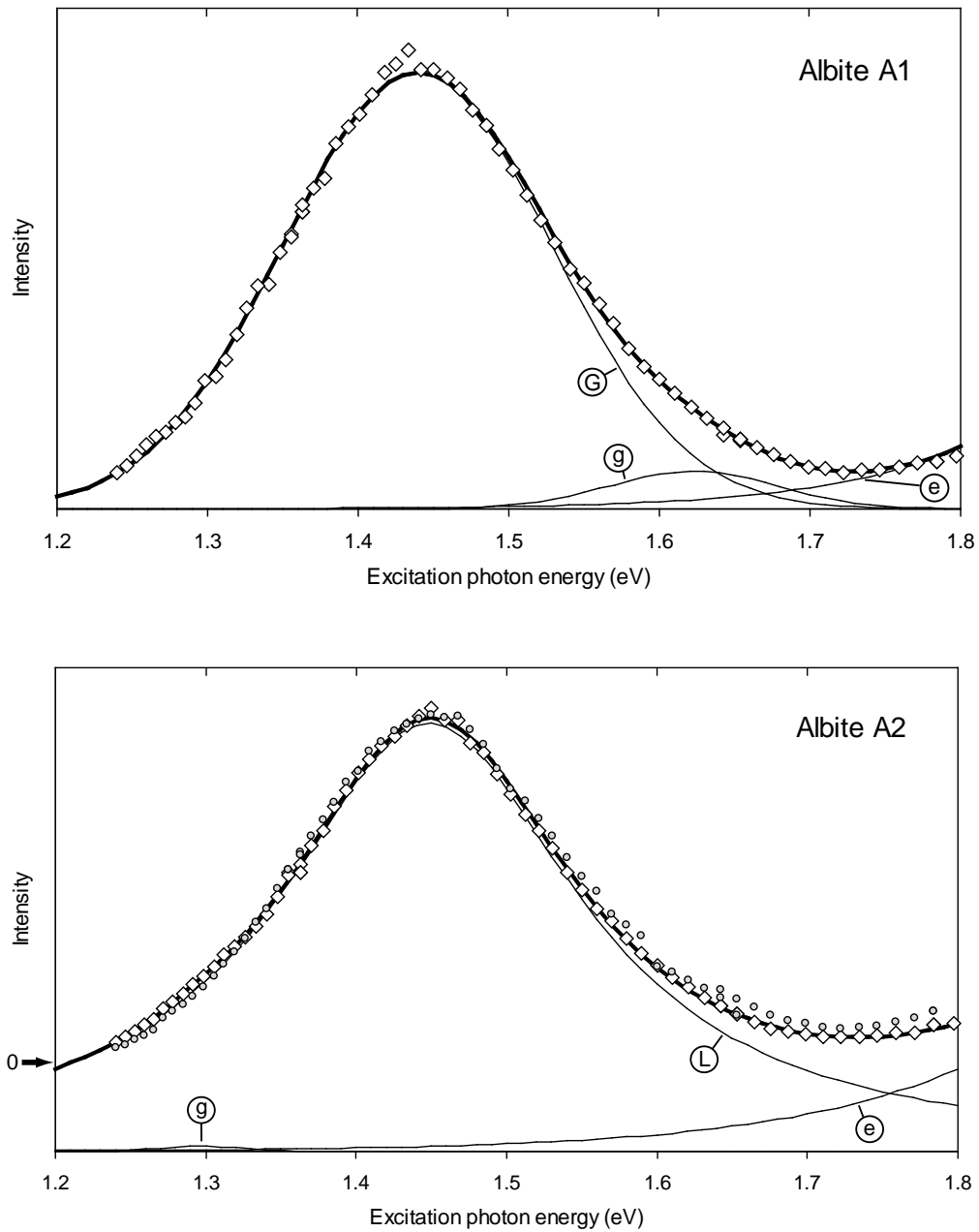
Figure 5.4: *A3 and A4 excitation spectra (top and bottom respectively). Open diamonds are for the violet emission band, small grey circles represent the yellow-green emission band. Solid line is a fit to the violet emission data. See text for details.*
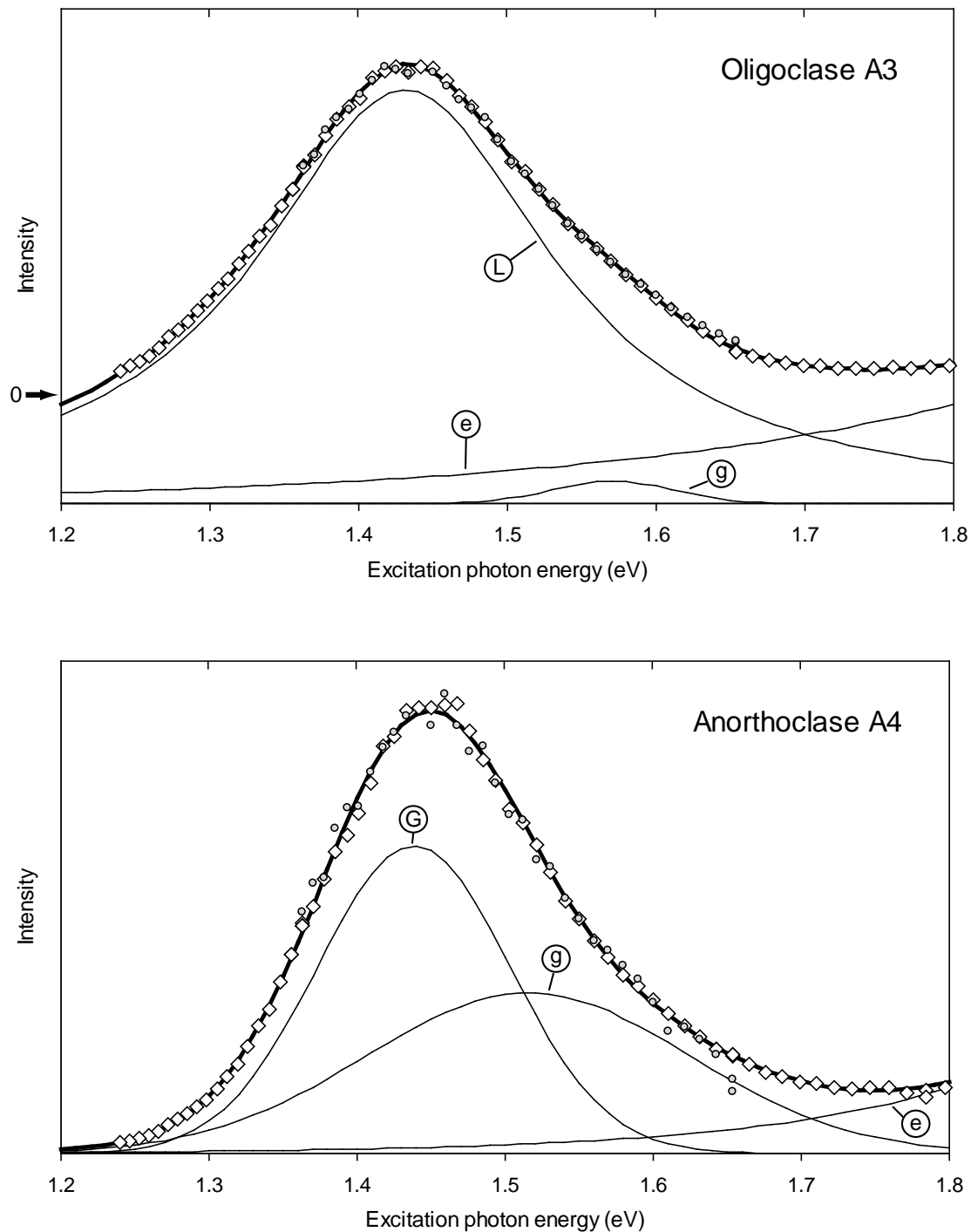
Figure 5.5: *A5 and A6 excitation spectra (top and bottom respectively). Open diamonds are for the violet emission band, grey circles represent the yellow-green emission band. Solid line is a fit to the violet emission data. See text for details.*
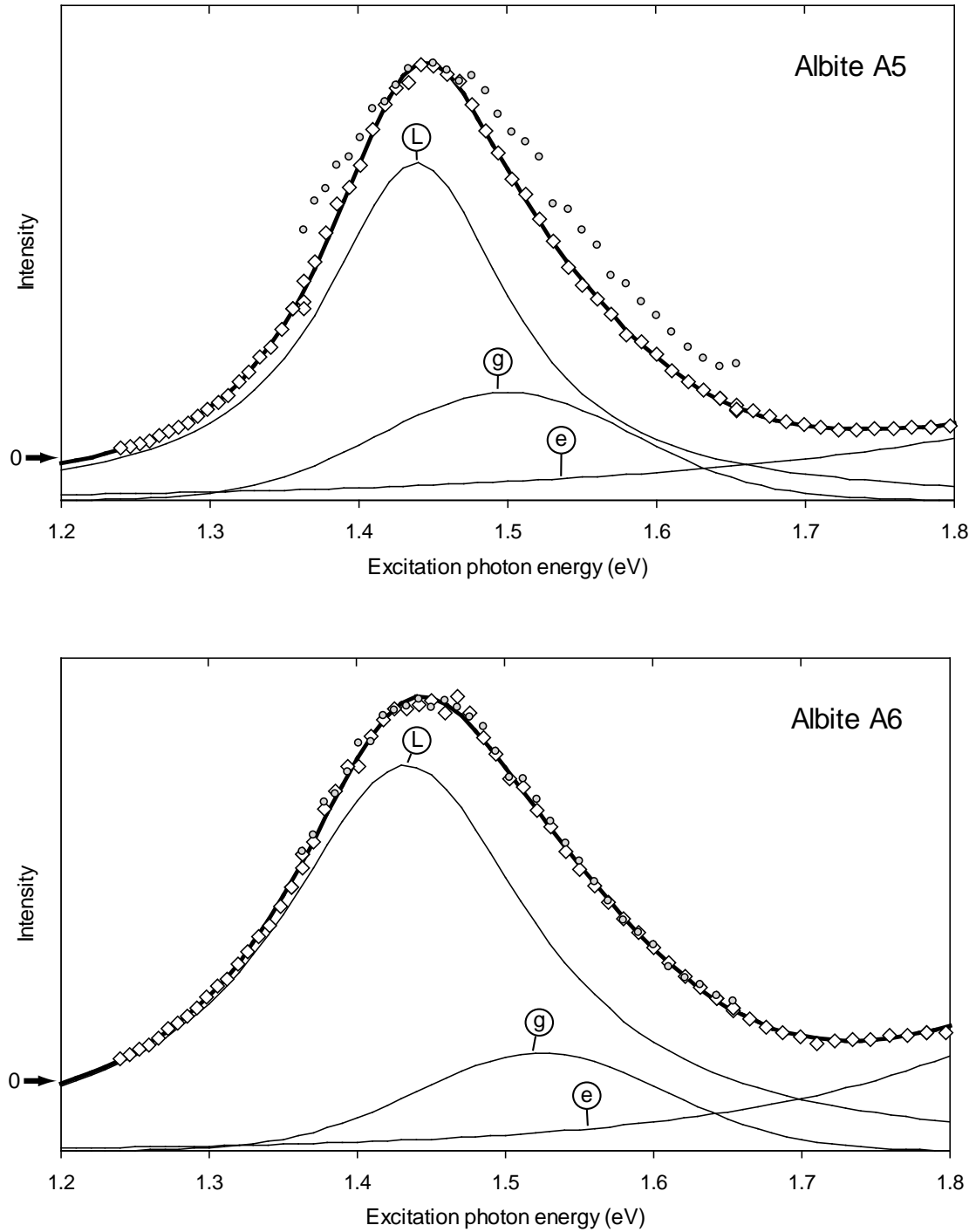
Figure 5.6: *K3 and K7 excitation spectra (top and bottom respectively). Open diamonds are for the violet emission band. In K7 grey circles are for the yellow-green emission band, in K3 these represent the UV band. Solid line is a fit to the violet emission data. See text for details.*
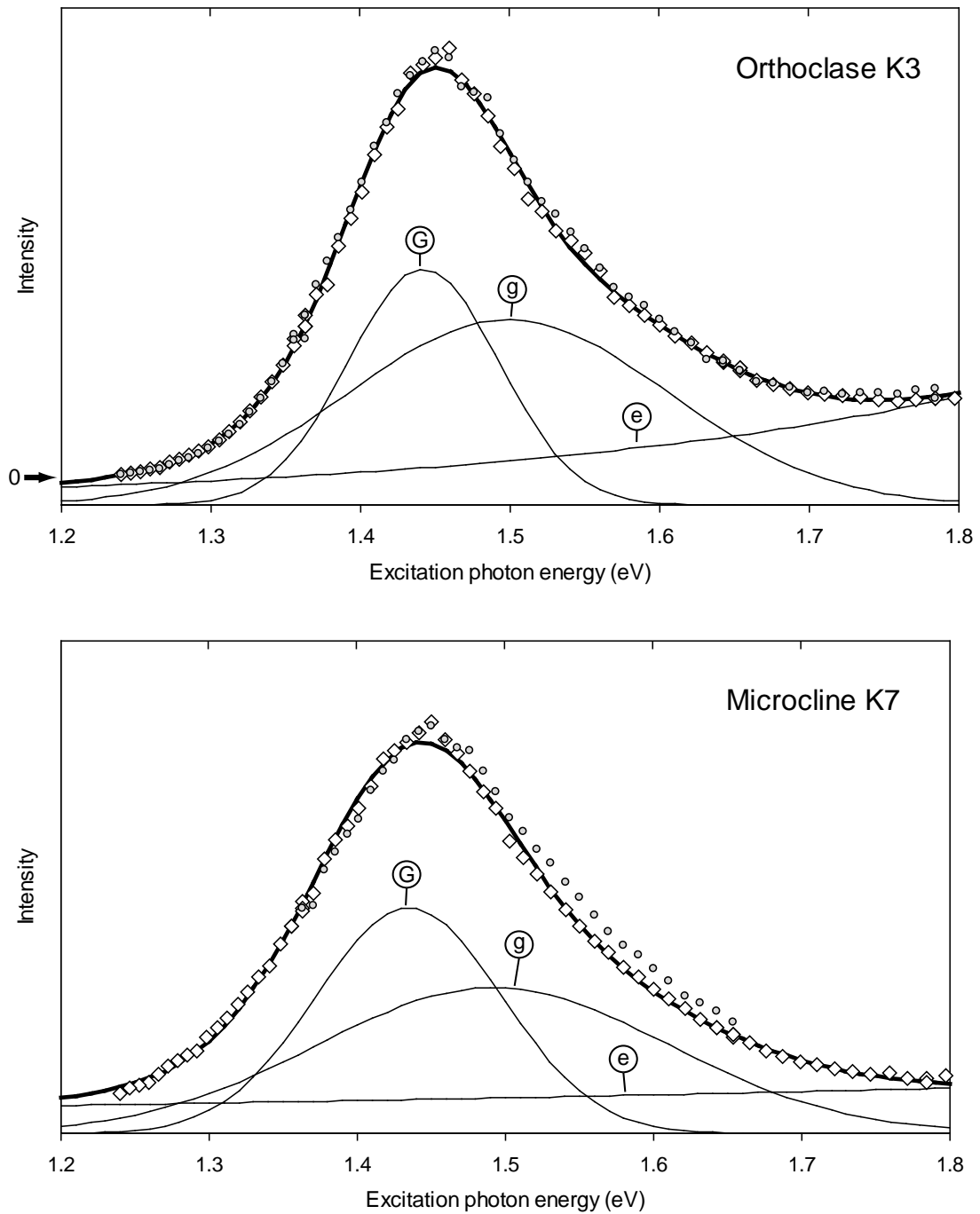
Figure 5.7: *K8 and K9 excitation spectra (top and bottom respectively). Open diamonds are for the violet emission band, smaller grey circles represent the yellow-green emission band. Solid line is a fit to the violet emission data. See text for details.*
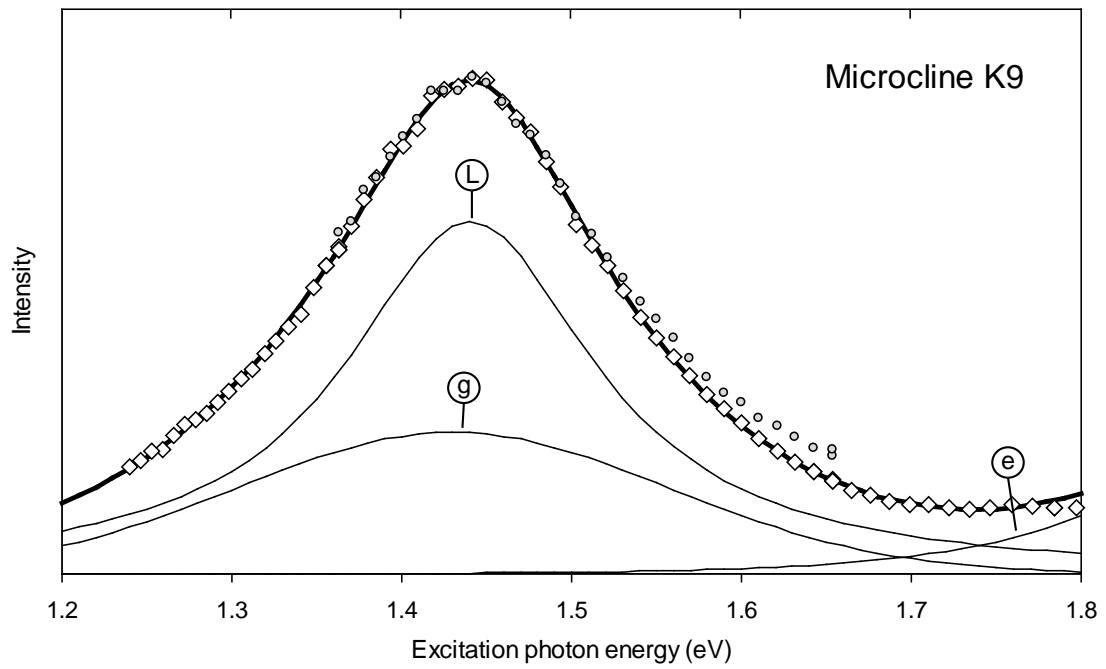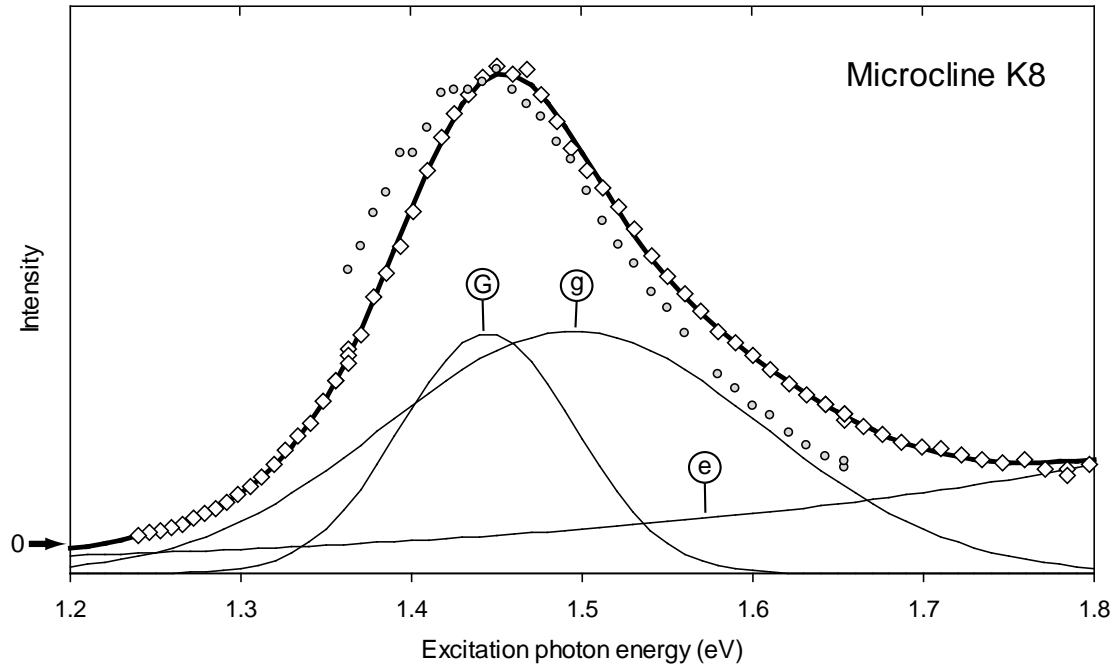
Figure 5.8: *K10 and K11 excitation spectra (top and bottom respectively). Open diamonds are for the violet emission band, grey circles represent the yellow-green emission band. Solid line is a fit to the violet emission data. See text for details.*
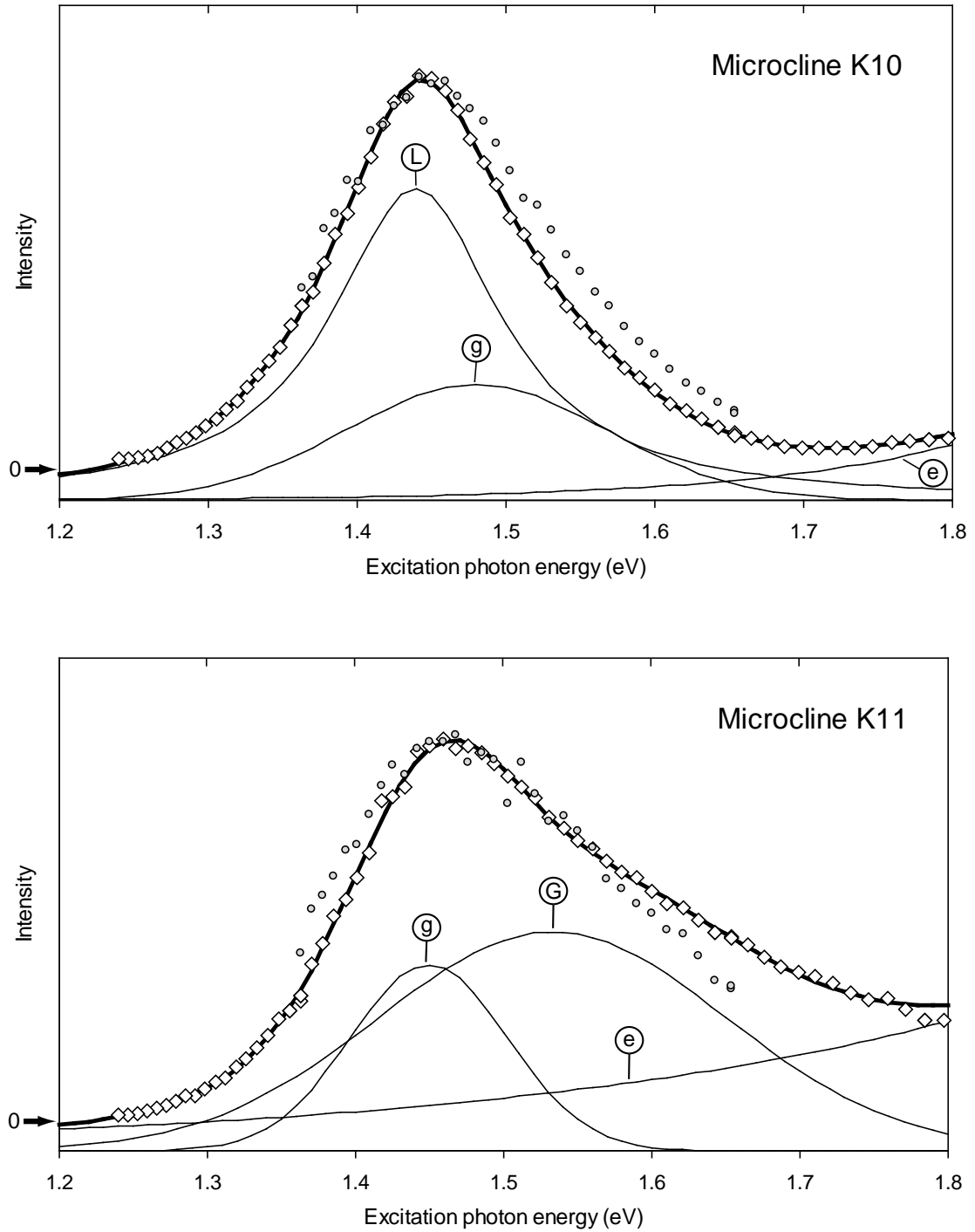
Figure 5.9: *P9 and P10 excitation spectra (top and bottom respectively). Open diamonds are for the violet emission band, grey circles represent the yellow-green emission band. Solid line is a fit to the violet emission data. See text for details.*
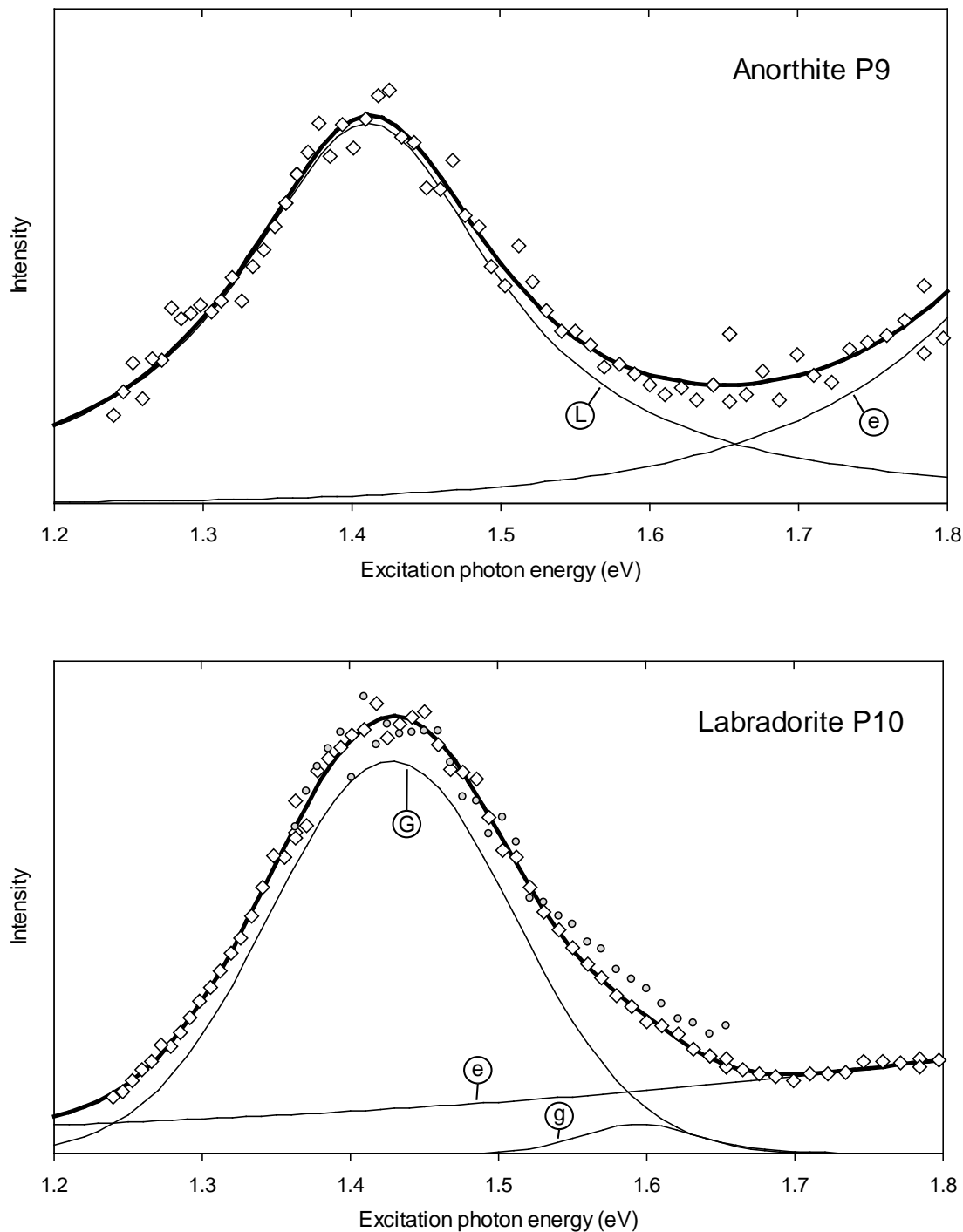
Figure 5.10: *P11 and P12 excitation spectra (top and bottom respectively). Open diamonds are for the violet emission band, grey circles represent the yellow-green emission band. Solid line is a fit to the violet emission data. See text for details.*
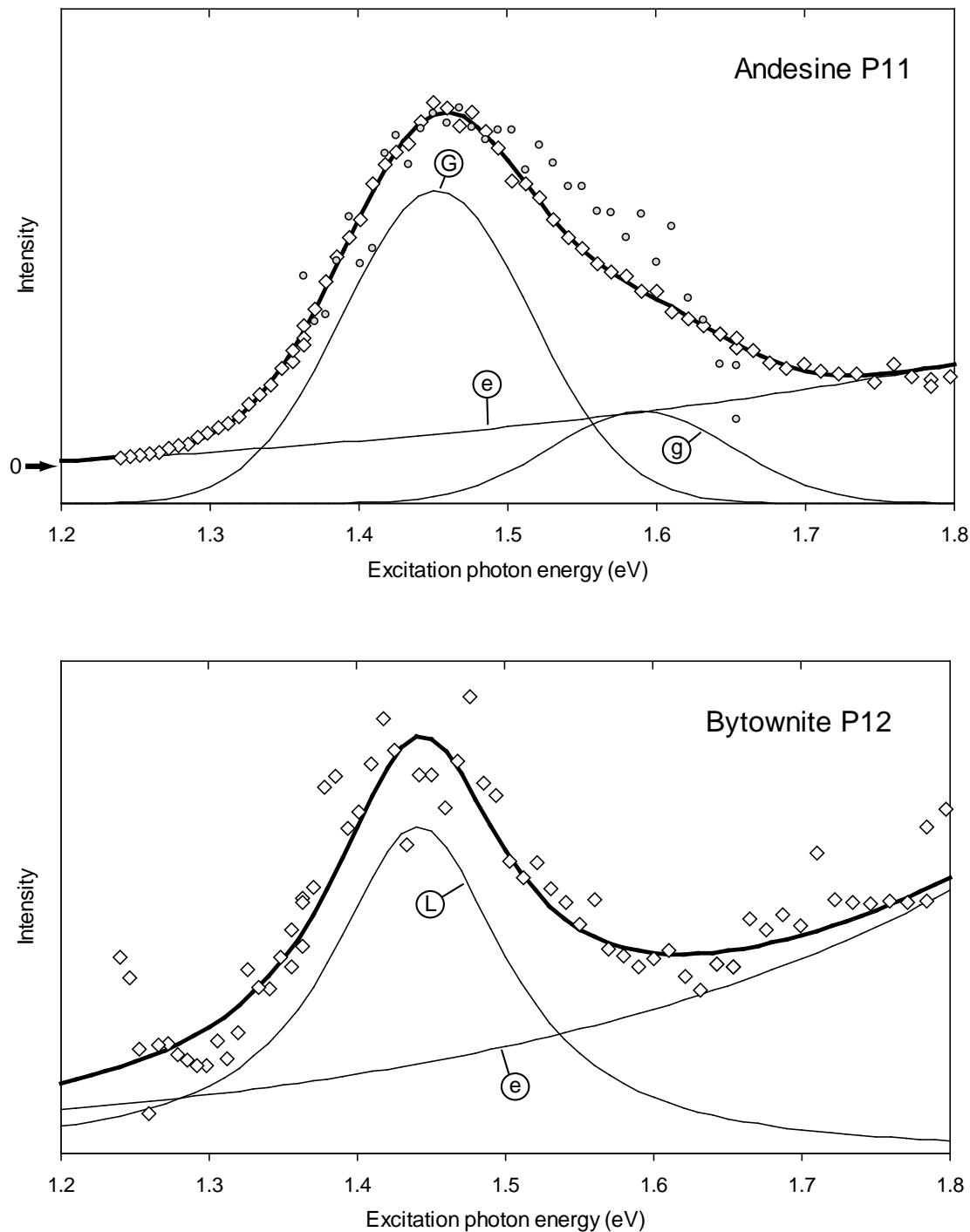
5.4 Feldspar grain separate excitation spectra

Figure 5.11: *AKHC and EIDS excitation spectra (top and bottom respectively) for the violet emission band. Solid line is a fit to the data, see text for details.*
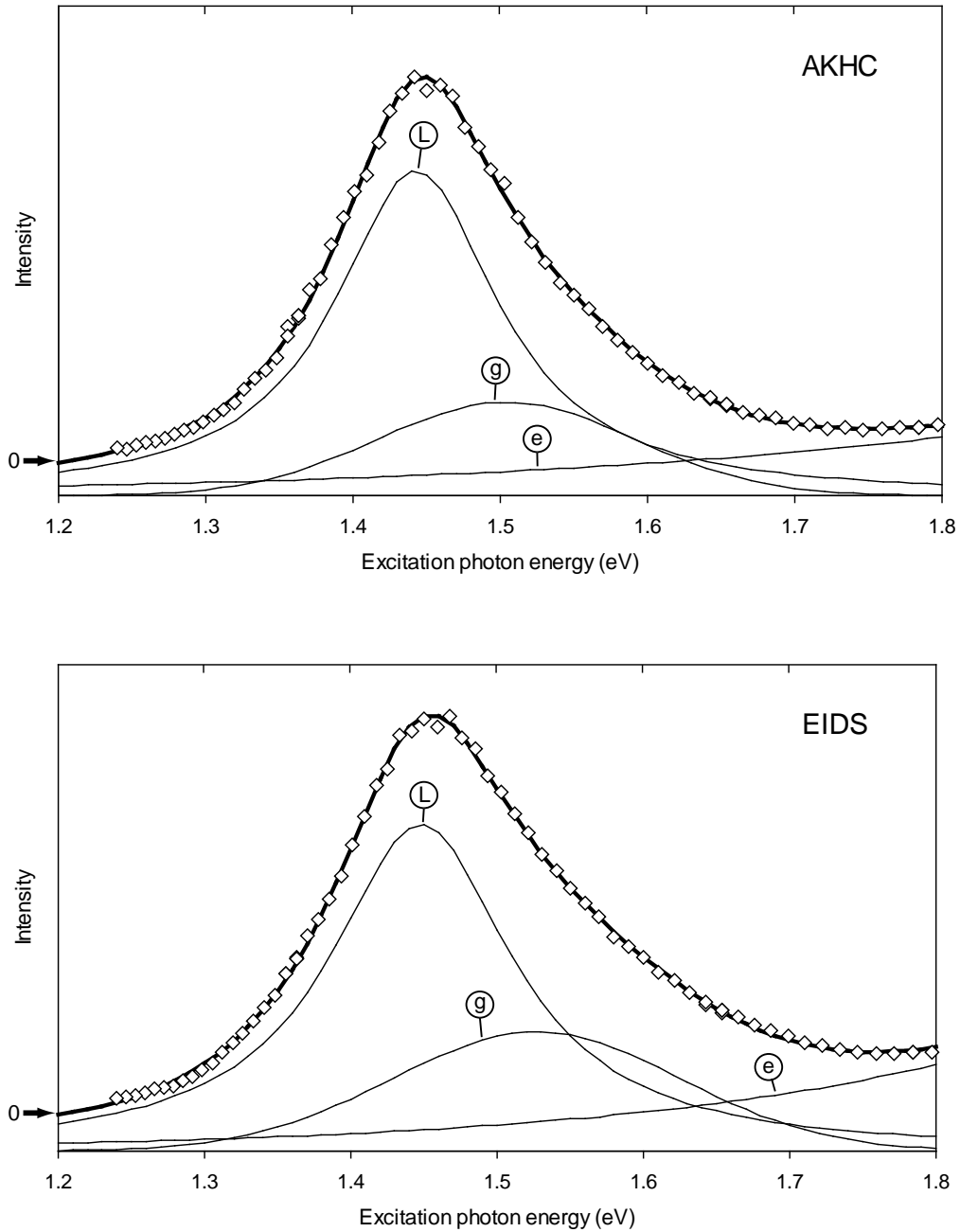
Figure 5.12: *IV-1 and OKA-4 excitation spectra (top and bottom respectively) for the violet emission band. Solid line is a fit to the data, see text for details.*
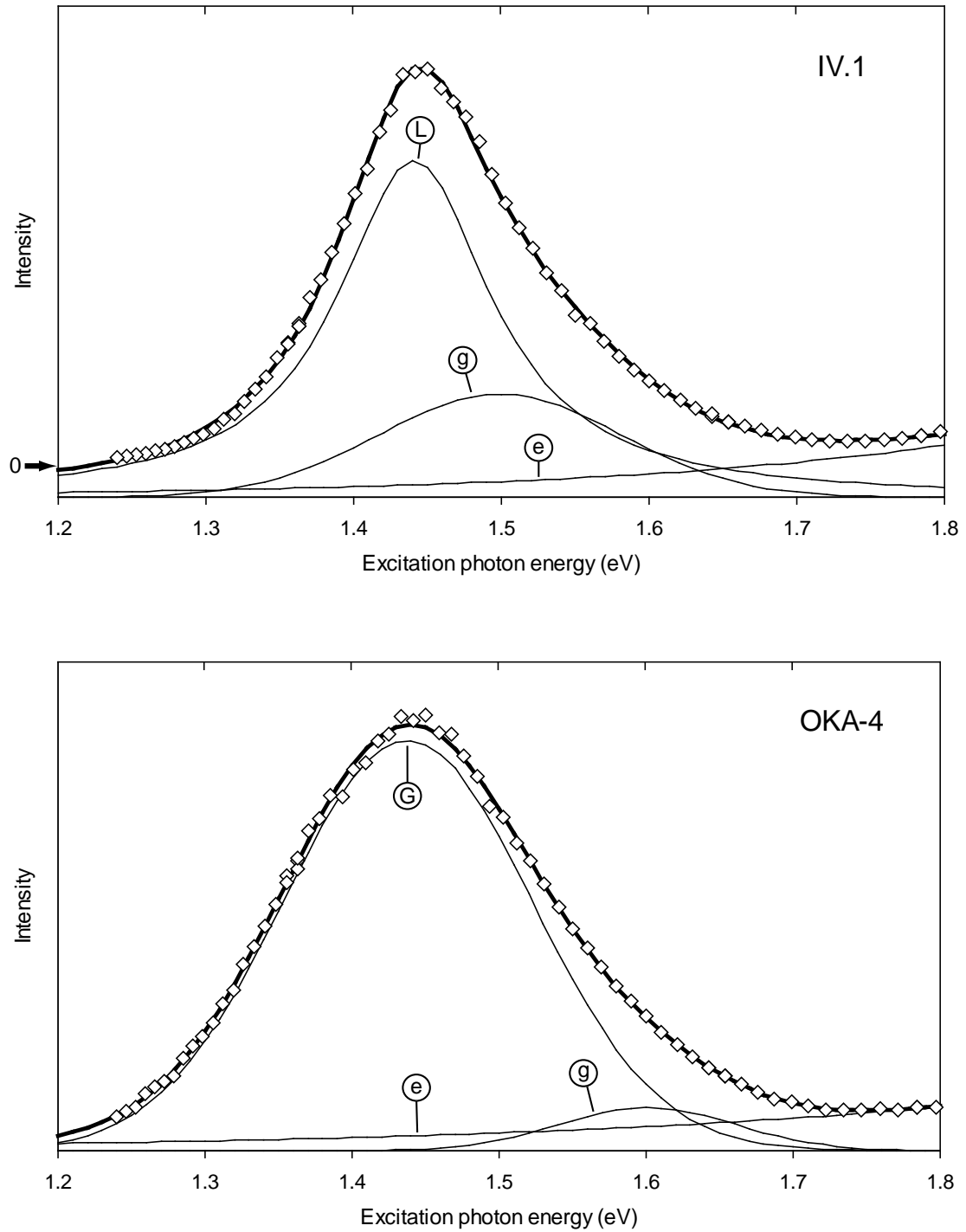
5.5 Discussion

5.5.1 Preliminary fits to the excitation spectra

Three fits were attempted on the excitation spectra using a Lorentzian, Gaussian and Voigt profile to model the excitation resonance near 1.44 eV. In all three fits, an additional minor Gaussian peak near 1.5 eV was necessary to adequately describe the data. In the "pure" Lorentzian and Gaussian fits the addition of a negative constant was often required to obtain a reasonable fit. An additive exponential term was included to describe the increase in luminescence at high excitation energy. These choices of fitting functions are clarified in Section 5.5.2 where the fits to the Voigt profile are discussed.

Fitting was performed using an implementation of the Levenberg-Marquardt algorithm (*e.g.* see Press *et al.*, 1992; p.393). Although the Lorentzian line-shape provided a slightly better fit than the Gaussian in many cases, the Gaussian provided a much better fit for a few samples (A3, A2, A6, K7) and often obviated the need for the negative constant B. The fitting parameters for the Lorentzian and Gaussian fits are compared in Tables 5.1–5.2. The χ^2 for the Gaussian, Lorentzian and Voigt profile fits are compared in Table 5.3. The model function for the luminescence intensity I as a function of excitation photon energy ε in the Lorentzian fit is,

$$I(\varepsilon) = \frac{A_0 \frac{1}{4} \Delta\varepsilon_0^2}{(\varepsilon - \varepsilon_0)^2 + \frac{1}{4}\Delta\varepsilon_0^2} + A_1 \exp\left(-\left[\frac{\varepsilon - \varepsilon_1}{\Delta\varepsilon_1}\right]^2\right) + A_2\, e^{+S\varepsilon} + B \tag{5.1}$$

whereas for the Gaussian fit the following was used,

$$I(\varepsilon) = A_0 \exp\left(-\left[\frac{\varepsilon - \varepsilon_0}{\Delta\varepsilon_0}\right]^2\right) + A_1 \exp\left(-\left[\frac{\varepsilon - \varepsilon_1}{\Delta\varepsilon_1}\right]^2\right) + A_2\, e^{+S\varepsilon} + B \tag{5.2}$$

where $\{A_0, \varepsilon_0, \Delta\varepsilon_0\}$ and $\{A_1, \varepsilon_1, \Delta\varepsilon_1\}$ are the intensities, positions and widths of the main and secondary peaks, respectively. The additive constant B is always negative.

A number of general observations can be made regarding the excitation response spectra. Firstly, the excitation resonance maximum occurs near 1.45 eV in most samples, irrespective of nominal composition (see Table 5.3). Of the 20 samples measured, 8 samples have a resonance centered at an energy that differs by more than 0.01 eV from the average value of 1.445 ± 0.012 eV.

Table 5.1: *Fitting parameters for a fit of the excitation spectra to the model function Equation 5.1 (violet emission band). Values in bold typeface are for the fit to a Lorentzian and Gaussian, values in regular typeface represent the fit to two Gaussians. A_2' is the intensity of the exponential term at ε_0, $A_2' = A_2 e^{+S\varepsilon_0}$. Continued in Table 5.2.*

Sample	Main peak ε_0 (eV)	$\Delta\varepsilon_0$ (eV)	Minor peak A_1/A_0	ε_1 (eV)	$\Delta\varepsilon_1$ (eV)	Exponential A_2'/A_0	S (eV^{-1})	B/A_0
A1	**1.439**	**0.130**	**0.014**	**1.48**	**0.16**	**0.026**	**6**	**-0.25**
	1.439	0.126	0.086	1.62	0.079	0.003	10.8	–
A2	**1.449**	**0.121**	**0.012**	**1.30**	**0.039**	**0.012**	**8**	**-0.20**
	1.447	0.162	0.39	1.45	0.069	0.082	6	-0.29
A3	**1.431**	**0.121**	**0.054**	**1.57**	**0.058**	**0.061**	**3.7**	**-0.27**
	1.433	0.119	0.11	1.59	0.064	0.14	1	-0.11
A4	**1.438**	**0.0816**	**0.39**	**1.50**	**0.14**	**0.12**	**3**	**-0.20**
	1.438	0.0921	0.52	1.52	0.15	0.018	6.1	–
A5	**1.439**	**0.0757**	**0.032**	**1.50**	**0.12**	**0.043**	**4**	**-0.12**
	1.467	0.139	0.74	1.44	0.065	0.063	4	-0.064
A6	**1.433**	**0.105**	**0.25**	**1.52**	**0.12**	**0.027**	**6**	**-0.19**
	1.448	0.116	0.12	1.60	0.064	0.044	3	–
K3	**1.442**	**0.0642**	**0.36**	**1.52**	**0.13**	**0.22**	**2**	**-0.24**
	1.442	0.0715	0.78	1.50	0.15	0.16	3	-0.11
K7	**1.440**	**0.0961**	**0.087**	**1.58**	**0.10**	**0.33**	**0.8**	**-0.38**
	1.435	0.0889	0.65	1.49	0.17	0.15	0.8	–
K8	**1.444**	**0.0741**	**0.37**	**1.53**	**0.14**	**0.076**	**4**	**-0.14**
	1.445	0.0730	1.0	1.495	0.157	0.16	3	-0.12
K9	**1.440**	**0.0899**	**0.40**	**1.43**	**0.18**	**0.002**	**12**	**0**
	1.433	0.188	0.64	1.44	0.075	0.011	10	–

Table 5.2: *Fitting parameters for a fit of the excitation spectra to the model function Equation 5.2 (violet emission band). Continued from Table 5.1.*

| Sample | Main peak | | Minor peak | | | Exponential | | |
| | ε_0 | $\Delta\varepsilon_0$ | A_1/A_0 | ε_1 | $\Delta\varepsilon_1$ | A_2'/A_0 | S | B/A_0 |
	(eV)	(eV)		(eV)	(eV)		(eV^{-1})	
K10	**1.439**	**0.0693**	**0.37**	**1.48**	**0.12**	**0.014**	**7**	**-0.096**
	1.460	0.131	0.73	1.44	0.061	0.028	6	-0.041
K11	**1.448**	**0.0704**	**0.61**	**1.55**	**0.14**	**0.20**	**3**	**-0.20**
	1.533	0.166	0.85	1.45	0.075	0.24	3	-0.14
P9	**1.411**	**0.106**	**–**	**–**	**–**	**0.022**	**8**	**–**
	1.405	0.132	–	–	–	0.12	4	–
P10	**1.420**	**0.119**	**0.13**	**1.48**	**0.13**	**0.053**	**5**	**-0.21**
	1.436	0.117	0.075	1.60	0.055	0.11	2	–
P11	**1.442**	**0.067**	**0.49**	**1.53**	**0.13**	**0.18**	**3**	**-0.18**
	1.453	0.0894	0.29	1.59	0.087	0.22	2	–
P12	**1.441**	**0.0721**	**–**	**–**	**–**	**0.27**	**3**	**–**
	1.442	0.0866	–	–	–	0.47	2	–
AKHC	**1.443**	**0.068**	**0.29**	**1.50**	**0.12**	**0.062**	**3**	**-0.11**
	1.442	0.0698	0.82	1.48	0.14	0.052	3	–
EIDS	**1.448**	**0.0755**	**0.36**	**1.53**	**0.14**	**0.065**	**4**	**-0.12**
	1.448	0.0795	0.84	1.51	0.159	0.005	6	–
IV.1	**1.441**	**0.0637**	**0.31**	**1.50**	**0.115**	**0.037**	**4**	**-0.089**
	1.442	0.0668	0.821	1.48	0.135	0.017	6	–
OKA	**1.440**	**0.133**	**–**	**–**	**–**	**0.057**	**4**	**-0.28**
	1.438	0.120	0.105	1.60	0.085	0.036	3	–

Table 5.3: *Comparison of the χ^2 obtained from fits to the three different model functions. ε_{max} is the energy of the peak response obtained from the fits (does not vary appreciably with the fitting function). Γ is the full-width at half-maximum measured directly from the excitation spectrum.*

Sample	χ^2			ε_{max}	Γ
	Lorentzian	*Gaussian*	*Voigt*	*(eV)*	*(eV)*
A1	0.24	0.23	0.20	1.440	0.21
A2	0.21	0.15	0.78	1.448	0.20
A3	63	98	140	1.434	0.20
A4	0.65	0.17	0.22	1.450	0.180
A5	4.9	4.1	9.6	1.446	0.16
A6	79	110	110	1.450	0.21
K3	0.42	0.14	0.25	1.451	0.16
K7	2.6	7.7	5.5	1.444	0.19
K8	51	27	82	1.454	0.18
K9	24	25	33	1.440	0.22
K10	40	42	92	1.444	0.15
K11	1.1	0.48	1.05	1.466	0.23
P9	8.1×10^{-3}	9.6×10^{-3}	7.9×10^{-3}	1.408	0.23
P10	5.7×10^{-2}	5.5×10^{-2}	5.2×10^{-2}	1.430	0.22
P11	6.5×10^{-2}	2.8×10^{-2}	3.1×10^{-2}	1.458	0.19
P12	1.1×10^{-2}	9.5×10^{-3}	1.1×10^{-2}	1.446	0.34
AKHC	3.2×10^{-2}	2.4×10^{-2}	3.6×10^{-2}	1.448	0.15
EIDS	6.6×10^{-3}	4.4×10^{-3}	6.5×10^{-3}	1.458	0.18
IV.1	0.19	0.095	0.11	1.448	0.14
OKA-4	1.4×10^{-2}	6.5×10^{-3}	9.2×10^{-3}	1.440	0.22

In many samples the resonance appears to have a significant Lorentzian character with varying amounts of asymmetric broadening. The asymmetry of the broadening is placed in evidence by the position of the Gaussian peak, which is generally at a higher energy.

Neither model function was found to provide a good fit for all of the samples. In the fits using two Gaussians, the "secondary" peak contributes a significant fraction of the intensity in the main peak (notably in albite A2), and is almost centered on the resonance maximum. This is interpreted as a bad fit in the sense that the two Gaussians combine in an attempt to reproduce what is essentially a single Lorentzian (or other) profile.

In almost all of the fits using a Lorentzian for the main peak, a significant background had to be subtracted to obtain a good fit. The intensity of the optimal negative background (parameter B in Equations 5.1 and 5.2) varied widely between samples, but often exceeded 10% of the main peak intensity (38% in K7). The value of B in the Gaussian fits was much less, principally because of the much faster descent of the Gaussian relative to the Lorentzian in the wings of the peak. In most cases a Gaussian provided a better fit for the peak wings, whereas the Lorentzian was required to describe points in the vicinity of the peak centre[4]. For this reason, the resonance is probably better described by the Voigt profile, which is effectively a convolution of Gaussian and Lorentzian distributions, as is shown in Section 5.5.2.

The excitation response for the yellow-green emission is not significantly different from that for the violet emission. Although the response for the full 1.2–1.8 eV excitation band was measured in only one sample (A2) for the 2.2 eV emission, one notices that in a few samples (in particular A5 and K10) the resonance appears to be somewhat broader than that seen in the violet emission. In some samples (*e.g.* K7 and K8) the response peak for the yellow-green emission is shifted slightly from that observed for the violet emission. It is interesting to note that in samples A2 and K3 (the only samples for which complete excitation spectra for two emission bands were measured) the excitation spectra for the violet and yellow green bands in A2, and the violet and UV bands in K3 are in excellent agreement.

These results differ significantly from those of Godfrey-Smith and Cada (1996), in that a much more idealized absorption line-shape is obtained in the present case. In addition, Godfrey-Smith and Cada report a resonance maximum at 1.46–1.48 eV whereas in the

---

[4]Note that the Lorentzian distribution has a much sharper peak and broader wings than the Gaussian.

present study it is closer to 1.45 eV. The excitation response spectra published by Bøtter-Jensen *et al.* (1994) are measured over a greater energy range than ours and indicate an additional excitation resonance at 2.1 eV in plagioclases. The shape of the long wavelength wing of the 1.44 eV resonance in Bøtter-Jensen's data is highly dependent on feldspar composition; this contrasts sharply with the present results which indicate a minimal dependence on the variety of feldspar measured. Our excitation spectra are generally consistent with those of Barnett and Bailiff (1997); however, the Lorentzian character is not evident in their results, probably due to the lack of points on the low energy wing of the resonance. In addition, the decrease at higher energies is more dramatic than in our data, and Barnett and Bailiff obtain satisfactory fits using a simple sum of two Gaussians, whereas this is rarely the case for the present spectra.

It is worth noting that the potentially important effect of the optical absorption of the samples has not been taken into account in this experiment. The absorption varies relatively smoothly over the excitation band 1.2–1.8 eV, but is highly sample dependent (Hofmeister and Rossmann, 1984). The problem of correcting for the absorption is complicated because it depends on the depth of the excited luminescence in the sample chip or grains. Since our samples are rarely of uniform optical quality, application of a correction for absorption is not practicable.

5.5.2 Interpretation of the line shape

The most fundamental spectral width of a radiative transition is due to the uncertainty in the energy of the initial and final states. The spectral intensity is written,

$$I(\varepsilon) \propto \frac{(\frac{\hbar\gamma}{2})^2}{(\varepsilon - \varepsilon_0 - \Delta)^2 + (\frac{\hbar\gamma}{2})^2} \tag{5.3}$$

which is the familiar Lorentzian absorption/emission line shape. The transition rate is peaked at the photon energy ε equal to the energy difference ε_0, between the electronic excited and ground states, shifted by a small energy Δ. The energy shift Δ is known as the second order perturbation energy shift (effectively the Lamb shift); it is small and usually neglected. The line width (full-width at half maximum, or FWHM) is given by $\Delta\varepsilon = \hbar\gamma/2$, where γ is the decay rate from the excited state (*i.e.* the inverse of the mean life τ of the

excited state, $\gamma = 1/\tau$). It is assumed here that the lifetime of the ground state is much longer than that of the excited state.

In the case above, the width of the emission line arises from the inherent uncertainty in the energy difference of the initial and final states caused by the uncertainty in the lifetime of the excited state. However, a Lorentzian line-shape can arise from any number of time-dependent perturbations so that in practice the line-width $\Delta\varepsilon_L$ consists of the sum of the contributions from various sources (Di Bartolo, 1968). In the case of a crystal, the "intrinsic" line width discussed above is usually overshadowed by other effects producing Lorentzian profiles. The most common such effect is the Raman scattering of phonons at the radiating (or absorbing) center; that is, the absorption of a phonon and the emission of another phonon by the radiating "ion". In this case, the time over which the perturbation evolves (*i.e.* the period of a lattice vibration) is much longer than the transition time so that the perturbation of the energy levels is effectively constant over the transition interval.

Gaussian line shapes generally arise from completely different processes. The profile may be thought of as arising from the superposition of a large number of spectral lines, with each line representing the energy level of a particular group of radiation centers. For example, in a crystal the levels of a particular emitting/absorbing ion will vary throughout the lattice due to local variations in the crystal field caused by the presence of defects. If the defects are spatially random then the spectral line will consist of the superposition of numerous lines at different energies. It is reasonable to expect that numerous types of defects are present in the crystal, furthermore, the density and distance of these defects from the emitting/absorbing center is also likely to vary greatly. In such a case, the distribution of energy levels for the center depends on the sum of a large number of independent random variables so that the resulting energy distribution is Gaussian[5].

Typically, the observed line-shape is a convolution of Lorentzian and Gaussian probability distributions called the Voigt profile (DiBartolo and Powell, 1976),

$$f_v(\varepsilon) = \frac{2\,ln\,2}{\pi\sqrt{\pi}} \frac{\Delta\varepsilon_L}{\Delta\varepsilon_G^2} \int_{-\infty}^{+\infty} \frac{e^{-\xi^2}}{a^2 + (b-\xi)^2} d\xi \tag{5.4}$$

$$a = \frac{\Delta\varepsilon_L}{\Delta\varepsilon_G}\sqrt{ln\,2}, \quad b = \frac{2(\varepsilon - \varepsilon_0)\sqrt{ln\,2}}{\Delta\varepsilon_G}$$

---

[5]This result is due to the central limit theorem.

where $\Delta\varepsilon_G$ and $\Delta\varepsilon_L$ are the Gaussian and Lorentzian line-widths respectively and ε_0 is the centre frequency. In the limit $\Delta\varepsilon_G \to 0$, the Lorentzian line-shape is obtained,

$$f_v(\varepsilon) = \frac{\frac{1}{2\pi}\Delta\varepsilon_L}{(\varepsilon - \varepsilon_0)^2 + \left(\frac{1}{2}\Delta\varepsilon_L\right)^2} \tag{5.5}$$

whereas the Gaussian line-shape is recovered when $\Delta\varepsilon_L \to 0$;

$$f_v(\varepsilon) = \frac{2\sqrt{\ln 2}}{\Delta\varepsilon_G} \exp\left\{-\left[\frac{2\sqrt{\ln 2}\,(\varepsilon - \varepsilon_0)}{\Delta\varepsilon_G}\right]^2\right\} \tag{5.6}$$

The line-width of the excitation resonance at 1.44 eV is $\Gamma \simeq 0.1$ eV. Assuming that the Lorentzian broadening arises from the uncertainty in the initial and final energies of the transition, this would indicate a lifetime for the excited state of $\sim 5.8 \times 10^{-16}$ s, which is significantly shorter than the period of the exciting electro-magnetic wave (2.9×10^{-15} s at 1.44 eV). However, other effects dominate the Lorentzian broadening of the absorption profile of optical transitions in solids. As mentioned earlier, the predominant perturbation at high temperatures arises from the Raman scattering of phonons. Since phonons are involved, this interaction has a strong dependence on temperature. The width $\Delta\varepsilon_L$ contributed by this process is (Di Bartolo and Powell, 1976),

$$\Delta\varepsilon_L = \overline{\alpha}\left(\frac{T}{\Theta_D}\right)^7 \int_0^{\frac{T}{\Theta_D}} \frac{\xi^6 e^\xi}{(e^\xi - 1)^2} d\xi \tag{5.7}$$

where Θ_D is the Debye temperature and $\overline{\alpha}$ is a constant that depends on the phonon scattering cross-section. The variation of $\Delta\varepsilon/\overline{\alpha}$ with T/Θ_D is shown in Figure 5.13. From this one expects that the line-width of the Lorentzian component of the excitation spectrum should increase as the sample is heated; this issue is approached in Section 5.6.

The previous analysis of the excitation spectrum has been in terms analogous to regular absorption and emission lines in a crystal. This is not entirely correct depending on the details of the charge-eviction mechanism. The total recombination rate is proportional to the product of the probabilities for each process along the route, from the trap to the recombination centre. In our analysis we have arbitrarily fit our excitation spectra to sums of functions, however this only applies to the case where multiple and independent traps or eviction processes are involved so that the individual recombination rates combine additively.

Figure 5.13: *The variation of $\Delta\varepsilon/\overline{\alpha}$ as a function of T/Θ_D.*
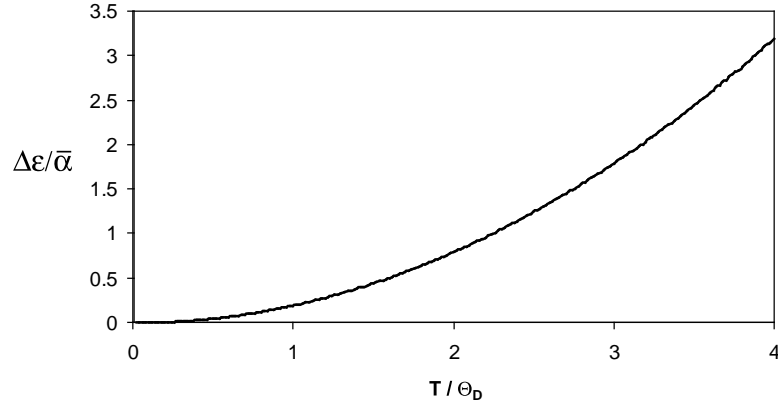
For example we might consider a model involving a single trap with a single meta-stable excited level. We will assume for simplicity that at room temperature the transition-rate from the trap level to the excited level as a function of excitation energy is described by a Voigt profile. It will also be assumed that the transition rate for direct excitation *out of the meta-stable level* into the conduction band increases exponentially with excitation photon energy, ε according to Urbach's rule (Kurik, 1971). In this case the recombination luminescence intensity follows,

$$I(\varepsilon) \, \propto \, f_v(\varepsilon, \varepsilon_0, \Delta\varepsilon_{0(L)}, \Delta\varepsilon_{0(G)}) \, e^{-\sigma(\varepsilon_1 - \varepsilon)/kT} \tag{5.8}$$

with $f_v(\varepsilon, \varepsilon_0, \Delta\varepsilon_{0(L)}, \Delta\varepsilon_{0(G)})$ being the Voigt function (Equation 5.4) centered on ε_0, ε_1 is a characteristic energy, and $\Delta\varepsilon_{0(L)}$, $\Delta\varepsilon_{0(G)}$ are parameters describing the contribution of the Lorentzian and Gaussian components to the line-width. In true Urbach absorption, σ has a temperature dependence approximated by,

$$\sigma \, = \, \sigma_0 \, \frac{2k_b T}{\varepsilon_p} \, \tanh \frac{\varepsilon_p}{2k_b T} \tag{5.9}$$

where ε_p is a characteristic energy that may in some cases be related to the energy of the phonons responsible for the formation of the absorption tail (Kurik, 1971). However, as was discussed in the introduction, a model in which the excitation-recombination route involves multiple photon interactions (*e.g.* see Figure 1.9) is considered unlikely.

At fixed temperature, the model function for the luminescence response must therefore only contain additive photon-energy dependent terms. The following model function is proposed,

$$I(\varepsilon) \; \propto \; A_0 \, f_v(\varepsilon, \varepsilon_0, \Delta\varepsilon_{0(L)}, \Delta\varepsilon_{0(G)}) \; + \; A_1 \, \exp\left(-4\ln 2 \left[\frac{\varepsilon - \varepsilon_1}{\Delta\varepsilon_1}\right]^2\right) \; + \; A_2 \, e^{+S\varepsilon} \quad (5.10)$$

where A_i are the relative contributions from each term, $\Delta\varepsilon_1$, ε_1 are the FWHM and position of the secondary resonance and $S = \sigma(T)/kT$ (if Urbach absorption is applicable). The secondary resonance is required to obtain satisfactory agreement with the data. A Gaussian line-shape was selected for simplicity, but in general it should be described by a Voigt distribution.

This last model function describes the excitation response for the samples almost as well as the *ad hoc* sum of Gaussian and Lorentzian lines with linear background described earlier[6]. The fitting parameters are given in Table 5.4. The dominance of the Gaussian component suggests that either the Debye temperature is significantly higher than room temperature and/or that the effect of lattice defects dominates (assuming that the interpretation in terms broadening by Raman phonon scattering is correct). It would be instructive to see whether the line-shape correlates with the obliquity of the samples, which is a measure of the ordering of Si-Al atoms in the lattice. "Sanidinized" microcline, that is, microcline that has been heated so that its structural phase (partial Si-Al order) changes to sanidine (no Si-Al order) would be useful for this purpose. It is clear however, at least from our data, that no generalizations can be made as to the relative contributions of the Gaussian and Lorentzian components to the excitation resonance for samples of a given nominal composition.

When the Voigt profile is used the Lorentzian component of the line-shape is generally found to be the minor contributor. If a negative background is included, then the Lorentzian character of the line-shape is enhanced at the detriment of the Gaussian component. Fits using Equation 5.10 with a negative background were not significantly better than the fits using the pure Gaussian and Lorentzian line-shapes (data for these fits are not shown). This reflects on the fact that the data are not good enough to allow a valid comparison of models containing over nine free parameters.

---

[6]Note that there are 9 free parameters in both fitting functions.

Table 5.4: *Fitting parameters for the excitation energy response spectra (violet emission band). Parameter symbols are defined in the fitting function, Equation 5.10. The resonance maximum and the effective FWHM are given in Table 5.3. The line-widths have been scaled to be commensurate with those for the pure Gaussian and Lorentzian fits. Numbers in parentheses indicate the uncertainty in the last digit. A_2' is the intensity of the exponential term at ε_0, $A_2' = A_2 e^{+S\varepsilon_0}$. Uncertainties represent the variation required to increase χ^2 by a factor of 2.*

Sample	Voigt component			Gaussian component			Exponential term	
	ε_0	$\frac{1}{2}\Delta\varepsilon_{0(L)}$	$\frac{\Delta\varepsilon_{0(G)}}{2\sqrt{\ln 2}}$	A_1/A_0	ε_1	$\Delta\varepsilon_{G1}$	A_2'/A_0	S
	(eV)	(eV)	(eV)		(eV)	(eV)		(eV^{-1})
A1	1.437(3)	0.025(7)	0.103(2)	0.10(2)	1.60(2)	0.09(2)	$2(1)\cdot 10^{-4}$	18(1)
A2	1.445(4)	0.033(5)	0.097(4)	0.08(3)	1.56(4)	0.14(6)	$5(4)\cdot 10^{-5}$	22(2)
A3	1.432(2)	0.010(3)	0.110(2)	0.13(3)	1.58(1)	0.07(1)	0.011(3)	5.8(7)
A4	1.445(3)	0.006(3)	0.095(3)	0.20(3)	1.59(1)	0.09(2)	0.019(3)	6.2(6)
A5	1.441(4)	0.020(4)	0.078(4)	0.22(4)	1.55(1)	0.10(2)	0.007(3)	7(1)
A6	1.445(2)	0.016(3)	0.104(3)	0.15(3)	1.59(1)	0.08(1)	0.010(2)	7.2(7)
K3	1.443(4)	0.002(4)	0.082(4)	0.47(4)	1.54(1)	0.14(1)	0.041(8)	5.3(7)
K7	1.443(2)	0.052(3)	0.069(4)	0.13(2)	1.60(1)	0.08(2)	0.021(4)	5.2(6)
K8	1.443(4)	0.014(4)	0.081(4)	0.40(4)	1.56(1)	0.12(1)	0.023(5)	6.5(7)
K9	1.439(2)	0.099(3)	0.026(8)	–	–	–	$3(1)\cdot 10^{-5}$	23(1)
K10	1.446(3)	0.016(3)	0.082(3)	0.12(3)	1.58(2)	0.06(2)	0.005(2)	8(1)
K11	1.448(6)	0.001(4)	0.088(5)	0.71(5)	1.57(1)	0.14(1)	0.08(1)	4.7(6)
P9	1.41(1)	0.10(1)	0.03(1)	–	–	–	0.023(9)	8(1)
P10	1.428(4)	0.028(5)	0.103(4)	0.07(4)	1.59(3)	0.06(4)	0.033(5)	5.2(5)
P11	1.453(3)	0.009(3)	0.087(3)	0.32(4)	1.60(1)	0.10(1)	0.034(5)	6.6(6)
P12	1.44(3)	0.087(5)	0.0(1)	–	–	–	0.09(4)	4(2)
AKHC	1.445(3)	0.023(3)	0.071(3)	0.20(3)	1.56(1)	0.09(2)	0.016(4)	5.0(9)
EIDS	1.448(3)	0.023(3)	0.077(3)	0.35(3)	1.57(1)	0.13(1)	0.004(1)	10.9(8)
IV.1	1.443(3)	0.019(2)	0.070(2)	0.20(3)	1.55(1)	0.10(1)	0.007(2)	6.8(9)
OKA-4	1.441(2)	0.012(2)	0.117(2)	0.09(2)	1.62(2)	0.08(2)	0.005(1)	8.5(7)

5.5.3 The negative background

Keeping in mind the last cautionary comment, one will note from comparison of the χ^2 for the various fits (Table 5.3) that in all instances either one of the fits using the pure Lorentzian or Gaussian with a negative constant background provide a better fit than the Voigt profile with no background. Although the improvement in the quality of the fit is modest in many cases, one cannot immediately discount the fits using a negative background term as being unphysical[7]. In particular, the improvement afforded by including the negative background generally occurs in the most important part of the curve, that is, points near the resonance maximum. This is due to the enhancement of the Lorentzian character of the line-shape afforded by the inclusion of the negative background.

Assuming that the apparently fixed amount of lost luminescence is real, the following two loss mechanisms are proposed. In the first mechanism a fixed number of the photo-excited electrons ejected from the traps recombine at non-radiative, or "killer" sites in the lattice. If the recombination probability at the non-radiative centers is high, but the total number of centers is low, then the number of electrons trapped at these locations will rapidly saturate so that the lost luminescence will reach a fixed constant value. To complete the picture, one must also surmise that the lifetime of the electrons in the killer sites is longer than the measurement time (in this case 2 seconds) but shorter than the time between measurements (10 to 15 seconds). In this way the killer sites are recovered by the time the second measurement is made.

The second mechanism might be called the "overflowing bucket" model. Suppose that the electrons evicted from the traps proceed to a set of overlapping meta-stable states in the lattice (the bucket). The electrons can hop relatively easily between the sites hosting the meta-stable states, but cannot easily recombine at the luminescence centers. In this case we might expect that the rate of recombination at the luminescence centers will have a strong non-linear dependence on the number of electrons in the meta-stable states. For example, if the dependence of the recombination rate depends exponentially on the occupation number of the meta-stable states then significant luminescence will only occur once the threshold (determined by the exponential constant) is reached; when the bucket spills, so to speak.

---

[7]There is no problem with the experiment that could lead to a fixed lost intensity because all photon-count losses in the experiment are proportional to the intensity of the luminescence.

The extension of excitation spectra to energies below 1.2 eV would be extremely helpful in determining the exact nature of the 1.44 eV resonance. In particular, if the luminescence intensity should vanish below 1.2 eV then this would be strong evidence for one of the non-linear loss mechanisms proposed here.

5.6 Temperature dependence

Excitation response spectra for temperatures between 240 K and 450 K were produced for sample K3. The excitation spectra were fit to the model function of Equation 5.10 and the fitting parameters are shown in Table 5.5. If the exponential factor is properly interpreted as an Urbach absorption edge then the constant $S = \sigma(T)/kT$ should be temperature dependent. The spectra for 290–450 K are shown in Figure 5.14. Despite the fact that the data do

Figure 5.14: *Excitation response spectra for K3 for temperatures 290–450 K. Solid lines are fits to Equation 5.10. Solid and open symbols are used for successive data. Absolute intensity between spectra at different temperatures is only approximate.*
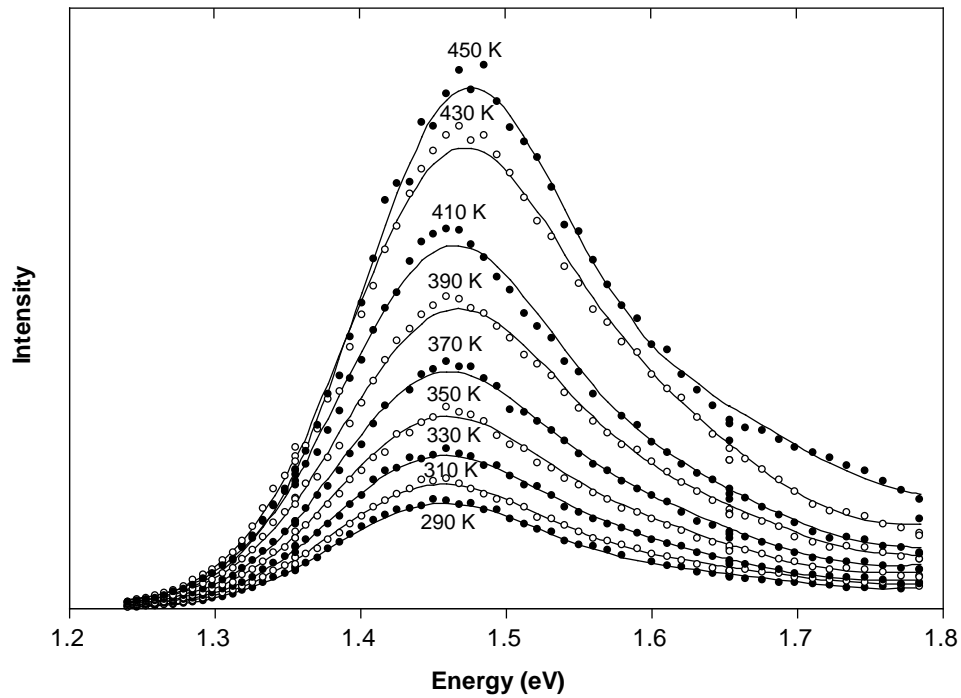
not strictly allow a meaningful determination of the 9 parameters in the fitting function, the fits indicate an almost pure Gaussian line-shape from 240–450 K. This is consistent with the previous room temperature measurement. The position of the resonance maximum ap-

Table 5.5: *Fitting parameters for the excitation energy response spectra of K3 for temperatures T between 240 K to 450 K. Fit is to Equation 5.10. Numbers in parentheses indicate the uncertainty in the last digit. Uncertainties represent the variation required to increase* χ^2 *by a factor of 2.* A_2' *is the intensity of the exponential term at* ε_0, $A_2' = A_2 e^{+S\varepsilon_0}$.

	Voigt component			*Gaussian component*			*Exponential term*	
T	ε_0	$\frac{1}{2}\Delta\varepsilon_{0(L)}$	$\frac{\Delta\varepsilon_{0(G)}}{2\sqrt{\ln 2}}$	A_1/A_0	ε_1	$\Delta\varepsilon_1$	A_2'/A_0	S
(K)	(eV)	(eV)	(eV)		(eV)	(eV)		(eV^{-1})
240	1.460(6)	0.001(1)	0.095(5)	0.22(6)	1.62(2)	0.10(4)	0.019(8)	6(1)
250	1.451(4)	0.004(4)	0.088(5)	0.34(5)	1.60(2)	0.12(2)	9(4)x10^{-4}	15(1)
260	1.454(7)	0.002(1)	0.092(5)	0.44(7)	1.57(2)	0.15(2)	3(2)x10^{-4}	18(2)
270	1.456(5)	0.004(4)	0.091(5)	0.34(5)	1.59(2)	0.14(2)	0.004(2)	11(1)
290	1.448(4)	0.002(2)	0.097(3)	0.40(3)	1.60(1)	0.16(1)	1.9(7)x10^{-5}	19(1)
310	1.447(4)	0.000(1)	0.098(3)	0.36(4)	1.59(1)	0.13(2)	0.022(5)	6.3(7)
330	1.442(4)	0	0.093(4)	0.49(5)	1.56(1)	0.13(1)	0.042(7)	4.8(5)
350	1.446(4)	0.050(3)	0.094(3)	0.44(4)	1.57(1)	0.13(1)	0.016(3)	7.4(6)
370	1.447(4)	0.006(3)	0.093(4)	0.44(4)	1.576(9)	0.13(1)	0.021(4)	6.4(7)
390	1.456(3)	0.005(3)	0.100(4)	0.36(3)	1.60(1)	0.13(1)	0.010(2)	8.1(8)
410	1.454(4)	0.008(4)	0.095(4)	0.36(4)	1.59(2)	0.13(2)	0.014(4)	7.0(9)
430	1.462(6)	0.001(1)	0.102(4)	0.33(5)	1.60(2)	0.11(2)	0.031(5)	5.4(8)
450	1.464(6)	0.004(4)	0.093(5)	0.51(5)	1.59(1)	0.17(1)	0.03(1)	10(1)

pears to shift to higher energy as temperature increases, however the line-width does not vary in a statistically significant manner with temperature. It would be useful to investigate whether samples in which a strong Lorentzian component was observed (*e.g.* K7 or K9) show a similar lack of temperature dependence in the line-width of the 1.44 eV excitation

resonance.

Bailiff and Barnett (1994) produced excitation spectra for a microcline microperthite at 145 K, 160 K and 290 K; the shape of the 1.44 resonance is similar to that seen in our measurements. Fitting their data to a single Gaussian, they found a shift of 0.022±0.003 eV to lower energies and a peak broadening of 0.012±0.005 eV as the temperature increased from 145 K to 290 K. The greatest increase occurred between 145 and 160 K; this might explain why the thermal broadening was insignificant over our temperature range. It should also be noted that Bailiff and Barnett's peak shift is in a direction opposite to that found in the present (high temperature) data. Further studies are required to determine whether the temperature dependence of the broadening is due to Raman phonon scattering.

5.7 Effect of polarization on the excitation response

It has been found by Short and Huntley (2000) that the intensity of the violet IRSL in orthoclase K3 is dependent on the polarization of the excitation light. In addition, K3's violet emission is also polarized. Both observations are consistent with dipole transitions, with a dipole aligned close to the [113] crystal direction in both cases. One question of interest is whether the excitation spectrum is dependent on the polarization of the exciting light; especially in view of the fact that the polarization had not been carefully monitored (although it was kept fixed) in the previous experiments.

Figure 5.15: *The faces of the K7 crystal. Face "F" corresponds to the* (001) *crystallographic plane whereas faces "A" and "B" correspond to the* $(1\bar{1}0)$ *and* (110) *planes respectively.*
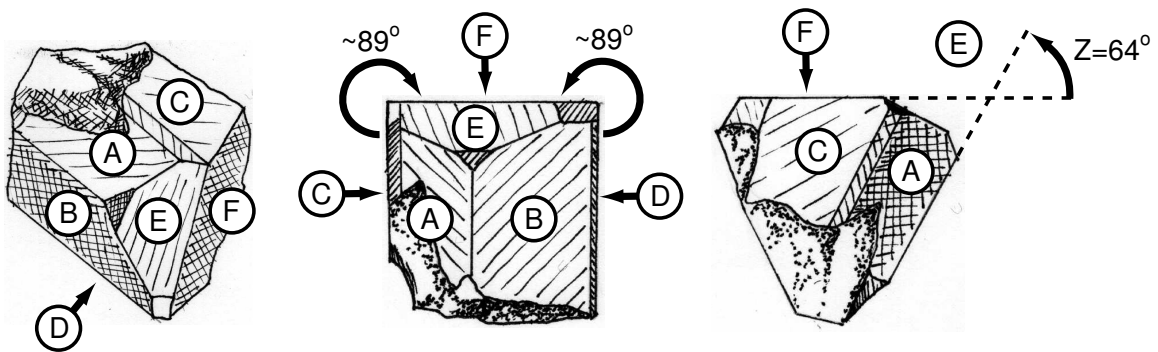
Although a dependence on the excitation polarization was found for many of the rock samples, microcline K7 was convenient for detailed study since its growth habit allowed a simple means by which to determine its orientation. A sketch of the rock from which the K7 chip was cleaved is shown in Figure 5.15.

The K7 microcline crystal exhibits a classic orthoclase habit. Cleavage parallel to face "F" is good which suggests that this face corresponds to the (001) crystallographic plane (Deer *et al.*, 1966). From this choice, it is clear that faces "C" and "D" must correspond to the $(0\bar{1}0)$ and (010) planes (*i.e.* this would give an angle close to 90° for the angle α between $[001]$ and $[010]$, as expected for a near monoclinic feldspar). If faces "A" and "B" correspond to the $(1\bar{1}0)$ and (110) planes respectively, then we expect that the angle Z shown in Figure 5.15 to be equal to the complement of the angle *beta* between the $[001]$ and $[100]$ axes. We find an angle of 64 ± 1° for Z, which is consistent with the expected value of β near 116°. In addition, the angle between faces "A" and "B" is 62°, which is close to the expected value of 60° (Dana, 1962).

Figure 5.16: *Symmetry of the albite and pericline twin laws. Albite twinning consists of a reflection about (010), whereas a π rotation about the b-axis results in pericline twinning. In the case of a nearly monoclinic crystal, the projection of angles onto the b-plane is preserved under both twin operations. This assumes that the angles π and 2π are indistinguishable, as is generally the case in a polarization experiment.*
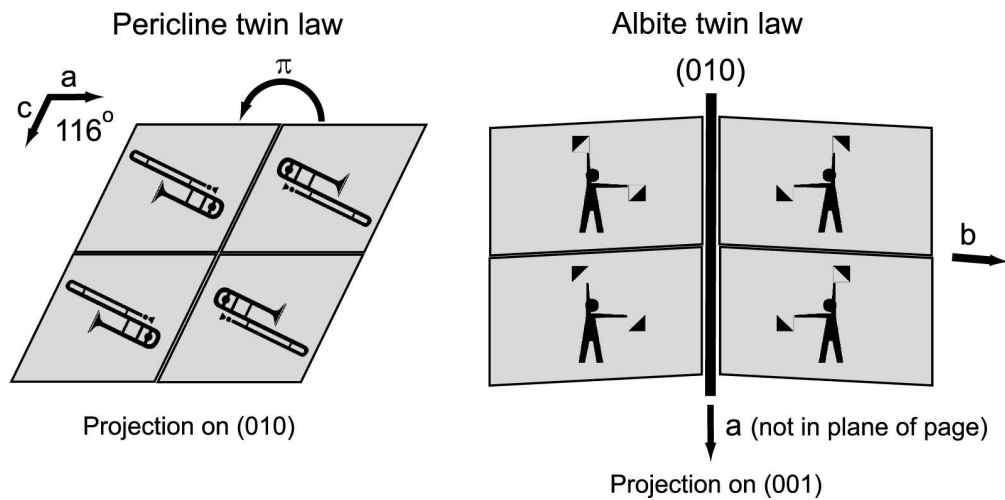
Figure 5.17: *Left: The effect of the polarization of the excitation on the emission intensity in microcline K7. "Chip-C" was cut parallel to (001) and "Chip-B" was cut parallel to (010). The solid lines are fit through the data. The polarization angle is measured with respect to [010] for "Chip-C" and [001] for "Chip-B". Right (top): Geometry of monoclinic feldspar unit cell. Right(bottom): Diagram of the relevant directions for the "Chip-C" and "Chip-B" measurements (note that the directions shown do not necessarily lie in the plane of the page).*
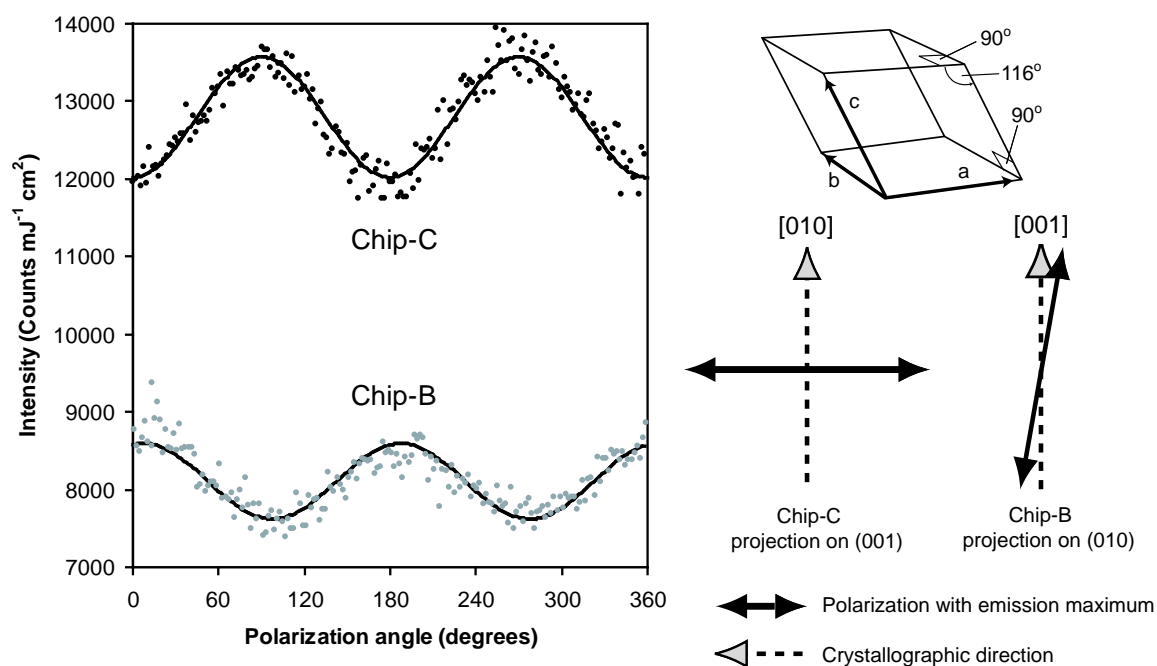
The effect of the polarization angle of the excitation beam on the violet luminescence band intensity of K7 is shown in Figure 5.17. The dependence was measured for two thin crystal slices cut parallel to the (001) (Chip-C) and (010) (Chip-B) planes. For excitation perpendicular to (001) (*i.e.* Chip-B) the maximum emission occurred when the excitation polarization approached the plane containing [100] and [001]. This differs by 10° from Short and Huntley's measurement on orthoclase K3. For excitation perpendicular to (010) (*i.e.* Chip-C) the emission maximum was found at a polarization angle $\sim 10^o$ away from the projection of [001] on the (010) plane; for K3, Short and Huntley found $\sim 0^o$ for this angle.

Figure 5.18: *Effect of the polarization direction of the excitation photons on the excitation spectrum of K7 (violet emission band). The polarization direction producing maximum violet emission is parallel to [010]; the spectrum for this orientation is labeled "0°". All other excitation spectra have been scaled so that the intensities roughly coincide with those of the 0° spectrum. Angles are measured with respect to the the 0° orientation. Excitation spectra from 105° to 180° have been averaged with those from 0° to 75° to simplify display.*
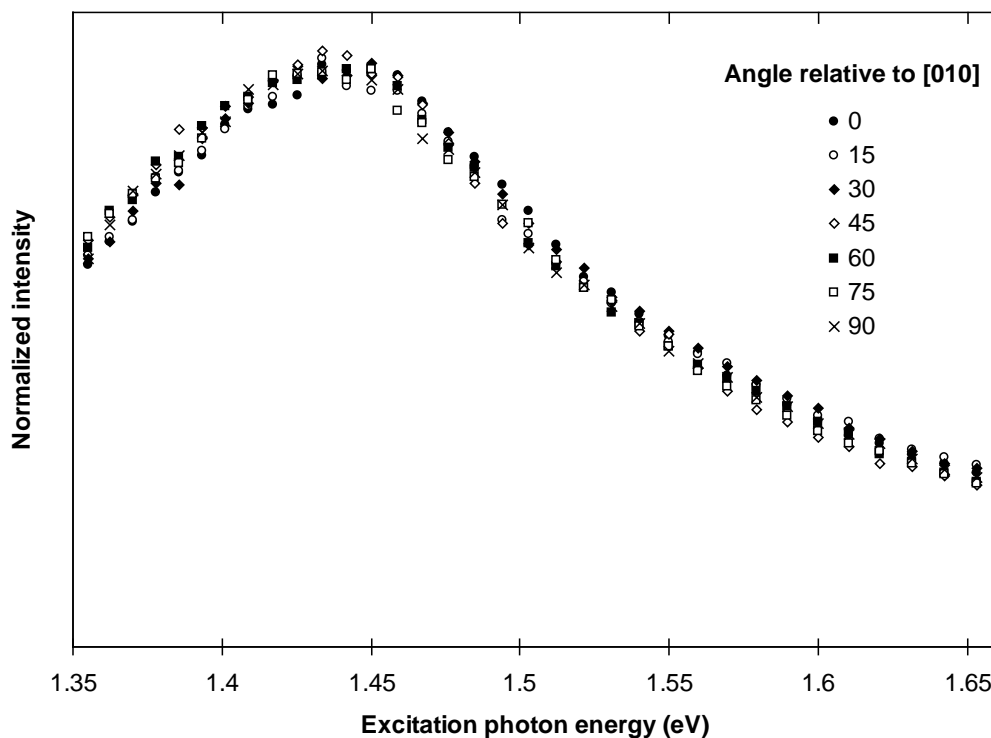
Extensive twinning is present in this crystal as indicated by the typical "tartan" pattern observed under a polarizing microscope. This pattern indicates that both albite twinning (mirror reflection in the (010) plane) and pericline twinning (π rotation about the [010] direction) are present in K7. Referring to Figure 5.16 one will note that under nearly monoclinic symmetry, angles projected onto the b-plane are preserved under both twin operations, but not in the *a* and *c* planes. One might therefore expect that if an equal density of right and left twins of both varieties were present, then if one were to measure a polarization

angle with the excitation incident on (001), one would obtain the average over the twins, specifically,

$$I(\theta) \propto I_0 + \frac{1}{2}\Delta I \cos^2(\theta - \theta_0) + \frac{1}{2}\Delta I \cos^2(\theta + \theta_0) \qquad (5.11)$$

where ΔI is the total variation of the intensity and θ_0 is the polarization angle measured relative to either the b-axis or a direction parallel to the projection of [100]. If the polarization dependence mixes in this way, then the polarization maximum will always be observed parallel to the projection of [100] or [010], whichever is nearest (at 45° the polarization dependence vanishes). This may explain why the maximum emission was found for excitation light polarized parallel to [100] in microcline K7 whereas in orthoclase K3 the maximum is 10° away from the projection of [100]. No twinning is evident in K3, so the mixing described above cannot occur.

The excitation energy response for the violet emission band was measured for an excitation beam perpendicular to (001) (Chip-C) at different polarization orientations (Figure 5.18). The experimental setup was identical to that described earlier in this chapter. No significant change in the shape of the excitation energy response was observed as the excitation polarization was varied, aside from the previously noted uniform change in intensity.

One should note that the connection between the polarization direction and the orientation of the presumed dipoles is nontrivial thanks to the ubiquitous birefringence of feldspars. In general, several assumptions have to be made in finding the relation between the polarization angles and the crystal orientation of the emitting or absorbing dipoles (Short and Huntley, 2000). Some of these assumptions involve knowledge of the optical axes of the crystal; these have not been determined in K7. It suffices to say that polarization measurements on several other feldspars are necessary to see if the effects Short and Huntley observed in K3 are generally applicable to feldspar IRSL.

5.8 Summary

Investigations of the excitation energy response of the luminescence in feldspars indicates very similar behaviour among a wide range of different nominal compositions. In addition, the excitation spectra are not significantly different for either the violet (3.1 eV) or yellow-green (2.2 eV) emission bands, as well as the UV (350 nm) band in sample K3. In all cases,

a maximum in the excitation response appears at 1.44 eV which is most simply described by a Voigt absorption profile. In addition, a secondary weak resonance appears at slightly higher energy ($\sim$1.56–1.6 eV). The relative contribution from the secondary resonance is highly sample dependent.

No significant temperature dependence is apparent in the shape of the excitation response profile of sample K3 within the range 290–450 K. If phonon-phonon Raman scattering is the dominant process broadening the infrared resonance, then this implies a Debye temperature significantly above 300 K in K3.

The effect of the polarization of the excitation on the luminescence in microcline K7 was found to be consistent with observations made previously on orthoclase K3 (Short and Huntley, 2000). The excitation polarization does not appear to affect the shape of the excitation response spectrum in K7. The combination of these facts favours a model in which the traps sampled by OSL measurements consist of a single defect level rather than multiple traps.

Chapter 6

Decay Kinetics

6.1   The effect of the excitation power on the decay kinetics

Since the decay of IRSL followed Becquerel's law in the laboratory dosed samples, an investigation was made as to whether this law also applied to naturally irradiated samples. The luminescence decay was measured using the PMT detection chamber described in Section 5.2 fitted with four Corning 5-58 and one Schott BG-39 filter to select the 3.1 eV emission. The excitation source was provided by an array of OD-50L diodes[1] biased to provide $\sim$30 mW/cm^2 of illumination near 1.41 eV (880 nm).

All of the natural sample luminescence shinedown curves fit the modified power law of Equation 4.2, however a relatively large value for the phenomenological constant t_0 was required when compared to the value of t_0 obtained from the spectral decay curves (Section 4.3). The only significant difference between the two experiments was that a much larger beam power was used in obtaining the spectral decay curves.

The effect of the beam power on the luminescence intensity was investigated for a wide range of excitation powers (using a Ti-Sapphire laser tuned to 1.43 eV) to help clarify these results. The experiment clearly indicated that the data were best interpreted if the total excitation energy E supplied to the sample during measurement was substituted for the

---

[1]Manufactured by Opto Diode Corp., 914 Tourmaline Dr., Newbury Park, CA 91320, USA.

illumination time. In these units our modified Becquerel law reads,

$$I(E) = \frac{I_0}{(1 + \frac{E}{E_0})^\alpha} \tag{6.1}$$

where the supplied energy E is related to the illumination time t by, $E = Pt$, with P being the excitation power. Expressed in these units, the luminescence curves measured at different excitation powers are directly comparable. Specifically, if the luminescence kinetics are independent of the beam power then E_0 and α should not vary between the aliquots of a given sample, assuming that they have all received the same treatment.

A similar but not entirely equivalent empirical relation that was found to provide an equally good fit to our data is the following,

$$I(E) = \frac{I_0}{1 + (\frac{E}{E_0})^\alpha} \tag{6.2}$$

This relation is identical to the conventional Debye-Edwards relation, $I(t) = \frac{I_0}{1+b(t-t_0)^\alpha}$. One will note that the slope dI/dE at $E = 0$ diverges for $\alpha < 1$ and is equal to zero for $\alpha > 1$. Either case is inconsistent with the scaling $dI/dE|(E = 0) \propto I(E = 0)^2$ observed in four of our samples (K3, K8, K9 and K10) which is described in Chapter 7. Although the above relation can provide an adequate fit to the data for small to moderately large E, it cannot describe the data for very short illuminations. For this reason the empirical relation of Equation 6.1 was adopted; this equation is heretofore referred to as the Becquerel law.

It should also be noted that the Becquerel law cannot account for the luminescence at short times, where a fast rise of the luminescence is observed. Nor can this law be correct at long times, for if $\alpha \leq 1$, then the luminescence sum will not converge. The law must therefore be only seen as an empirical one that holds at the intermediate times of usual concern in most measurements.

The shinedown curves for IV.1, DY-23 and RHIS as a function of total beam power[2] are shown in Figure 6.1. The curves were plotted as the $\log(I(E)/I_0)$ versus $-\log(E + E_0)$ to show the agreement with Becquerel's law (Equation 6.1). The best-fit values of E_0 and α for the decay curves at different beam powers are shown in Figure 6.2. Due to the large beam powers used in the experiment, the condition of isothermal decay was not entirely

---

[2]Note that a narrow beam was used in this experiment, so that a 1.6 mW beam power produced a spatially non-uniform irradiance of ~ 20 mW/cm^2 at the sample.

applicable so we did not expect ideal results to be observed. Nevertheless, the natural sample DY-23 provided surprisingly ideal behaviour; E_0 and α being relatively unaffected by the beam power. In RHIS and IV-1, E_0 and α varied considerably with beam power, but not in a consistent fashion.

Noticeable deviations from the form of Equation 6.1 are apparent in the data for this experiment when compared to other measurements on the same sample (*e.g.* see the later data for DY-23). In particular, α, the slope of the decay curve as shown in Figure 6.1, is somewhat greater in the initial part of the decay. Not all the deviation from the Becquerel law can be attributed to heating since strong deviation from the power law is observed even at low beam powers. This is especially evident in RHIS and may be due to the spatial non-uniformity of the excitation beam power.

What should be retained here is the necessity of using integrated illumination energy rather than time when comparing decay curves from different experiments; an almost obvious point when seen in retrospect. This is not necessary in conventional isothermal phosphorescence decay where recombination is achieved by simple thermal excitation of electrons out of their traps.

6.2 The effect of dose on the decay kinetics

The principal question is what do the phenomenological parameters E_0 and α correspond to physically. In order to answer this one must look at the four easily controlled variables that can affect the decay law; radiation dose, the storage time after the radiation dose (under isothermal conditions), temperature and excitation energy. It will be assumed on the basis of the results of Section 6.1 that excitation power plays a negligible role in the decay law under isothermal conditions.

I started by looking at the effect of the dose on the decay law parameters in DY-23, *i.e.* the sample with the nearest "ideal" behaviour under varying excitation power. A number of aliquots of natural DY-23 were bleached down to less than 2% of their initial luminescence intensity under 1.43 eV laser excitation. The natural intensity of the luminescence was used to normalize the relative response of the individual aliquots. Sets of aliquots were given a series of gamma radiation doses ranging from 10 Gy to 1300 Gy. The irradiated aliquots were given a 120 $^\circ$C preheat for 20 hours.

Figure 6.1: *Effect of the excitation power on the luminescence decay of DY-23, IV.1 and RHIS. E is the integrated luminous excitation energy provided to the sample during the decay, E_0 is a constant determined from a fit to Equation 6.1. Note that E_0 varies for each decay curve.*
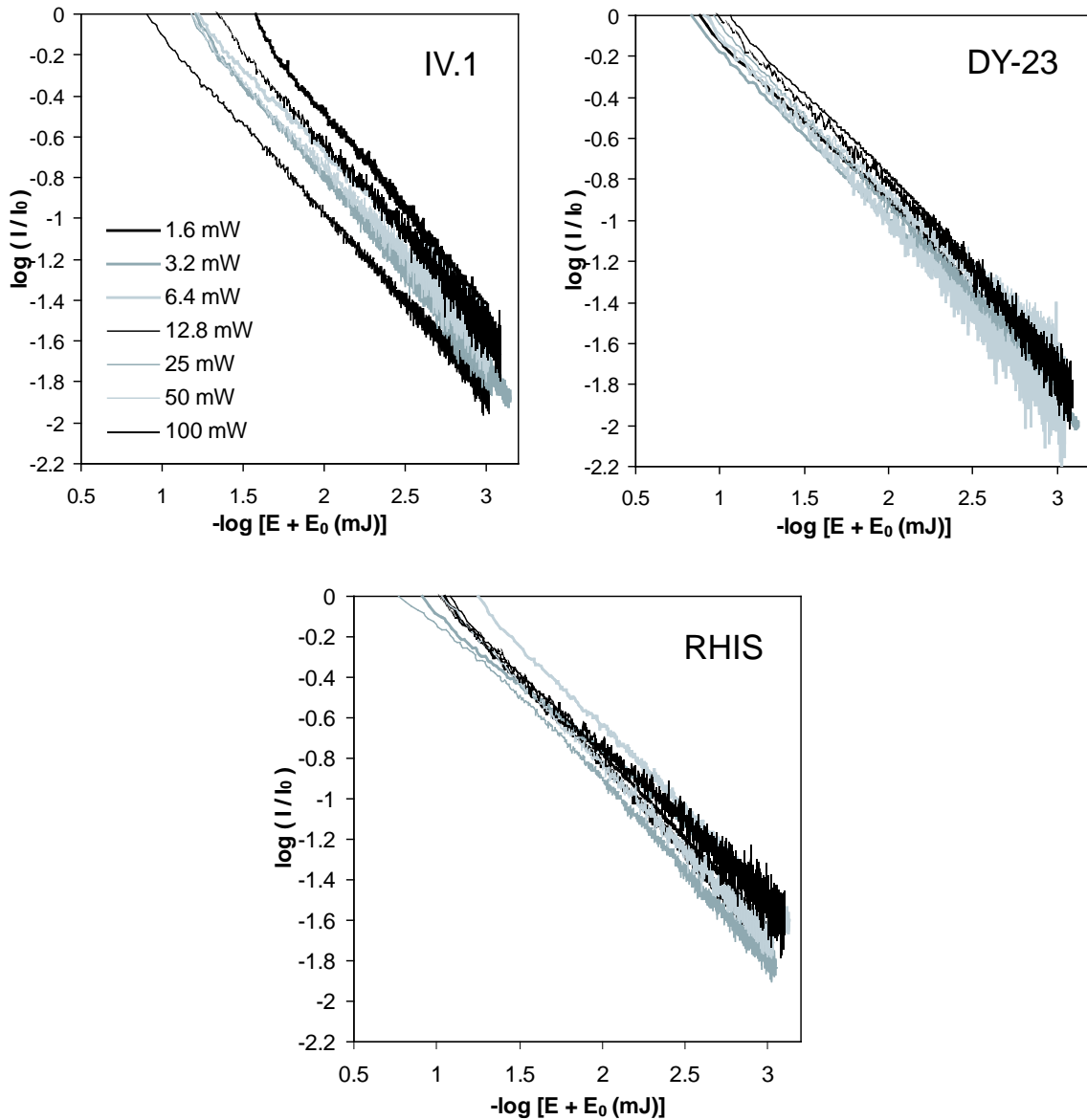
Figure 6.2: *Effect of the excitation power on the decay law of DY-23, IV-1 and RHIS.*
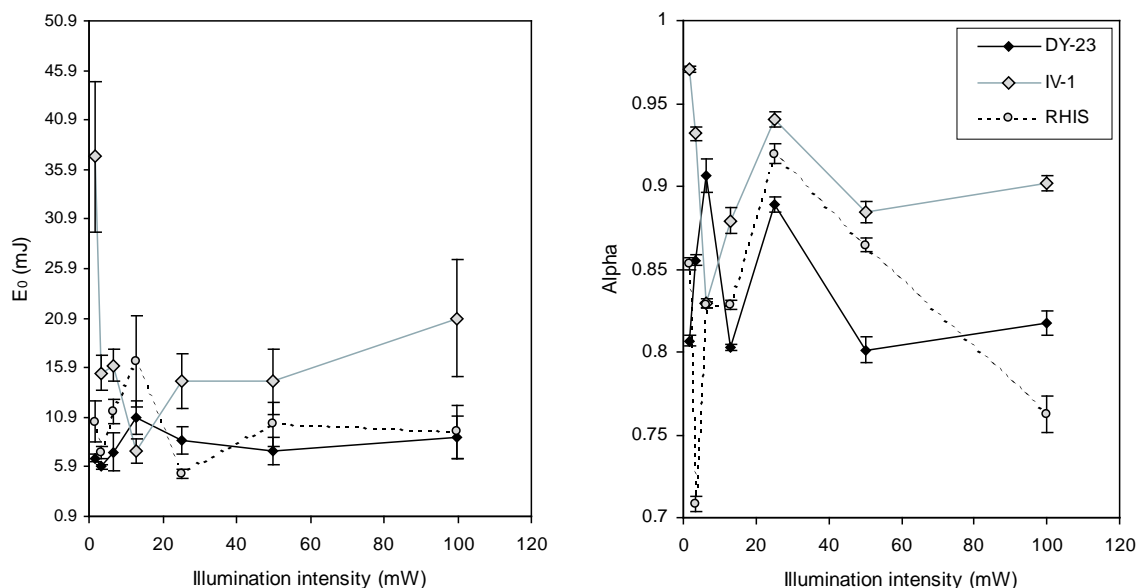
The luminescence decay was measured using a 1.43 eV tuned Ti-Sapphire laser, providing uniform $\sim$12 mW/cm^2 illumination over the sample area. Fits to the Becquerel law were obtained using the full decay curve (down to 2%-15% of the initial luminescence intensity) as well as the initial portion of the curve (down to $\sim$50% of the initial intensity). As noticed in the previous experiment, the initial decay exponent is slightly lower than in the later decay. The effect of the dose on α and E_0 is shown in Figure 6.3 and the luminescence growth curve is shown in Figure 6.5.

The data very clearly indicate a near logarithmic increase of the scaling exponent α up to moderately large radiation doses (Figure 6.4). The exponent in the initial part of the decay appears to "saturate" at a slightly lower dose than that in the late luminescence. For the late luminescence, the total variation over from 10 to 1300 Gy is from $\alpha \sim$0.5 to $\alpha \sim$1.2, with a trend suggesting saturation of α somewhere above 1.2 at very large doses. An earlier experiment in which the same set of doses were applied to natural DY-23 aliquots is consistent with this last observation. In this case all doses resulted in the sample being near saturation and resulted in an average α near 1.2. One will note that the luminescence

Figure 6.3: *Effect of the applied radiation dose on E_0. Solid diamonds indicate values obtained from a fit to the entire decay curve (down to 2–15% of I_0). Open diamonds indicate values obtained from a fit to the initial portion of the decay curve (down to 50% decay).*
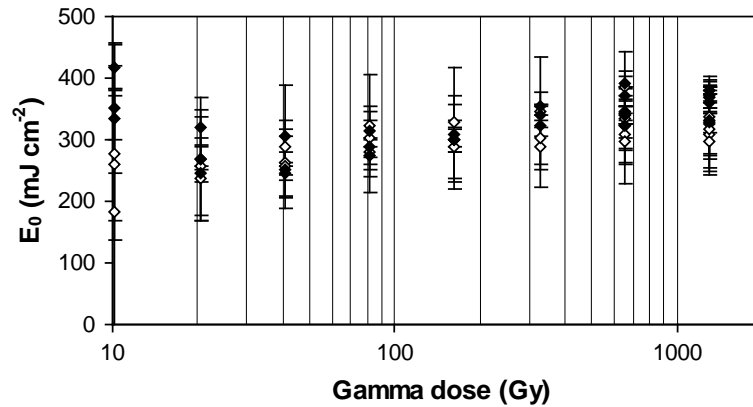
Figure 6.4: *Effect of the applied radiation dose on α. Black diamonds indicate values obtained from a fit to the entire decay curve (down to 2–15% decay). Open diamonds indicate values obtained from a fit to the initial portion of the decay curve (down to 50% decay). The fitting uncertainties (not shown) are much smaller than the scatter. The line through the data is a linear regression fit to α vs. dose (α determined from the entire decay curve).*
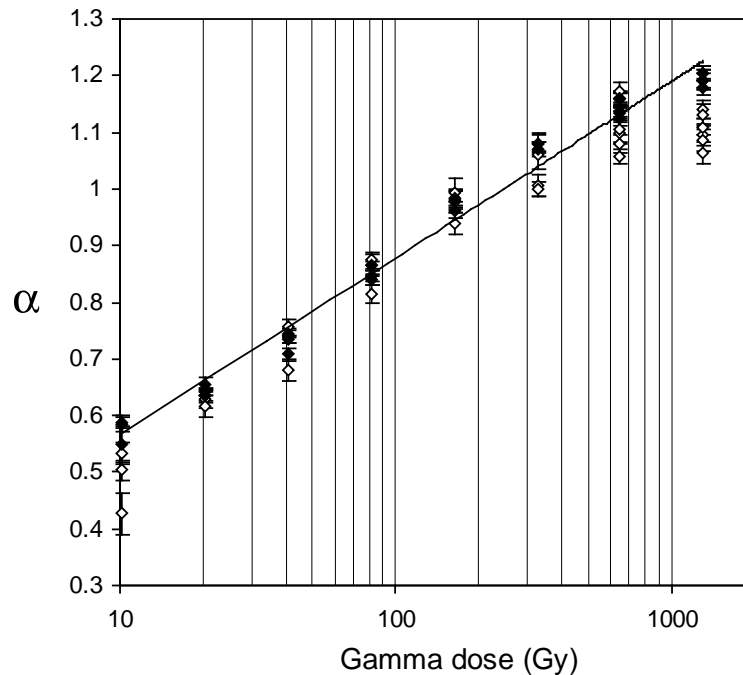
Figure 6.5: *The fitting parameter I_0 as a function of the applied γ dose for DY-23. Note the saturation of the luminescence at high doses.*
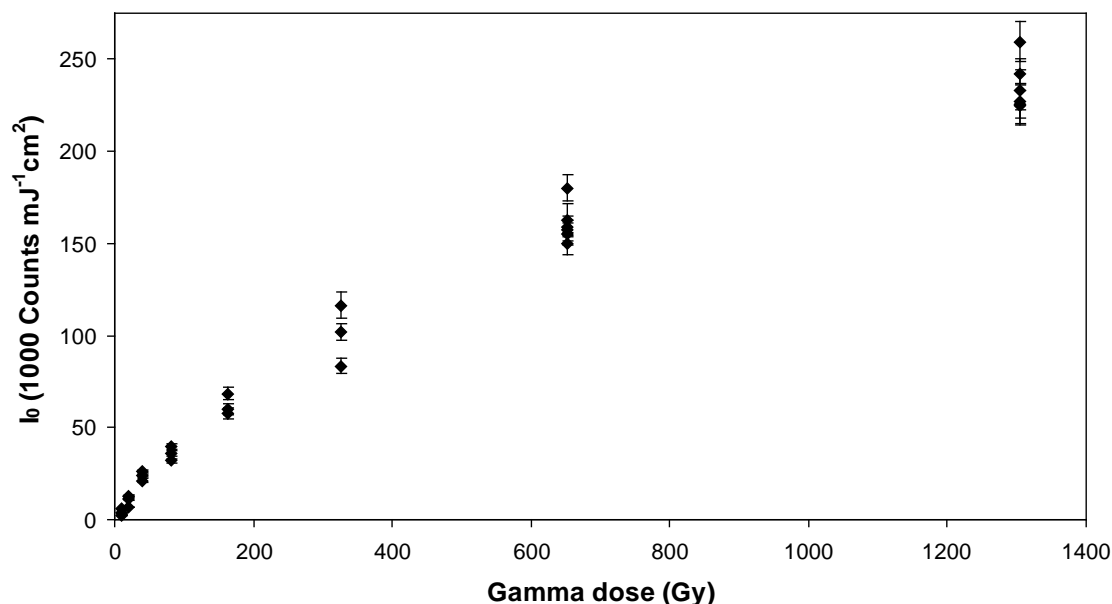
itself is also approaching saturation above 1200 Gy, as can be seen in Figure 6.5. The deviation at high doses from the logarithmic increase of α may be connected to this effect.

Aside from a slight trend towards larger E_0 at large doses (observed both in the fit to the initial and late portions of the decay curve), E_0 does not appear to be affected by the dose and averages around 300 mJ/cm^2. This is generally consistent with our experiment using naturally saturated + lab dose DY-23 aliquots; an average E_0 of 350 mJ/cm^2 was found in that case. One should note that an E_0 of 300 mJ/cm^2 corresponds to the luminous excitation exposure (at 1.43 eV) required to produce $\sim$50% decay of the luminescence in laboratory saturated DY-23.

Extended shinedown curves were also available (from D.J. Huntley) for another K-feldspar extract sample, SAW-94-61 which had been previously dated. The excitation energy was not available for this data so we fitted to the decay function, $I(t) = I_0/(1 + t/t_0)^\alpha$; the variation of α and t_0 with dose is shown in Figure 6.6. A similar, nearly linear increase of the exponent α with log(dose) was noted, however the saturation value of α was attained at a much lower dose in SAW-94-61 than DY-23. The parameter t_0 ($\propto E_0$) exhibited a clear increase with dose, saturating around 100 Gy at a value 45% larger than the value at zero dose.

Figure 6.6: *Effect of the applied γ dose on the fitting parameters t_0 (top) and α (bottom) for SAW-94-61. Inset is the luminescence intensity versus dose curve.*
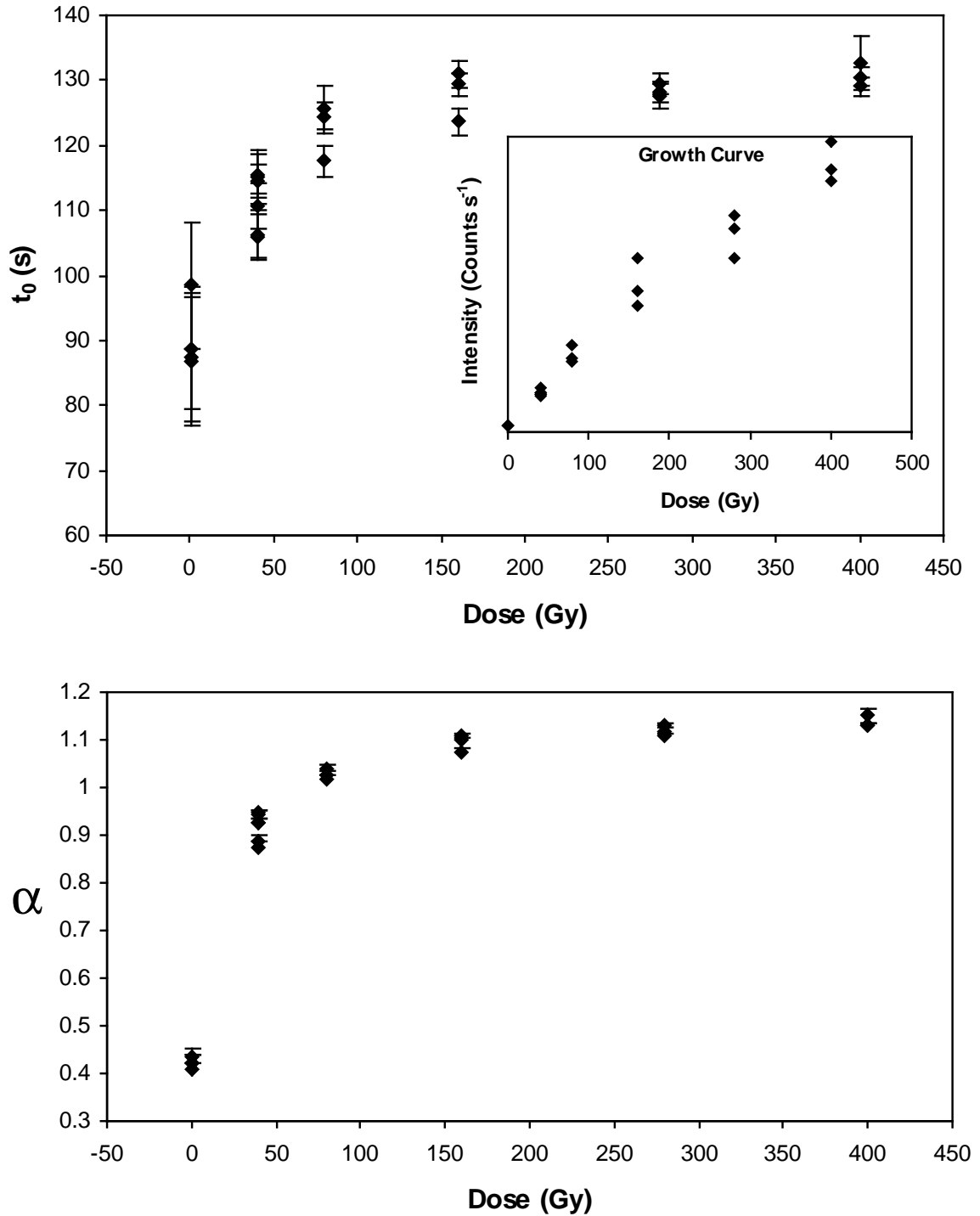
It is interesting to compare the results for DY-23 and SAW-94-61, both of which are K-feldspar sediment extracts, with those obtained for the "model" orthoclase (rock) sample K3 (Figure 6.7, 6.8). The apparent trend towards smaller E_0 at very low doses was similar to that observed in DY-23. The effect of dose on the power law exponent in K3 was similar to that observed in SAW-94-61, the saturation value of $\alpha \simeq 1$ is attained at a dose of approximately 30 Gy. This is much lower than in DY-23 where saturation of α occurs well above 1000 Gy.

Figure 6.7: *I_0 as a function of applied γ dose for K3.*
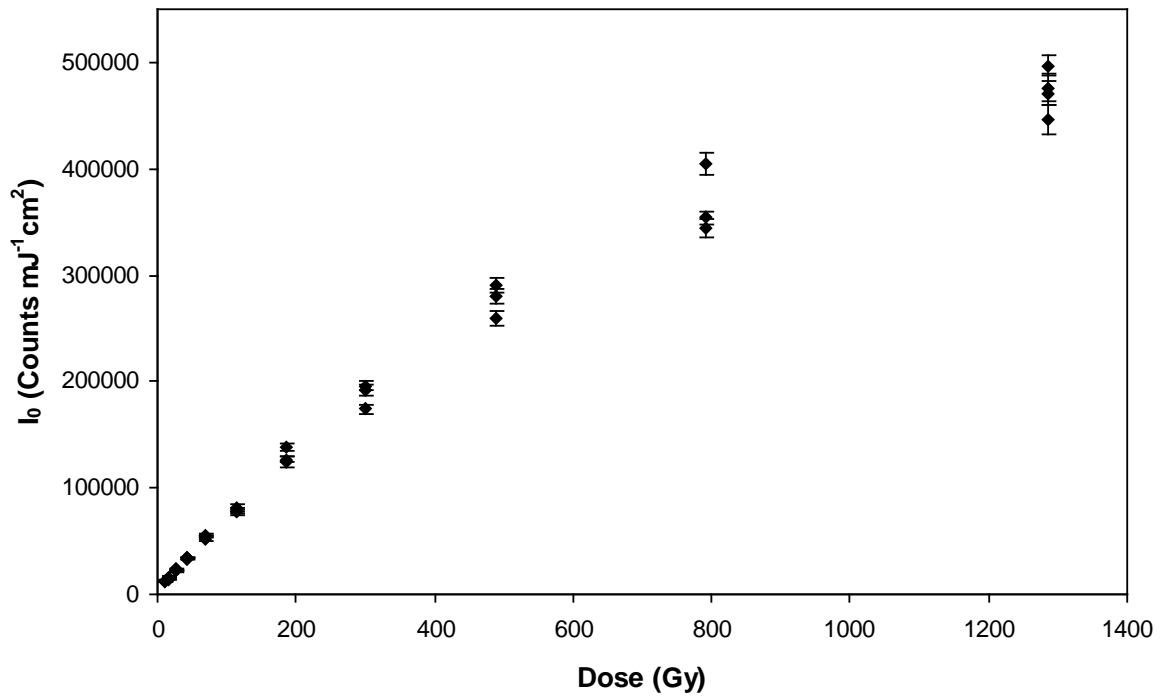
Figure 6.8: *Effect of the applied γ dose on the fitting parameters E_0 and α for K3.*
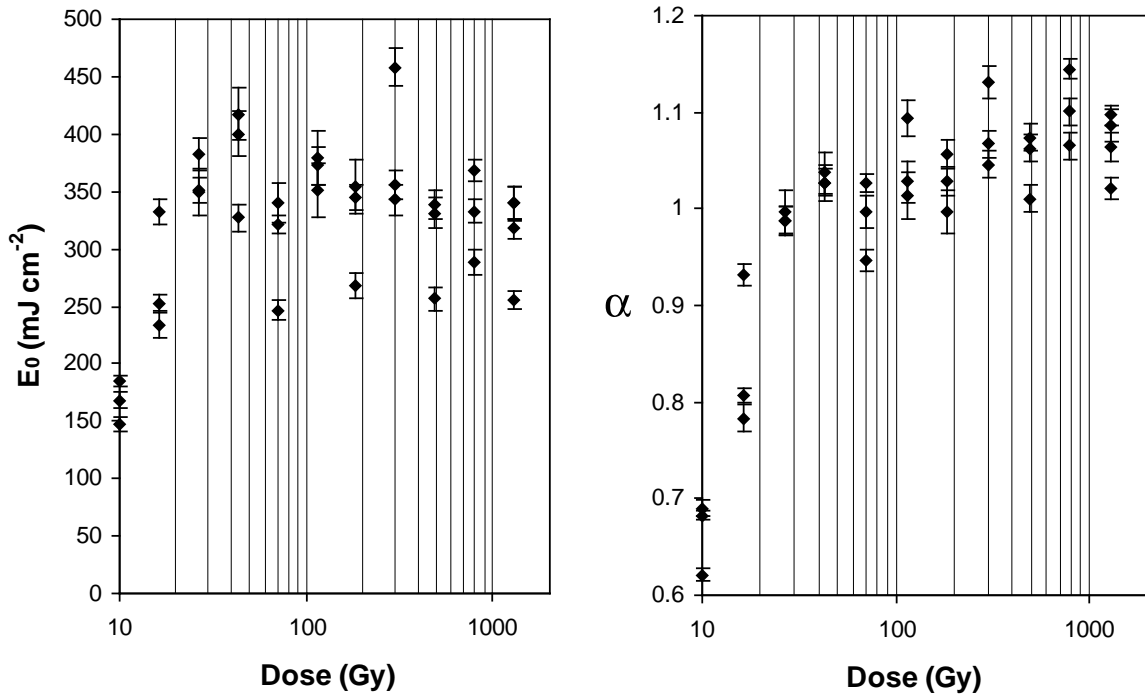
6.3   The effect of the preheat on the decay law

The effect of the preheat time on the decay law was investigated because it was conceivable that the number of occupied, thermally unstable shallow traps could affect the decay kinetics. Aliquots of sample DY-23 were bleached and given a dose of 166 Gy; this dose was selected on the basis that it is large enough to provide sufficient luminescence while remaining below the saturation regime of the exponent, α. Sets of aliquots were preheated at 120 °C for times ranging from 0 minutes to 512 minutes (8.5 hours) in binary increments of time (*i.e.* 0 min, 4 min, 8 min, 16 min, etc...). Samples that were not in the oven over the preheat period were stored in a freezer ($\sim$-10 °C) to reduce room-temperature thermal eviction of the shallow traps.

Excellent agreement with the Becquerel equation was found in all measurements, regardless of the preheat time. An E_0 scattered around 360 mJ/cm^2 was found, with a possible trend to lower values at longer heating times (Figure 6.9); this E_0 is within the range

Figure 6.9: *Effect of the 120 °C preheat time on the Becquerel fitting parameters for DY-23. Aliquots that received no preheat are shown at t=1 minute. Closed diamonds represent values obtained for a fit to the full decay curve, open diamonds represent values obtained from the data in the initial portion of the curve (first 50% reduction in intensity). Arrows indicate average values.*
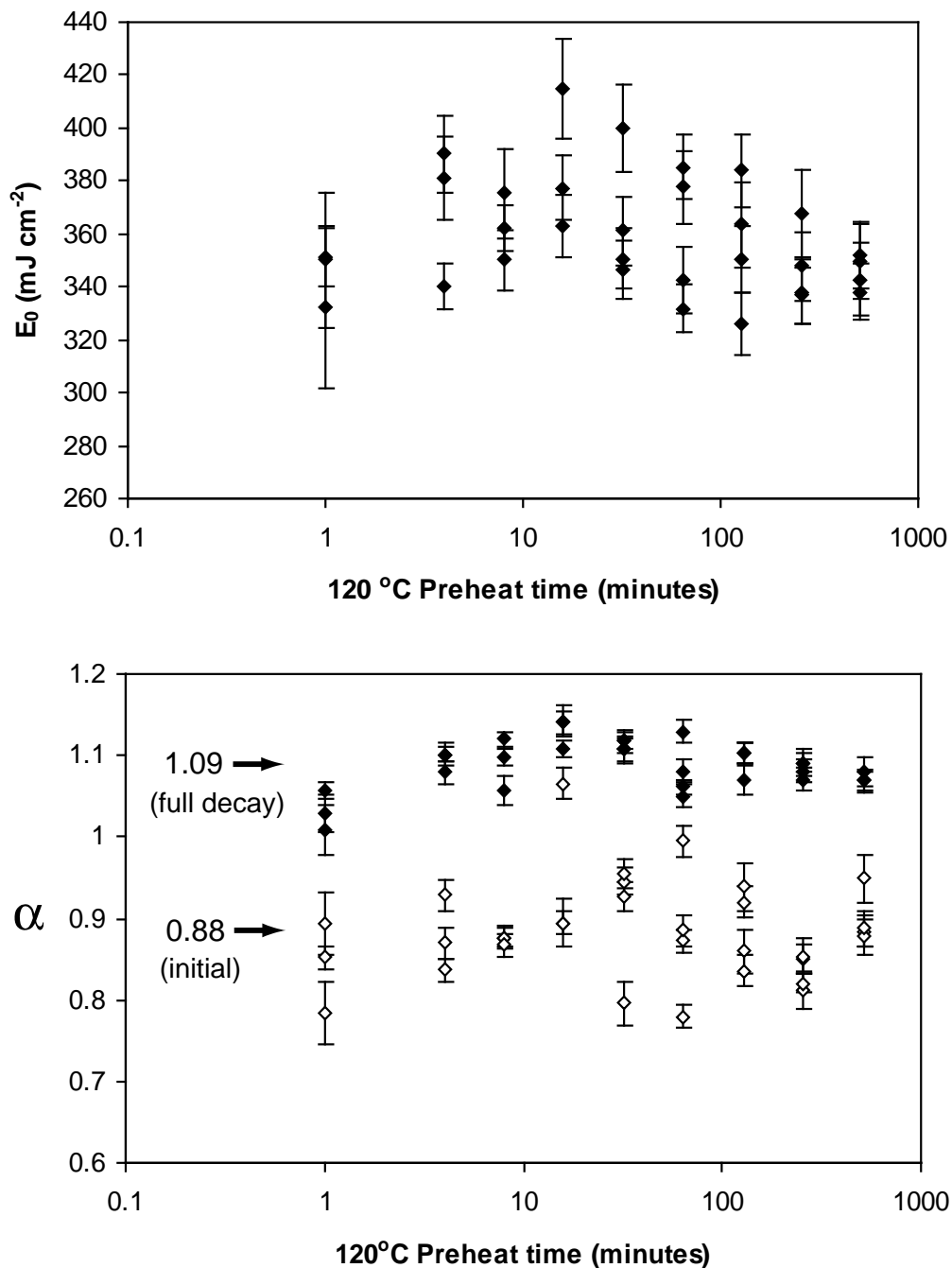
found in the dose-effect experiment. Similarly, the variation of α with the preheating time did not vary in a significant manner. An average value for α of 1.08 ± 0.03 was obtained for a fit to the full decay curve whereas 0.88 ± 0.06 was found for the initial portion of the decay curve (first 50% reduction in intensity). It should be noted that the exponent (for the full curve) is somewhat greater than that observed for the same dose in our previous experiment ($\alpha \simeq 0.95$). This may indicate that the bleaching procedure is not entirely adequate for restoring the aliquots to their physical state prior to irradiation.

6.4 The effect of temperature on the kinetics

The temperature dependence of the decay kinetics of the violet emission was investigated in sample DY-23. Several well bleached aliquots were prepared and given a moderate gamma dose of 160 Gy. Intrinsic brightness normalization of the aliquots was performed at room temperature (18 $^{\circ}$C) and all measurements were performed using 1.43 eV laser excitation. Decay curves were measured in the temperature range 300–470 K and fits to Equation 6.1 were obtained to determine E_0 and α.

Good fits to the proposed decay law were obtained at all temperatures in the range covered. The variation of α and E_0 in this temperature regime was apparently minimal, with a trend to smaller E_0 at higher temperatures; Figure 6.10. The absolute value of E_0 (300–400 mJ/cm^2) and α (1.1) is consistent with the results of our previous experiments using 1.43 eV excitation. It is worth noting that this is a stark contrast to what is observed in quartz, where the temperature strongly affects the decay rate (*e.g.* McKeever *et al.*, 1997). The fact that the decay parameters are relatively unaffected by temperature is remarkable in that it places a severe restriction on the possible models for the decay kinetics as will be discussed in Chapter 10. These results are in concordance with those of Bailiff and Barnett (1994) who found essentially no change in the form of the IRSL decay curve over the range 160–290 K for an orthoclase sample.

The initial intensity was observed to increase with temperature according to the usual Arrhenius factor, e^{-E_a/k_bT}. The thermal activation energy was found to be 0.147 ± 0.003 eV from a plot of $ln(I)$ against $1/k_bT$; Figure 6.11. This temperature dependence of the IRSL had been investigated by many workers, for example, Bailiff and Poolton (1991) found 0.10 eV, 0.09 eV and 0.08 eV for microcline, sanidine and albite samples respectively,

Figure 6.10: *Effect of temperature on the parameters E_0 and α of the decay law for sample DY-23.*
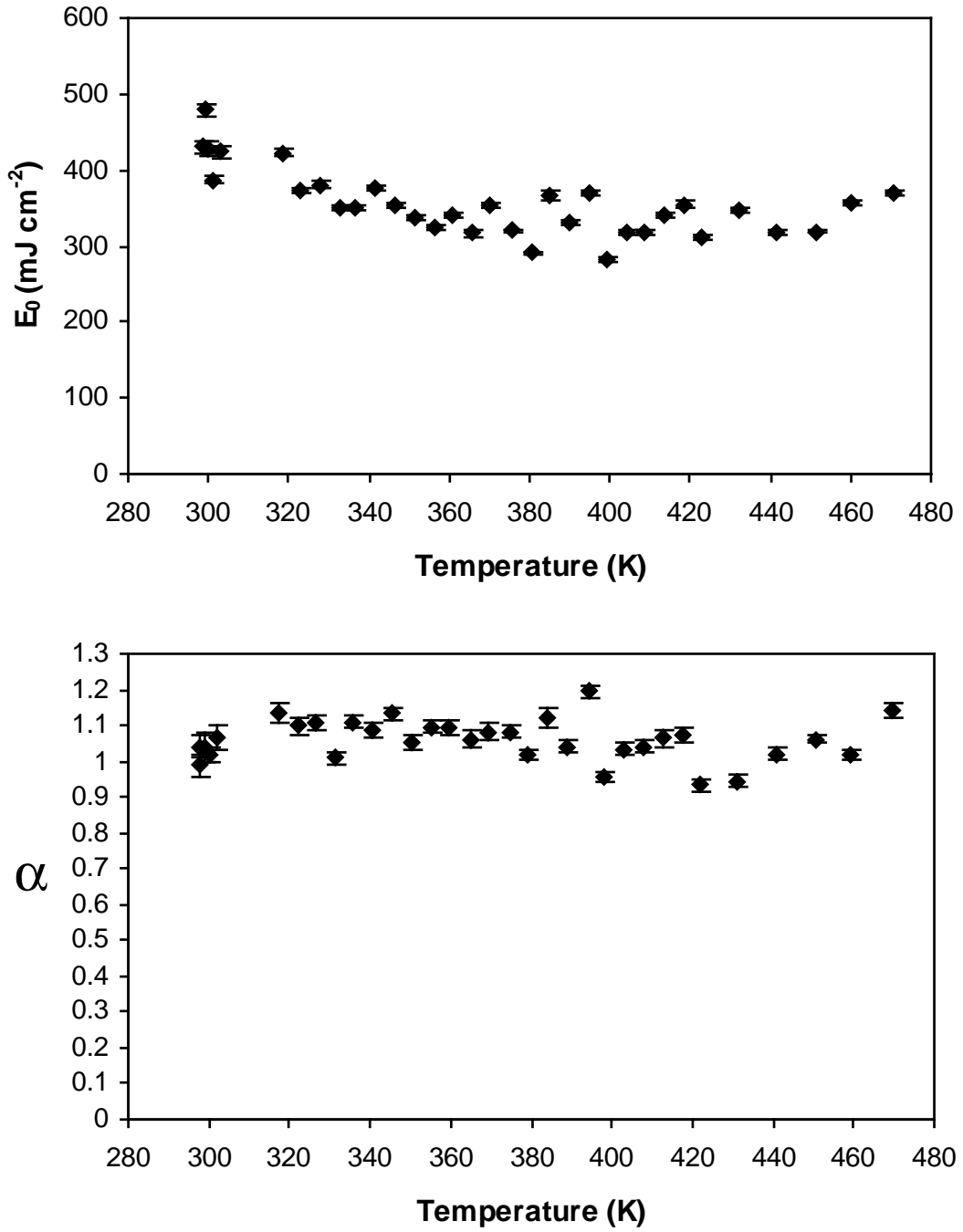
Figure 6.11: *Arrhenius plot for the the 1.43 eV stimulated luminescence in DY-23.*
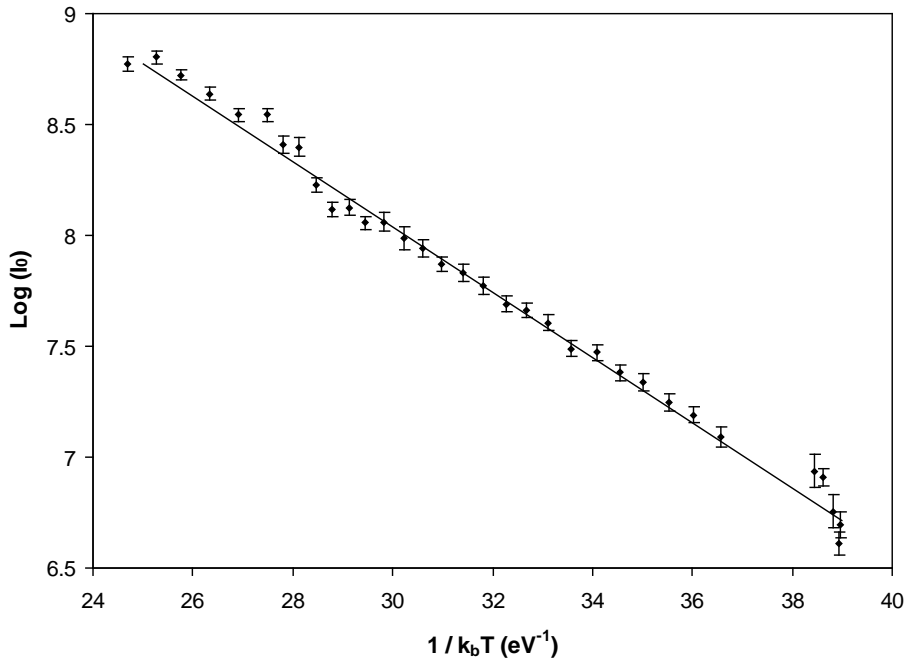
Duller and Bøtter-Jensen (1997) found E_a ranging from 0.111 eV to 0.122 eV in six K-rich sediment feldspar extracts. Bøtter-Jensen *et al.* (1997) found that E_a varies with the excitation energy; they found $E_a \sim 0.05$ eV for excitation photon energies above 2 eV with a maximum at 1.75 eV ($E_a \sim 0.12$ eV) and a local minimum in E_a at 1.5 eV ($E_a \sim 0.07$ eV) in a sample of Amelia albite[3]. The dependence of E_a on excitation photon energy was also investigated by Poolton *et al.* (1994) and Poolton *et al.* (1995). Bailiff and Barnett (1994) found a "kink" in the Arrhenius plot for the IRSL of a sediment extracted microcline near 220 K; at temperatures above 220 K E_a was 0.1 eV whereas at lower temperatures E_a was ~ 0.048 eV. A sharp kink is clearly seen in Rieser *et al.*'s (1997) Arrhenius plot for the IRSL of a sediment extracted microcline; they found an E_a of 0.15 eV for temperatures above 220 K and $E_a \sim 0.05$ eV below this temperature.

It should be noted that the thermal activation energy determined in this experiment should not be confused with the thermal energy E_t necessary to evict an electron from the trap(s). The latter is much more difficult to determine and generally involves heating

---

[3]This sample is probably similar to our A2.

the sample for a set length of time. The heating empties a fraction of the traps with a probability determined by the Arrhenius factor, $e^{-E_t/k_b T}$, so that the IRSL decreases after heating. The heating function may be either isothermal[4] or may follow a hyperbolic heating ramp of the form $T(t) = T_0/(1 - \beta t)$, where $T(t)$ is the temperature at time t; Short and Tso (1994). By measuring the reduction in luminescence intensity in aliquots subjected to heating treatments at different temperatures, E_t may be determined. Trautmann *et al.* (1997) attempted to determine E_t using Short and Tso's technique, using both hyperbolic and isothermal heating functions. The values of E_t obtained by these authors varied widely, depending on the sample and the method of measurement, from as little as 0.5 eV, up to 3.2 eV.

6.5 The effect of the excitation energy on the kinetics parameters

A moderate dose (163 Gy) was given to a number of bleached aliquots of DY-23. The initial luminescence intensity of each aliquot under a "short-shine"[5] of 1.43 eV excitation was used to normalize the response of the aliquots. Luminescence decay curves were measured for a range of energies between 1.2 and 1.8 eV so that the behaviour in the vicinity of the nominal 1.44 eV excitation resonance could be observed. This experiment was also performed on the orthoclase K3. The experiment was repeated for both sets of sample aliquots to verify the repeatability of the results. Between irradiations, the samples were bleached for 12 hours under red/IR light of $\sim$15 mW/cm^2 intensity.

The results of this experiment clearly indicate that the excitation energy has a significant effect on the decay kinetics of DY-23 and K3. The behaviour of E_0 is probably the most interesting; it is peaked at 1.31, 1.33 eV (K3, DY-23) and 1.57, 1.6 eV (K3, DY-23) with local minima at 1.44 eV and 1.7 eV (both samples), Figure 6.12. For DY-23, E_0 rapidly decreases below 1.3 eV so that the decay law begins to approach $I(E) \propto E^{-\alpha}$; this decrease is not as marked in K3. For sample DY-23, E_0 at 1.44 eV is $\sim$300 mJ/cm^2, which is consistent

---

[4]Here the sample is rapidly heated up and held at fixed temperature. The assumption is that the number of electrons removed from traps during the rapid temperature ramp is negligible compared to the number of traps emptied during the isothermal heating period.

[5]A short illumination time at low power selected so that no significant decay of the luminescence occurs.

Figure 6.12: *Effect of the excitation energy on the fitting parameter E_0 for DY-23 (top) and K3 (bottom).*
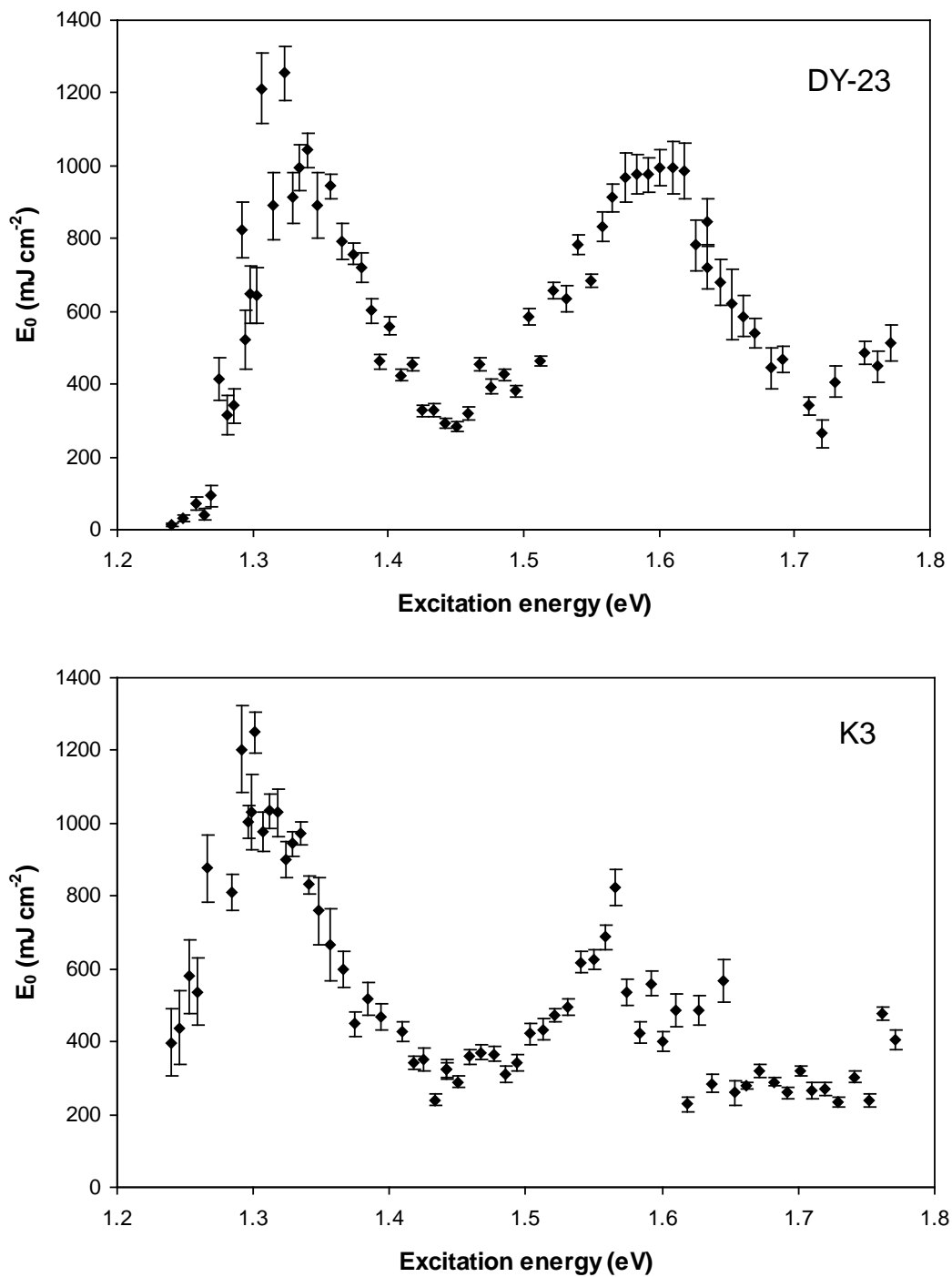
Figure 6.13: *Effect of the excitation energy on the fitting parameter α in DY-23 (top) and K3 (bottom). Two sets of measurements were combined to produce these plots; one will note that α was not entirely reproducible between the two measurements, especially in the vicinity of the 1.44 eV resonance for sample DY-23.*
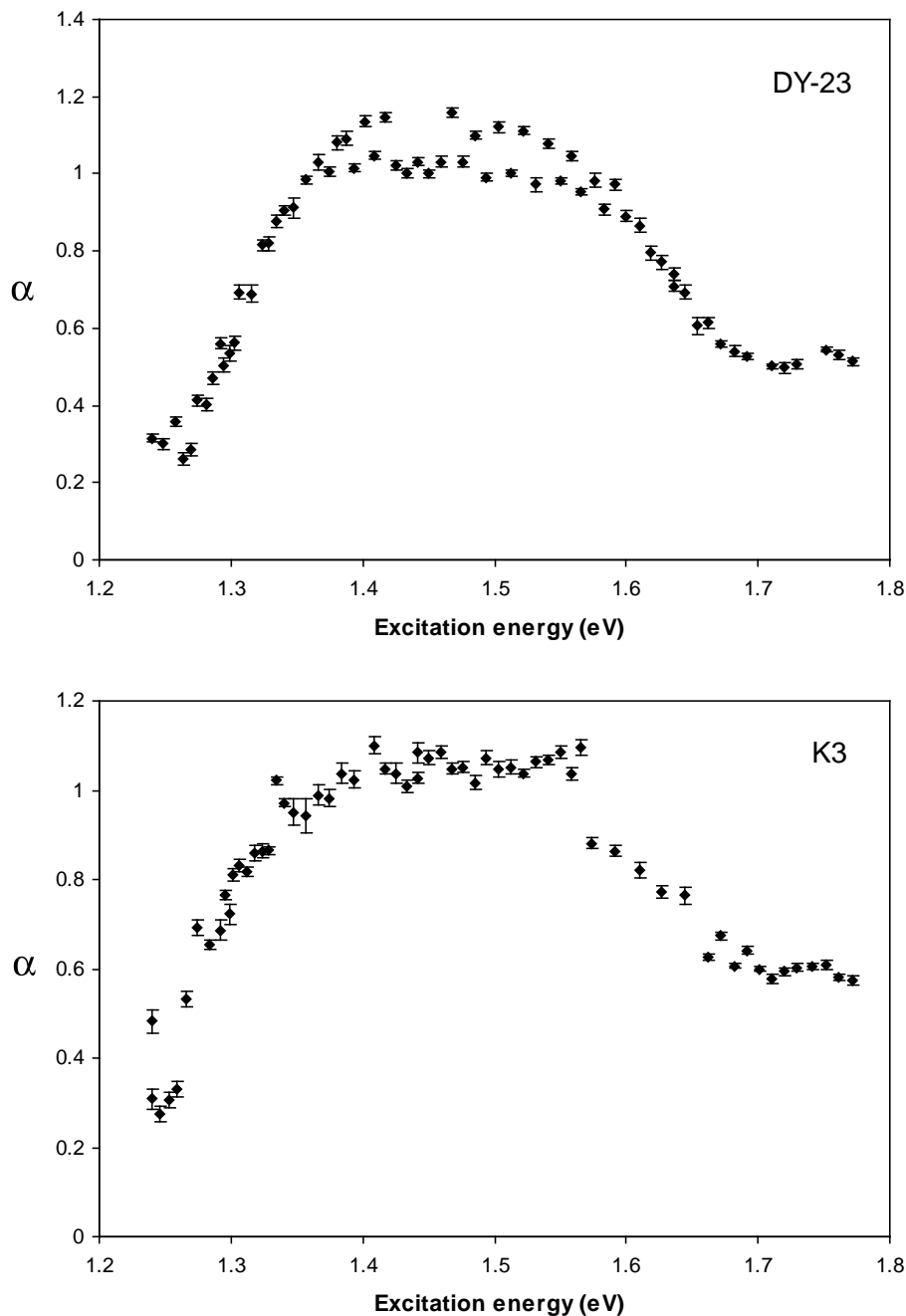
Figure 6.14: *The excitation energy response of I_0 for DY-23 (top) and K3 (bottom).*
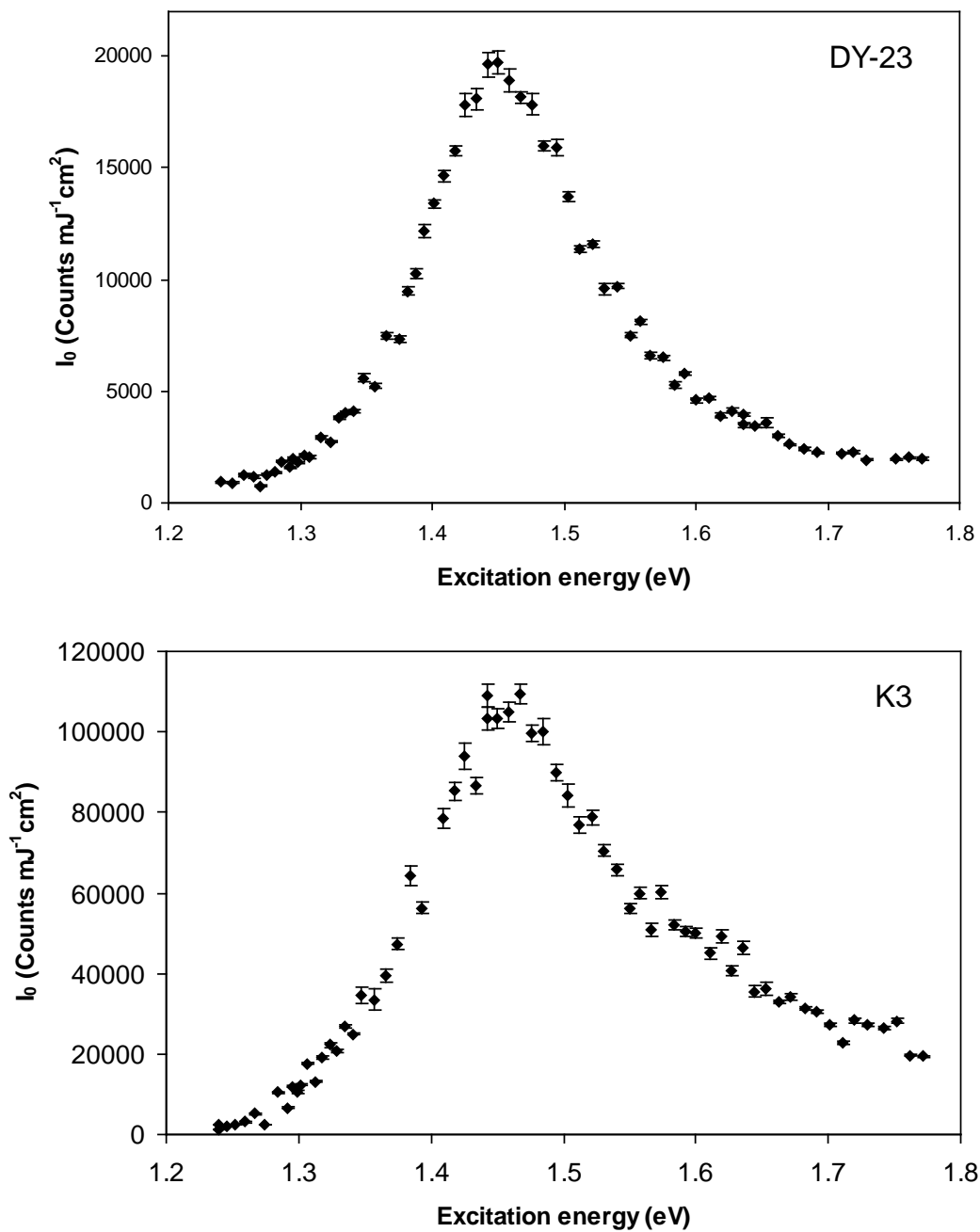
with the value found in our previous experiments performed using 1.43 eV excitation.

The exponent α also exhibits a strong dependence on the excitation photon energy, with a broad peak centered on 1.45 eV; Figure 6.13. At excitation energies less than 1.3 eV, α appears to attain a minimum value of 0.3, whereas it dips to 0.59 at 1.7 eV. It was also noted that the fit to the decay law represented by Equation 6.1 was only good for energies in the vicinity of $\alpha = 1$. At excitation energies significantly removed from 1.45 eV, the best-fit exponent in early part of the decay was smaller than that in the later part of the decay. Generally, fits that ignored the initial 5% of the decay produced less scatter in the plots of E_0 and α as a function of excitation energy and these are used for the plots shown here.

The excitation resonance of the (prompt) luminescence was found to peak at 1.45 eV in DY-23 and 1.445 eV in K3. The resonance exhibited the same line-shape typical of feldspars described in Chapter 5 (Figure 6.14).

6.6 Summary

It is evident that the results of the present study on the decay kinetics of DY-23 and K3 have significant implications for the possible models for the de-trapping and recombination mechanisms in feldspars. An interpretation in terms of a number of traps of different depths, with luminescence being simply proportional to de-trapping rate (with minimal retrapping) is manifestly incorrect. Such kinetics will always lead to a decay law that is described by a sum of exponentially decreasing terms, as will be discussed in the Chapter 10.

The Becquerel law, $I(E) = \frac{I_0}{(1+\frac{E}{E_0})^\alpha}$, where E is the integrated luminous excitation energy provided to the sample and I_0, E_0 and α are constants, provides a good fit to all of the luminescence decay curves. This law was found to apply to the IRSL of several samples (15 total, see also Chapter 4) as well as the prompt phosphorescence of AKHC, SAW-95-09 and GP-1. The greatest departure from this law occurs early in the luminescence decay curve, where the decay rate is somewhat less than at long decay times. This is manifested by the generally lower value of the best-fit power-law exponent α in the initial portion of the decay curve.

In DY-23 the IRSL intensity depends on temperature through the Boltzmann factor, e^{-E_a/k_bT}, with an activation energy E_a of 0.147 ± 0.003 eV for the violet emission. This value for E_a is within the range found for other samples by different authors. In DY-23 the kinetics parameters are not affected by sample temperatures in the range 300–460 K; this concords with the results of Bailiff and Barnett (1994) for an orthoclase sample (from 160 K to 290 K). The question as to whether this rather simple temperature dependence is generally applicable to the violet emission of feldspars awaits testing on other samples.

The preheat-time appears to have no significant effect on the kinetics of the violet IRSL. This might be interpreted as an indication that the initial number of electrons in shallow traps has little effect on the recombination dynamics. Perhaps this is due to the redistribution of the electrons in the shallow traps upon photonic excitation. If one accepts that the electrons in the shallow traps may be evicted by the excitation light and that a significantly redistribution of electrons from the deep (optical) into the shallow traps occurs, then it is not surprising that the initial distribution of electrons in the shallow traps should have little effect on the decay parameters. Within a short time after the excitation is applied, the redistribution of electrons in the shallow traps completely "erases" the initial distribution

established by the preheat.

The power law exponent depends on the applied radiation dose in a way that varies from sample to sample. For DY-23 α varies linearly with the logarithm of the dose. For K3 and SAW-94-61 the (presumed) logarithmic increase of α with dose appears to saturate rapidly so that α achieves a constant value at doses above 100-200 Gy. The parameter E_0 does not appear to be strongly affected by the applied radiation dose for either K3 or SAW-94-61. It seems unlikely that α is affected by the initial density of trapped electrons (which is proportional to dose, below saturation), since we would expect to see a strong variation of α along the decay curve as this density decreases. The evidence clearly indicates that there is only a slight reduction in α for the initial portion of the decay curve. The dependence of α on dose might be explained by the creation of defects during irradiation that are essential to the recombination process. For example, if one considers a model involving electrons hopping between Al-O$^-$-Al defects to reach the recombination centers, then the decay rate would increase (*i.e.* higher α at fixed t_0 and I_0) when a larger number of these defects was present. It would interesting to know how the kinetics parameters of well bleached samples are affected by very low doses (below 50 Gy).

The excitation photon energy is a factor in the kinetics. For sample DY-23, the parameter E_0 in Becquerel's law reaches a minimum at the excitation resonance, 1.44 eV. In addition, two other minima in E_0 are observed below 1.3 eV and at 1.7 eV. The variation of α with excitation energy is equally peculiar; a broad, flattened peak in α centered near the 1.44 eV resonance was observed in both K3 and DY-23. In both cases α varies from about 0.3, for excitation energies below 1.3 eV, up to 1–1.1 for energies near the excitation resonance. The flat peak is immediately interpreted as the attainment of an upper threshold in the decay rate, limited by a process other than that of the excitation of charges out of the traps; for example, the hopping mechanism suggested above. There is no doubt that the plateau in the α vs. excitation energy plot would lower if the experiment were repeated with samples that were given a smaller radiation dose.

Chapter 7

Initial Slope Versus Intensity Experiment

7.1   Single or multiple electron traps?

The most fundamental question in beginning to develop a model for the electron traps responsible for OSL in feldspars is whether the traps consist of a single or multiple defect(s). A simple means of determining which is the case is as follows. Consider the functional form of the luminescence decay law; a reasonable assumption to make is that the intensity as a function of the total applied luminous excitation energy (*i.e.* the decay curve) should follow a function of the form,

$$I(E) = I_0 \, f \left(\frac{E}{E_0} \right) \tag{7.1}$$

where $I(E)$ is defined as the luminescence intensity emitted per unit excitation energy, E_0 is a characteristic energy (not necessarily the same as E_0 in Chapter 6), I_0 is the initial intensity and E is the integrated excitation energy,

$$E = n\hbar\omega t \tag{7.2}$$

where the number of photons incident on the sample per unit area, per unit time, n is assumed to be constant and the excitation is monochromatic. Examples of functions of the form of Equation 7.1 are Becquerel's law (Equation 6.1) and Debye-Edwards' law (Equation 6.2). The monomolecular law is also an example of a function that follows the form of

Equation 7.1; it may be written as,

$$I(E) = I_0 e^{-E/E_0} \tag{7.3}$$

This last equation describes the luminescence decay when no other processes occur between eviction of the electron from the trap and recombination at the luminescence center (*e.g.* there can be no re-trapping of the electron in another trap). In this case, E_0 may be directly connected to the excitation cross section of the trap, σ,

$$E_0 = \hbar\omega/\sigma \tag{7.4}$$

If several *non-interacting* traps with different depths are present, then the luminescence intensity would be proportional to a sum of such exponential terms,

$$I(E) = \sum_i^N I_{0i} e^{-E/E_{0i}} \tag{7.5}$$

where the sum is over the N different traps. This is an example of a decay law that does not adhere to the form of Equation 7.1.

Although it cannot be generally proven that E_0 will depend on the details of the trap in every conceivable luminescence decay law (as it does in the simple case outlined above), it is reasonable to expect that this is likely to be true, at least by analogy to the case of monomolecular decay. Adherence of the decay to the form of Equation 7.1 would therefore be taken as strong evidence that the luminescence involves a single trap.

It is easily shown that the functional form of Equation 7.1 requires that the initial slope, S_0, be proportional to the square of the initial intensity, I_0 (Ditlefsen and Huntley, 1994),

$$S_0 = \frac{dI}{dE}\mid_{E=0} \propto I_0^2 \tag{7.6}$$

The derivation is as follows. Assume that the total integrated luminescence L is constant; this implies,

$$L = \int_0^\infty I(E)dE = I_0 E_0 \int_0^\infty f(x)dx \tag{7.7}$$

The definite integral on the right is constant as long as $f(x)$ does not depend on the excitation energy, that is, the same light sum is obtained for all excitation energies. The initial slope is,

$$S_0 \equiv (dI/dE)_{E=0} = \frac{I_0}{E_0} f'(0), \quad S_0 = \frac{I_0^2}{L} f'(0) \int_0^\infty f(x)dx \tag{7.8}$$

Equation 7.6 follows given the previous restriction made on $f(x)$.

7.2 Initial slope versus intensity experiment

The relation derived above is useful in distinguishing the difference between kinetics that follow $I(E) \propto f(E/E_0)$ and $I(E) \propto f(E/E_0, E/E_1...E/E_n)$ (Equation 7.5 is an example of the latter). Only the first case will produce a linear relation between the square root of the initial slope $\sqrt{S_0}$ and I_0. Ditlefsen and Huntley tested this relation over a wide range of excitation energies ranging from 2.54 eV to 1.77 eV for three feldspar sediment extracts and one quartz sediment extract. A linear relationship between I_0 and $\sqrt{S_0}$ was only observed for the quartz sample; for the feldspars a strongly nonlinear relation was obtained.

Since Ditlefsen and Huntley's measurements did not extend below 1.77 eV, they were not able to test Equation 7.6 in the vicinity of the excitation resonance. This region is of particular concern because one would like to know whether the excitation at 1.44 eV samples the same traps as the light above 2 eV. Also, since this experiment had only been performed on three K-feldspar sediment extracts, it was useful to see if the same behaviour would be seen in cut-rock feldspar samples. Chips of samples K3 (orthoclase), K8 (perthitic microcline), K9 (microcline) and K10 (microcline) were cut and bleached under a sun lamp fitted with a short cut filter for 70 hours[1]. The chips were given a γ dose of 800 Gy followed by a preheat at 120 °C for 16 hours. Chips were normalized for their intrinsic brightness by measuring the luminescence produced under 1.43 eV laser excitation. The violet emission band was selected by using three 4 mm thick Corning 5-58's, one Corning 7-51 and a single Schott 2.2 mm thick BG-39 filter. An EMI 9635QB photomultiplier tube with bi-alkali photocathode was used to provide efficient counting of the 3.1 eV luminescence band but a poor response to the 1.43 eV excitation light.

Several light sources were used to provide the excitation. For this reason care was taken to ensure that the sample illumination was very broad and uniform. Energies between 1.24–1.77 eV were obtained using a tunable Ti-Sapphire laser. Measurements at 2.54 eV (488 nm), 2.5 eV (496 nm), 2.47 eV (501 nm) and 2.41 eV (514 nm) were made using an argon-ion laser operated in single line mode. Points at 1.96 eV (632.8 nm) were obtained using a He-Ne laser, whereas those at 2.1 eV (589 nm) and 2.27 eV (546 nm) were provided using a Na-lamp/Na-doublet filter and a Hg-lamp/546 nm narrow-band filter combination, respectively. The 1.89 eV (656 nm) source consisted of a tungsten filament lamp combined

---

[1]3 sheets of #106 Lee gelatin filter.

with a narrow band line filter centered on the H_α emission line.

When using the laser sources the excitation power was monitored using a calibrated silicon photo-diode detector and a beam-splitter pick-up. The beam-splitter was calibrated for the wavelength dependence of its reflectivity by comparing the power measured at the sample position and at the beam splitter pick-up for each wavelength. For the lamp sources, the excitation power was measured before and after the measurement at the sample position. For these measurements, the power never varied by more than 3% over the measurement period.

Figure 7.1: *Initial intensity as a function of excitation energy for feldspar rock samples K3, K8, K9 and K10. Solid line is a cubic spline through the data to aid visualization. Data for the different samples have been shifted along the ordinate axis for clarity.*
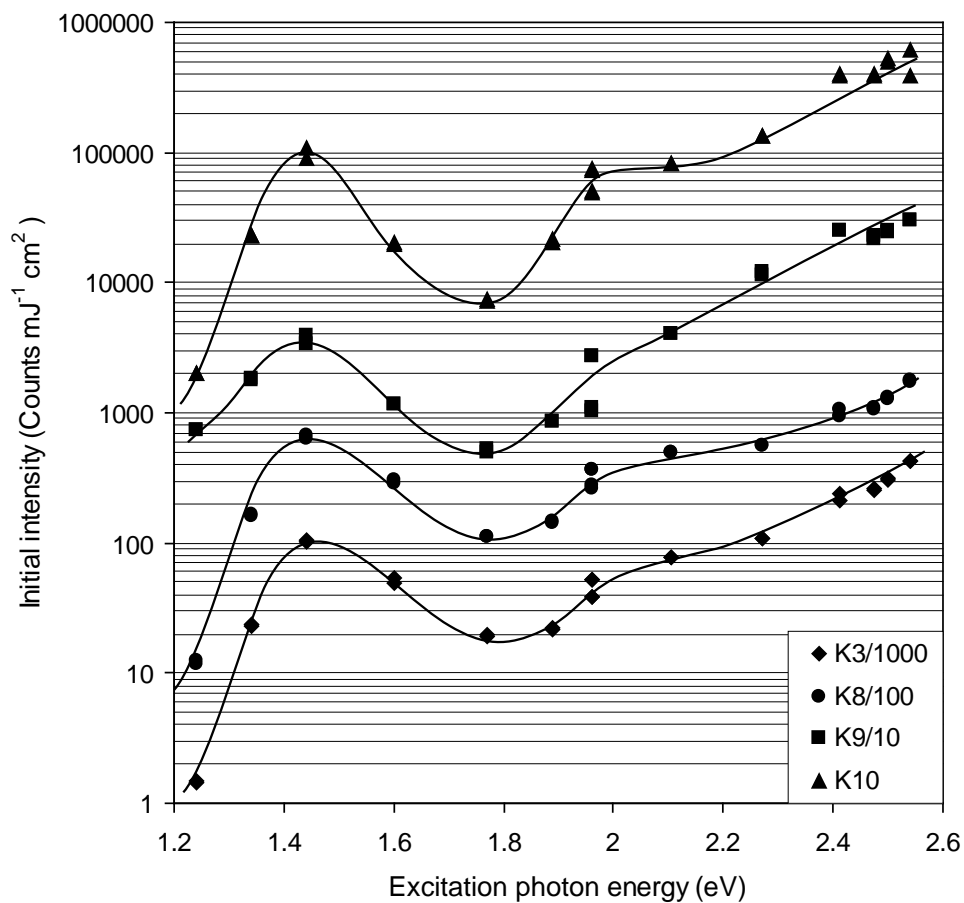
The initial intensity as a function of excitation energy is shown in Figure 7.1. In addition to the excitation resonance at 1.44 eV a smaller peak is present near 1.9 eV; this second "resonance" was also evident in the data of Ditlefsen and Huntley (1994). It is possible that this peak is due to a peculiarity in the measurement at 1.96 eV however this is not borne out by the plots of the square root of the initial slope versus intensity; no special deviation from linearity is observed for these points[2]. The near-exponential rise of the luminescence at excitation energies above 2 eV is most easily attributed to the direct photo-ionization of the trapped electron to low lying conduction band "tail states".

The initial intensity expressed in PMT counts per unit excitation energy versus the square root of the initial slope is shown in Figures 7.2 and 7.3. The uncertainties in the initial slope represent the 68% confidence interval for the linear coefficient in the fit of the initial portion of the decay curve to a second-order polynomial.

7.3 Discussion

The plots of the square root of the initial decay rate against intensity are remarkably linear up to relatively high excitation energy ($\sim$2.4 eV) in the four samples measured. This is encouraging because it suggests a simpler picture than what was indicated by the preliminary work of Ditlefsen and Huntley (1994). The interpretation is slightly problematic in view of our present kinetic work since for $\alpha \leq 1$ the total light sum does not converge for Becquerel's law. Clearly, if the power law is to remain valid at long illumination times, the exponent must increase to a value above 1 so that the total integrated luminescence is finite. Evidence for this increase in the value of α at long times was seen in the decay of DY-23 at excitation energies significantly removed from the 1.44 eV excitation resonance.

The scaling $S_0 \propto I_0^2$ implies that the parameters α, E_0 and I_0 in the decay law are not entirely independent. The initial slope of Equation 6.1 is $S_0 = I_0\alpha/E_0$, so that α/E_0 must be proportional to I_0 for the scaling $S_0 \propto I_0^2$ to hold.

This condition is easily verified from our measurements of the excitation energy dependence of α and E_0. If α/E_0 is plotted against the excitation energy, the general shape of the excitation resonance is recovered (see Figure 7.4). The unexpected rise at low and high

---

[2]It is possible that the short term periodic fluctuations of the He-Ne laser power led to an incorrect assessment of the average beam power.

energies is due to the use of E_0 and α determined from the late part of the decay curve; this rise is not as marked if the initial values of α/E_0 are used.

Although this result provides strong evidence against multiple traps, it is not entirely conclusive because the connection of the parameter E_0 to the trap parameters (*e.g.* its photo-ionization cross-section) has not yet been established for the case of Becquerel-like decay. However, the multiple exponential model for the decay is certainly ruled out. In addition, the initial IRSL decay rate versus intensity experiment has established a connection between the decay parameters α, E_0 and I_0.

Figure 7.2: *Square root of initial absolute slope against initial intensity for orthoclase K3 (top) and perthitic microcline K8 (bottom). Energies correspond to the photon energy of the excitation light used to obtain the respective point.*
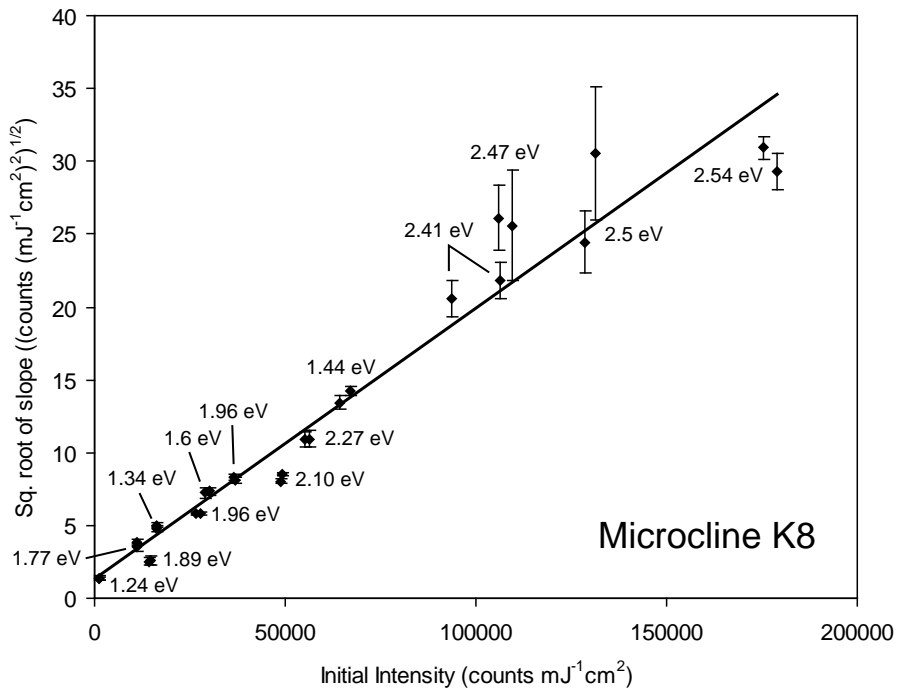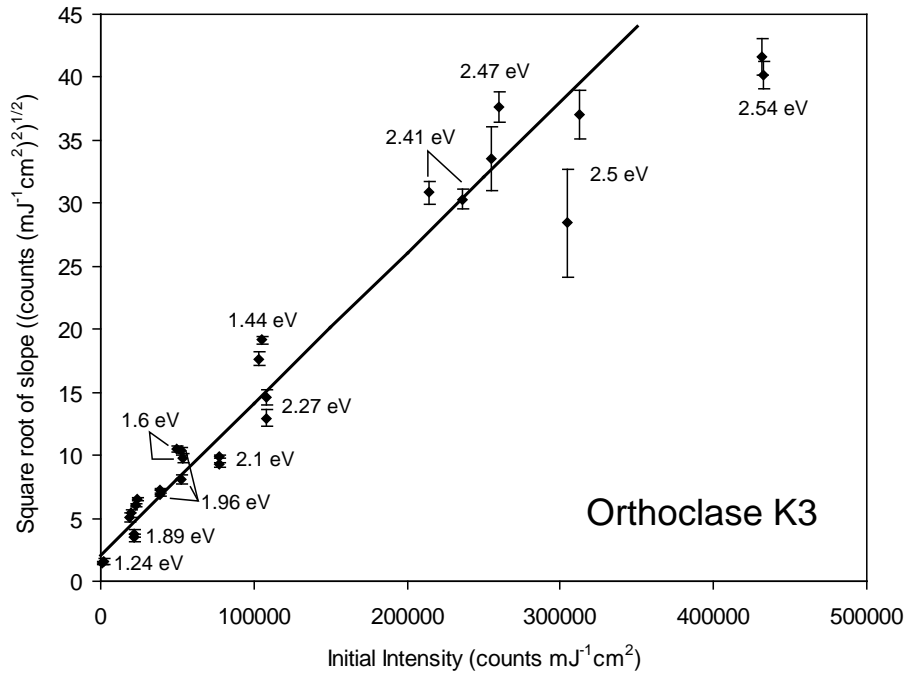
Figure 7.3: *Square root of initial absolute slope against initial intensity for microclines K9 (top) and K10 (bottom). Energies correspond to the photon energy of the excitation light used to obtain the respective point.*
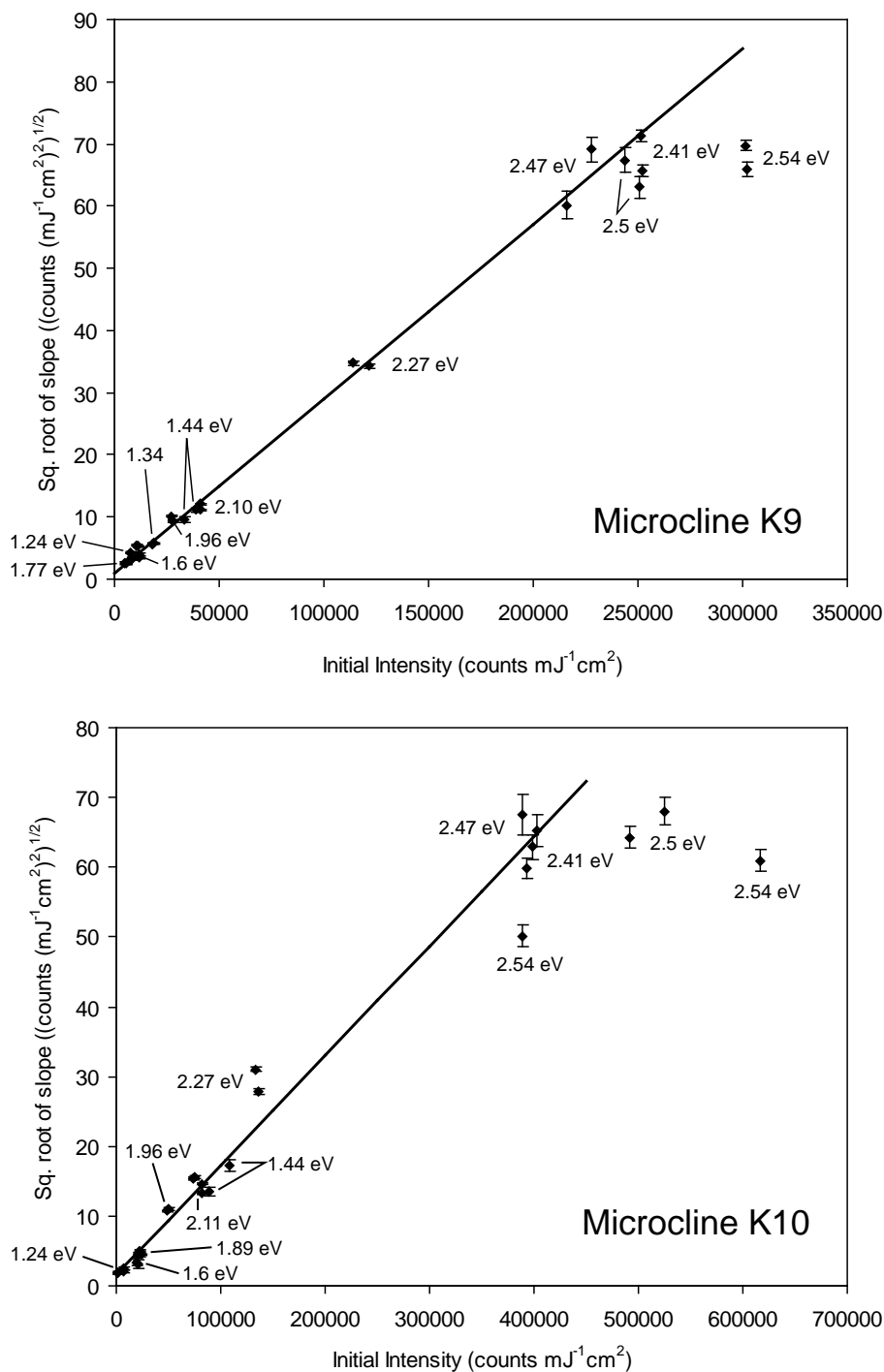
Figure 7.4: α/E_0 for K3 (top) and DY-23 (bottom) obtained from the experiment described in Section 6.5.
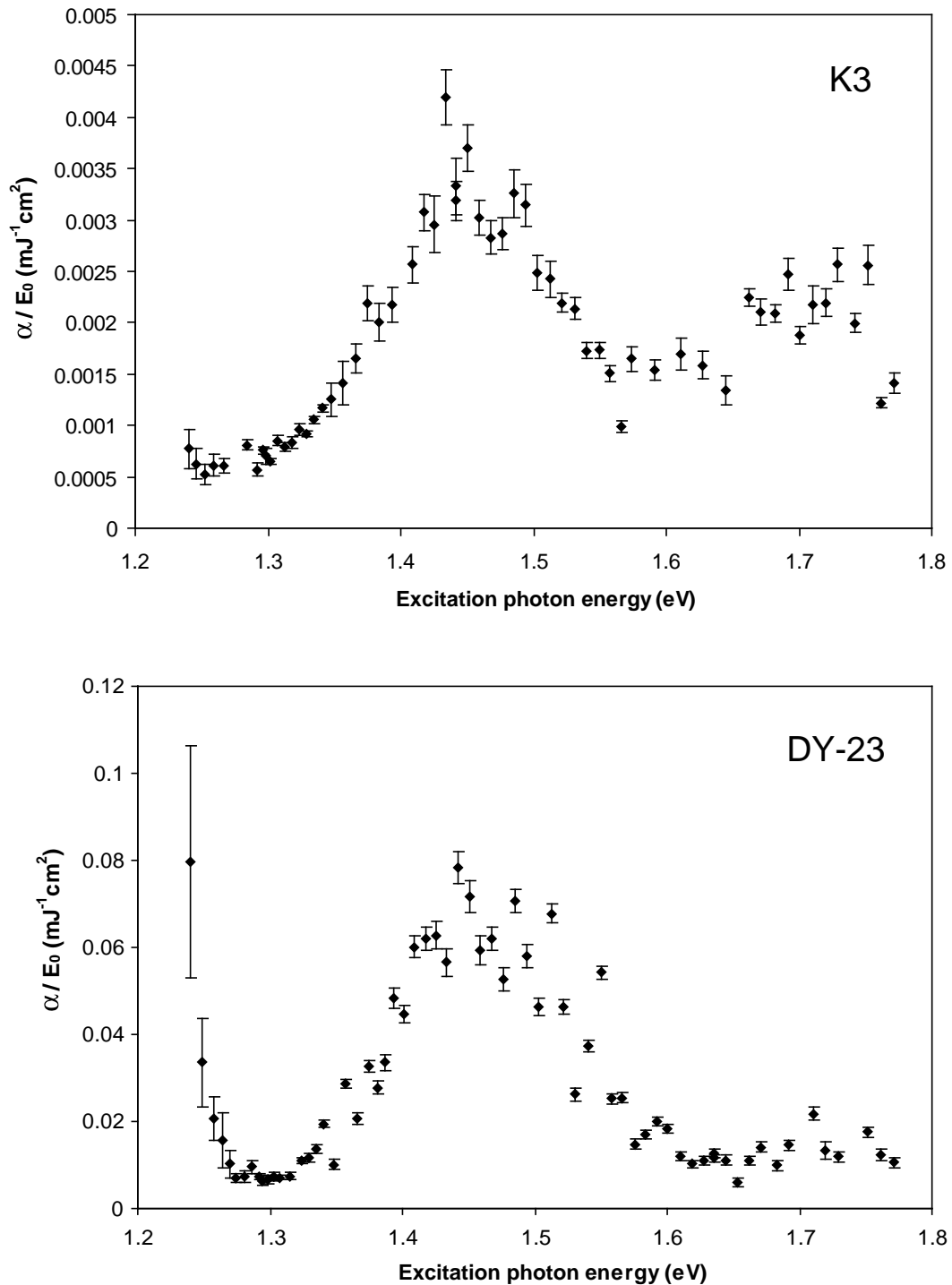
Chapter 8

Luminescence Imaging

8.1   Infrared stimulated luminescence images

The correlation of the violet and yellow-green IRSL with K-rich ("orthoclase") and Na-rich ("albite") feldspars respectively was discussed in in Chapter 4. One will also recall that in most alkali feldspars, notably perthitic microclines the Na and K ions are incorporated in exsolved phases of albite and orthoclase rather than evenly mixed throughout the crystal. For these reasons, it is interesting to consider the spatial distribution of the luminescence of the violet (3.1 eV) and yellow-green (2.2 eV) emission bands in feldspar rock samples.

Images of the thermoluminescence of quartz have been published by Spooner (2000), Ganzawa *et al.* (1997) and Hashimoto *et al.* (1995). Optically stimulated luminescence images were obtained by this latter group using glass fibres to provide both excitation and detection while scanning over the sample surface. The technique presented here is considerably simpler and could potentially be used to provide quantitative measurements of the distribution of emission bands among individual grains in a sediment sample.

The chief difficulty in imaging the IRSL is that a finite and relatively small light-sum is available so that resolution below ~ 50 μm is not practical. A cooled CCD-camera using Kodak's KAF-401e monochrome sensor was used to capture the luminescence images[1]. The violet and yellow-green emission bands were separated using a Schott BG-39 + Corning 5-60 filter, and a BG-39 + Schott GG-495 filter respectively. The broad band-passes of

---

[1]The design of this camera is described in Appendix C.

Figure 8.1: *Schematic of the setup used for imaging the IRSL.*
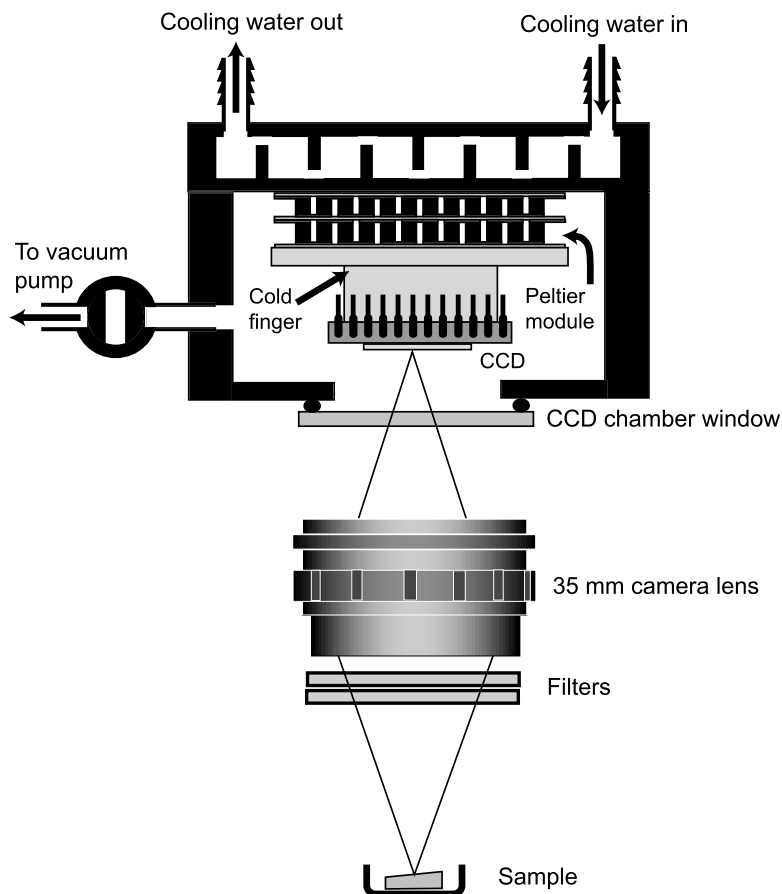
these filters were required to obtain sufficient light at the CCD (the bandpasses are shown in Figure 8.2). A 35 mm Takumar lens fitted with a 12 mm extension tube produced a magnification close to 1 so that the image of the 1 cm diameter sample planchets just over-filled the ~1cm wide CCD chip[2]. In this manner a good balance between resolution and light collection was achieved. In most cases, pixels were binned 2x2 to increase the signal to noise ratio (SNR), however for some of the brighter samples (*e.g.* A1 and A3) the full CCD resolution was used.

The intrinsically brightest samples from our collection were selected for imaging; these were the orthoclase K3, the microclines K8, K9 and K10, albite A1 and oligoclase A3. The

---

[2]The effective focal ratio using this combination was f2.7

Figure 8.2: *Convolution of the CCD quantum efficiency with the transmission of the two fil-ter combinations used to isolate the violet and yellow-green emission bands. IRSL emission spectrum for EIDS is shown for comparison.*
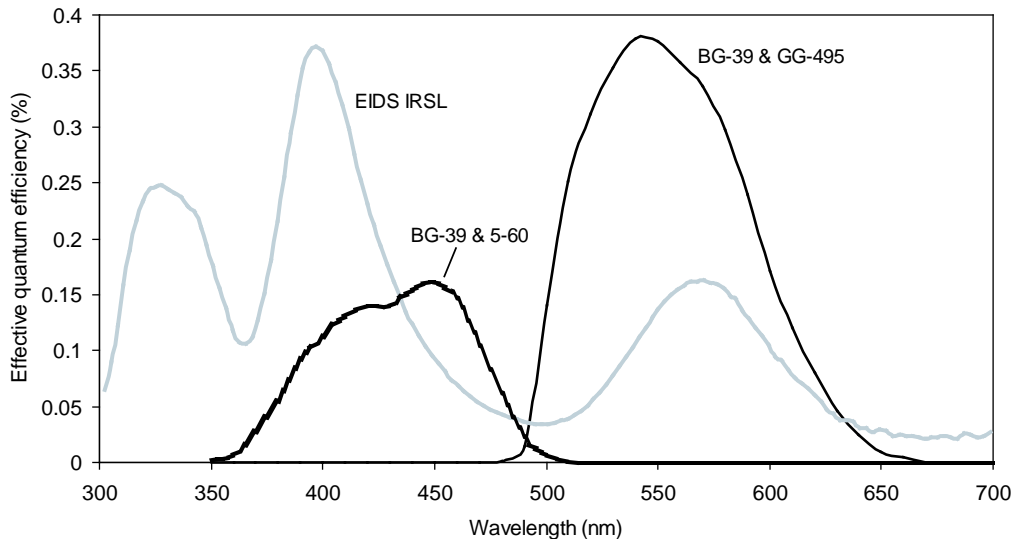
cut feldspar chips were approximately 1–2 mm thick. In addition to these rock samples, we also imaged three bright K-feldspar sediment separate samples; AKHC, EIDS and IV-1. Aliquots were given an 800 Gy γ dose and an image of the violet IRSL was obtained a short time after removal from the γ source. The violet IRSL was integrated for 1 minute using 20 mW/cm^2 1.43 eV excitation. The aliquots were then bleached for 1 hour under a sun-lamp and given another 800 Gy γ dose. As for the violet IRSL, the yellow-green emission was imaged promptly after removal from the γ source.

Once the images were corrected for thermal background noise they were processed in the following manner. The "violet" or (B) and "yellow-green" (YG) IRSL images were aligned to correct for small displacements and rotation of the sample between the two mea-surements[3]. The B image was assigned a linear blue palette, the YG image a linear yellow-orange palette and the two images combined additively. The intensity of the B relative to

---

[3]All image manipulation was performed using a custom program written for the format used by our cam-era. The final images were exported as 24-bit color bitmaps. In this way losses from the conversion of the 14-bit grayscale output of our camera to 24-bit color during the image processing was avoided.

the YG images was scaled so that the variation in both emission bands could be easily compared. The scaling factor used was held constant in a given sample to simplify comparison among aliquots.

The images in Figures 8.3–8.8 present a qualitative indication of the distribution of the luminescence centers in the cut feldspar samples. It is most interesting to compare the perthite K8 with microclines K9 and K10. In K9 and K10 the ratio of the B and YG luminescence is relatively constant across the sample whereas in K8 the two emission bands are segregated. S(TEM) X-ray fluorescence element maps of chip K8-1 suggest a correlation between regions that have bright B emission and are rich in potassium. On the other hand, Na-rich regions of the chip show bright YG emission (Figure 8.9).

We interpret this as the YG emission being primarily found in the albite phases of the crystal whereas most of the B emission originates in the orthoclase (K-rich) phases. In samples K9 and K10, either the Na and K is uniformly mixed in the crystal or the exsolved orthoclase and albite phases occur on a finer scale than that resolvable by our technique[4].

The IRSL emission maps for albite A3 clearly indicate large regions of the crystal with almost no B or YG emission. Where the IRSL was present, the ratio of the B to the YG emission was uniform, as can be seen from the even colour of the IRSL composites (Figure 8.7). The regions of low emission correlated to areas which were relatively visually transparent in the chips (see the back-illuminated visual image in Figure 8.10. S(TEM) element maps indicate that the low IRSL areas correspond to regions which are highly deficient in Na, K, Ca and Al but high in Si; these regions are likely composed of quartz.

---

[4]Na-Or intergrowths on the order 10 μm are not uncommon, Smith and Brown, 1988.

Figure 8.3: *False colour composite of B and YG images in A3. The relative scaling factors for the intensities of the B and YG images is 40:2. Intensity scales linearly with palette on right.*
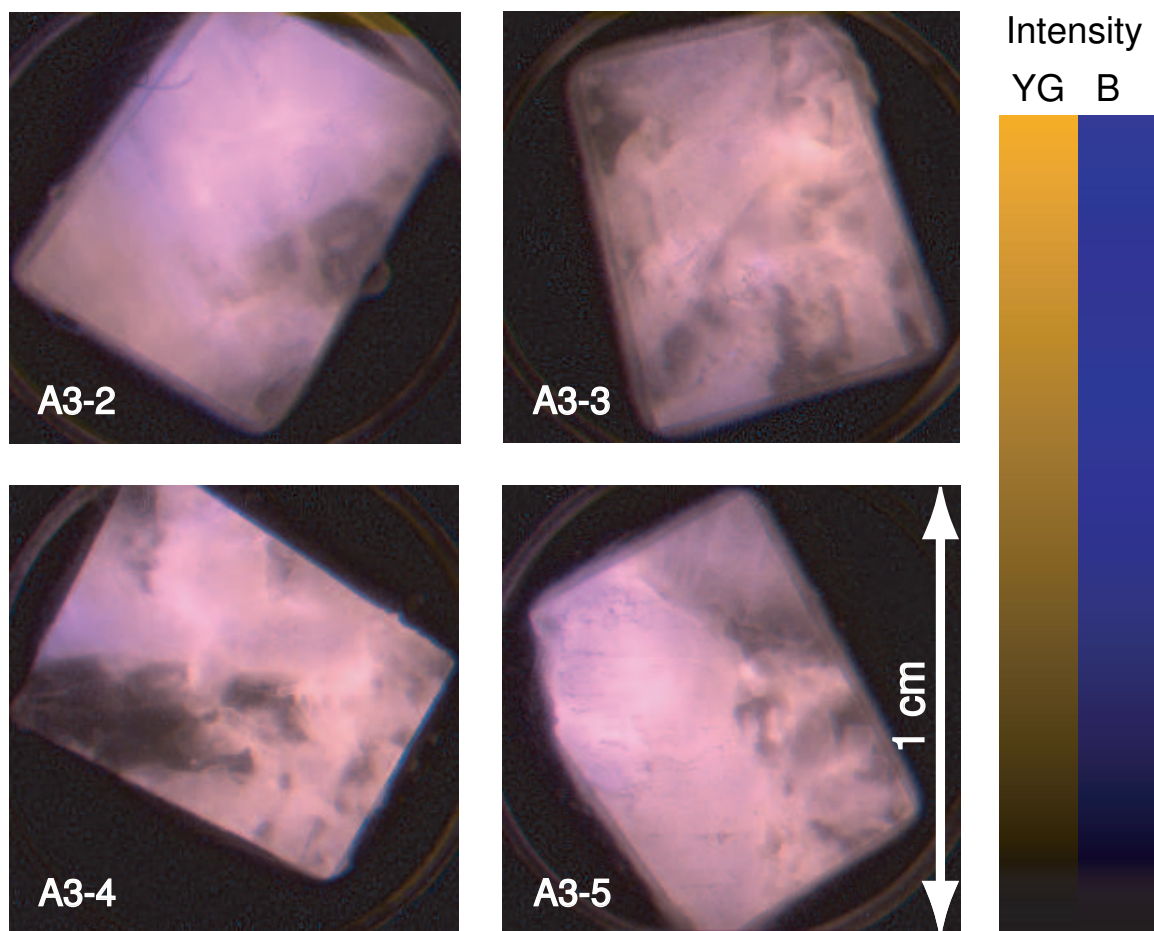
Figure 8.4: *False colour composite of B and YG images in K9. The relative scaling factors for the intensities of the B and YG images is 1:1. Intensity scales linearly with palette on right.*
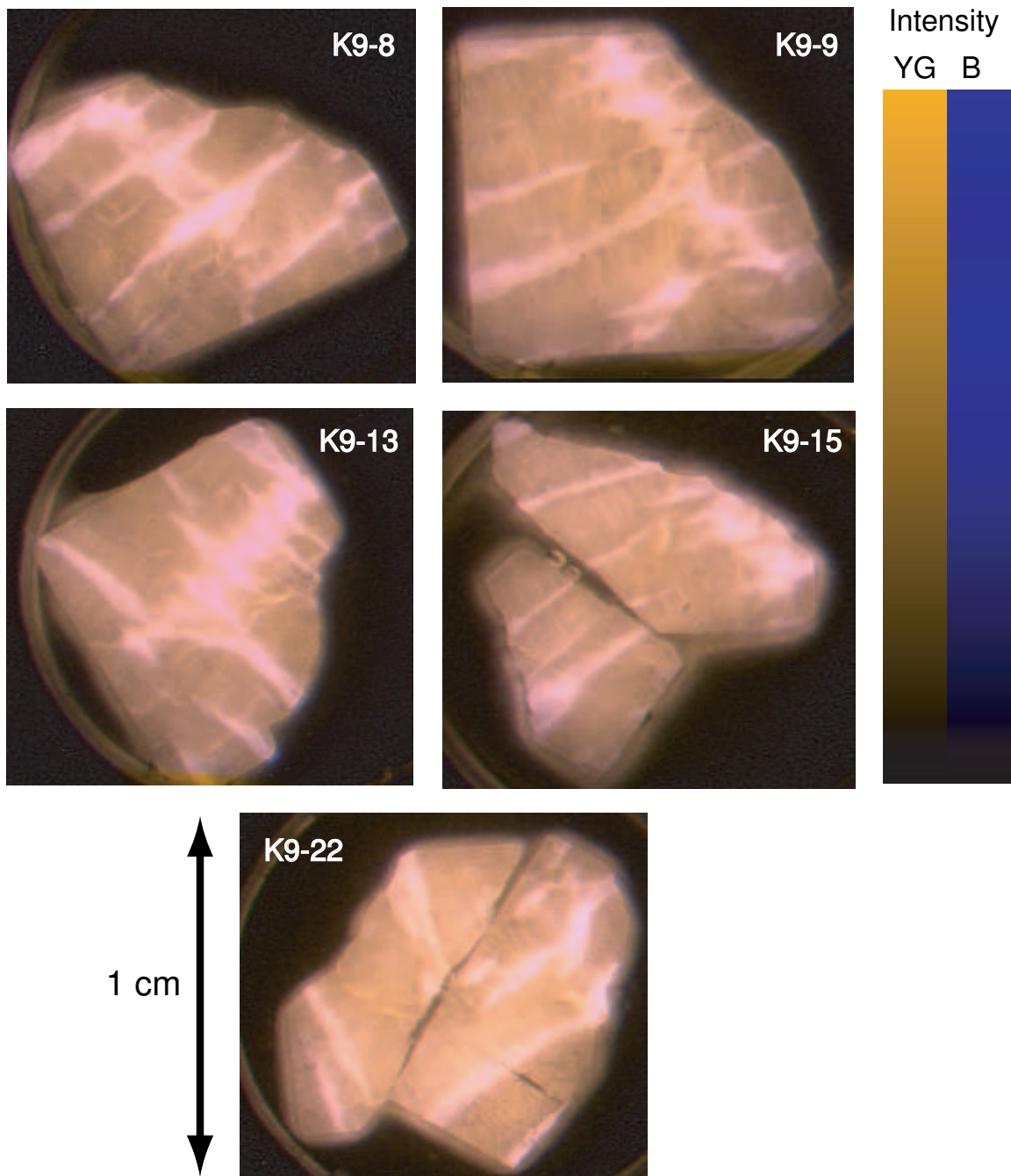
Figure 8.5: *False colour composite of B and YG images in K10. The relative scaling factors for the intensities of the B and YG images is 3:2. Intensity scales linearly with palette on right.*
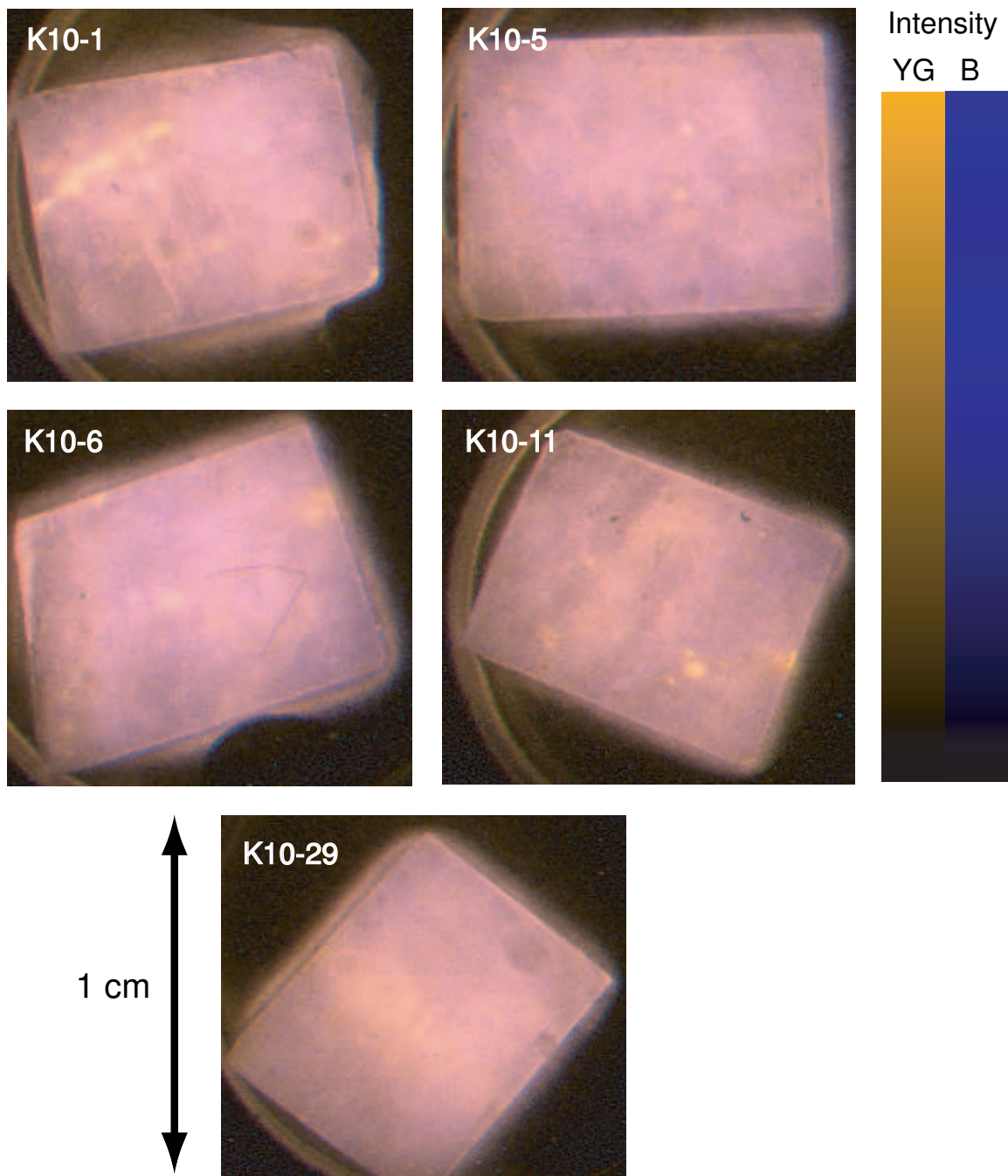
Figure 8.6: *False colour composite of B and YG images in A1. The relative scaling factors for the intensities of the B and YG images is 20:3. Intensity scales linearly with palette on right.*
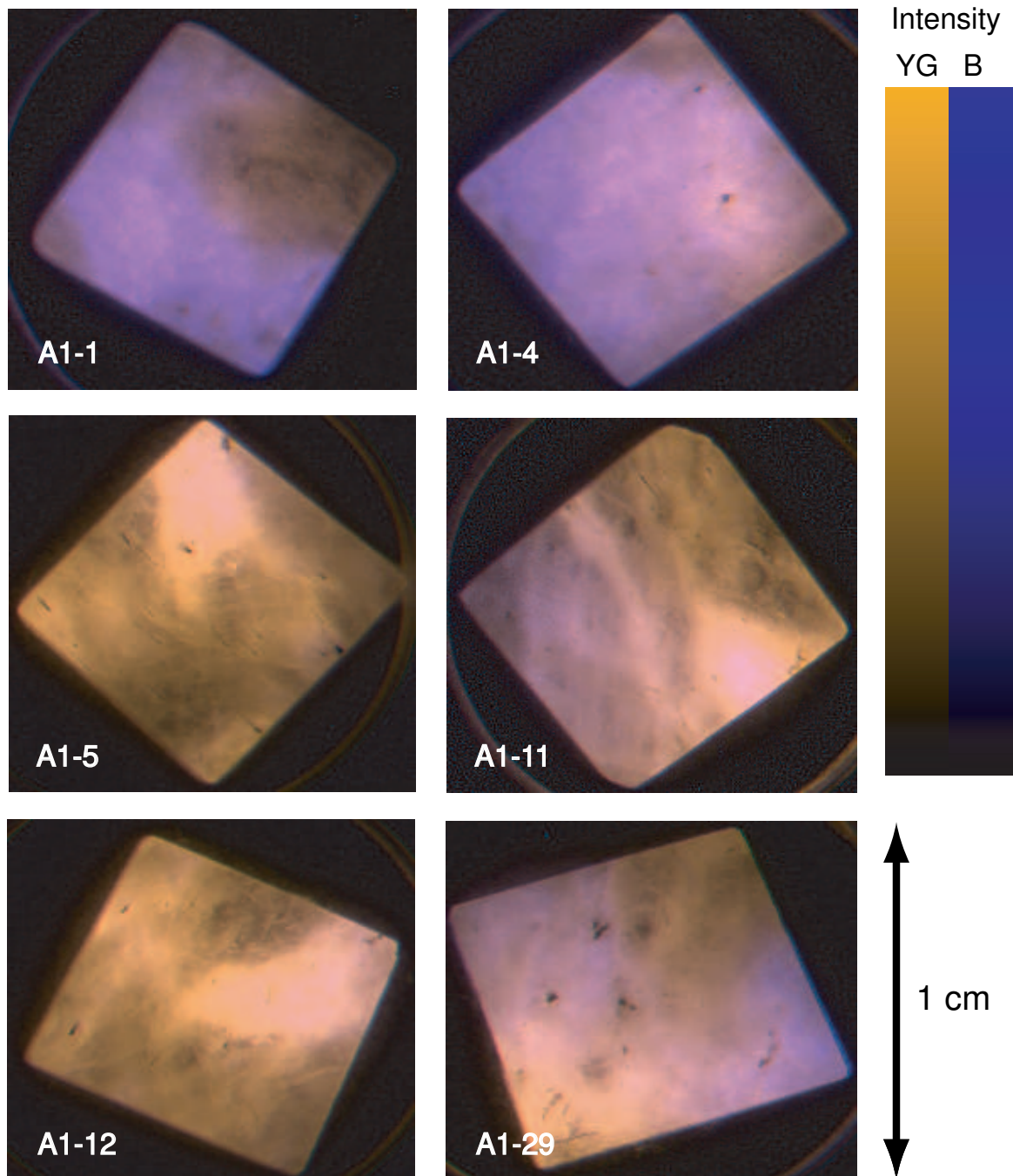
Figure 8.7: *False colour composite of B and YG images in K3. The relative scaling factors for the intensities of the B and YG images is 1:1. Note stray "albite" grain in K3-2 (circled) and the bright linear YG feature in K3-17. Intensity scales linearly with palette on right.*
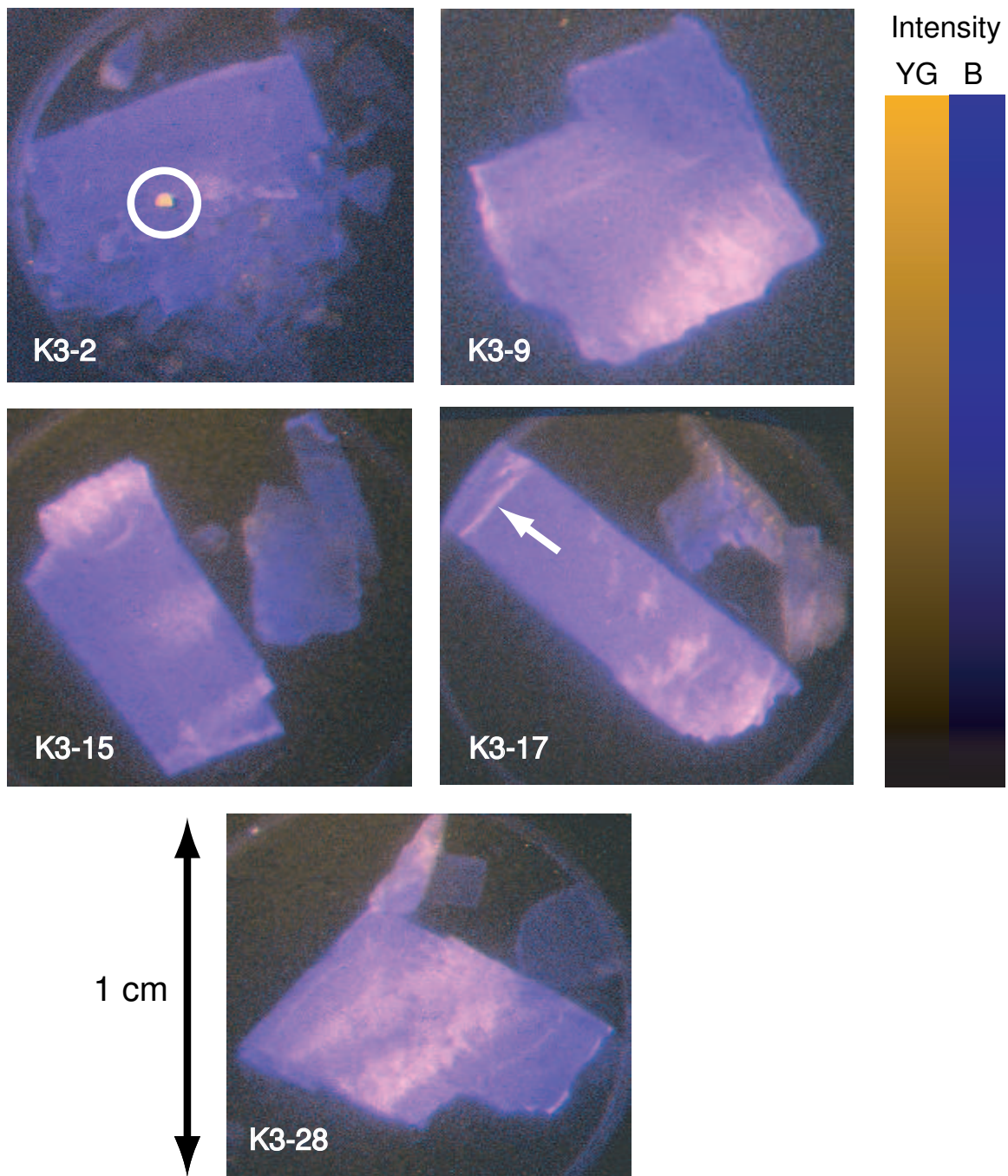
Figure 8.8: *False colour composite of B and YG images in K8. The relative scaling factors for the intensities of the B and YG images is 80:5. Intensity scales linearly with palette on right.*
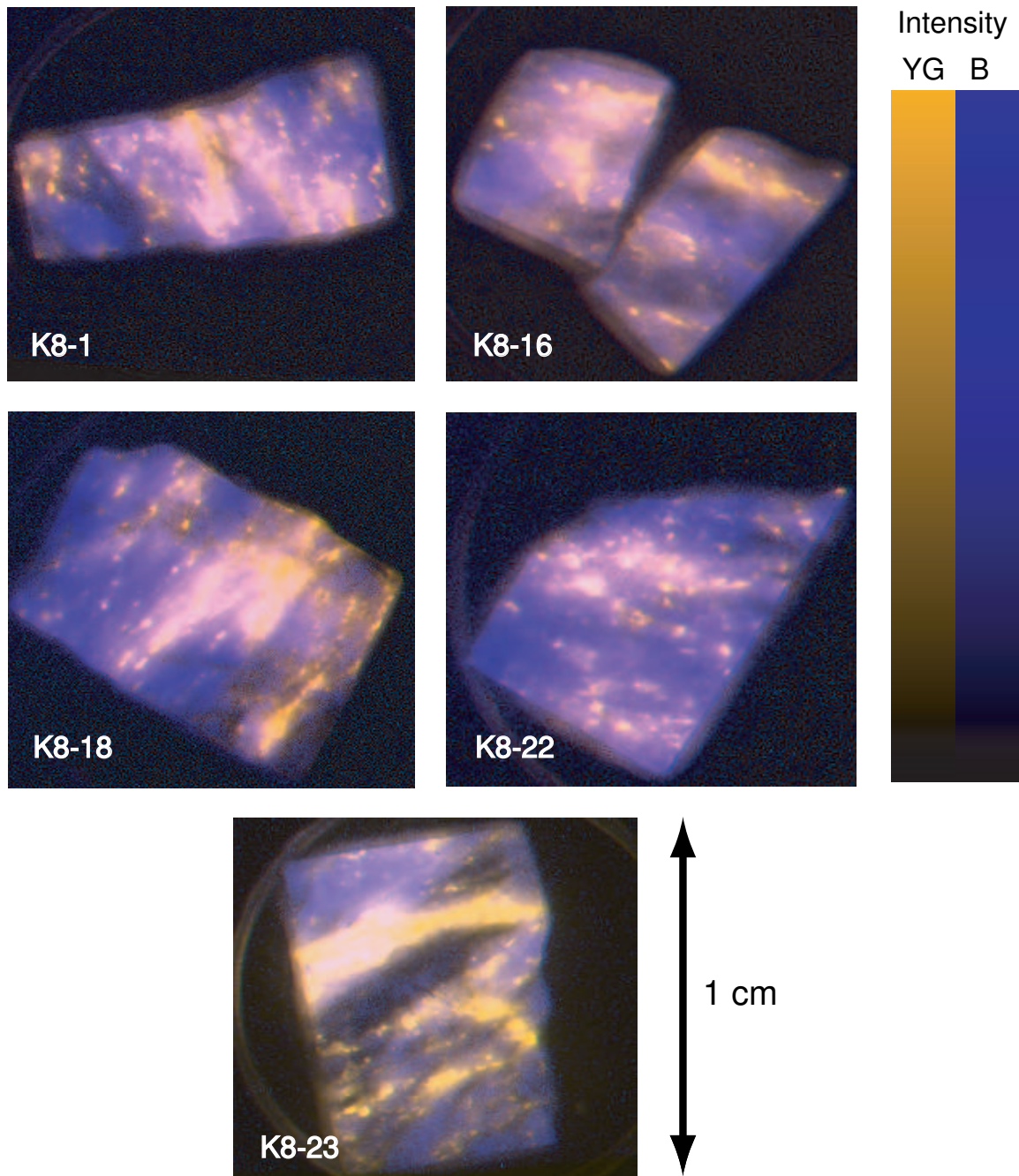
Figure 8.9: *Comparision of STEM X-Ray fluorescence element maps to the B and YG IRSL emission maps for perthite chip K8-1. Black indicates higher content/emission intensity. Field of view is approximately 200 µm wide. Note correlation of K-rich areas with regions where B emission is bright. In contrast, Na-rich regions are bright in the YG emission band (note circled regions in top-right images).*
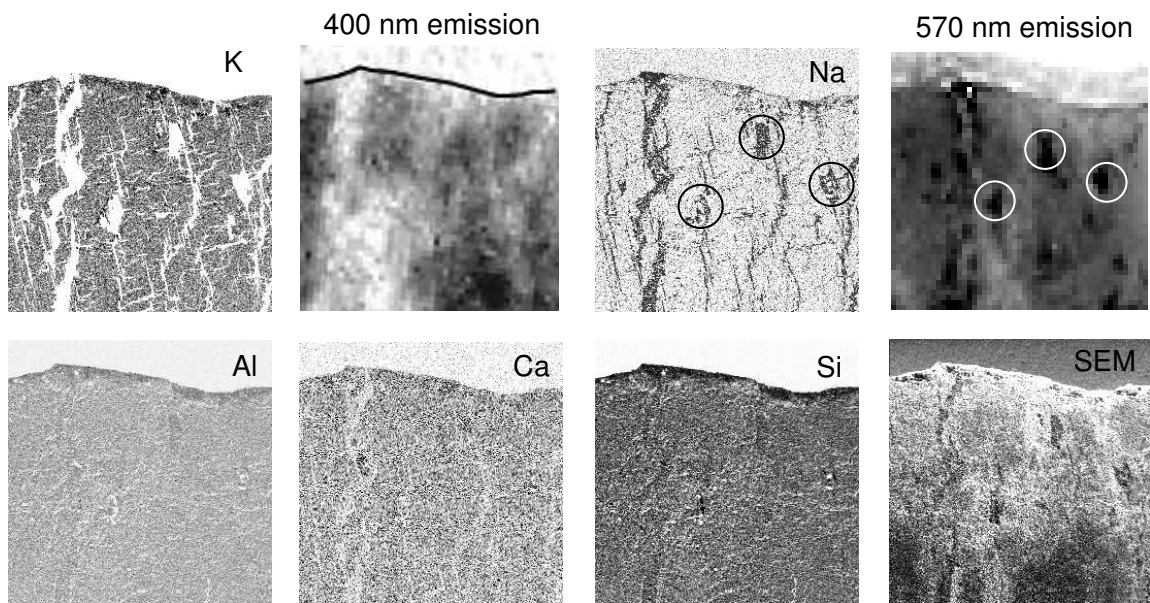
Figure 8.10: *Comparision of STEM X-Ray fluorescence element maps to the YG IRSL emission maps for albite chip A3-4. Black indicates higher content/emission intensity. Visible light photo of backlit chip (positive image; bright areas are transparent). Field of view is approximately 200 μm wide. Note correlation of transparent/high silicon areas with regions where YG emission is absent. High silicon domains are low in Na, Ca and Al which are abundant in plagioclase (potassium is low throughout the chip) and are likely to be composed of quartz.*
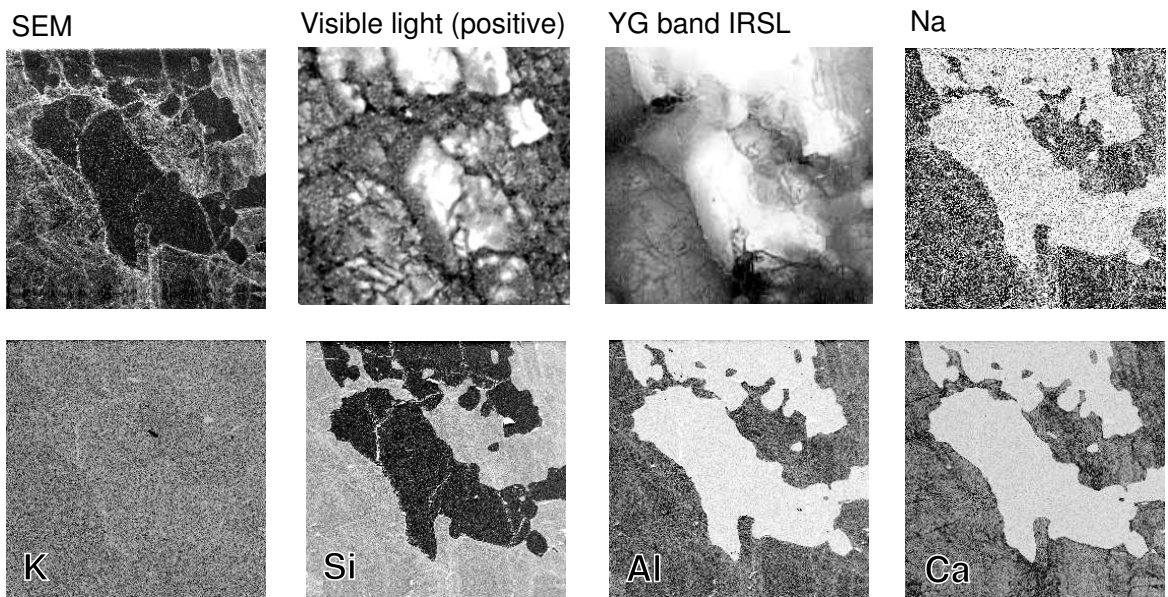
Figure 8.11: *False colour composite of B and YG images in AKHC, EIDS and IV-1. The relative scaling factors for the intensities of the B and YG images is 40:2. Intensity scales linearly with palette on right.*
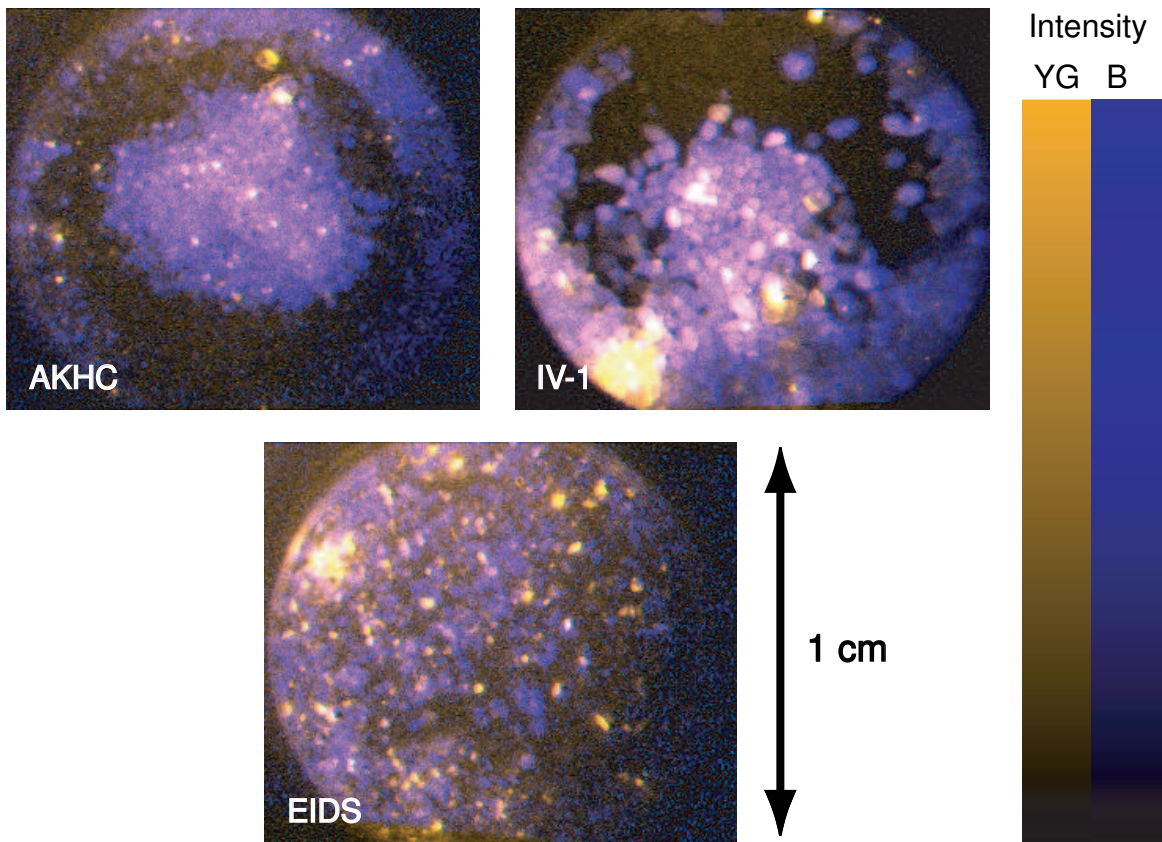
The IRSL maps for the three bright separated K-feldspar samples, AKHC, EIDS and IV-1 clearly indicate that most of the YG emission originates from a few grains in the sample. These likely consist of albite grains that failed to be removed by the density separation. One will note that the luminescence from these bright "albite" grains is sufficient to illuminate the surrounding grains and the aluminum planchet. It is also noteworthy to mention that in these samples at least, the violet luminescence appears to be relatively uniform among the grains. This is probably a feature specific to laboratory dosed samples, one might expect that natural samples would show a greater scatter in individual grain intensities due to uneven bleaching and dose rates acquired in the natural environment.

Chapter 9

Feldspar Inclusions in Quartz

9.1   Introduction

The possibility of separate quartz and feldspar phases in a sand granule is not to be over-
looked, especially in view of the work presented in Chapter 8 on oligoclase A3. Quartz
appears to have a single optically stimulated luminescence (OSL) emission band at 3.4 eV
(Huntley *et al.*, 1991). Unlike feldspars, quartz does not exhibit an excitation resonance in
the near IR; the excitation efficiency increases more or less exponentially with the excita-
tion photon energy (Ditlefsen and Huntley, 1994; Huntley *et al.*, 1996). The appearance
of 3.1 eV emission under 1.44 eV excitation in quartz therefore immediately suggests the
presence of feldspar inclusions within the quartz grains.

The possibility of incomplete separation of quartz and feldspar grains is unlikely due
to the much slower HF etching rate of quartz relative to feldspar. Any feldspar remaining
after the etch can only survive as protected inclusions within the quartz. In the quartzes from
south-east South Australia (SESA series) this is not an issue since the untreated sediments
consist almost entirely of quartz and calcium carbonate (Huntley *et al.*, 1993b).

Godfrey-Smith *et al.* (1988) reported the infra-red excitation of violet luminescence in
quartz. Spectral studies by Short and Huntley (1992) indicated that the emission spectrum
of quartz under 2.41 eV stimulation was significantly different from that under 1.44 eV
excitation. In the case of IRSL the 400 nm component typical of K-feldspars was domi-
nant. Quartz excitation spectra in the range 780–920 nm produced by Godfrey-Smith and
Cada (1996) indicate an excitation peak at 1.48 eV for the two quartzes studied. Using

a well dated sequence of stranded beach dunes in southeast South Australia, Huntley *et al.* (1993b) demonstrated that reasonable optical ages can be obtained by measuring the 3.1 eV emission of (presumably feldspar) inclusions under IR stimulation.

The purpose of the present study is to combine measurements of IRSL stimulation spectra with emission spectra on the same samples. The objective is to provide much better evidence that the 3.1 eV IRSL emission in quartz is due to feldspars.

9.2 Emission spectra

Measurement of the spectral emission of our quartzes under 1.44 eV excitation proved difficult due to the low intrinsic intensity of the samples. For this reason, emission spectra were only obtained for the three brightest samples, SESA-63, SESA-101 and NL-1; these

Figure 9.1: *IRSL emission spectra for quartzes SESA-63, SESA-101 and NL-1 under 1.43 eV excitation. Spectra have been normalized to the 3.2 eV peak, except that for the feldspar sample EIDS which is shown for comparison (arbitrary scaling).*
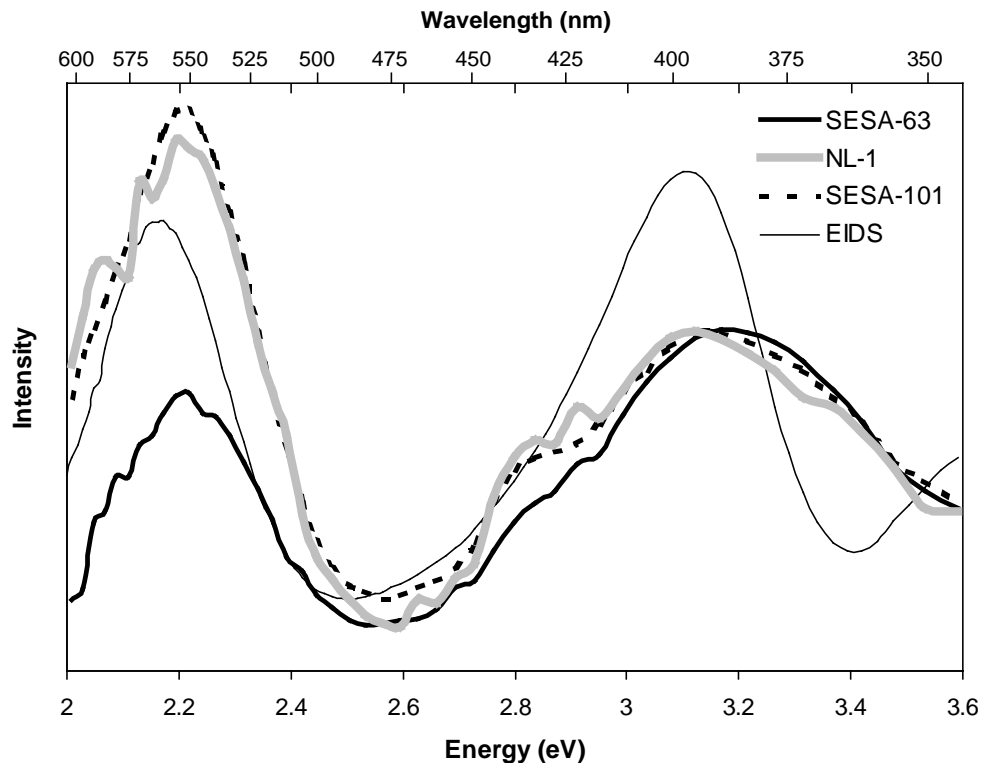
are shown in Figure 9.1. The samples were held at 320 K during the measurement and were measured promptly after irradiation (750 Gy, γ) to increase the luminescence intensity. In addition, the spectra represent the average taken over three aliquots. Only the "Visible" band defined in Chapter 4 was measured, using a spectrometer bandwidth of 25 nm. The measurement technique was identical to that described in Chapter 4.

The emission in the visible regime is dominated by two broad bands centered at 3.1–3.2 eV and 2.22 eV. The violet emission is at somewhat higher energy than the 3.1 eV found for the bulk feldspar samples. Aside from this difference, the IRSL spectra for the quartz samples is generally consistent with that expected for feldspars. The 2.2 eV emission is strong in all three quartz samples (it dominates in NL1 and SESA-101) which suggests that the albite content is significant in all three samples.

9.3 Excitation spectra

Excitation spectra for the 3.1 eV emission band were produced for eight quartz sediment separate samples; SESA-63, SESA-71, SESA-101, SESA-121, DY-23, TAG-8, CBSS and NL-1. The provenance of these samples is described in Table 3.4 and the experimental procedure was identical to that described in Chapter 5. The excitation spectra are shown in Figures 9.2–9.5.

The excitation resonance at 1.44 eV typical of feldspars is evident in all of the samples measured. The intensities in the excitation spectra exhibit a significant amount of scatter that cannot be solely attributed to photon noise. Nevertheless, the shape of the excitation response is at least qualitatively similar to that observed in the "pure" feldspar samples. The sharp rise at photon energies above 1.65 eV in this case is undoubtedly due to the excitation of the 3.44 eV (360 nm) OSL in quartz which overlaps with our pass-band centered on 3.1 eV.

The combination of these excitation spectra with the emission response described provides strong evidence that the violet IRSL in these quartzes is due to feldspar inclusions.

Figure 9.2: *Excitation spectra for quartzes SESA-63 (top) and SESA-71 (bottom).*
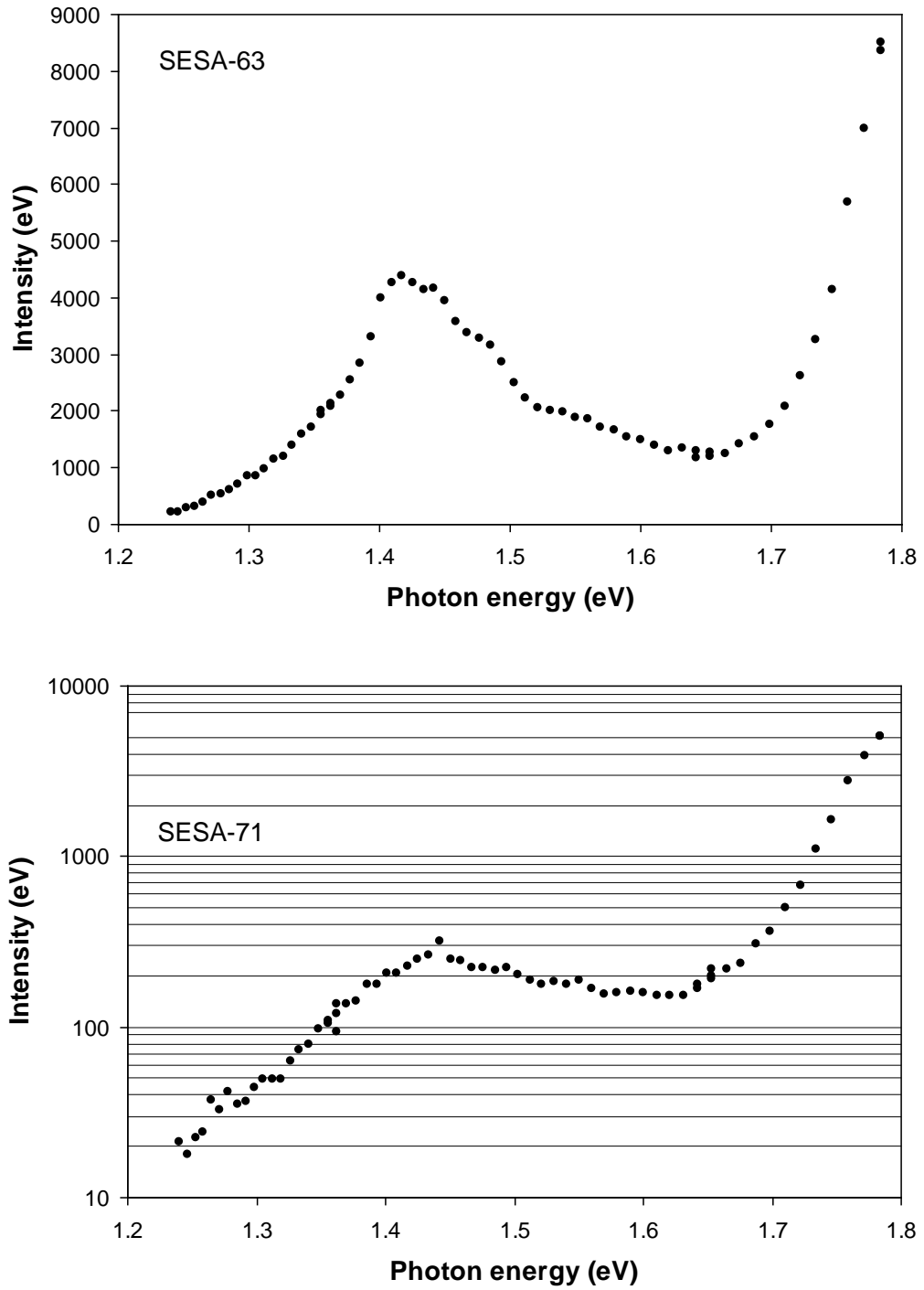
Figure 9.3: *Excitation spectra for quartzes SESA-101 (top) and SESA-121 (bottom).*
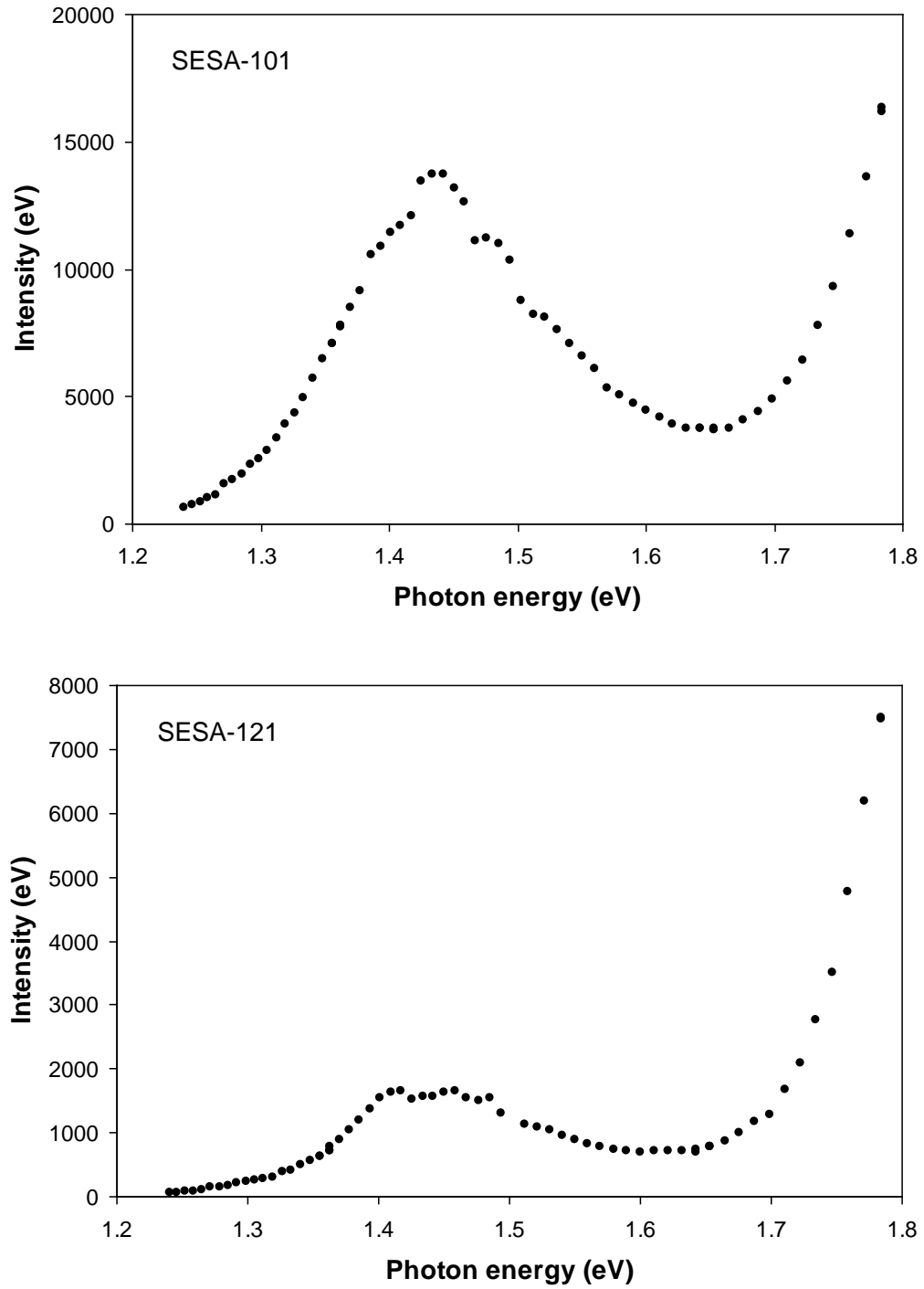
Figure 9.4: *Excitation spectra for quartzes DY-23 (top) and TAG-8 (bottom).*
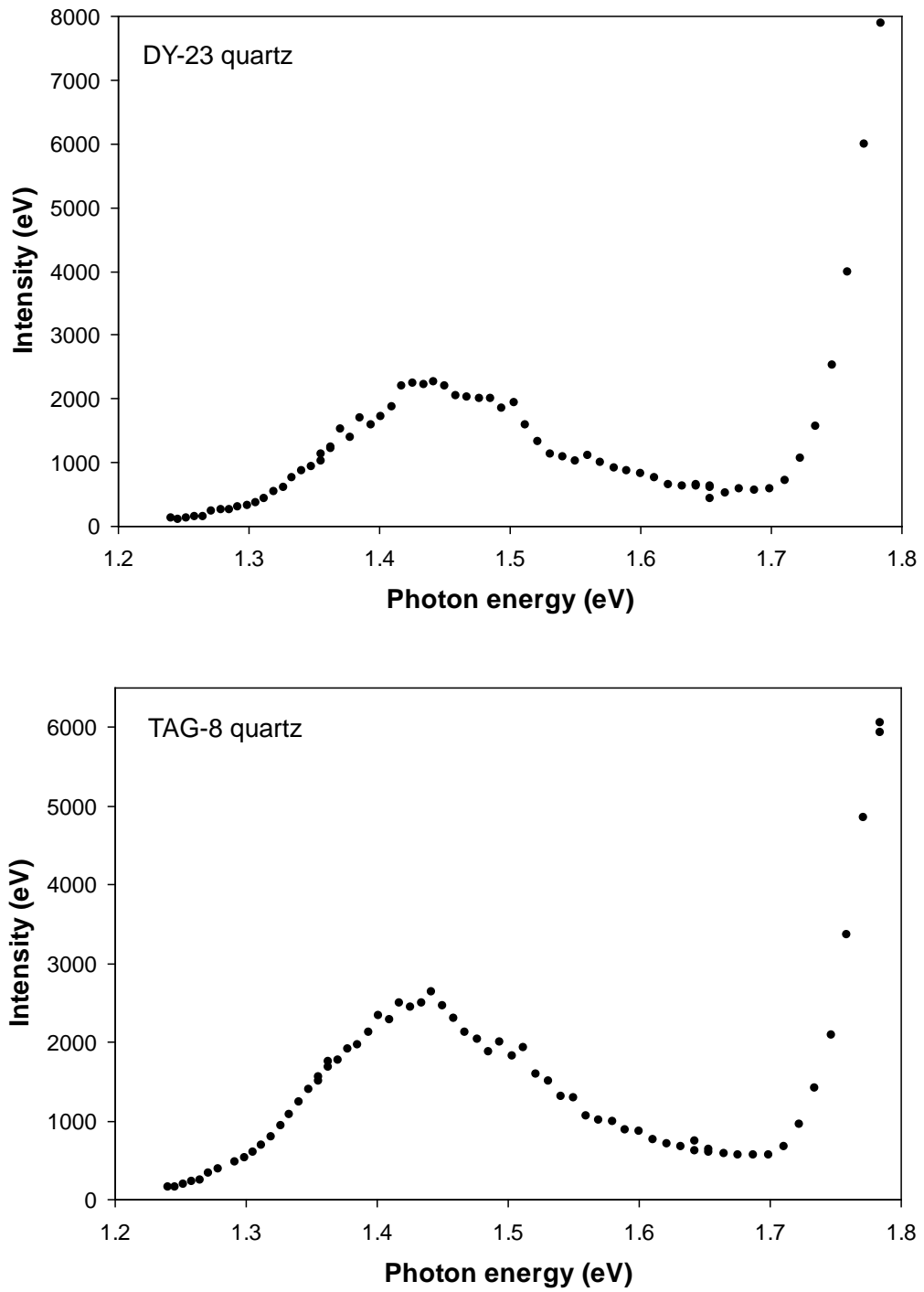
Figure 9.5: *Excitation spectra for quartzes CBSS (top) and NL-1 (bottom).*
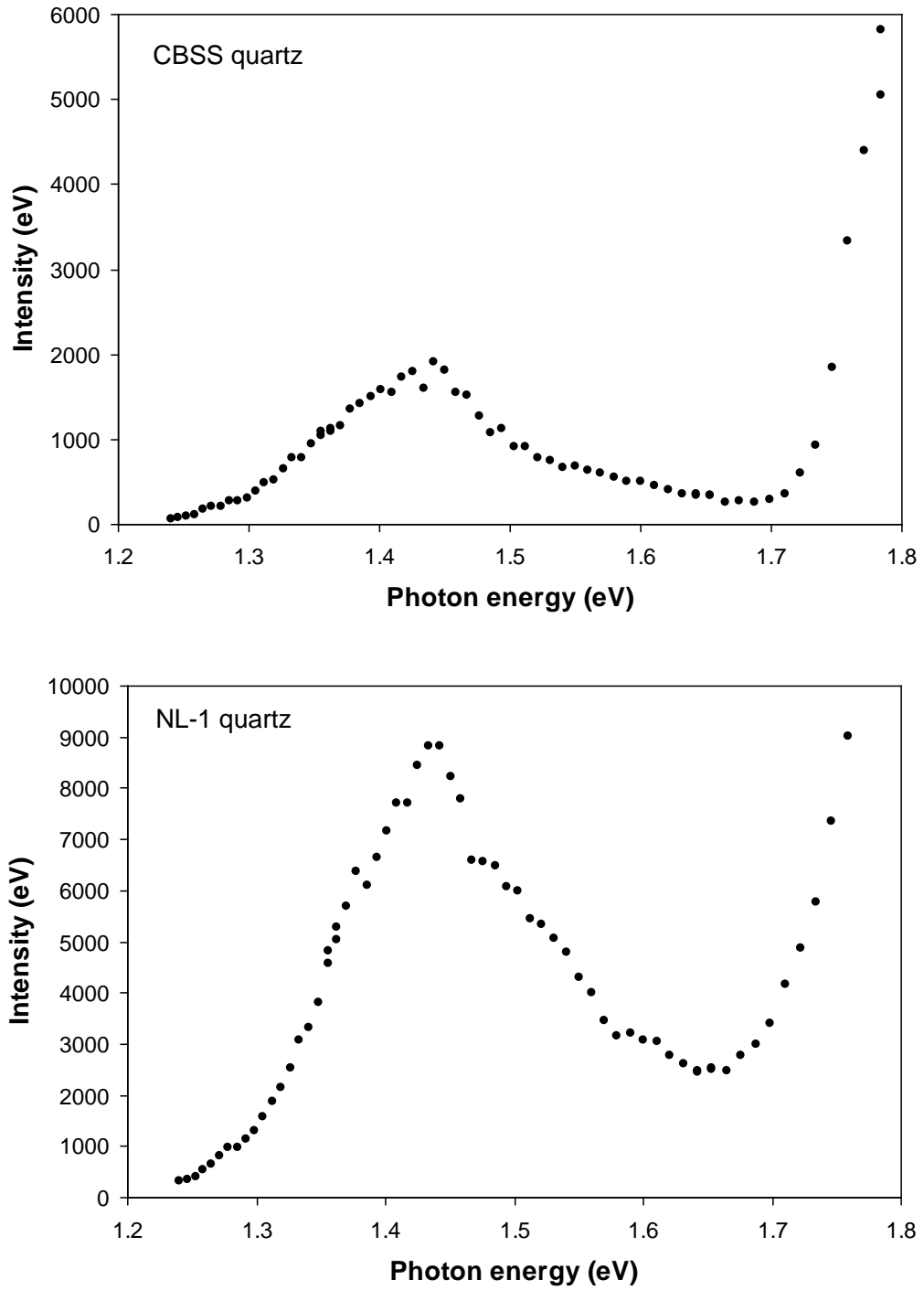
Chapter 10

Models

10.1 Review of basic kinetic theory

For a single trap, a constant probability of eviction (at fixed excitation energy) and negligible retrapping, the rate equation giving the number of trapped electrons n(t) is,

$$\frac{dn(t)}{dt} = -a_i n(t) \tag{10.1}$$

where a is the probability per unit time that the electron be excited into the conduction band. In general a will depend on temperature, the excitation energy, the trap depth ε and other details of the trap. The excitation power and temperature are assumed to be fixed so that a is constant.

If one assumes that the photo-excited electrons proceed directly to the recombination centers, the recombination rate and hence the luminescence intensity $I(t)$ will be proportional to the eviction rate of the electrons, $-\frac{dn(t)}{dt}$. The time dependence of $n(t)$ is easily solved from the previous equation, whence,

$$I(t) \propto -\frac{dn(t)}{dt} = aNe^{-at} \tag{10.2}$$

with N being the total number of trapped electrons at $t = 0$. This is referred to as monomolecular or first-order kinetics, by analogy to the time dependence of concentration seen in monomolecular chemical reactions. If retrapping and charge pair interactions are negligible, then for a discrete distribution of traps of depth ε_i the time dependence of the intensity

will simply be of the form,

$$I(t) \propto \sum_{i=1}^{N_t} a_i N_i e^{-a_i t} \tag{10.3}$$

where the sum is over the N_t trap depths and N_i is the number of electrons in the traps with excitation probability a_i. For a small number of discrete trap depths the long time behaviour will depend on the trap with the smallest excitation probability, a_i.

For a continuous distribution of trap depths, the situation is more complicated. The sum is replaced by an integral,

$$I(t) \propto \int_0^\infty -n(\varepsilon)a(\varepsilon)e^{-a(\varepsilon)t}d\varepsilon \tag{10.4}$$

where $n(\varepsilon)d\varepsilon$ represents the number of traps in the energy range ε to $\varepsilon + d\varepsilon$. The first case of special interest is that in which the distribution of trap depths is uniform, *i.e.* $n(\varepsilon)$ is constant. In the case of photo-ionization just below the conduction band, one can expect the excitation probability to depend exponentially on the excitation photon energy $\hbar\omega$ according to Urbach's rule (Kurik, 1971), for $\hbar\omega < \varepsilon$,

$$a(\varepsilon) = a_0\, e^{-\sigma(\varepsilon - \hbar\omega)/kT} \tag{10.5}$$

where a_0 is a constant and the parameter σ depends on temperature[1]. This excitation probability results in the following time dependence of the intensity,

$$I(t) \propto \int_0^\infty -e^{-\sigma(\varepsilon - \hbar\omega)/kT}\exp(-a_0 \cdot t\, e^{-\sigma(\varepsilon - \hbar\omega)})d\varepsilon \tag{10.6}$$

which is readily solved,

$$I(t) \propto \frac{NkT}{\sigma t}[1 - \exp(-a_0 t e^{\sigma\hbar\omega/kT})] \tag{10.7}$$

Once a time greater than $a_0^{-1}e^{-\sigma\hbar\omega/kT}$ has passed, the intensity is proportional to the inverse of time. A similar expression is found in the case of phosphorescence, *i.e.* thermal eviction from the traps (*e.g.* Randall and Wilkins, 1945).

The other special case for which a simple solution to the rate law is obtained is that of an exponential trap distribution[2].

$$n(\varepsilon) = Ae^{-\beta\varepsilon} \tag{10.8}$$

---

[1]At high temperatures σ approaches a constant value. The temperature at which this occurs depends on the energy of the phonons involved in producing the absorption edge (Kurik, 1971).

[2]For example this trap distribution accounts for the phosphorescence of certain ZnS phosphors (Randall and Wilkins, 1945).

Now, substituting this and Urbach's rule into Equation 10.4 leads to,

$$I(t) \propto \int_0^\infty A e^{-\beta\varepsilon} a_0 e^{-\sigma(\varepsilon-\hbar\omega)/kT} exp(-a_0 \cdot t\, e^{-\sigma(\varepsilon-\hbar\omega)}) d\varepsilon \qquad (10.9)$$

Making the substitution, $\xi = a_0 t\, e^{-\sigma(\varepsilon-\hbar\omega)/kT}$ one obtains,

$$I(t) \propto \frac{kT A e^{-\beta\hbar\omega}}{\sigma t\, (a_0 t)^{\beta kT/\sigma}} \int_0^\infty \xi^{\beta kT/\sigma} e^{-\xi} d\xi \qquad (10.10)$$

The integral is constant at fixed temperature so we are left with a time dependence,

$$I(t) \propto t^{-(\frac{\beta kT}{\sigma}+1)} \qquad (10.11)$$

A similar power law for the time dependence of the luminescence intensity is obtained in the case of phosphorescence, in that case the exponent is $\alpha = -(\beta kT + 1)$. The case $\beta = 0$ is identical to that of the uniform trap distribution and results in $1/t$ dependence of the intensity. If $\beta kT/\sigma = 1$, then the inverse square law referred to as bimolecular or second-order kinetics is obtained.

One cannot generally interpret the observation of an inverse power law in the time dependence of the luminescence as an indication of the existence of a distribution of traps with different depths. The following example taken after Nakazawa (1999) should further clarify this point. Consider a model in which free electrons may recombine with holes or be retrapped, with the probabilities r and b respectively. Let n_c be the number of electrons in the conduction band, n_t the number of electrons in traps and p the number of free holes. The number of holes is equal to the total number of free and trapped electrons so that, $p = n_t + n_c$. The trap density is denoted by N and as before, a is the probability per unit time for eviction out of the trap. The rate equations are,

$$\frac{dn_t}{dt} = -an_t + b(N - n_t)n_c \qquad (10.12)$$

$$\frac{dp}{dt} = -rpn_c$$

The luminescence intensity is proportional to the rate of transfer of charge into the holes (luminescence centers), $-\frac{dp}{dt}$. If one assumes that the number of electrons in the conduction band is always much smaller than that in the traps then one may approximate $p \simeq n_t$. The above equations may be explicitly solved for two cases, $b \ll r$ and $b = r$. In the first case

($b \ll r$) first-order kinetics are obtained, that is the intensity follows a decaying exponential in time. For the case $b = r$, when the hole-capture and trap-capture probabilities are equal, the solution is,

$$I(t) \propto \frac{I_0}{(1 + Nt/an_t)^2} \tag{10.13}$$

which in the long time limit reduces to the bimolecular rate law derived earlier using an exponential distribution of electron traps. McKeever and Morris (1994) proposed a model of essentially this type (with additional traps) to describe the OSL decay curve.

The classic model for TL is due to Randall and Wilkins (1945), it involves electrons from a single trap level recombining at one luminescence center (hole-trap). Under quasi-equilibrium conditions the following rate equations describe the trap emptying kinetics (Halperin and Braner, 1960; Levy, 1985; Faïn *et al.*, 1994),

$$\frac{dn_t}{dt} = -an_t + \frac{ab(N - n_t)n_t}{b(N - n_t) + rp} \tag{10.14}$$

$$\frac{dp}{dt} = -rpn_c$$

where n_t and n_c are the electron densities in the traps and conduction band respectively, p is the hole density ($p = n_t + n_c$) and N is the density of traps. The recombination probability per unit time is r and the re-trapping probability is b. In the case of TL, the probability to thermally excite the electron out of the trap, a, is given by,

$$a = se^{-E/k_bT} \tag{10.15}$$

The long-time solutions of Equation 10.14 are similar to those of Equation 10.12; if $a = 0$ then there is no re-trapping and first-order kinetics ensue, whereas if $r = a$ or $n_t \ll N$, then second-order kinetics obtain.

What should be retained from the above discussion is the fact that one cannot use the form of the decay curve as a definite indication of the electronic processes occurring in the crystal. Different mechanisms can lead to similar decay laws, as was shown for the bimolecular rate law.

In general, monomolecular decay is rarely observed in luminescent systems, the power-law decay being by far the most commonly observed rate law (*e.g.* see the review of

Jonscher and Polignac, 1984). It is not entirely surprising therefore that the slope-vs.-intensity experiment (Chapter 7) has shown that the quasi-monomolecular law of Equation 10.3 does not apply to the OSL of feldspars. Specifically, Equation 10.3 is of the form $I(E) \propto f(E/E_0, E/E_1, E/E_2, ...)$ rather than the form $I(E) \propto f(E/E_0)$ implied by the observed scaling of S_0 with I_0^2. These results strongly suggest that there is a single trap rather than a distribution, but this cannot be conclusively stated. The connection (if any) of the parameter E_0 in the power law decay to the excitation probability out of the trap is not proven, so that a distribution of traps cannot be entirely ruled out from this experiment alone.

This being said, there are at least two additional pieces of empirical evidence that suggests that a distribution of traps is unlikely. Firstly, the Becquerel decay law has been observed in many systems, most of which involve a single trap (Jonscher and Polignac, 1984). One may reasonably argue from this that it is unlikely that the power law decay arises from a distribution of trap depths but rather from other details of the recombination, for example retrapping. Secondly, the fact that the 1.45 eV excitation resonance in many cases displays a strong Lorentzian line-shape is strong evidence that a single trap is involved. A distribution of traps is likely to lead to a Gaussian profile to the excitation resonance.

10.2 Towards a model for the 3.1 eV IRSL

At this point it is useful to summarize the information concerning the violet (3.1 eV) IRSL that must be accounted for in any new models. The following observations have been made concerning the violet luminescence;

- The excitation resonance at 1.44 eV may be interpreted as arising from a single transition with a Voigt absorption profile. The contribution from the secondary resonance at 1.55–1.6 eV varies widely for different samples; although it is a significant contributor in some samples, it is a minor contributor in most and should be given secondary importance in developing a basic model.

- A near exponential increase in the excitation energy response occurs for photon energies greater than ~2 eV.

- The excitation spectrum is unaffected by the polarization of the excitation light (K7). However the luminescence intensity depends on the polarization of the excitation

which suggests that the excitation resonance is associated with a dipole transition.

- The recombination luminescence intensity depends on temperature through the Boltzmann factor, e^{-E_a/k_bT}. At temperatures above 200 K E_a is of the order 0.1–0.15 eV, below 200 K, E_a is abruptly reduced to about half this value (0.05 eV). The shape of the luminescence decay curve is unaffected by temperature which implies that the total integrated IRSL intensity must increase with temperature.

- The decay kinetics are of the Becquerel type; this appears to apply universally to the IRSL and the prompt phosphorescence. Slight departures from the Becquerel law have been noted early in the decay curve; generally the power law exponent α of the decay is somewhat smaller in the early part of the decay.

- The preheating time appears to have no significant effect on the decay parameters.

- At low doses the decay parameter α varies roughly with the logarithm of the irradiation dose. At high doses α reaches a fixed value, generally below 1.2. The dose at which α saturates is highly sample dependent.

- The decay parameter E_0 reaches a minimum at the excitation resonance 1.44 eV. In addition, two other minima in E_0 are observed below 1.3 eV and at 1.7 eV.

- The initial slope of the decay is proportional to the square of the initial intensity up to energies much higher than the 1.4 eV resonance. This appears to be consistent with the Becquerel decay law, specifically the initial intensity I_0 is roughly proportional to α/E_0 as expected (although there is significant scatter in the wings of the excitation resonance).

- There are substantive differences between the IRSL emission spectra and the phosphorescence spectra. Furthermore, the phosphorescence following irradiation differs from that which occurs after cessation of illumination of an irradiated sample. This implies that the certain recombination centers are connected to specific traps (*e.g.* the center associated with the 2.5 eV phosphorescence). Other centers appear to be more "universally" available, for example the center responsible for the 1.76 eV emission.

There are other known effects that are not listed above, for example the slow rise of the luminescence in samples that have been partially "bleached" (McKeever *et al.*, 1997), but these are not critical in determining the choice of model[3]. The principal problem that any new model must address is the dependence of the decay parameters α and E_0 on excitation energy and radiation dose and their relative insensitivity to temperature.

Models involving rate equations of the form of Equation 10.12 (*e.g.* McKeever and Morris, 1994; McKeever *et al.*, 1997; Bailey *et al.*, 1997 (for quartz)) and Equation 10.14 (Faïn *et al.*, 1994) cannot account for an exponent α in the decay law, ranging between 0.3 and 1.2. This was verified through numerical solutions of both models, solving for the hole rate dp/dt (which is proportional to the recombination luminescence intensity) in both cases. Although the numerical solutions were often close to the Becquerel form, both models could not provide solutions with α less than 1 that remained consistent with the data[4]. This is essentially due to the second order nature of the differential equations that lead to a $1/t^2$ dependence at long times.

The model of Thomas *et al.* (1965) was also considered. This model assumes that the recombination rate depends exponentially on the average separation of the trap (donor) and the luminescence center (acceptor). For example, in the case of tunnelling recombination the recombination probability w(r) for a donor and acceptor separated by distance r may be written as,

$$w(r) = w_0 e^{-r/r_0} \tag{10.16}$$

where w_0 is an arbitrary constant and r_0 is the pair separation. In the case of either the donor or acceptor species in excess Thomas *et al.* derive,

$$
\begin{aligned}
I(t) = {} & \left\{ 4\pi n \int_0^\infty w(r) \exp[-w(r)t] r^2 dr \right\} \times \\
& \left\{ \exp\left[4\pi n \int_0^\infty (\exp[-W(r)t] - 1) r^2 dr \right] \right\}
\end{aligned}
\tag{10.17}
$$

where the intensity $I(t)$ is given by the probability of finding an electron on a donor and n is the density of the majority species. The solution to the above rate equation is either

---

[3]Several models can produce a slow rise in the luminescence, all that is needed is a delay between the excitation of charge out of the traps and recombination at the luminescence centers; *e.g.* diffusion or retrapping.

[4]The only solutions with α less than 1 approached an exponential decay, or only fit the initial 30% decay portion of the decay curve. Neither of these cases apply to the experimental decay curves.

exponential in time or follows $1/t$ at long times, so that the free parameters (w_0, r_0 and n) cannot be adjusted to allow a good fit to the decay curves for small excitation photon energies[5].

The diffusion model proposed by Hong *et al.* (1981) to explain electron-hole recombination in amorphous semiconductors produces $t^{-3/2}$ long time behaviour. Given the lack of success obtained in trying to "force" a fit using rate equations that produce $1/t$ or $1/t^2$ in the long time limit, it is obvious that the Hong's diffusion model is equally incapable of producing the required continuous variation in α.

Jonscher and Polignac (1984) approached the problem of the ubiquitous nature of the power law decay in luminescent systems by considering the time dependence of the dielectric polarization in the material. In their view, the power law dependence of the luminescence is connected to the relaxation of dielectric polarization in the material following a strong perturbation (such as eviction of an electron from a trap). Several relaxation phenomena have been shown to obey a power laws in time in disordered or partially disordered materials (see the review by Jonscher, 1983). Dissado and Hill (1983) developed a theory to describe the dissipation of fluctuations in strongly coupled disordered systems in response to an external perturbation. In the Dissado-Hill model the fluctuations dissipate as a fractional power law, with the exponent given by an index k (ranging between 0 and 1) describing the correlation between separate interacting clusters. In the case of luminescence decay, Jonscher and Polignac suggest that it is the degree of inter-correlation between the traps that would control the decay exponent α. For strong coupling ($k = 1$) the time dependence of the electron density would follow $1/t$, so the luminescence intensity would follow the bimolecular law $1/t^2$ at long times. For weak coupling ($k = 0$) the luminescence intensity would follow $1/t$.

This heuristic explanation is consistent with our results in the sense that the decay exponent at lower doses is smaller than that at higher doses. At higher doses, the number of occupied traps is greater and the degree of coupling between traps would correspondingly be expected to be larger so that $k \to 1$. Jonscher and Polignac's model obviously fails to explain a range of exponents between 0.3 and 1.2; whether Dissado and Hill's model may be modified to account for a wider range of decay exponents remains a matter for speculation.

---

[5]This was verified by numerical solution of Equation 10.17.

10.2.1 An empirical model for the luminescence decay

It was shown that the decay parameters are approximately consistent with scaling implied from the initial-intensity vs. initial-slope (I_0 vs. S_0) experiment, namely $I_0(\varepsilon)$ varies in proportion to $\alpha(\varepsilon)/E_0(\varepsilon)$, where ε is the excitation photon energy. Also, the increase of α approaching the excitation resonance is not entirely surprising because one expects that the luminescence efficiency, and correspondingly the decay rate (which is equal to $\alpha I_0/E_0$ at $E = 0$) to increase near the resonance[6]. However, for whatever reason α appears to be limited to a value below 1.2 (and more generally to a value determined by the radiation dose) so that a plateau in α is reached near the excitation resonance. The decrease of E_0 near the resonance is therefore seen as a natural consequence of having to maintain the scaling,

$$S_0 \propto I_0^2 \tag{10.18}$$

which is simply the expression of the conservation of the total light sum at all excitation energies. In the absence of the plateau in α, specifically, at low radiation doses, one predicts by the above argument that the dip in $E_0(\varepsilon)$ should vanish.

Since α saturates at doses lower (in two cases, much lower) than the dose required to saturate the luminescence intensity, it is reasonable to suppose that α is not directly connected to the occupied trap density. Nevertheless, the dose response of α does suggest a dependence on the density of some radiation produced defect that is saturating with dose, perhaps the violet recombination centre or a second (non-optical) trap essential to the recombination process. This motivates trying the following empirical dose dependence for α,

$$\alpha = \alpha_0(\varepsilon)[1 - e^{-D/D_0}]^\gamma \tag{10.19}$$

where $\alpha_0(\varepsilon)$ represents the maximum value of α at the particular excitation photon energy ε of the measurement, D is the dose and D_0 is the saturation dose. The exponent γ was found to be necessary to provide an adequate fit to the data. Using Equation 10.19 one finds that the approximate linear dependence of α to to logarithm of the dose in DY-23 is only a coincidence. Equation 10.19 very accurately describes the variation of α with dose in DY-23, with $\gamma = 0.21$, $\alpha_0 = 1.20$ and $D_0 = 390$ Gy. Approximate fitting parameters for K3 and SAW-94-61 are given in Table 10.1 and the fits to Equation 10.19 are shown in Figure 10.1.

---

[6]This assumes that the total light sum is independent of the excitation energy.

Table 10.1: *Approximate fitting parameters for the dose dependence of alpha using Equation 10.19.*

Sample	α_0	D_0 (Gy)	γ
DY-23	1.20	390	0.21
K3	1.07	11	1
SAW-94-61	1.15	90	0.22

The interpretation of Equation 10.19 is that α depends on the density of a center n_x created during irradiation through a power law,

$$\alpha \propto n_x{}^{\gamma}, \quad n_x \propto (1 - e^{-D/D_0}) \tag{10.20}$$

where n_x depends on dose through a saturating exponential. The meaning of the exponent γ in this expression is open to speculation, however the proliferation of power laws here is reminiscent of the general behaviour of strongly correlated complex systems (Carlson and Doyle, 1999).

Even without a detailed understanding of the charge transfer mechanisms it is clear that at least two competing processes are present in the kinetics. α increases with dose as well as in the vicinity of the excitation resonance, this suggests a connection to the excitation cross-section. On the other hand, it is foiled by a second effect, perhaps the availability of certain traps or recombination centers. Suppose that the excitation photon energy dependence of α follows the form of the excitation spectrum in the absence of the limiting process in the kinetics. This is analogous to the case of first order kinetics where the constant E_0 in the time decay of the luminescence,

$$I(E) = I_0 e^{-E/E_0} \tag{10.21}$$

should simply have an excitation energy dependence proportional to that of the excitation cross section (which is proportional to I_0). E_0 is then adjusted to maintain the required scaling of I_0 with S_0 at different excitation energies.

The saturation of alpha near the excitation resonance may be approximated by a saturating exponential,

$$\alpha(\varepsilon) = \alpha_0(1 - e^{-a(\varepsilon)/a_0}) \tag{10.22}$$

Figure 10.1: *Fits to the model for the variation of* α *with dose, Equation 10.19. Fits are the continuous lines.*
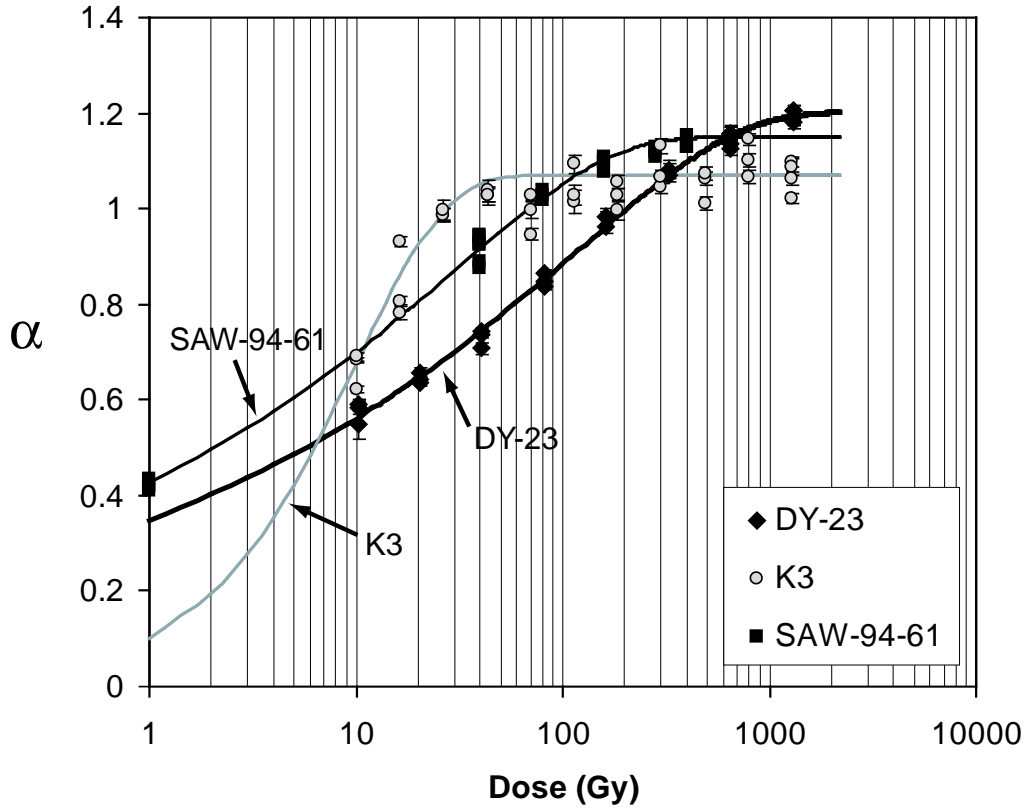
where ε is the excitation photon energy, a_0 is a constant, α_0 is the saturation value of α (it has the same value as α_0 in Equation 10.19) and $a(\varepsilon)$ is the excitation cross-section, whose energy dependence is given by Equation 5.10. A fit to the above equation using Equation 5.10 to model the excitation energy response of K3 and DY-23 is shown in Figure 10.2. The fit is satisfactory for sample DY-23 but a significant underestimate of α at low ε is apparent for sample K3. $E_0(\varepsilon)$ is determined by requiring $S_0 \propto I_0^2$,

$$E_0(\varepsilon) = \frac{k\alpha(\varepsilon)}{I_0(\varepsilon)} \tag{10.23}$$

where k is a constant. The parameter $E_0(\varepsilon)$ calculated in this way is shown by the grey curves in Figure 10.2. Satisfactory agreement with the data is only obtained near the excitation resonance, the model function diverges rapidly from the data in the wings of the

resonance. This is partly resolved by noting that the scaling $S_0 \propto I_0^2$ does not exactly hold. As can be seen in Figures 7.2–7.3, the best-fit line through the data on the $\sqrt{S_0}$ vs. I_0 graph does not pass through zero. A plot of S_0 vs. I_0 on log-log axes (not shown) indicated that the shift required to obtain a linear relationship was best applied to S_0, so that the data follows,

$$S_0 = k_1 I_0^2 + k_2 \tag{10.24}$$

The parameter E_0 must then obey,

$$E_0(\varepsilon) = \frac{\alpha(\varepsilon)I_0(\varepsilon)}{k_1 I_0(\varepsilon)^2 + k_2} \tag{10.25}$$

where the constant k_2 may be determined from the S_0 vs. I_0 experiment. Since E_0 does not vary significantly with radiation dose, whereas α does, it should be clarified that that the $I_0(\varepsilon)$ defined in the above equation refers to I_0 at a fixed radiation dose as do the parameters k_1 and k_2.

The solid black line in Figure 10.2 represents a fit to the E_0 data using the above equation. In the case of K3, the constant k_2 used was that obtained from the S_0 vs. I_0 experiment. Although the fit using Equation 10.25 is qualitatively closer to the data, significant departure from the data is observed, especially at higher ε. Since the linear relation between S_0 and I_0^2 is a purely experimental fact, it can only be concluded that the disagreement implies that Becquerel equation does not provide a complete description of the decay kinetics. This is not entirely surprising because it was noted earlier in Chapter 6 that Becquerel's law did not adequately describe the early part of the decay curve. The departure from proportionality of S_0 vs. I_0^2 indicates that the decay equation is not entirely of the form $f(E/E_0)$, which is yet another indication that assumed form for the decay law is incorrect.

10.2.2   Comment on Hütt's model and a possible alternative

Given what was observed in the IRSL emission compared to the phosphorescence spectra, any model involving a "conduction band" in the traditional sense seems extremely unlikely. Although one can argue that the bands appearing in the phosphorescence emission bands are much dimmer than the IRSL bands and are therefore swamped out by the IRSL, it is difficult to argue the contrary situation; namely, the IRSL emission bands should appear in the phosphorescence as well. It seems much more likely that some traps are tied to specific

Figure 10.2: *Fits to the model for the variation of* α *(left) and* E_0 *(right) with excitation photon energy. In the fits to* $E_0(\varepsilon)$ *the grey line represents the fit assuming* $S_0 \propto I_0^2$ *and the black line is the fit using* $S_0 = k_1 I_0^2 + k_2$.
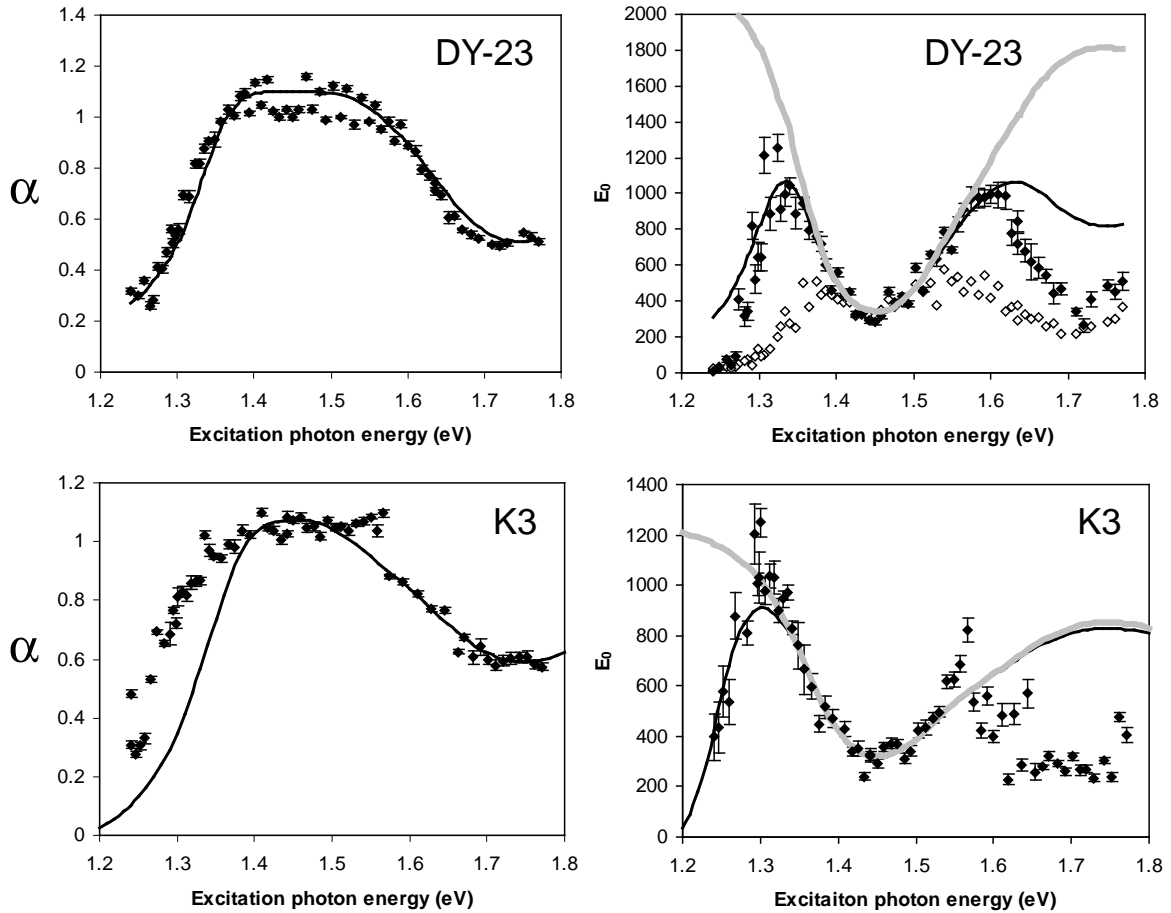
recombination centers whereas other traps share the same recombination pathway. This is suggestive of the defect clusters known to exist in several dosimetry materials (Townsend *et al.*, 2001).

Poolton *et al.*'s (1994) model involving hopping between shallow traps appears to be better suited to explaining the differences in the different emission spectra. A configurational coordinate diagram representation of this model is shown in Figure 10.3. The motion between the shallow traps may involve a combination of tunnelling (as shown in the diagram) and thermally activated hopping. The thermal activation in this particular version

of the model arises primarily from the transition from the excited state of the trap to the acceptor state.

Figure 10.3: *A configurational coordinate diagram representation of Poolton's hopping conduction model. All states in this model lie below the conduction band.*
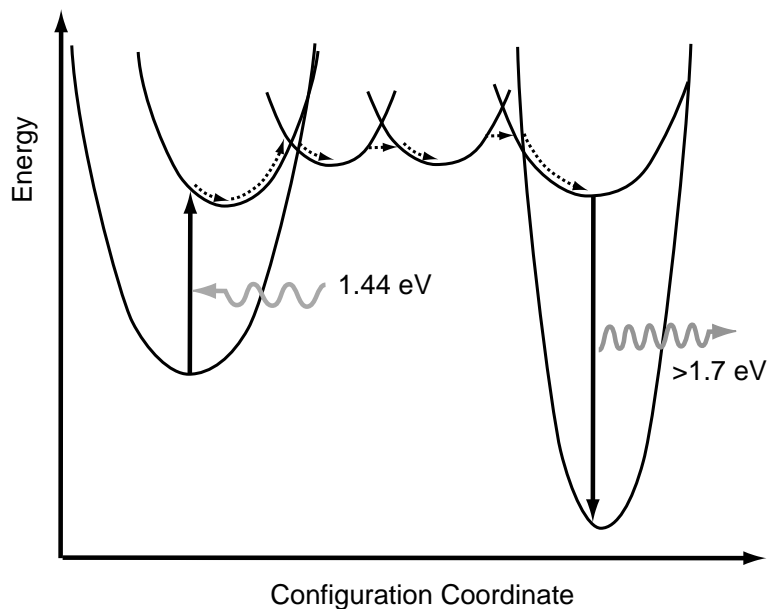
A natural choice for the shallow traps are oxygen defects because these defects are ubiquitous in silicates. As mentioned in the introduction, six oxygen defects have been identified, four due to Al–O^{1-}–Al bridges, one from an Si–O^{1-}–Al(2Na) center and one due to an Si–O^{1-}–X^{2+} center. It is conceivable that the electron hops between several of these centers before reaching the recombination center; this requires a "chain" of such centers connected through the material. In that case, the decay kinetics will depend on the average number of hops the electron must make (the chain length so to speak), which may increase as the decay progresses (*i.e.* the shorter pathways are depleted first). In general, the lifetime in the O^{1-} traps must be much shorter than the time-scale of the phosphorescence decay to explain the absence of the IRSL emission bands in the post-illumination phosphorescence. It is assumed here that retrapping in the optical trap is significant.

The principal difficulty with this model (and all other models mentioned so far) is that it cannot explain why the total integrated luminescence should increase as temperature in-

creases. Assuming that the thermally activated recombination process dominates over tunnelling, this model predicts that intensity would increase with temperature as expected, however the total light sum would not change. The shape of the decay curve would change with temperature to maintain a fixed light sum; this however is not supported by observations. This problem may be resolved by introducing a non-radiative recombination center into the model. In order to obtain the correct temperature dependence, the recombination probability at the non-radiative centers relative to that at the luminescence centers would have to decrease with increasing temperature.

The 2.5 eV phosphorescence may be explained by the trapping of charge along "deadend" pathways where the only possible recombination is through a thermally activated process. The time-constant of this thermally activated process must be much longer than the lifetime in the O^{1-} traps to explain the absence of the 2.5 eV band in the IRSL. Recombination at the optical trap remains a possibility and would explain the 1.3–1.4 eV phosphorescence band.

Speit and Lehmann (1976) proposed that the hopping of a hole between a cluster of three aluminum ions in sanidine,

$$Al–O^{2-}–Al–O^{1-}–Al$$

was responsible for the broadening of the EPR peak arising from O^- centers in sanidine. Speit and Lehmann claim that only the symmetrical arrangements in which the aluminum ions occupy tetrahedral sites, $T_1–T_2–T_1$ and $T_2–T_1–T_2$ would allow hopping to occur. However, in view of Petrov's work it is seen that the O^{1-} defect can occupy virtually all oxygen sites in the lattice involving at least one Al ion or the O nearest the M cation. There is no reason why hopping could not occur between any two such neighbouring defects, although the energy barrier for the hopping between the various defects is not known.

Thermally activated hopping of holes centered on Si–O^{1-}–Al sites was proposed by Schnadt and Schneider (1970) to explain the disappearance of the ESR spectrum of smoky quartz above 170 K. The activation energy of the hopping was determined by Schnadt and Rauber (1971) to be 70±10 meV. This barrier is sufficiently small to allow a short timeconstant for the hopping between the hole centers. It is not unreasonable to suggest that the activation energy for some of the O^{-1} defects in feldspars would be of a similar order of magnitude as in quartz.

Chapter 11

Conclusion

This investigation into the luminescence characteristics of feldspars has in certain instances simplified the overall view of the physics, while in others a much more complicated picture has emerged. The S_0 versus I_0 experiment demonstrated that the initial slope S_0 scales (almost) in proportion with I_0^2 up to relatively high excitation energies. This implies that the function describing the luminescence decay with integrated excitation energy E must follow the form $I(E) = f(E/E_0)$. The fact the extrapolated line of S_0 versus I_0^2 does not pass through the origin indicates that this functional form is only approximate and that another processes dominates at low excitation photon energies. Nevertheless, the results here were much simpler than what had been observed in earlier studies. These results tend to suggest that a single trap is involved in the luminescence, however since E_0 has not been connected to any specific trap parameters by the kinetics experiments this remains a matter of debate.

The kinetics experiments were performed almost as an afterthought, the initial focus having been on the emission and excitation spectra, yet they yielded some of the richest results of this study. Becquerel's law appears to apply universally to the luminescence decay in feldspars, with the power law exponent α varying between 0.25 to just over 1. Conventional models that do not take into account many-body interactions cannot account for such a large variation in α with both excitation photon energy and radiation dose. The multi-exponential decay that has been suggested in the past is certainly incorrect and must be abandoned; this is also supported by the observation of the $S_0 \propto I_0^2$ scaling. Unfortunately a universal mechanism explaining the power law decay of luminescence in materials has yet to be developed and has proved to be one of the most challenging problems of solid-state

physics (Jonscher and Polignac, 1984; Carlson, 1999). A complete physical interpretation of the decay parameters will only be possible following the development of this theory.

While an accurate representation is not yet possible, modest success was achieved in applying a simple empirical model to the behaviour of the decay parameters. The variation of α with radiation dose is consistent with the interpretation that it is connected to the density of an (as yet unknown) radiation generated defect. Assuming that this view is correct, the unknown defect density appears to saturate at a much lower dose than that of the principal IRSL trap. Also, the interpretation that α is proportional to the excitation cross-section up to some saturation value is well supported by the data for sample DY-23 but not as well for sample K3. The disagreement between the value of E_0 expected given α, I_0 and the scaling $S_0 \propto I_0^2$ implies that the assumed Becquerel decay form cannot be completely correct.

Comparison of the IRSL with the phosphorescence spectra indicates that the conventional model for the IRSL in terms of thermally assisted transfer into the conduction band (*i.e.* Hütt's model) cannot be correct. The spectra clearly indicate that the different traps are connected to specific recombination centers, which is better explained by localized transitions lying below the conduction band. Specifically, the violet and yellow-green IRSL emission bands are absent in both the post-irradiation and post-illumination phosphorescence. The behaviour of the 1.76 eV (red) emission band is particularly difficult to explain since it is absent in the IRSL of samples preheated at 120 $^{\circ}$C but peaks above 200 $^{\circ}$C in TL.

The excitation resonance near 1.45 eV exhibits a strong Lorentzian character in several samples. This suggests that the principal broadening in these samples occurs due to time-dependent perturbations, such as the Raman scattering of phonons. This requires further verification by careful measurements of the effect of temperature on the broadening of the peak, although the effect of temperature on the shape of the excitation spectrum seems to be almost negligible in the orthoclase sample K3. The existence of a second resonance near 1.5–1.6 eV appears likely, but it is not strongly present in all samples so that its study is not likely to aid in the development of a general model for the luminescence.

The effect of the polarization of the excitation on the intensity of the violet IRSL in microcline K7 is in general agreement with the work of Short and Huntley (2000) on the orthoclase K3. The observation is consistent with the interpretation of a dipole transition for the transition associated with the 1.45 eV excitation resonance. The polarization of the

excitation was found to have no measurable effect on the shape of the excitation resonance, which is further evidence that the violet IRSL involves a single trap.

Further directions

It will be appreciated from the work of Chapters 8 and 9 and comments concerning the chemical analyses (Chapter 3) that natural feldspar samples rarely consist of pure minerals. They are often mixed with quartz and other minerals, and consist of separate phases of different end-member feldspars (*e.g.* Na-feldspar and K-feldspar in microcline K8). Future systematic studies should concentrate on the pure end-member feldspars. This possibly means avoiding microcline altogether since the segregation of the feldspar phases is ubiquitous in this mineral.

Greater efforts must be taken in ensuring that intrinsic intensities are directly comparable between samples when undertaking systematic studies of natural feldspars. The principal stumbling block here is the large variation in the optical absorption of the natural feldspars which complicates the comparison of intrinsic intensities between samples. Valid correlations between elemental contents and luminescence behaviour cannot be made without consideration for this effect.

Much useful work remains to be done concerning the decay kinetics. In particular, the variation of α with dose should be extended to lower doses to verify the validity of the proposed model (*i.e.* $\alpha \propto n_x^\gamma$, where n_x is the concentration of some unknown radiation created defect). Furthermore, the dependence of α and E_0 with excitation photon energy should especially be extended to higher energy to see if α "saturates" at high energies in the same way as near the excitation resonance. I believe that these experiments may be instructive, even if they are unlikely to lead to the development satisfactory model to explain the power law decay.

Polarization effects in the IRSL have only begun to be considered. In particular, the polarization of the luminescence has only been measured for two bands (the violet and the red) by Short (2003). Differences in polarization between the emission bands would be helpful in indicating differences between the electronic environments of the defects. Such comparative measurements would be useful, even if the crystallographic orientation of the emission dipole (assuming that the transition allows polarized emission) cannot be

determined due to the problems of birefringence and twinning.

Additional studies of excitation spectra should concentrate on samples in which a strong Lorentzian character is apparent. This is particularly necessary in view of the different temperature dependence that is expected to arise from the predominant time-dependent perturbation (Raman phonon scattering) and time-independent broadening (which is expected to have a smaller temperature dependence).

As a final point, I wish to note that the full possibilities of CCD imaging of the optically stimulated luminescence have hardly begun to be appreciated. The only work that has been performed in this field has been by Rieser (1999) and the study presented here. In particular, CCD's allow the possibility of measurement in the near IR so that the location of the phosphorescence in rock slices could be determined and compared to the IRSL, at least in principle.

Appendix A

Fabricating a Fast Collection Mirror

A.1   Fabricating the blank

The standard technique for generating accurate spherical surfaces is to grind two glass disks together with abrasives until the desired radius of curvature is attained (see for example Strong, 1989). In this process, the upper disk will naturally become concave and the lower disk convex due to the greater wear at the center of the upper disk as it bears on the edge of the lower disk. The mating surfaces of these two disks become spherical to within the diameter of the abrasive grains used.

The accuracy obtained by this technique is limited only by the care with which the grinding is performed and the size of the final fine abrasives used. In practice however, one cannot use abrasives smaller than 5 μm due to the risk of adhesion of the tool and mirror blank.

If one wishes to produce very fast optics (f/2 or less), this process can be quite time consuming and wasteful of glass if one begins with flat glass blanks. The process can be accelerated by beginning with a blank that has been molded or milled with a curve generating machine. If one does not require a particularly accurate surface, as is typical in non-imaging/light-collection applications, then a suitable glass blank may be inexpensively produced using resources commonly found in most laboratory facilities. The f/1 mirror required approximately 3 weeks to produce, including time spent experimenting with slumping the glass and making forms.

For the 28 cm diameter collection mirror, a 5/8" thick circular ordinary plate glass blank

was cut using a trepan mounted in a drill press and a slurry of 60 grit silicon-carbide abrasive and water[1]. The trepan was constructed from a wooden disk with a flange and axle mounted in the centre for chucking into the drill press. A thin notched steel strip screwed to the circumference of the disk provided the grinding action.

The disk may also be cut using a glass cutting chisel and mallet, but one must have the facility to grind off the rough edges thus produced. Either way, the edge of the disk on the mirror side must be bevelled generously, with a bevel at least 3 mm wide to prevent glass chips from breaking off the edge of the glass during fine grinding and polishing. This bevel should be re-ground as it wears away during the grinding operation.

A.2   The slumping form

The glass blank was slumped in a spherical form at a temperature of 600 $^{\mathrm{o}}$C; this placed somewhat stringent requirements on the composition of the form. The most inexpensive and readily available material from which to make the form is plaster of Paris, however it crumbles when heated to high temperatures. Acceptable results were obtained with a mixture of plaster of Paris and 20% powdered silica by weight. The form cracked severely during heating but retained its shape sufficiently to produce a satisfactory glass blank.

A negative (convex) form was made by pouring a pure plaster of Paris mixture into a circular mold in which three circles of 1/4" steel screen (also known as hardware cloth) were laid. The hardware cloth would later help to prevent cracking of the mold when it was used to grind the positive mold to shape. The bottom of the mold consisted of a heavy plastic sheet that deformed once the plaster was poured in. The tension of the plastic sheet was adjusted so that the curvature of the plastic bottom matched a precut template.

The positive form was made by lining the negative form with aluminum foil and pouring the plaster of Paris/silica mixture over the convex surface. A foil lined cardboard dam taped around the circumference of the form prevented spillage of the plaster. Here again, hardware cloth circles were used as to reinforce the form. These mesh disks were critical in maintaining the bulk integrity of the form once it had been heated in the kiln.

Once dry, the positive and negative forms were ground together until the two surfaces

---

[1]A ready source of coarse abrasive is a lapidary supply house. Do not use lapidary abrasives for fine grinding or polishing, these often contain stray large grains that can produce scratches.

were approximately spherical and matched the curvature template. It was found that this procedure is best done without abrasives, using generous amounts of water to wash away the plaster slurry.

The concave form was dried in an oven at 120 $^{\circ}$C overnight. The form thus produced was quite brittle but showed very little cracking.

A.3   Slumping the glass

The dry mold was placed in an oven on a bed of crushed refractory brick to ensure even support of the form in the event that it should crack. The glass blank was centered on the mold and was subjected to the heating schedule shown in Table A.1.

Table A.1: Heating schedule used to slump the glass mirror blank.

Temperature ($^{\circ}$C)	Soak/Ramp Time
60 to 300	4 hour
300 to 600	1 hour
600	1 hour
600 to 500	40 minutes
500	3 hours
500 to 425	6 hours
425 to 20	8 hours
	Total: 24 hours

The initial heating rate must be slow to avoid cracking, however there is little danger of breakage above 300 $^{\circ}$C as the glass becomes sufficiently plastic. The glass was allowed 1 hour to slump into the form and was then rapidly cooled to just above the annealing temperature (500 $^{\circ}$C). The glass must be very slowly cooled through the annealing temperature ($\sim$480 $^{\circ}$C) down to 425 $^{\circ}$C otherwise strain can become locked into the glass causing the finished mirror to lose its optical figure or even crack.

A.4 Optical surface generation

The glass mirror blank was ground to the desired spherical figure using a 20 cm diameter tile faced tool. The tool was made by laying 1" hard ceramic tile[2] onto the foil covered glass blank and pouring polyester resin (fiberglass resin) over the back of the tiles. This tile tool was backed with a wooden disk and painted to reduce the possibility of coarse abrasive grains dislodging from the tool and scratching the mirror in finer grinding stages.

Optical surface generation proceeded as usual with the mirror blank held face up in the center of a rotatable table and grinding done by hand (see for example Strong, 1989). Rough grinding of the mirror took approximately 3 hours with 60 grit silicon-carbide, this was continued until all of the depressions and broad folds in the glass caused by the slumping procedure were removed from the surface.

The mirror was ground with successively finer grades of abrasives, ensuring that the tool and mirror perfectly mated at the end of each grade. A good indication that the mirror is not spherical is if the tool tends to grab or stick to the mirror during the grinding stroke. One must exercise great care with the fine grades of abrasives, ensuring that used abrasive is removed frequently and replaced with fresh abrasive, otherwise it is likely that the tool and mirror will bind together. Binding can be remedied by soaking the tool and mirror in warm water. It may take several hours before the tool and mirror slide apart while applying only moderate force.

Approximately 1 hour was spent grinding with each of the finer abrasives, except for the 5 micron grade which was used for only 30 minutes. The sequence of abrasives used was #60 silicon-carbide, #120, #220, #320, #500 aluminum-oxide, followed by 12 μm and 5 μm aluminum-oxide. Less than a kilogram or of the #60 silicon-carbide should be required for the rough grinding, and less than a few hundred grams of the finer abrasives are necessary. In addition, a small amount (<100 g) of fast polishing compound such as cerium-oxide should be procured, although the 5 μm abrasive can be used for polishing if polishing compound isn't available[3].

For optics of this quality, the use of a traditional pitch polishing lap is completely un-

---

[2]Solid ceramic tiles must be used, glazed tiles are too soft and will not wear the glass at a sufficient rate.

[3]Optical quality abrasives may be purchased in suitable quantities from Willmann-Bell, Inc., or Newport Glass, Inc.

warranted. At 2 cm thick or less, the mirror will experience flexure that will make achieving or maintaining a true optical (<1/4 wavelength of sodium D light) figure impossible. A honeycomb foundation (HCF) polishing lap is far easier to use and HCF is easily procurable[4].

To make the lap, a single 30 x 30 cm square HCF sheet is warmed in hot water for several minutes and then quickly laid on the grinding tool. The bees-wax is painted with a slurry of polishing compound and the mirror is then pressed against the bees-wax. Once the HCF has adhered to the tool the HCF is trimmed along the edge of the tool. The adhesion of the HCF to the tool is weak, therefore it may be easily removed once it needs replacement during the polishing operation.

Polishing proceeds as in grinding, rotating the mirror occasionally and using a moderately long stroke (1/3 overhang of the tool and mirror at the tool's furthest excursion). Polishing action is greatest when the greatest resistance to the motion of the tool is felt. However, the polishing motion should be smooth and continuous; the lap should be rebuilt when the polishing motion becomes jerky or the lap no longer conforms to the mirror. In our case, 5 hours of hand polishing was required before an acceptably bright polish was achieved on the mirror surface.

---

[4]HCF, or honeycomb foundation can be procured at an apiary supply or other supplier of bees-wax products.

Appendix B

Spectrometer Acquisition System

B.1   The parallel interface card

The parallel interface card is built around Intel's 82C55A programmable interface chip. The 82C55A was designed as a simple interface to the 8-bit ISA bus of an IBM personal computer, providing access to three 8-bit parallel input/output ports. Although this method of interface is commercially obsolete, it remains a convenient way to interface multiple data lines to a PC with an ISA or EISA bus.

The interface card is particularly simple, consisting only of the 82C55A programmable peripheral interface chip and two 74LS138 decoders (see Figure B.1). The cascaded 74LS138 decoder chips decode the address bits 2 to 9 on the ISA bus, providing a low input to the $\overline{CS}$ (chip select) pin of the 82C55A only when addresses 300h to 303h are present on the bus. When $\overline{CS}$ is low the data lines (A2-A9) of the ISA bus are available to the 82C55A. The $\overline{IOR}$ and $\overline{IOW}$ lines of the ISA bus indicate to the 82C55A the direction of data on the bus (*i.e.* reading from or writing to the 82C55A).

The A0 and A1 address lines are used to address the 4 ports on the 82C55A; 300h addresses the control port, 301h is PORTA, 302h is PORTB and 303h is PORTC. Data can be sent to, or read from, each of these ports as one would do for any other addressable hardware on the PC. Note that the address range 300h-375h is explicitly left free by the PC BIOS for the purpose of testing prototype boards. An example of how one might access the three data ports on the 82C55 is the following code written in Borland in-line C assembler. The code writes a byte (the number 13 = Dh) to PORT C and reads a byte from PORT A

and saves the value in the variable *DataIn*;

short DataIn = 0;
asm{
   Write a byte to PORT C
   mov dx, 303h   \\ *Place output address in the data register.*
   mov al, 00dh   \\ *Place output data byte in register AL.*
   out dx, al   \\ *Write data in AL to address DX.*
   \\ *Input a byte from PORT A*
   mov dx, 301h   \\ *Place input address in the data register.*
   in al, dx   \\ *Read data at address DX and place in register AL.*
   mov OFFSET DataIn, al   \\ Move data in AL to the local variable DataIn.
}

The 82C55A is programmed so that PORTA and PORTB are always in input mode and PORTC is in output mode. Directional conflicts with the ISA bus are automatically avoided through the circuitry of the 82C55A which sets the impedance of its data pins according to state of the $\overline{IOR}$ and $\overline{IOW}$ lines. The pin assignments on each port are as follows,

PORTA: Least significant byte of the CCD data word.
PORTB: Most significant byte of the CCD data word.
PORTC: BIT 0   Software generated CCD clock.
             BIT 1   CCD start read signal.
             BIT 2   CCD mode set (full frame or binning mode).
             BIT 3   Shutter 1 control.
             BIT 4   Shutter 2 control.
             BIT 5   Unassigned.
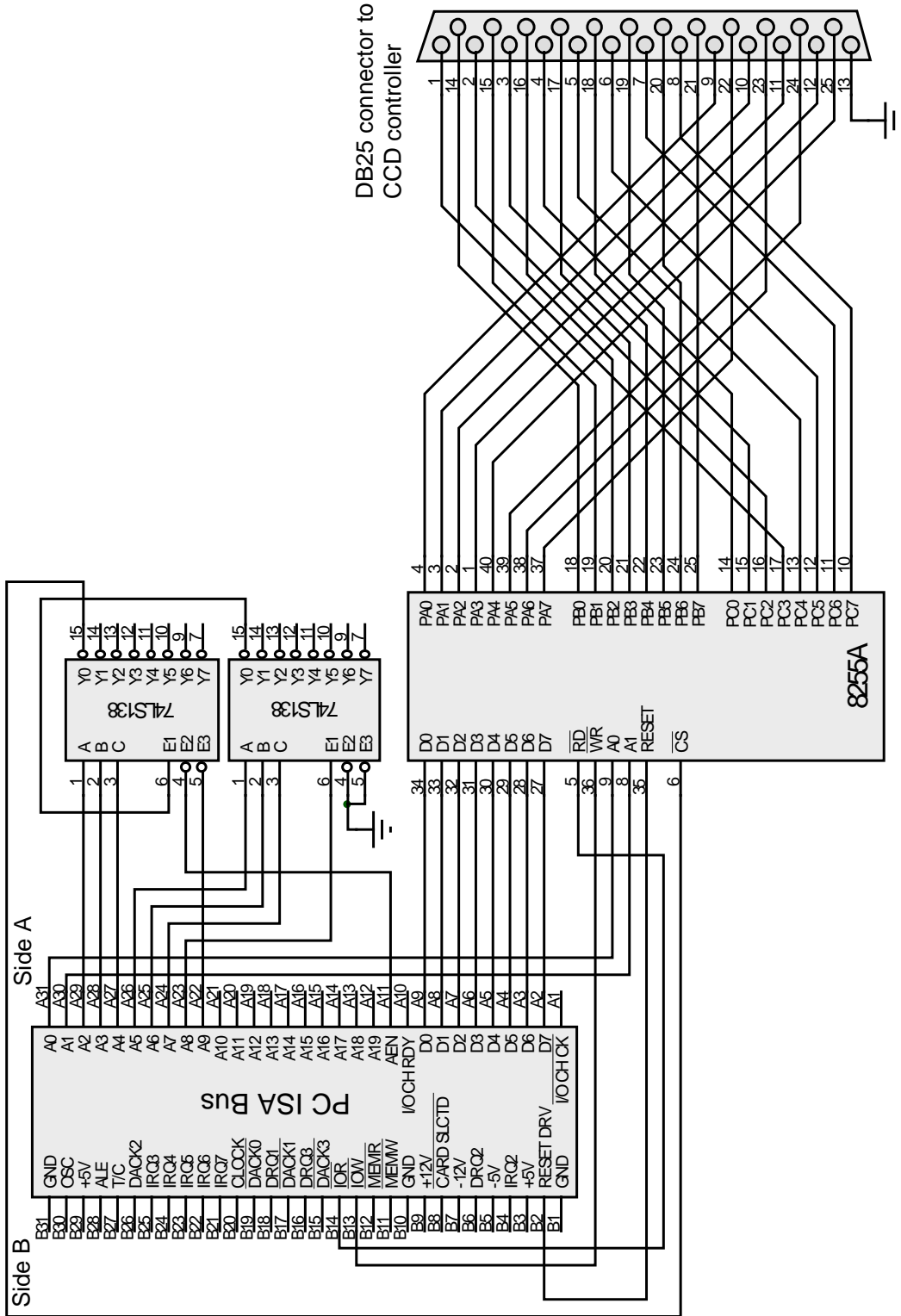   BIT 6   Unassigned.
             BIT 7   Unassigned.

Figure B.1: *Schematic of the 82C55A parallel interface card.*
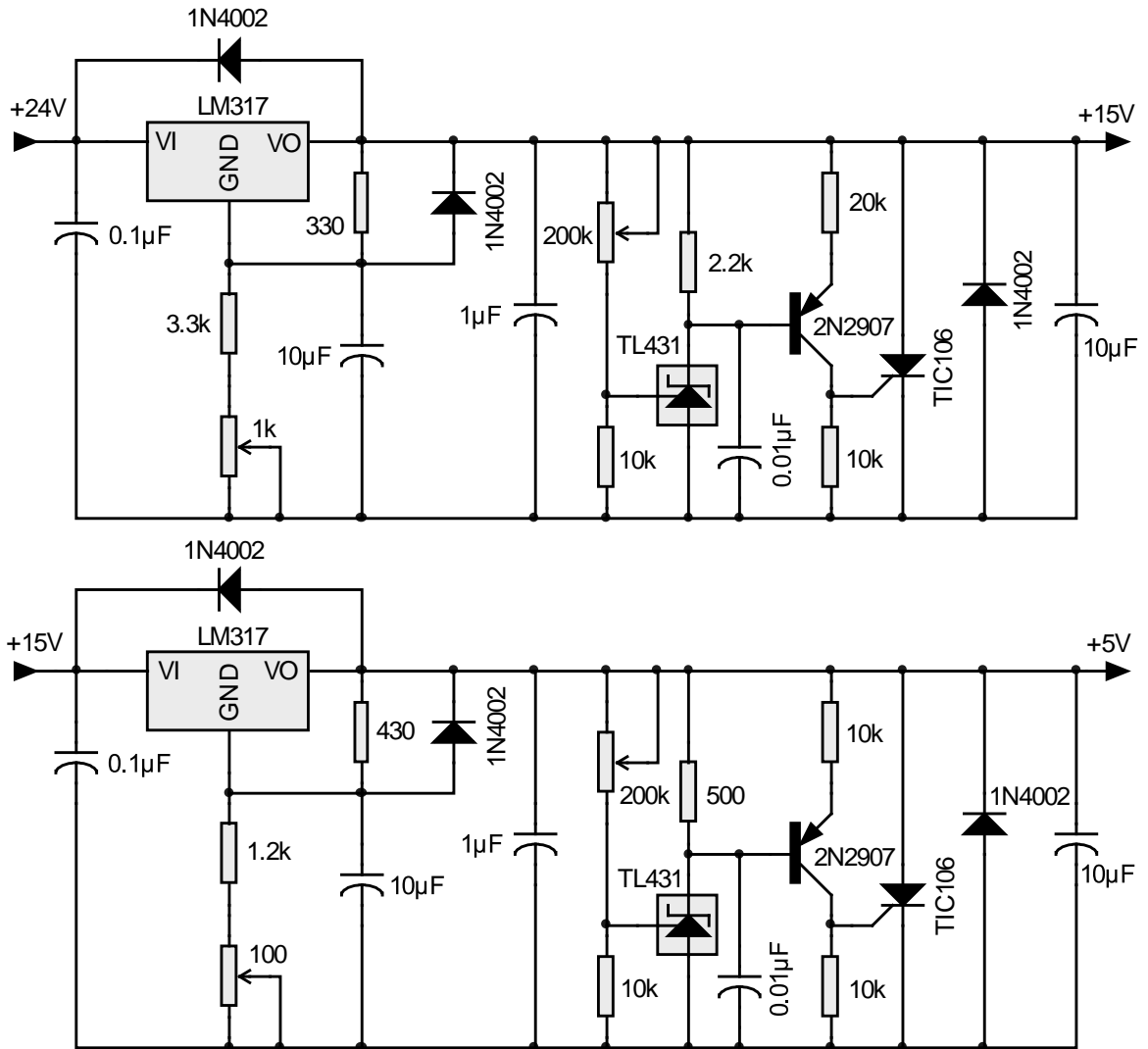
B.2 Power Supply

The power supplies for the CCD electronics were kept separate from the cooling power supply to avoid the introduction of noise from the cooling lines. Most of the critical CCD power supplies were based on the industry standard LM317, 1.5A adjustable output linear regulator. The LM317 regulator provides better ripple rejection and regulation than its standard fixed voltage counterparts; LM7805 (+5V), LM7815 (+15V) and LM7915 (-15V). Note that switching regulators must be avoided in such applications due to the noise introduced at the switching frequency of the supply (typically, $\sim$30-60kHz).

The 24V supply, shown in Figure B.2, has a slow turn-on circuit provided by a 2N2222 transistor, with a time constant determined by a resistor and capacitor ($\tau = RC = 47k\Omega \cdot 10\mu F \sim 0.5s$). The voltage is adjusted by trimming the 2.2k potentiometer. Over-voltage protection is provided with a TL431 adjustable Zener diode (TL431) and a silicon controlled rectifier or SCR (TIC106). The 200kΩ trim-pot sets the voltage threshold for over-voltage protection. When the supply output exceeds the threshold voltage, the TL431 begins to conduct current so that the base of the 2N2907 (PNP) transistor is brought close to ground. This causes the 2N2907 to conduct, bringing the control gate of the SCR to a voltage well above ground. The SCR then latches into a highly conducting conducting state that effectively shorts the supply to ground, blowing the 1A fuse[1]. Similar protection circuits are provided for the other critical voltages in the system (the $\pm$15 V and +5V CCD supplies).

The -15V supply (the bottom half of the circuit in Figure B.2) is designed to accurately follow the magnitude of the +15V supply (shown in Figure B.4). This is achieved through a simple feedback loop employing a 741 op-amp and a 1A PNP transistor (TIP30). The +15V and +5V supplies (Figure B.4) are similar to the +24V supply without slow turn-on circuits; the slow turn-on feature is already present because these supplies are derived from the +24V regulated output.

---

[1]This over-voltage protection scheme is known as an SCR "crowbar".

Figure B.2: *+24 V and -15V supplies. All positive (CCD power) supplies are derived from the +24V supply.*

Figure B.3: *+15 V and +5V supplies.*

The cooling power supply consists of a 5V, 3A fixed linear voltage regulator (LM323) with a simple crowbar over-voltage circuit (6.5V threshold set by a Zener diode). The fan power and digital cooling power supplies are provided by LM7812 and LM7805, +5V and +12V, 1A fixed voltage regulators respectively.

Figure B.4: *The CCD Peltier cooler power supply.*
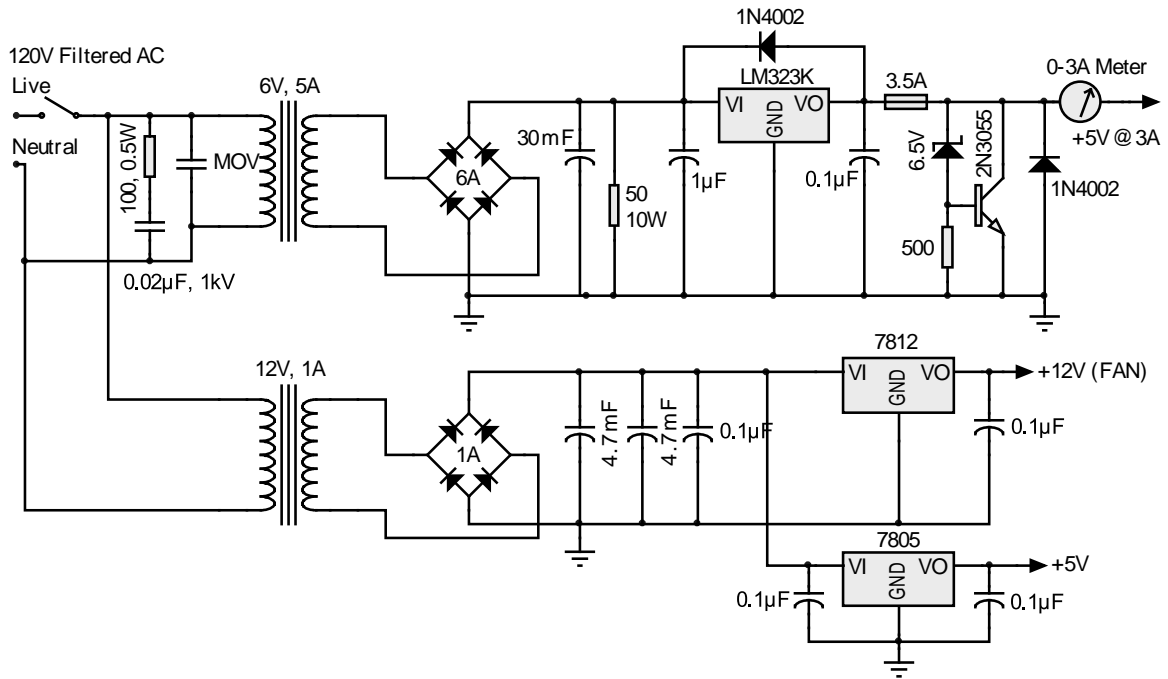
A temperature controlled current limit was later introduced in the cooling power line to override the Hamamatsu C7041's temperature control (see Figure B.5). The thermistor voltage is input into a unity gain inverting amplifier. Large feedback resistors are used in this amplifier to ensure a large input impedance; the resulting loss of high-frequency response helps to stabilize the feedback loop. A 20kΩ potentiometer sets the temperature in the feedback loop. The stability of the circuit is limited primarily by the temperature coefficient of the control transistors, 2N3904 and 2N3055.

Figure B.5: *Temperature control feedback circuit. The current limiting transistor is inserted on the return line of the Peltier element supply.*
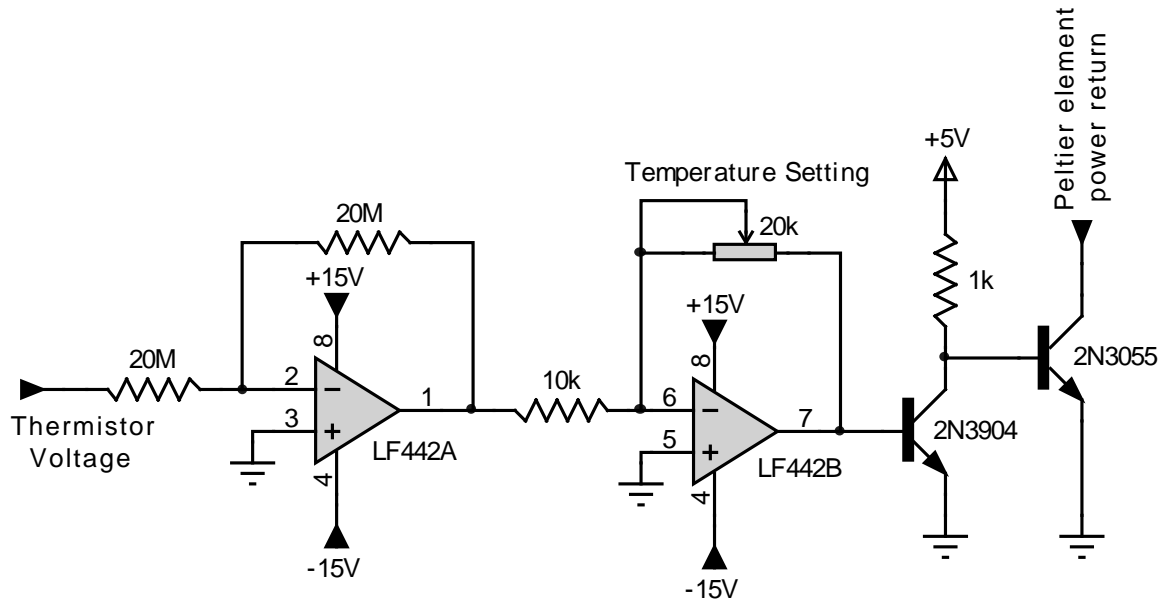
B.3 Video processing electronics

The analog signal processing circuit schematic for the Hamamatsu C7041 CCD detector head is shown in Figures B.6 and B.7. The analog processing board, or ADC board, also includes a circuit to produce the clock pulses required to drive the camera.

The video signal from the CCD head is fed into a unity gain inverter provided by a high speed operational amplifier (AD-845), Figure B.6. The inverted signal is sent to a second AD-845 op-amp variable-gain inverting amplifier to scale the signal to the 10V input of the ADS-917 analog to digital converter (ADC). This op-amp also provides a voltage offset adjust to allow subtraction of any DC offset in the video signal.

The OP-77 op-amp is a unity gain buffer for the 10V reference output from the ADS-917. The 10V buffered output from this amplifier is useful for testing the full-scale response of the ADS-917 and setting the offset adjust to 0. It is not necessary for normal operation of the circuit.

Analog and digital grounds are kept separate on the ADC board to avoid coupling of

Figure B.6: *Schematic of the pre-amplifier for the Hamamatsu CCD video output.*
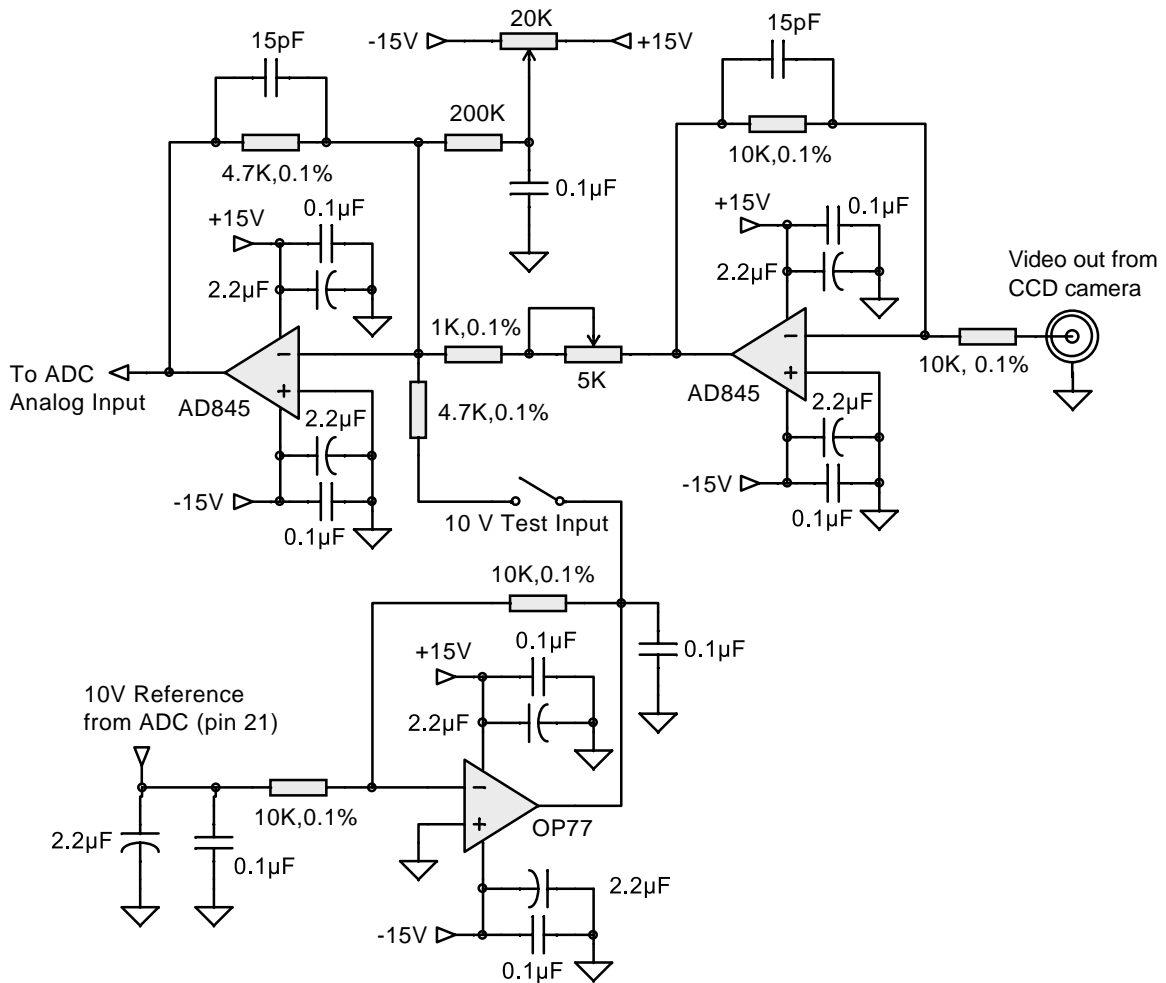
power supply noise into the analog signal. The two grounds only meet near pins 14 and 19 of the ADS-917; this is essential for low-noise operation. The 14-bit parallel digital output of the ADS-917 ADC is connected to two 8-bit three-state line drivers (74LS541), Figure B.7.

The ADS-917 begins conversion of the analog signal on the rising edge of the start convert signal. The start convert signal is provided by the $\overline{EOS}$ (end of scan) signal from the CCD head; this signal indicates that the video pixel level is available on the output. The $\overline{EOS}$ pulse is reconditioned with a half-monostable circuit constructed from a 74HC244 so

Figure B.7: *Schematic of the analog to digital converter and CCD clock driver circuit.*
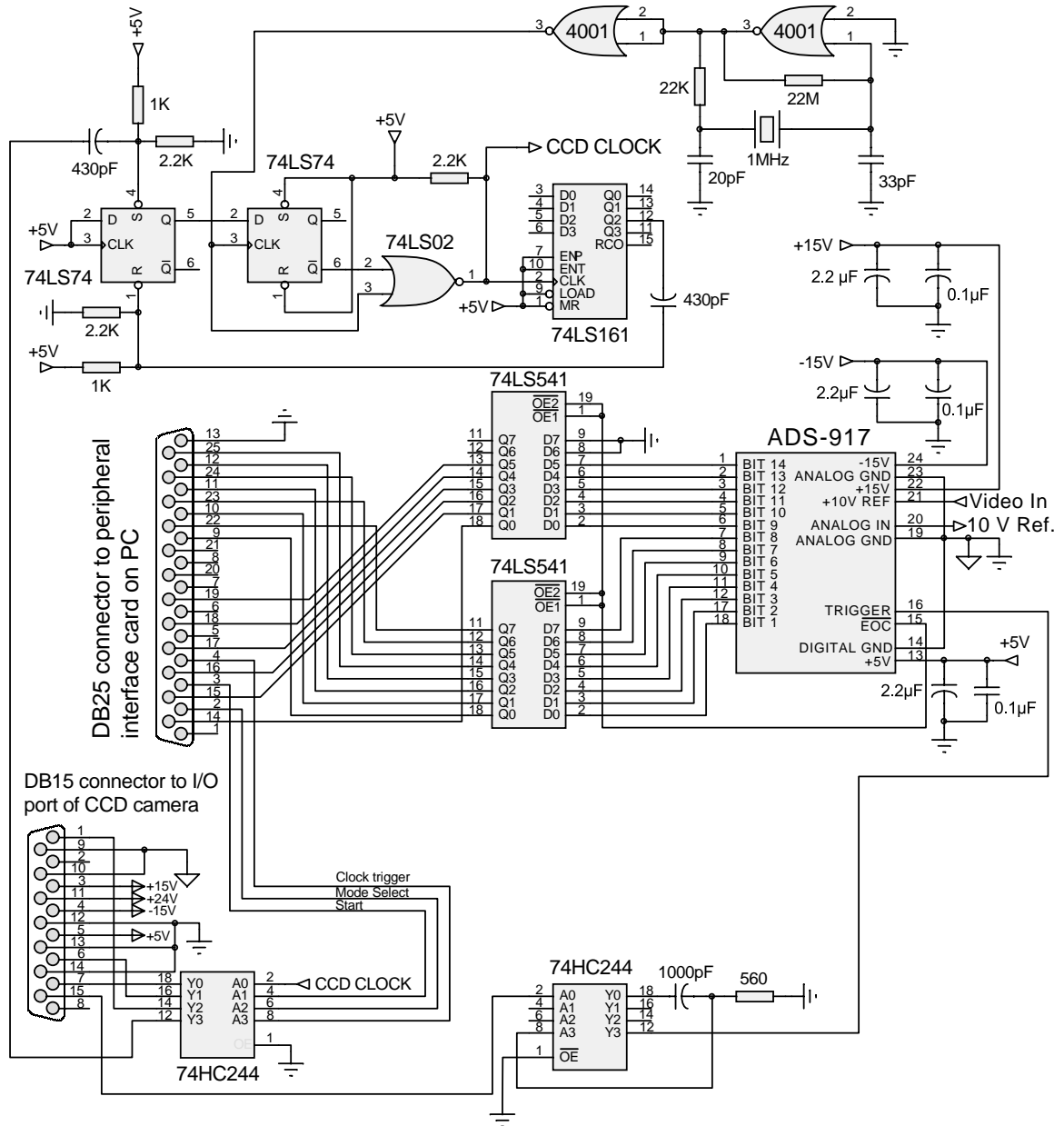
that its length is approximately 200 ns. A second 74HC244 line driver is used to buffer the four digital signals sent to the CCD head.

Since the maximum frequency of operation of the ISA bus is 1Mhz, software production of clock signals on the bus is limited to 500kHz. The C7041 head shifts out the signal from 1 horizontal pixel every 4 clock pulses. This means that if the CCD clock pulses are generated through the PC software, then the maximum readout rate is lower than 125 kHz. One solution to this problem is to use a hardware frequency multiplier to produce 4 clock pulses on each rising edge of the software generated clock. This is the purpose of the clocking circuitry on the ADC board.

A 1MHz CMOS crystal oscillator provides the basic clock rate (note that the maximum clocking rate of the C7041 is 1MHz). The 74LS74 D flip-flops re-synchronize the software pulses with the 1 MHz clock. The re-synchronized pulse enables the output of the 1Mhz clock through a 74LS02 OR-gate to the CCD and to a preset counter (74LS161). Once the counter reaches the preset count value (either 2 or 4, as determined by a jumper setting), the D flip-flop is reset, disabling output of the 1MHz clock. Thus the circuit may be set to produce either 2 or 4 1MHz clock pulses on each software clock. In practice, the 4 pulse setting was not reliable due to synchronization issues between the PC and the detector head, therefore the 2 pulse setting was used exclusively. With this arrangement, readout of an image frame was reduced from $\sim$9 s to $\sim$6 s.

B.4 The shutter controller

The shutter controller was designed to operate shutters employing 6V solenoids. Typically, solenoid shutters require a voltage pulse exceeding 4 to 5 times their rated holding voltage in order to open the shutter. The required voltage pulse is typically between 20 to 50 ms long. After opening, the voltage on the solenoid is reduced to its nominal rated holding voltage.

The shutter controller consists of a +20V, +12V and +5V linear regulated power supply and a pair of identical controller circuits to control two shutters. The controller operates by switching the output applied voltage from 20V to 5V during opening of the shutter. The length of the 20V pulse is determined by the half-monostable circuit shown in the lower left corner of Figure B.8. An OR-gate allows input from either a switch (for manual control)

or a CMOS compatible signal. Switching of the solenoid voltages is performed by a pair of power MOSFET's (IRF530). The 5V holding voltage is sufficient to operate 6V Melles-Griot and Uniblitz shutters.

Figure B.8: *Controller circuit for 6V solenoid shutters.*
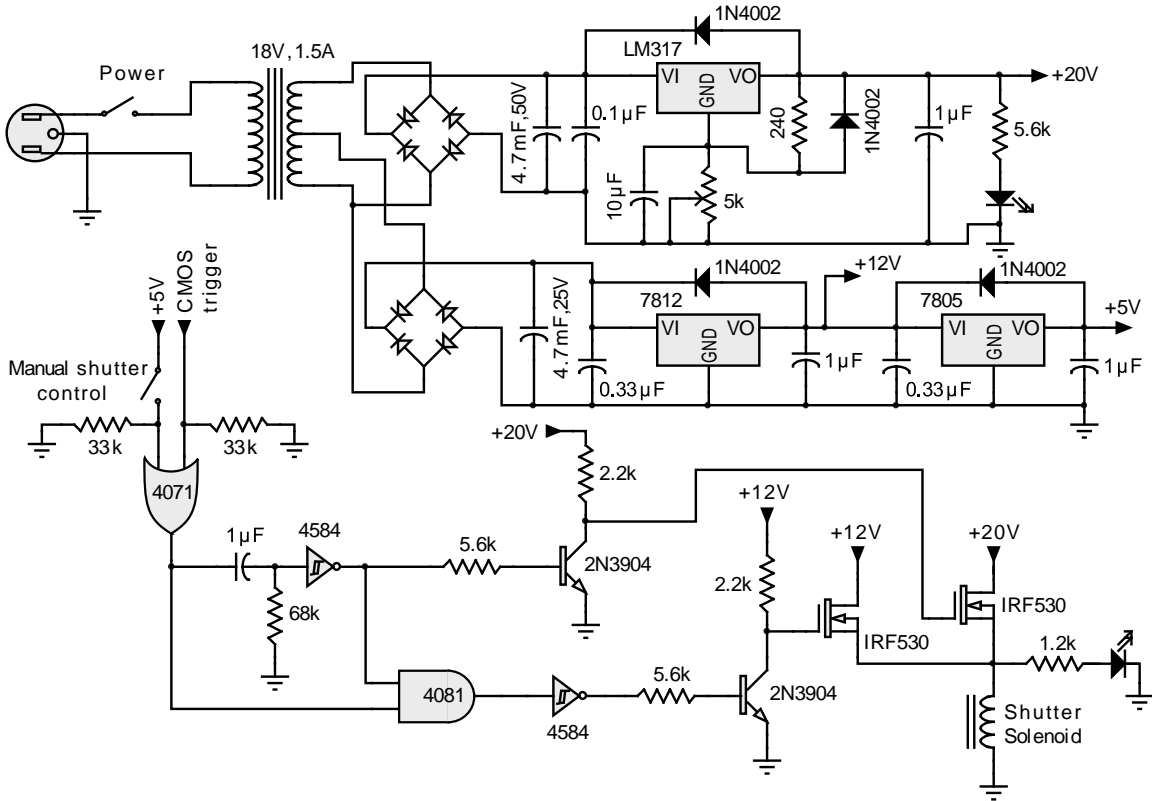
Appendix C

Design for a high sensitivity CCD camera

C.1   Introduction

In the process of my thesis research I designed a low-cost, moderate resolution imaging CCD camera based on Kodak's KAF-401e CCD sensor (796 horizontal x 520 vertical pixels). This camera was originally intended for astronomical photography however it proved to be a useful tool in our mineral luminescence work (Chapter 8). The camera interface design supports two cameras, one for imaging and the other for guiding the imaging camera when it is mounted on an astronomical telescope. The design is summarized here for the benefit of others who wish to undertake the construction of a camera of their own. Printed circuit board patterns and software can be obtained by contacting the author.

C.2   Architecture

The "Pyxis" camera consists of 4 principal modules; the power supply, the controller, the main imaging camera and the guiding camera. The camera interfaces to a PC running a Windows 95/98/ME$_{TM}$ platform using custom software. A schematic of the basic architecture is shown in Figure C.1.

Figure C.1: *Basic architecture of the Pyxis CCD camera.*
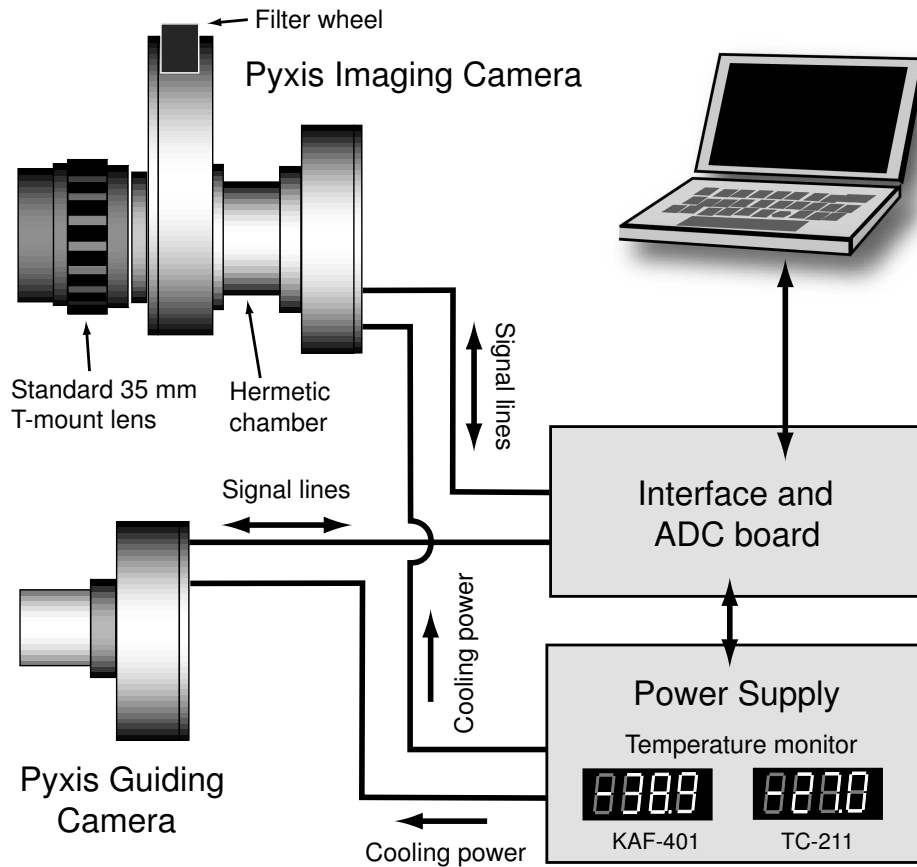
C.2.1   Power supply

The CCD sensors require several fixed and well regulated voltage supplies for correct operation. Most of these voltages are produced on the clock boards located in the camera housing. The power supply provides ±15V and 5V supplies from which the other voltages are derived. In addition, the power supply provides separate ±5V lines for use by the temperature display. These are isolated from the camera supplies due to the large power fluctuations caused by switching the LED's in the display. The power supply also houses the temperature controllers for the Peltier elements as well as the 6V solenoid shutter driver.

C.2.2 Computer interface and ADC

The heart of the Pyxis camera is the controller and ADC board. This board contains relatively few chips because most of the work is done in the firmware of a Microchip PIC-16C62B microcontroller. The PC interface is provided by a standard parallel port operated in bidirectional mode. Some of the chips on the board are directly tied to the parallel port control lines, however most control is mediated through the PIC microcontroller. Analog to digital conversion is provided by an Analog Devices AD9241, 14 bit 1.2Mhz sampling ADC. The ADC input is switched from the main camera to the guiding camera through an analog switch. The four telescope control lines are directly accessed through the parallel port (*i.e.* without the use of the microcontroller).

C.2.3 The main camera

The main camera employs a Kodak KAF-401e, 768x512 pixel full frame transfer CCD sensor. The camera contains two printed circuit boards; the main clock and preamplifier board and the CCD board. The CCD board is particularly simple, since it only holds the CCD sensor, a few decoupling capacitors and the video output buffer transistor. The clock board contains the CMOS clock drivers that drive the CCD phases, the sample-hold circuit and video amplifier, the temperature sensor signal amplifier and a small number of low-power supplies. The clock board and interface is also compatible with the larger KAF-1602e sensor.

The prototype camera incorporates a 25 mm aperture 6V Uniblitz electronic shutter, however the shutter driver should work with any shutter employing a 5-6V solenoid. The CCD is cooled using a two stage Melcor[1] Peltier element. Excess heat is removed by a fluid heat exchanger. Two 10 W resistors are glued on the chamber window and connected in parallel with the TE cooler to curb condensation.

The camera contains a built in filter wheel (6 slots) for colour photography and uses a Pentax T-mount to connect camera lenses.

---

[1]Part number: 2-SC 040 050-127-63, Melcor Thermoelectrics, 1040 Spruce St., Trenton N.J., U.S.A. 08648.

C.2.4 The guiding camera

The guiding camera is considerably simpler and smaller in construction than the main camera. This camera is based on the inexpensive Texas Instruments 192x165 pixel TC-211 full frame transfer CCD sensor. The CCD chip is directly mounted on the printed circuit board (PCB) and the thermoelectric element is cooled with a CPU fan. As in the main camera, the clock board contains a number of low power supplies, the phase clocks, the video pre-amplifier and sample-hold circuit as well as the temperature signal amplifier.

C.2.5 Pyxis Camera Specifications

The following table provides a summary of the specifications of the Pyxis camera.

Table C.1: *Specifications of the Pyxis camera (continued on next page).*

Main CCD sensor	Kodak KAF-401e or KAF-401le
Useful pixels	796 horizontal, 520 vertical
Upgrade sensor	Directly interchangeable with Kodak KAF-1602e or KAF-1602le.
Total readout noise	33 electrons RMS at -16 °C
ADC resolution	14 bits
Antiblooming Transfer constant	Supported in KAF-401le and KAF-1602le chips $\sim$ 3 electrons/ADU
Cooling	Main camera: Two stage TE cooler, $\sim$-45 °C from ambient, fluid heat exchanger. Guiding camera: Single stage TE cooler, $\sim$-35 °C from ambient, fan cooled.
Temperature control	Better than 1 °C per hour. $\sim$ 5 minute stabilization. LED temperature readout.
Shutter	6V solenoid.

Table C.1: *Specifications of the Pyxis camera (continued from previous page).*

Image cycle time	Main camera: 6-7 seconds readout and save time at full resolution + 1-2 seconds display time (system dependent). Guiding camera: ~1.5 second readout and display.
Main CCD sensor	Kodak KAF-401e or KAF-401le
Interface	Bidirectional parallel port.
Software compatability	Windows 95, 98, ME.
File format	Pyxis native format, Flexible Image Transfer System (FITS) or Windows bitmap.
Additional features	User can select to read out any sub-section of the image frame to reduce the image cycle time. Vertical and horizontal binning up to 255x255 pixels.

C.3 Basic CCD operation

C.3.1 The MOS capacitor

A complete description of CCD operation is beyond the scope of this text[2], however a basic understanding of the operation of these devices is necessary to appreciate the operation of the acquisition electronics.

CCD's or charge coupled devices, operate using the principle of the MOS (metal-oxide semiconductor) capacitor. Voltages applied to the electrodes (gates) on the CCD top surface produce voltage wells that trap thermally generated free electrons in addition to electrons generated by the photoelectric effect. The photo-generated electrons form the basis for the video signal in each CCD pixel. Cooling reduces the thermally generated electrons so that long exposure times (greater than a few seconds) are possible.

By switching the applied gate voltages (clocks) the potential wells may be shifted allowing the electrons to move to the neighbouring gate. Eventually the charges in each line

---

[2]Readers interested in CCD camera construction may consider Buil, 1991 as a good primer.

Figure C.2: *Left: Cross-sectional view through a MOS capacitor. Right: A MOS capacitor biased with 10V. Thermally and photo-electrically generated charges migrate towards the electrode (gate) whereas holes collect deep in the substrate. This results in the formation of a "depletion region" that is deficient in minority carriers (electrons).*
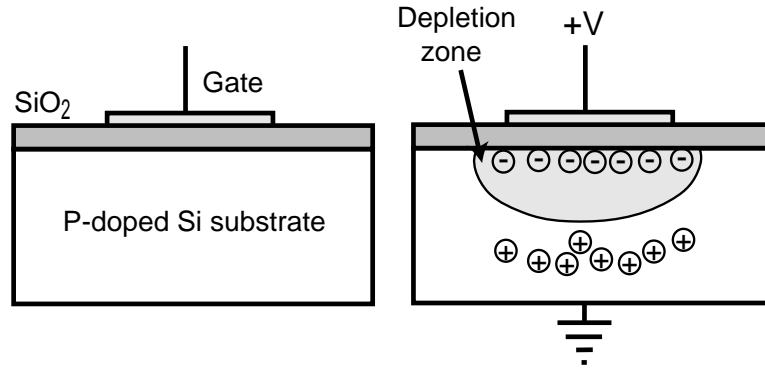
are shifted out into a horizontal register. Here the charges in each pixel are shifted out to an output amplifier by a process similar to that used to shift out the charges from each line into the horizontal register. The output amplifier senses the charge packet and produces a voltage on its output proportional to this charge.

The basic structure of a photo-site (light collecting element or pixel) in a front illuminated CCD is the MOS capacitor shown in Figure C.2. The gate (or electrode) consists of a semi-transparent conductive material. A thin layer of silicon oxide prevents conduction between the gate and the silicon substrate, a capacitor is thus formed between the conductive gate and the semiconducting substrate.

Suppose that the MOS capacitors that form the CCD pixels are constructed on a P-doped silicon substrate. If a ∼10V bias is applied across the gate and substrate (the substrate is grounded), the holes in the silicon are drawn away from the gate by the applied electric field so that a region is formed directly below the gate that is depleted in majority carriers (holes). However, a certain number of minority carriers are available through thermal excitation of "regular" valence electrons into the conduction band. Every time an electron is thermally excited into the conduction band a hole is created; the electrons eventually migrate towards the gate (positive electrode) and the holes migrate down into the substrate. Eventually a negative charge builds up directly below the gate whereas a positive charge collects deeper

in the substrate below this. Equilibrium is reached when the accumulated charge generates an electric field that cancels the applied field.

Depending on the MOS structure, the time required for thermal equilibrium to be reached (the thermal relaxation time), may be less than a second up to 10 seconds or more. The CCD sensor is operated in the regime where the charge balance in the MOS structure remains in disequilibrium. In order to increase the thermal relaxation time, thermal excitation of electrons into the conduction band must be prevented. This is achieved by cooling the CCD to low temperatures.

What makes the MOS capacitor a light sensor is that light can penetrate through the gate and silicon oxide layers into the silicon substrate. If a photon of sufficient energy enters the depletion region in the silicon below the gate it may excite an electron-hole pair into the conduction band by the photo-electric effect. The photo-generated electrons collect at the Si/SiO$_2$ interface until either the thermal relaxation time is reached or saturation of the MOS capacitor is caused by the accumulated photo-electrons.

C.3.2 Transferring the charge

In order to read the CCD one must provide a means for transferring the charge between the photo-sites on the CCD. To understand how the charge collected in a MOS-capacitor may be transferred into its neighbouring capacitor, it is useful to think of the charge as being trapped in a voltage well below the gate. The charges are not likely to escape the potential well as long as its depth is much greater than the average thermal energy of the charges.

The collected charge produces a potential of its own that is of opposite polarity to that due to the externally applied voltage. Therefore, as the charge accumulates, the depth of the voltage well decreases and eventually, once the photo-site is "saturated", the voltage well vanishes.

Now consider raising the voltage on the right-most gate in Figure C.3 to a large bias (say 10V) and reducing the voltage on the central gate to an intermediate voltage (say 5V). The gates are sufficiently close together that there is coupling of of the potentials below the gates, this means that charge will flow from the shallow central well into the deeper potential well under the right gate. This is the principle by which charge is transferred between photo-sites on the CCD.

Figure C.3: *The potential plotted in the horizontal direction at the Si/SiO$_2$ interface in the MOS capacitor. As the accumulated charge increases, the voltage "well" originally of depth $V_1 = +V$, decreases to a depth V_2. The neighbouring gates are held close to ground and therefore act as voltage barriers to the charge collecting below the central gate.*
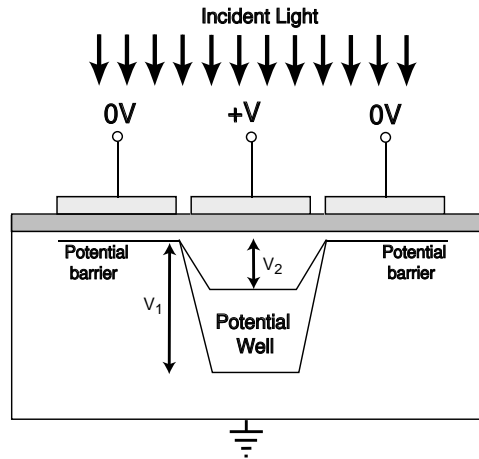
The gate at each photo-site is connected in parallel with a number of other gates whose voltages are clocked together on the chip; collectively these connected gates are referred to as a *phase*. The photo-sites from the various phases are so arranged that charge may be transferred first vertically then horizontally through the CCD structure.

A minimum of three phases are required to ensure unidirectional charge flow through the CCD (if symmetrically profiled voltage wells are used). The clocking sequence employed in three-phase charge transfer is illustrated in Figure C.4.

A two phase CCD may be constructed by forming the gate electrodes from two (separately deposited) layers of polysilicon with different dopant concentrations. This produces a voltage well with an asymmetric profile as shown in Figure C.5, the asymmetry defines the direction of (efficient) flow of charge in the device. The asymmetric voltage wells may also be produced by implanting impurity ions into the substrate. Since only two clocks are required, the driving electronics for a two-phase CCD are considerably simple compared to those required for a three-phase or four-phase transfer sensor. The Kodak KAF-401e sensor is an example of a CCD's employing two-phase transfer.

CCD readout is performed by shifting entire lines of photo-sites, or pixels, into the next

Figure C.4: *The clocking sequence employed in three-phase transfer. Represented is the potential below the gates at each time step in the clocking sequence.* Φ_1, Φ_2 *and* Φ_3 *are the three different CCD phases. Three time steps are required to shift the charge by one pixel.*
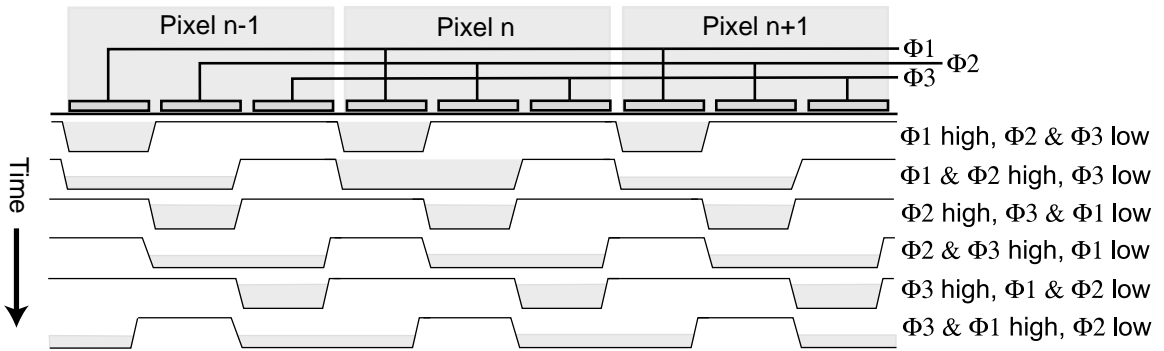
Figure C.5: *Two-phase transfer clocking sequence.* Φ_1 *and* Φ_2 *are the two CCD phases. Only two time steps are required to shift the charge by one pixel.*
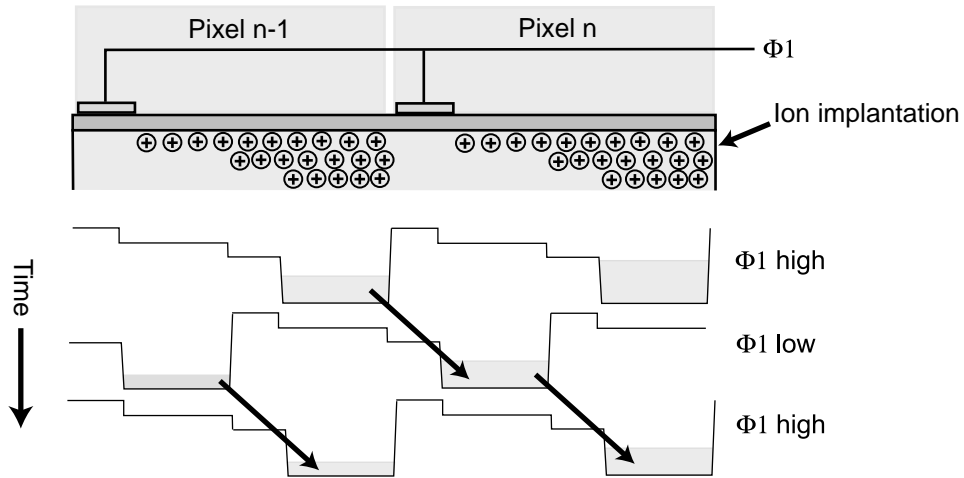
line of photo-sites. This is performed by clocking the "vertical" CCD phases one full cycle. The line of charge at the bottom of the array is shifted into a "horizontal register". The charges collected in the horizontal register are then individually shifted onto a detection node where they are sensed by an amplifier, Figure C.6.

Figure C.6: *Left: Readout in a two-phase FFT CCD, a line is shifted into the horizontal register, followed by readout of the individual pixels in the shift register. Right: A FFT CCD divided into 4 output sections; this architecture is used on large arrays to reduce readout time.*
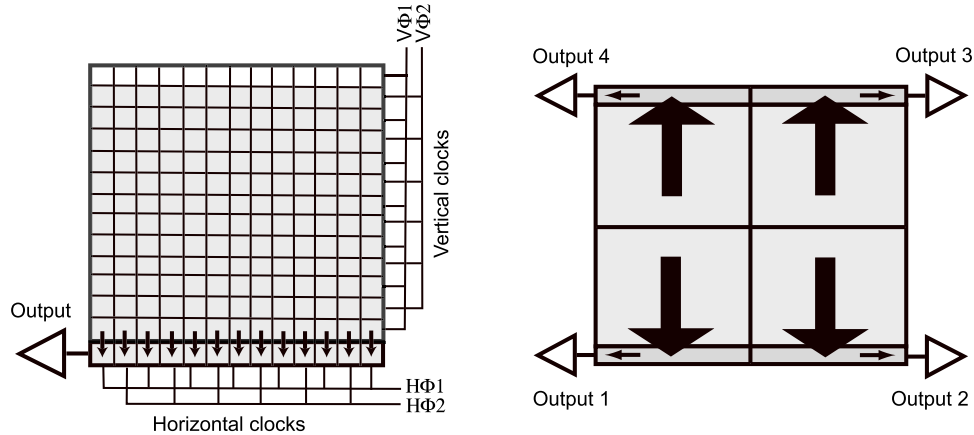
C.3.3 The CCD output structure

A conventional CCD output structure is shown in Figure C.7, it consists of a *floating diffusion* sensing node coupled to a charge to voltage converter (the output amplifier) and a reset structure to clear the charge from the sensing node.

The process of reading out the charge from a single pixel begins by clearing any charge present on the floating diffusion node. This is done by bringing the reset clock high so that charge can flow across the reset gate into the reset drain. Note that the silicon in the reset drain is connected to a highly conductive layer so that charge flows easily from the silicon into the drain (which is usually held at a fixed voltage). At this point the voltage output of the amplifier is at the *reset level*, shown in Figure C.8.

When the reset clock is brought low again, charge is prevented from flowing out of the floating diffusion into the reset drain; the voltage at the output of the amplifier is then at the *reference level* of Figure C.8. The reference level is generally not constant from pixel to pixel due to parasitic capacitive coupling of the amplifier input to the floating diffusion (*i.e.* the reference level has "memory" of charge present on floating diffusion). Compensating for the reset noise in the reference level is essential in obtaining low-noise

Figure C.7: *Floating diffusion CCD output structure.*
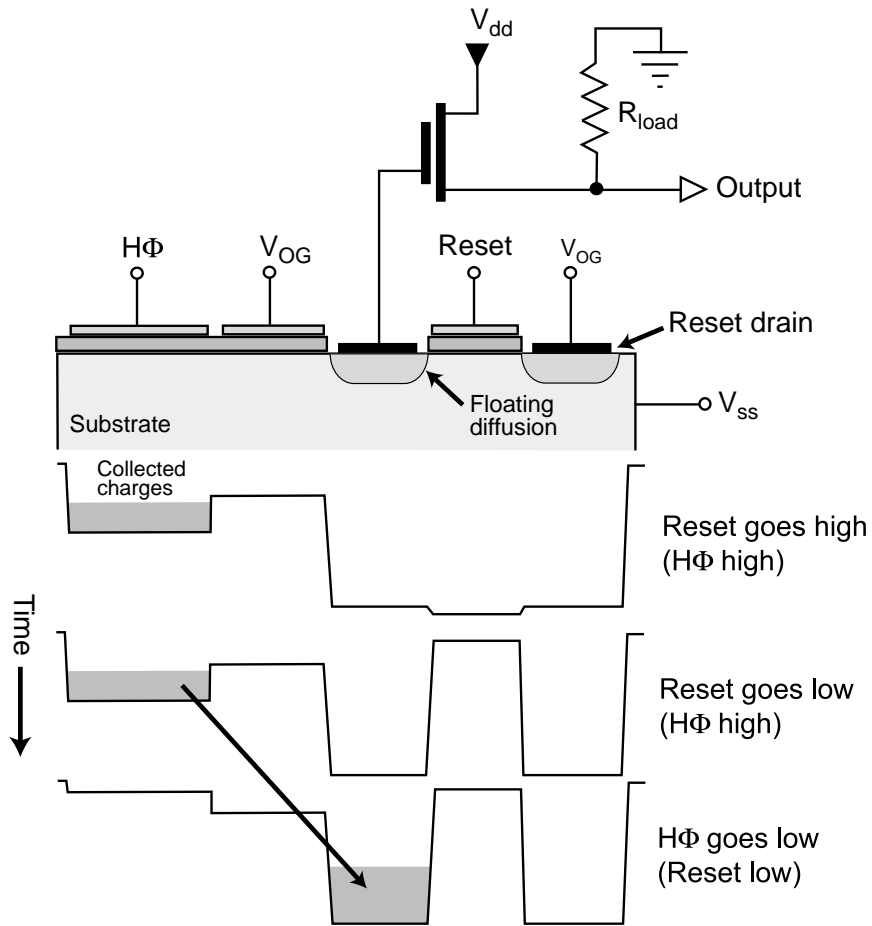
performance from the CCD.

Next, the clock on the last pixel gate (HΦ) is lowered so that charge may flow over the output gate onto the floating diffusion. This charge packet modifies the potential in the floating diffusion which is connected to the output amplifier. The difference between the voltage level on the amplifier output minus the earlier reference level provides the correct pixel video level.

Figure C.8: *Clock timings related to the CCD output. Only one horizontal CCD phase HΦ is shown for simplicity.*
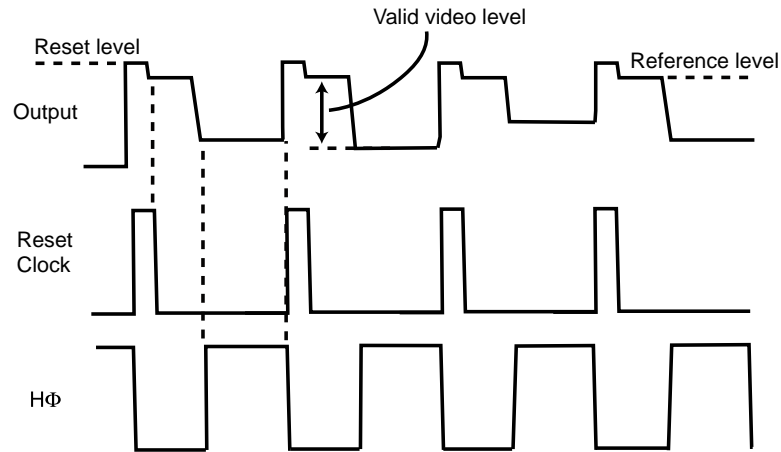
C.4 The ADC and interface board

A schematic of the computer interface and analog to digital converter (ADC) board is shown in Figure C.4. The Microchip PIC-16C62 micro-controller (the "PIC") forms the heart of the interface circuit, it is programmed to generate the clock sequences required to read the CCD's. The PIC is operated at 20 MHz so that the shortest clock pulse that may be generated is 200 ns[3]. The PIC micro-controller provides three parallel I/O ports and sufficient internal EPROM memory to store simple programs[4]. The I/O pins on each port may be individually programmed for input or output. The PIC communicates with the PC by polling the state of the RB0 input pin. When this pin goes high it reads the signal present on the four lowest RA port pins (RA0 to RA3) to determine what action to perform; in this way, up to 16 different 4-bit control words may be sent to the PIC. The PC sends the control word to the PIC by writing a 4-bit word to one of the 74LS75 latches connected to the parallel port; the output of the latch is connected to the RA port on the PIC[5].

 Connections to the parallel port must be buffered because it is accessed by several chips

---

[3]The PIC requires 4 clock cycles to execute each instruction.

[4]For a tutorial text on this subject see Predko, 1998.

[5]A second 74LS75 latch is used to store the 4-bit telescope tracking control word; this turns on or off the east/west/north/south slewing actions.

on the board. The 74HC541 8-bit tri-state line driver is used to connect the ADC output to the parallel port. The 14-bit ADC output is connected to two 74HC157 data-selectors; this allows the PC to select reading either the lower or upper byte of the 16-bit video data word[6].

The Analog Devices AD-9241 14-bit sampling ADC requires a minimum 800 ns processing time between conversion cycles. In order to achieve this fast acquisition time this ADC introduces a pipeline delay of 3 conversion cycles, so that the converted input data only appears at the output on the third conversion cycle. This delay is of no consequence to the present application. The input to the ADC is switched from the output of the main imaging camera (KAF-401) and the guiding camera (TC-211) using a Harris DG-301A analog switch.

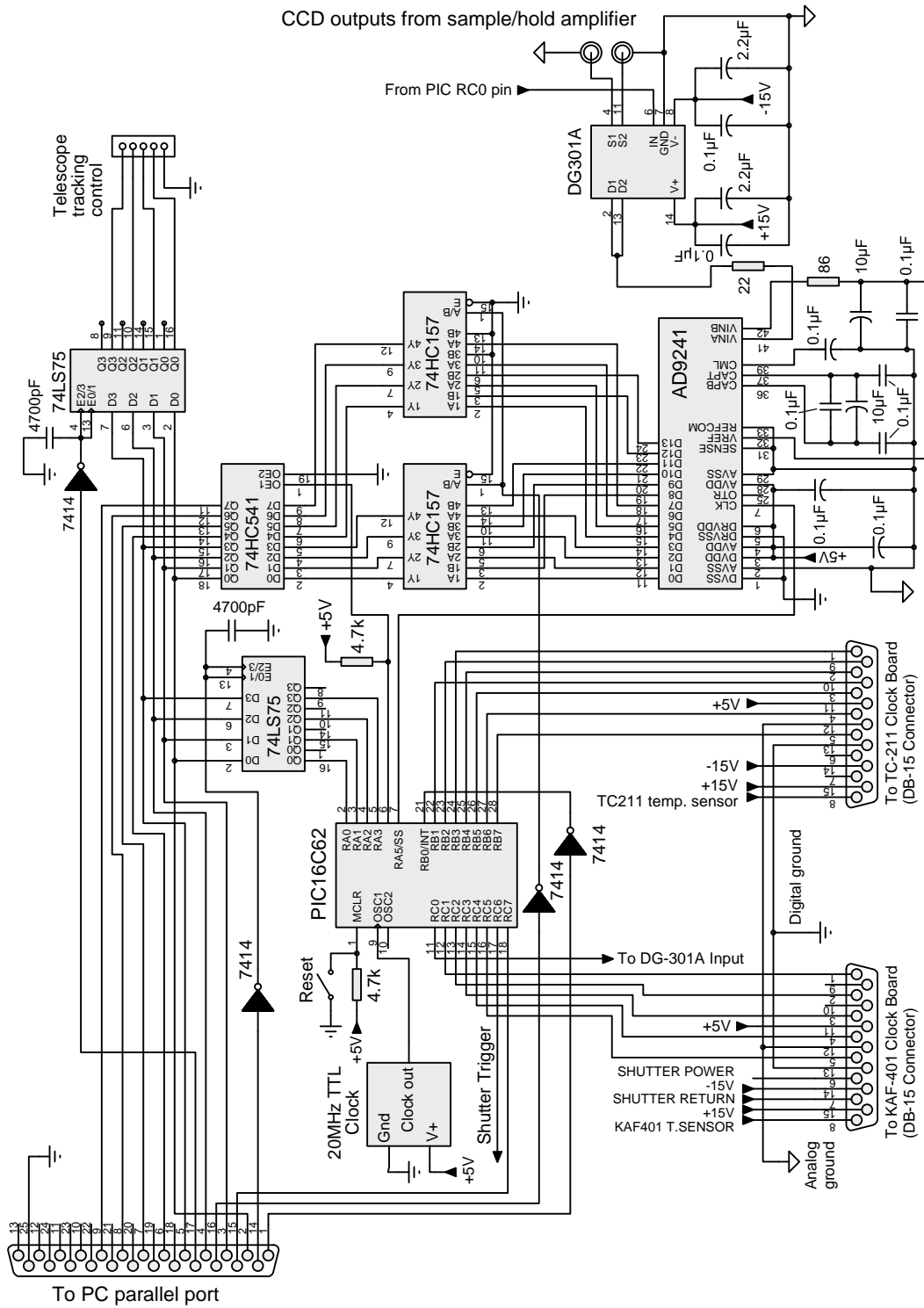[6]Only the lowest 14 bits of the data word are valid.

Figure C.9: *Schematic of the PC interface and ADC board for the Pyxis camera. CCD clock sequences are generated by a Microchip PIC-16C62 micro-controller. The 14-bit ADC is an Analog Devices AD-9241.*

C.5 The CCD clock drivers

One will appreciate from the previous discussion of the CCD structure, that the principal problem in rapidly switching the voltages on the CCD phases arises from the capacitive load introduced by having several MOS capacitors connected in parallel. The vertical phases in particular present a large capacitive load to the CCD clock drivers. In the KAF-401e the effective capacitance of the vertical phases is 6 nF; this is considerable when the ~ 10 V vertical phase clock must be switched in a time of less than 50 ns.

Figure C.10: *Schematic of the circuit driving the vertical CCD phases VΦ1 and VΦ2.*
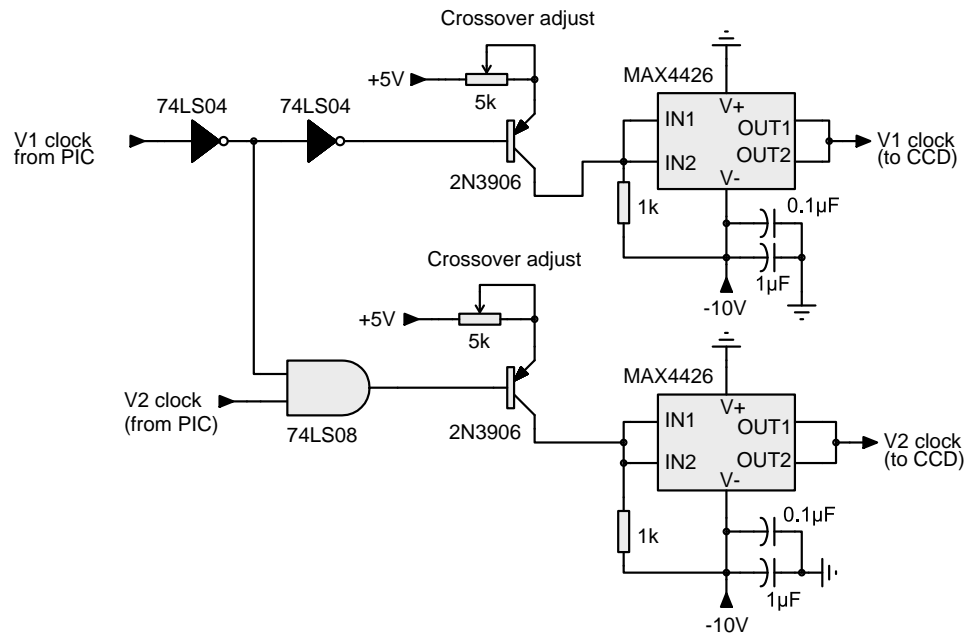
The two vertical phases VΦ1 and VΦ2 are driven by a pair of Maxim 4426 CMOS clock drivers, Figure C.10. Each clock driver has its dual outputs connected in parallel driving a single phase to achieve the necessary peak current. The PNP transistors act as level translators, so that the incoming 0-5V CMOS pulse from the PIC can trigger the CMOS clock driver whose output low level is set to -10 V. The cross-over of the rising edge of VΦ1 with the falling edge of VΦ2 is adjusted by trimming the collector-emitter current through the PNP transistors. The DC output at "V1 out" is 0 V when "V1 in" is high and

-10 V when "V1 in" is low. The ouput for VΦ2 is the complement of VΦ1, unless VΦ1 is low – in which case VΦ2 is also low.

The horizontal register presents a much smaller load capacitance to the clock drivers. For this reason, a single Maxim 4426 clock driver is used to drive the horizontal phases HΦ1 and HΦ2, Figure C.11. HΦ1 and HΦ2 are complements of one another, so that when

Figure C.11: *Schematic of the circuit driving the horizontal CCD phases HΦ1 and HΦ2. The reset clock circuit is at the bottom of the diagram.*
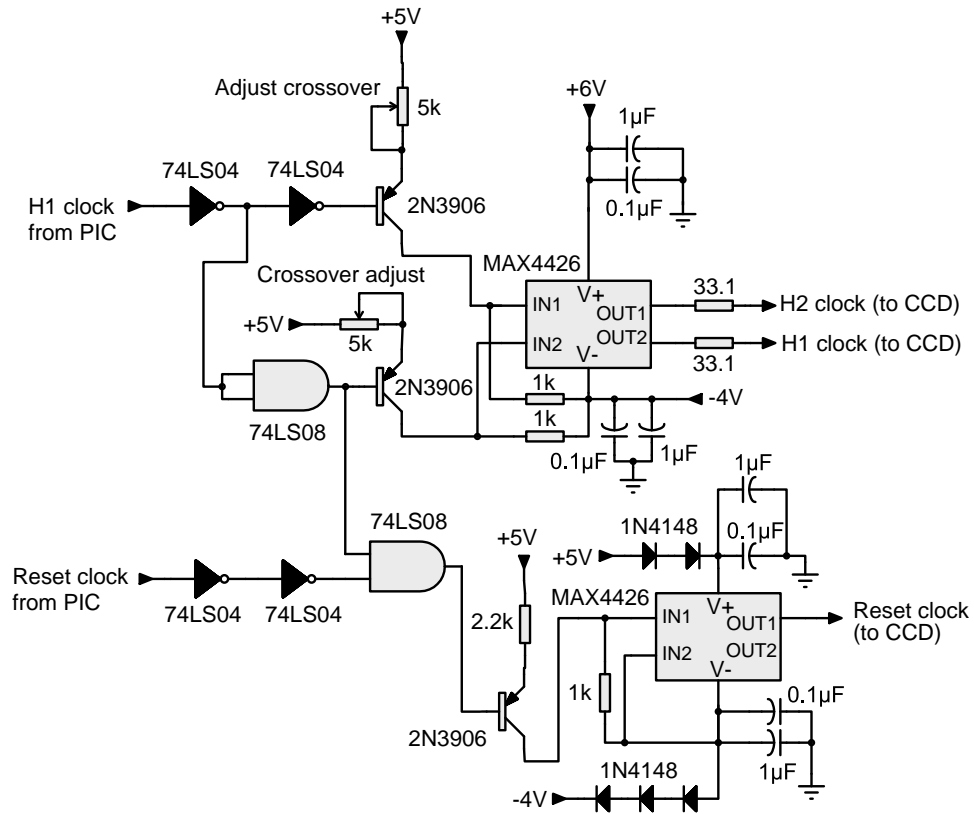
"H1 in" is high, HΦ1 is at +6 V and HΦ2 is -4 V. The small output resistors suppress ringing of the horizontal clocks.

The reset clock is produced using a single channel of a Maxim 4426 driver. Since the CCD reset structure presents a very small switching load, the diodes provide a simple means of deriving the +4 V (high) and -3 V (low) levels from the available +5 V and -4 V supplies.

C.6   Analog processing of the video level: correlated double sampling

Referring to Figure C.8 one will note that the valid video signal is given by the "reference" level minus the "output" voltage level. Measurement of the output level alone introduces "reset" noise caused by the small fluctuations in the reset level. Therefore, a means must be provided to "remember" the reference level so that it may be subtracted from the output level. This technique is known as correlated double sampling (CDS) because it allows the removal of the reset noise by first sampling the reset level, and then sampling the output level.

CDS is achieved in the Pyxis camera by holding the reference level with a sample/hold (S/H) amplifier (Analog Devices, AD781) and performing the subtraction with a differential amplifier, Figure C.12. The difference of the reference level and output level is sampled internally by the AD9241 ADC, so that a second sample/hold amplifier is unnecessary in this design.

The buffered[7] CCD output signal is inverted, and a fixed ∼9 V level is subtracted by the upper-left AD812 op-amp in Figure C.12. The output of this op-amp goes to the S/H amplifier and the non-inverting input of a second AD812 (lower-left in diagram) operating as a unit gain differential amplifier. The S/H amplifier holds the reference level when the "S/H" line goes low. The output of the differential amplifier is then the difference between the video level and the reference level held by the S/H amplifier.

The output from the differential amplifier is inverted once more and a small offset voltage is subtracted[8] by the AD845 op-amp. This output is directed to the ADC, which converts the video-level into its digital representation.

---

[7]A single transistor source follower transistor is connected close to the CCD output pin; this is not shown in Figure C.12.

[8]A small offset appears in the KAF-401e signal even when the thermal signal is negligible and the sensor is not exposed to light.

Figure C.12: *Schematic of the video pre-amplifier for the Pyxis camera. Diodes on the output clamp the signal to a range of 0–5 V to avoid damaging the AD9241 ADC input.*
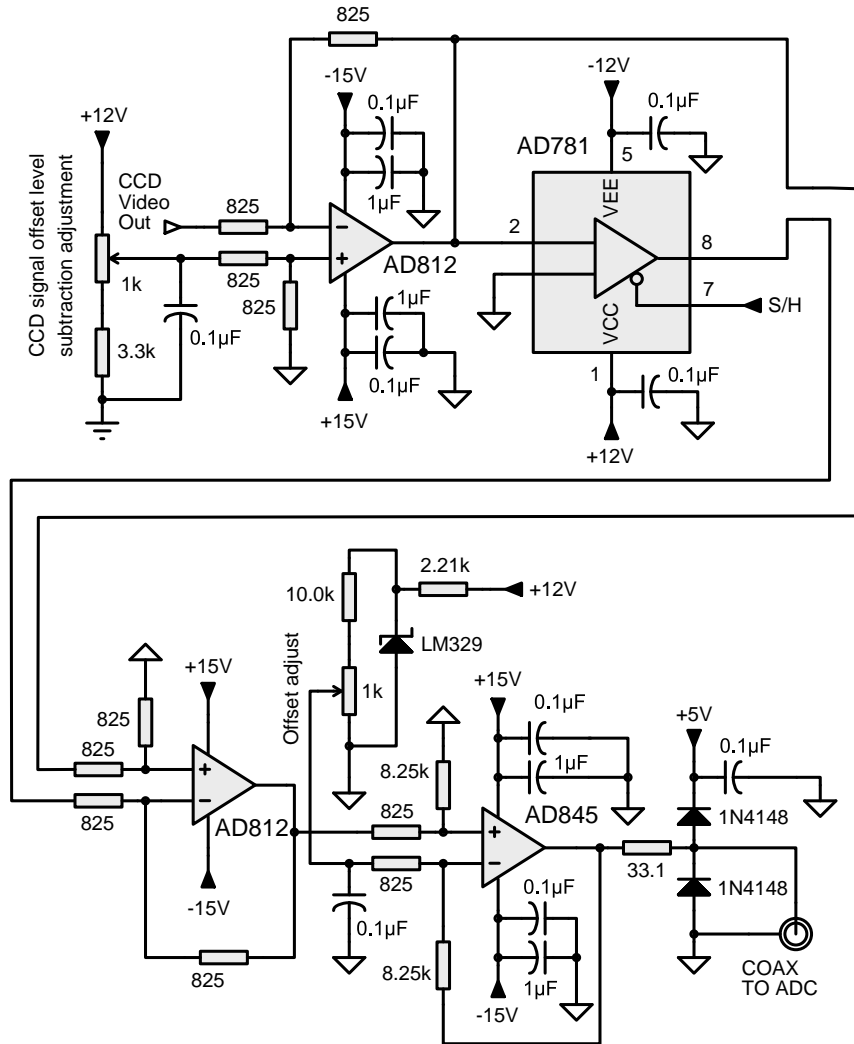
C.7 Software

Software development for the Pyxis camera proceeded along three lines; writing the PIC micro-controller routines in PIC Assembler, writing the Windows 95/98/Me$_{TM}$ camera drivers and developing the user interface. To this one should add the writing of an extensive data processing suite to easily handle the image files specific to the camera and its

intended use. The user interface and camera drivers were developed using Borland's C++ Builder$_{TM}$ 3.0. The image files may also be saved in FITS format (Flexible Image Transport System) which is the standard format used for astronomical data.

C.8 Measurement of the camera noise

In an ideal sensor the only source of noise is due to the random arrival time of photons at the detector. In an ideal CCD the signal to noise ratio (SNR) in any individual pixel is,

$$SNR = N_e/\sigma = \frac{N_e}{\sqrt{N_e}} \tag{C.1}$$

where σ is the standard deviation and N_e is the number of photo-electrons generated at the pixel site. Note that the relevant SNR is that given by the number of photo-generated electrons, not the number of photons incident on the detector (*i.e.* the above relation takes into account the quantum efficiency of the detector).

The SNR in a real camera will always be smaller than that given by Equation C.1 due to readout noise and dark-current. It is useful to determine the total amount of noise in the camera signal relative to the expected photon noise. One may then separate the electronic readout noise arising in the support electronics from the intrinsic noise in the CCD detector and the photon noise. This measurement is necessary if one wishes to optimize the operation of the video sampling electronics in the camera.

To do this, one must first determine the relation between the CCD output voltage V to the number of photo-generated electrons N_e, or gain, g_{ccd}. For the KAF-401e CCD, Kodak quotes a value of approximately 9-11μV/e$^-$. One must also know the relation between the CCD output voltage to the number of ADC units (ADU) used to represent this voltage. This is given by the gain of the output electronics stages, g_e, the number of digitization bits n and the full-scale input voltage V_{ADCmax} of the ADC;

$$\text{ADC units per CCD output voltage} = \frac{g_e \cdot (2^n - 1)}{V_{ADCmax}} \tag{C.2}$$

The number of photo-generated electrons representing a single ADU is defined as the transfer constant, κ, and is given by,

$$\kappa = \frac{V_{ADCmax}}{g_e \cdot (2^n - 1) \cdot g_{ccd}} \tag{C.3}$$

For the KAF-401e module of the Pyxis camera we have $g_e = 10.0$, $V_{ADCmax} = 5V$, $(2^n - 1) = 16383$ and $g_{ccd} \simeq 10\mu V/e^-$, so we find $\kappa \simeq 3.0e^-/ADU$. One should note that the output node capacity of the KAF-401e sensor is 220000 electrons; this corresponds to 66000 ADU, however only 16383 ADU are available on the 14 bit ADC. In this case the dynamic range of the camera has been limited in favour of being able to easily measure the noise level of the camera.

The noise may be separated into three terms; the photon noise σ_p, the CCD noise σ_{ccd} and the readout noise due to the peripheral electronics σ_e. It is assumed that the CCD is cooled sufficiently so that the dark current is negligible. The total noise σ_t is given by the sum of the individual variances,

$$\sigma_t{}^2 = \sigma_p{}^2 + \sigma_{ccd}{}^2 + \sigma_e{}^2 \tag{C.4}$$

What one measures is the signal S and its associated noise $\Delta S = \sigma_t$ expressed in ADU. Rewriting the above so that the noise is expressed in electron units,

$$(\kappa \cdot \Delta S)^2 = \kappa \cdot S + \sigma_{ccd}{}^2 + \sigma_e{}^2 \tag{C.5}$$

where the photon noise variance, $\sigma_p^2 = \kappa \cdot S_t$ has been substituted, and the standard deviations, σ_{ccd} and σ_e, are now expressed in numbers of photo-electrons.

In particular one is interested in determining the noise in the electronics, σ_e. The CCD noise floor σ_{ccd} may be obtained from the manufacturer's specifications; for the KAF-401e this is approximately 15-20 electrons at 25 °C[1]. In order to accurately measure the noise a light source with a very steady flux is required. In practice, it is best to take an average over several pixels to compensate for the variation in sensitivity from pixel to pixel.

Unfortunately, a single series of measurements at a fixed uniform intensity level will not yield sufficient information to accurately determine the electronic noise. The primary reason for this is that the calculated transfer constant, κ is only approximate. In particular, the manufacturer's specification of the output amplifier sensitivity is poorly characterized (10% uncertainty).

In order to determine the transfer constant κ and the electronic noise floor, one must measure the signal variance at several signal levels. Equation C.5 can be rewritten as,

$$(\Delta S)^2 = \frac{S}{\kappa} + \frac{\sigma_{ccd}^2 + \sigma_e^2}{\kappa^2} \tag{C.6}$$

---

[1]The noise floor decreases as the CCD is cooled.

If we plot the variance $(\Delta S)^2$ versus the signal S then the slope will be the inverse of the transfer constant, $1/\kappa$ and the intercept will provide the combined readout and CCD output variances.

When illuminating the CCD, care must be taken to use a sufficiently bright source that the CCD will respond linearly. The integration time should be sufficiently long that jitter in the time taken to open or close the CCD shutter does not affect the noise. Also, the CCD must be cooled to a temperature where the the dark current does not significantly contribute to the noise. The problem of varying exposure time or light flux can be partially solved by averaging the intensities across the entire frame. In this way the intensities may be normalized for small variations in exposure time/light flux between frames.

One can speed up the measurement process by using images that exhibit a gentle intensity gradient across the frame; say, by a total intensity variation of 2:1 from the brightest to the dimmest image regions. In the measurement of the noise in the Pyxis camera, 7 series of 100 images were used, with each image series a factor of 2 brighter than the last. The diode light source provided a 2:1 illumination intensity gradient across the image frame; in this way, data for all intensity levels between 400 and 16000 ADU were obtained using only 7 series of images. The following summarizes the procedure used to acquire and process the images:

- A series of 100 frames was taken at 6 different intensity levels. Each intensity level differed by a factor of 2 from the last.

- For a given 100 frame series, the average intensity of each image was computed. This was used to produce a normalization value for each image in the series. The purpose of the normalization is to remove any frame-to-frame variations in the uniform intensity level due to small fluctuations in the illuminating diode power or the exposure time. The normalization value is computed by dividing each average frame intensity by the average of the average frame intensities in the series.

- The intensity of each image in the series was divided by its normalization value.

- For a given series, several 4x4 pixel regions were selected and the standard deviation of each pixel in the selected region was computed across the series of images.

- The standard deviations and intensities for each 4x4 pixel region were averaged and the variance (given by the square of the standard deviation) were plotted against the intensity (in ADU).

The result of the noise measurement is shown in Figure C.13. The nonlinearity of the transfer curve at higher intensities indicates that the electronic noise increases at higher pixel intensities. At low intensities, the transfer curve is linear and the best-fit regression line provides a transfer constant of $2.95 \pm 0.02 \, e^-/\text{ADU}$, which is in good agreement with the value calculated from the electronic gain and Kodak's output amplifier sensitivity; $3.0 \, e^-/\text{ADU}$. The variance at the origin is $130 \pm 15 \, \text{ADU}^2$, so the total electron noise in the CCD and electronics is, $\sqrt{130} \, \text{ADU} \cdot 2.95 \, e^-/\text{ADU} = 33 \, e^-$, at -16ºC. This is an acceptable level if one considers that the electronic noise floor of the CCD is $20 \, e^-$ at room temperature.

Figure C.13: *Transfer curve for the KAF-401e Pyxis CCD camera at -16 ºC. Inset is expanded view of the low intensity region.*
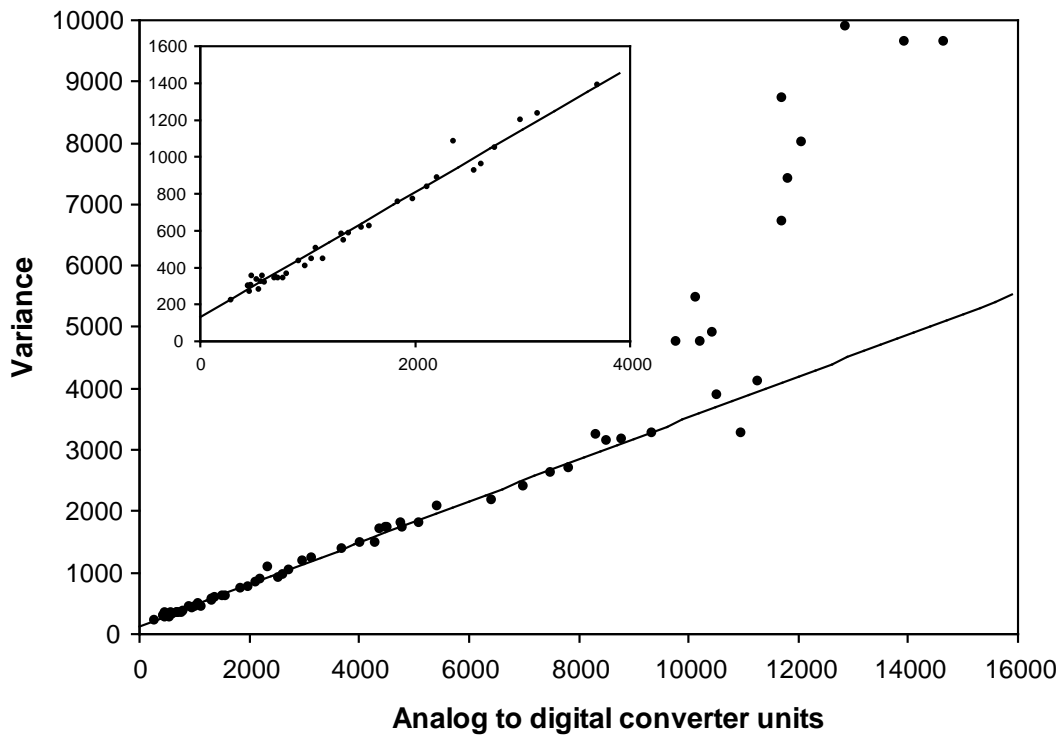
References

Aitken, M. J. (1985). *Thermoluminescence Dating.* Academic Press, London.

Aitken, M. J. (1994). Optical dating: a non-specialist review. *Quaternary Science Reviews*, **13**: 503–508.

Aitken, M. J. (1998). *An introduction to optical dating.* Oxford University Press, Oxford.

Almond, P.C., Moar, N.T. and Lian O.B. (2001). Reinterpretation of the glacial chronology of south Westland, New Zealand. *New Zealand Journal of Geology and Geophysics*, **44**: 115.

Bailey, R. M., Smith, B. W. and Rhodes, E. J. (1997). Partial bleaching and decay form characteristics of quartz OSL. *Radiation Measurements*, **27**(2): 123–136.

Bailiff, I. K., Morris, D. A. and Aitken, M. J. (1977). A rapid-scanning interference spectrometer: application to low-level thermoluminescence emission. *Journal of Physics E (Scientific Instruments)*, **10**(11): 1156–1160.

Bailiff, I. K. and Barnett, S. M. (1994). Characteristics of infrared-stimulated luminescence from a feldspar at low temperatures. *Radiation Measurements*, **23**(2/3): 541–545.

Bailiff, I. K. and Poolton, N. R. J. (1991). Studies of charge transfer mechanisms in feldspars. *Nuclear Tracks and Radiation Measurements*, **18**(1/2): 111–118.

Bakas, G. V. (1984). A new optical multichannel analyser using a charge coupled device as detector for thermoluminescence measurements. *Radiation Protection Dosimetry*, **9**(4): 301–305.

Baril, M. R. (1997). *Optical Dating of Tsunami Deposits*. Simon Fraser University, Burnaby, B.C., Canada.

Barnett, S. M. and Bailiff, I. K. (1997). Infrared stimulation spectra of sediments containing feldspars. *Radiation Measurements*, **27**(2): 237–242.

Bazin, M., Aubailly, M., Santus R. (1977). Decay kinetics of the delayed fluorescence of aromatic compounds. *The Journal of Chemical Physics*, **67**(11): 5070–5073.

Berger, G. W. (1995). Progress in luminescence dating methods for Quaternary sediments; *in* Dating methods for Quaternary Deposits. (ed.) Rutter, N. W. and Catto, N. R. *Geological Society of Canada, Geotext 2*, pp. 81–104.

Blake, W. Jr. (1992). Holocene emergence at Cape Herschel, east central Ellesmere Island, Arctic Canada: implications for ice sheet configuration. *Canadian Journal of Earth Sciences*, **29**: 1958–1980.

Bøtter-Jensen, L., Duller, G. A. T. and Poolton, N. R. J. (1994). Excitation and emission spectrometry of stimulated luminescence from quartz and feldspars. *Radiation Measurements*, **23**(2/3): 613–616.

Brovetto, P., Delunas, A., Maxia, V. and Spano, G. (1990). On the spectral analysis of thermoluminescence by means of a continuous interferential filter. *Il Nuovo Cimento*, **12**(3): 331–337.

Buil, Christian (1991). *CCD Astronomy: Construction and use of an astronomical CCD camera.*, Willmann-Bell, Richmond, Virginia.

Carlson, J. M. (1999). Highly optimized tolerance: A mechanism for power laws in designed systems. *Physical Review E*, **60**(2): 1412–1427.

Chao, C. C. (1971). Charge transfer luminescence of Cr^{3+} in magnesium oxide. *Journal of the Physics and Chemistry of Solids*, **32**: 2517–2528.

Clarke, M. L. and Rendell, H. M. (1997a). Infra-red stimulated luminescence spectra of alkali feldspars. *Radiation Measurements*, **27**(2): 221–236.

Clarke, M. L. and Rendell, H. M. (1997b). Stability of the IRSL spectra of alkali feldspars. *Physica Status Solidi (b)*, **199**: 597–604.

Clarke, M. L., Rendell, H. M., Sanchez-Muñoz, L. and Garcia-Guinea, J. (1997). A comparison of luminescence spectra and structural composition of perthitic feldspars. *Radiation Measurements*, **27**(2): 137–144.

Cordier, P., Delouis, J. F., Kieffer, F., Lapersonne, C. and Rigaut, J. (1974). Étude cinétique de la luminescence différée isotherme d'un verre organique après une impulsion d'électrons accélérés. *Comptes Rendus Académie des Sciences (Paris), Série C*, **279**: 589–591.

Dana, Edward, S. (1962). *Minerals and how to study them*, John Wiley, New York.

Debye, P., Edwards, J. O. (1952). Long-lifetime phosphorescence and the diffusion process. *Journal of Chemical Physics*, **20**(2): 236–239.

Deer, W. A., Howie, R. A. and Zussman, J. (1966). *An introduction to the rock forming minerals.* Wiley, New York, 1st edition, pp 528.

De St Jorre, L. and Smith, D. G. W. (1988). Cathodoluminescent Ga-enriched feldspars from the Thor Lake rare-metal deposits, NW Territories, Canada. *The Canadian Mineralogist*, **26**: 301–308.

Di Bartolo, Baldassare (1976). *Optical Interactions in Solids.* John Wiley & Sons, New York, pp. 357–377.

Di Bartolo, Baldassare and Powell, Richard C., (1976). *Phonons and Resonances in Solids.* John Wiley & Sons, New York, pp. 456–459.

Dissado, L. A. and Hill, M. R. (1983). A cluster approach to the structure of imperfect materials and their relaxation spectroscopy. *Proceedings of the Royal Society of London, A*, **390**: 131–180.

Ditlefsen, C. and Huntley, D. J. (1994). Optical excitation of trapped charges in quartz, potassium feldspars and mixed silicates: the dependence on photon energy. *Radiation Measurements*, **23**(4): 675–682.

Donati, Silvano (2000). *Photodetectors: devices, circuits and applications*. Prentice Hall, Inc., Upper Saddle River, NJ, 1st edition.

Duller, G. A. T. and Bøtter-Jensen, L. (1997). Optically stimulated luminescence emission spectra from feldspars as a function of sample temperature. *Radiation Measurements*, **27**(2): 145–151.

Faïn, J., Sanzelle, S., Miallier, D., Montret, M. and Pilleyre, Th. (1994). A TL model based on deep traps competition. *Radiation Measurements*, **23**(2/3): 287–291.

Faure, Gunter (1991). *Principles and applications of inorganic geochemistry.* MacMillan, New York.

Finch, A. A. and Klein, J. (1999). The causes and petrological significance of cathodoluminescence emissions from alkali feldspars. *Contributions to Mineralogy and Petrology*, **135**: 234–243.

Fulton, R. J., Irving, E. and Wheadon, P. M. (1992). Stratigraphy and palaeomagnetism of Brunhes and Matuyama (>790 ka) Quaternary deposits at Merritt, British Columbia. *Canadian Journal of Earth Sciences*, **29**: 76–92.

Garcia-Guinea, J., Rendell, H. M. and Sanchez-Muñoz, L. (1996). Luminescence spectra of alkali feldspars: some relationships between structural features and luminescence emission. *Radiation Protection Dosimetry*, **66**(1-4): 395–398.

Godfrey-Smith, D. I. and Cada, M. (1996). IR stimulation spectroscopy of plagioclase and potassium feldspars, and Quartz. *Radiation Protection Dosimetry*, **66**(1-4): 379–385.

Halperin, A. and Braner, A. A., (1960). Evaluation of thermal activation energies from glow curves. *Physical Review*, **117**: 408.

Hamill, William H. (1979). Debye-Edwards electron recombination kinetics. *Journal of Physical Chemistry*, **71**(1): 140–142.

Hofmeister, A. M. and Rossmann, G. R. (1984). Determination of Fe^{3+} and Fe^{2+} concentrations in feldspars by optical absorption and EPR spectroscopy. *Physics and Chemistry of Minerals*, **11**: 213–224.

Huntley, D. J., Godfrey-Smith, D. I. and Thewalt, M. L. W. (1985). Optical dating of sediments. *Nature*, **313**: 105–107.

Huntley, D. J., Godfrey-Smith, D. I., Thewalt, M. L. W. and Berger, G. W. (1988). Thermoluminescence spectra of some mineral samples relevant to thermoluminescence dating. *Journal of Luminescence*, **39**: 123–136.

Huntley, D. J., Godfrey-Smith, D. I. and Haskell, E. H. (1991). Light-induced emission spectra from some quartz and feldspars. *Nuclear Tracks and Radiation Measurements*, **18**(1/2): 127–131.

Huntley, D. J., Hutton, J. T. and Prescott, J. R. (1993a). The stranded beach-dune sequence of south-east South Australia: a test of thermoluminescence dating, 0–800 ka. *Quaternary Science Reviews*, **12**: 1–20.

Huntley, D. J., Hutton, J. T. and Prescott, J. R. (1993b). Optical dating using inclusions within quartz grains. *Geology*, **21**: 1087–1090.

Huntley, D. J., Hutton, J. T. and Prescott, J. R. (1994). Further thermoluminescence dates from the dune sequence in the southeast of South Australia. *Quaternary Science Reviews*, **13**: 201–207.

Huntley, D. J. and Berger, G. W. (1995). Scatter in luminescence data for optical dating – some models. *Ancient TL*, **13**: 5–9.

Huntley, D. J. and Clague, J. J. (1996). Optical dating of tsunami-laid sands. *Quaternary Research*, **46**: 127–140.

Huntley, D. J. and Lian, O. B. (1999). Using optical dating to determine when a sediment was last exposed to sunlight; *in* Holocene Climate and Environmental Change in the Palliser Triangle: A Geoscientific Context for Evaluating the Impacts of Climate Change on the Southern Canadian Praries. (ed.) Lemmen, D. S. and Vance, R.E. *Geological Society of Canada, Bulletin 534*, pp. 211–222.

Huntley, D. J., Short, M. A. and Dunphy, K. (1996). Deep traps in quartz and their use for optical dating. *Canadian Journal of Physics*, **74**: 81–91.

Huntley, D. J. and Lamothe, M. (2001). Ubiquity of anomalous fading in K-feldspars and the measurement and correction for it in optical dating. *Canadian Journal of Earth Sciences*, **38**: 1093–1106.

Huntley D. J. and Prescott, J. R. (2001). Improved methodology and new thermoluminescence ages for the dune sequence in south-east South Australia. *Quaternary Science Reviews*, **20**: 687–699.

Hutley M. C. (1982). Diffraction gratings. Academic Press, Inc., London.

Hütt, G., Jaek, I. and Tchonka, J. (1988). Optical dating: K-feldspars optical response stimulation spectra. *Quaternary Science Reviews*, **7**: 381–385.

Hütt, G., Jaek, I., Brodski, L. and Vasilchenko, V. (1999). Optically stimulated luminescence characteristics of natural and doped quartz and alkali feldspars. *Applied Radiation and Isotopes*, **50**: 969–974.

Jonscher, A. K. (1983). *Dielectric Relaxation in solids.* Chelsea Dielectrics Press, London.

Jonscher, A. K. and de Polignac, Anne (1984). The time dependence of luminescence in solids. *Journal of Physics C: Solid State Physics*, **17**: 6493–6519.

Jungner, H. and Huntley, D. J. (1991). Emission spectra of some potassium feldspars under 633 nm stimulation. *Nuclear Tracks and Radiation Measurements*, **18**(1/2): 125–126.

Kingslake, Rudolf (1978). Lens design fundamentals. Academic Press, San Diego.

Krbetschek, M. R. and Rieser, U. (1995). Luminescence spectra of alkalifeldspars and plagioclases. *Radiation Measurements*, **24**: 473–477.

Krbetschek, M. R., Götze, J., Dietrich, A. and Trautmann, T. (1997). Spectral information from minerals relevant for luminescence dating. *Radiation Measurements*, **27**(5/6): 695–748.

Kurik, M. V. (1971). Urbach rule. *Physica Status Solidi*, **8**: 9–45.

Lamothe, M. (1996). Datation par les méthodes de luminescence des feldspaths des milieux sédimentaires: le problème de la remise à zéro". *Géographie Physique et Quaternaire*, **50**: 365–376.

Lamothe, M. and Auclair, M. (1997). Assessing the datability of young sediments by IRSL using an intrinsic laboratory protocol. *Radiation Measurements*, **27**: 107–117.

Lamothe, M. and Auclair, M. (1999). A solution to anomalous fading and age shortfalls in optical dating of feldspar minerals. *Earth and Planetary Science Letters*, **171**: 319–323.

Levy, P. W. (1985). Thermoluminescence kinetics of in materials exposed to the low doses applicable to dating and dosimetry. *Nuclear Tracks and Radiation Measurements*, **10**:547–556.

Loewenstein, W. (1954). The distribution of aluminum in the tetrahedra of silicates and aluminates. *American Mineralogist*, **39**: 92–96.

Luff, B. J. and Townsend, P.J. (1992). High sensitivity thermoluminescence spectrometer. *Measurement Science and Technology*, **3**: 65–71.

Marfunin, A. S. (1979a). *Physics of minerals and inorganic materials.*, Springer-Verlag, Berlin.

Marfunin, A. S. (1979b). *Spectroscopy, Luminescence and Radiation Centres in Minerals*, Springer-Verlag, Berlin.

Mariano, A. N. (1988). Some further applications of cathodoluminescence. *in* Cathodoluminescence of geological materials. Unwin Hyman, Boston. pp 94–123.

Markey, B. G., Colyott, L. E. and McKeever, S. W. S. (1995). Time-resolved optically stimulated luminescence from α-Al_2O_3:C. *Radiation Measurements*, **24**: 457–463.

Martini, M., Paravisi, S. and Liguori, C. (1996). A new high sensitivity spectrometer for 3-D thermoluminescence analysis. *Radiation Protection Dosimetry*, **66**(1-4): 447–450.

McKeever, S. W. S. and Morris, M. F. (1994). Computer simulations of optical bleaching of TL and OSL signals. *Radiation Measurements*, **23**(2/3): 301–306.

McKeever, S. W. S., Bøtter-Jensen, L., Agersnap Larsen, N. and Duller, G. A. T. (1997). Temperature dependence of OSL decay curves: experimental and theoretical aspects. *Radiation Measurements*, **27**(2): 161–170.

Megaw, H. D. (1956). Notation for feldspars structures. *Acta Crystallographica*, **9**: 56–60.

Mochanov, Y. A. (1988). The most ancient palaeolithic of the Diring and the problem of nontropical origin for humanity. English translation in; *Arctic Anthropology*, 1993, **30**: 22–53.

Mora, C. I. and Ramseyer, K. (1992). Cathodoluminescence of coexisting plagioclases, Bœhls Butte anorthosite: CL activators and fluid flow paths. *American Mineralogist*, **77**: 1258–1265.

Mott, N. F. and Gurney, R. W. (1948). *Electronic Processes in Ionic Crystals*. Oxford University Press, London, 2nd edition.

Nakazawa, Eiichiro (1999). Fundamentals of Luminescence, Section Seven, in *Phosphor Handbook*, Shionoya, Shigeo and Yen, William M., editors. CRC Press LLC, Boca Raton (English language version).

Nelkowski, H., Pfützenreuter, O. and Schrittenlacher, W. J. (1979). Comparison of luminescence and ESR-investigations in ZnS:Fe. *Journal of Luminescence*, **20**: 403.

Parkhomenko, E. I. (1967). *Electrical Properties of Rocks*. Plenum Press, New York.

Petrov, I. and Hafner, S. S. (1988). Location of Fe^{3+} ions in sanidine, $KAlSi_3O_8$. *American Mineralogist*, **73**: 97–104.

Petrov, I., Agel, Andreas and Hafner, S. S. (1989). Distinct defect centers at oxygen positions in albite. *American Mineralogist*, **74**: 1130–1141.

Piters, T. M., Meulemans, W. H. and Bos, A. J. J. (1993). An automated research facility for measuring thermoluminescence emission spectra using an optical multichannel analyzer. *Review of Scientific Instruments*, **64**(1): 109–117.

Plischke, M. and Bergersen, B. (1994). *Equilibrium statistical physics*. World Scientific, p.163.

Poolton, N. R. J., Bøtter-Jensen, L., Ypma, P. J. M. and Johnsen, O. (1994). Influence of crystal structure on the optically stimulated luminescence properties of feldspars. *Radiation Measurements*, **23**(2/3): 551–554.

Poolton, N. R. J., Bøtter-Jensen, L. and Johnsen, O. (1995). Thermo-optical properties of optically stimulated luminescence in feldspars. *Radiation Measurements*, **24**(4): 531–534.

Predko, Mike (1998). *Programming and Customizing the PIC microcontroller*. McGraw-Hill, New York.

Prescott, John R., Fox, Phillip J. and Jensen, H. E. (1988). Thermoluminescence emission spectrometer. *Applied Optics*, **27**(16): 3496–3502.

Prescott, J. R. and Fox, P. J. (1993). Three-dimensional thermoluminescence spectra of feldspars. *Journal of Physics D: Applied Physics*, **26**: 2245–2254.

Press, W. H., Teukolsky, S. A., Vetterling, W. T. and Flannery, B. P. (1992). *Numerical recipes in C: the art of scientific computing*. Cambridge University Press, Cambridge, 2nd edition, 994 p.

Randall, J. T. and Wilkins, M. H. F. (1945) Phosphorescence and Electron Traps II, the interpretation of long-period phosphorescence. *Proceedings of the Royal Society (London)*, **A184**: 390–407.

Rendell, H. M. and Clarke, M. L. (1997). Thermoluminescence, radioluminescence and cathodoluminescence spectra of alkali feldspars. *Radiation Measurements*, **27**(2): 263–272.

Rendell, H. M., Townsend, P. D. and Wood, R. A. (1995). TL and IRSL emission spectra of detrital feldspars – new experimental data. *Physica Status Solidi (b)*, **190**: 321–330.

Rieser, U., Krbetschek, M. R. and Stolz, W. (1994). CCD-Camera Based High Sensitivity TL/OSL-Spectrometer. *Radiation Measurements*, **23**(2/3): 523–528.

Rieser, U., Hütt, G., Krbetschek, M. R. and Stolz, W. (1997). Feldspar IRSL emission spectra at high and low temperatures. *Radiation Measurements*, **27**(2): 273–278.

Rieser, U. (1999). *Spektrometrie an feldspäten als Beitrag zur Aufklärung physikalischer Grundlagen der Lumineszenz-Datierungstechnik*. Ph. D. Thesis. Ruprecht-Karls-Universität, Heidelberg, Germany.

Rieser, U., Habermann, J. and Wagner, G. A. (1999). Luminescence dating: A new high sensitivity TL/OSL emission spectrometer. *Quaternary Geochronology*, **18**: 311–315.

Schnadt, R. and Rauber, A. (1971). Motional effects in the trapped-hole center in smoky quartz. *Solid State Communications*, **9**(2): 159–161.

Schnadt, R. and Schneider, J. (1970). The electronic structure of the trapped-hole center in smoky quartz. *Physik der Kondensierten Materie*, **11**(1): 19–42.

Schuler, Frederic and Schuler, Lilli (1970). *Glassforming: Glassmaking for the Craftsman*. Chilton Book Company, Philadelphia, 1st edition.

Shane, P., Alloway, B., Black, T. and Westgate, J. (1996). Isothermal plateau fission-track ages of tephra beds in an early-middle Pleistocene marine and terrestrial sequence, Cape Kidnappers, New Zealand. *Quaternary International*, **34-36**: 49–53.

Short, M. A. and Huntley, D. J. (1992). Infrared stimulation of quartz. *Ancient TL*, **10**: 19–21.

Short, M. A. and Tso, Man-Yin W. (1994). New methods for determining the thermal activation energies of light sensitive traps. *Radiation Measurements*, **23**(2/3): 335–338.

Short, M. A. and Huntley, D. J. (2000). Crystal anisotropy effects in optically stimulated luminescence in K-feldspar. *Radiation Measurements*, **32**: 865–871.

Short, M. A. (2003). *An investigation into the physics of the infrared excited luminescence of irradiated feldspars*. Ph. D. Thesis, Simon Fraser University, Burnaby, Canada, in preparation.

Smith, Joseph V. and Brown, William L. (1988). *Feldspar Minerals (Volume 1)*. Second Edition. Springer Verlag, New York.

Speit, B. and Lehmann, G. (1976). Radiation defects in feldspars. *Physics and Chemistry of Minerals*, textbf8: 77–82.

Speit, B. and Lehmann, G. (1982). Hole centers in the feldspar sanidine. *Physica Status Solidi (a)*, textbf36: 471–481.

Spooner, N. A. (1992). Optical dating: preliminary results on the anomalous fading of luminescence from feldspars. *Quaternary Science Reviews*, **11**: 139–145.

Spooner, N. A. (1993). *The validity of optical dating based on feldspar*. Ph.D. Thesis, Linacre College, Oxford University, Oxford.

Spooner, N. A. (1994). The anomalous fading of infrared-stimulated luminescence from feldspars. *Radiation Measurements*, **23**(2/3): 625–632.

Strong, John (1989). *Procedures in Applied Optics*. Marcel Dekker Inc., New York, New York, 1st edition.

Taylor, W. H. (1933). The structure of sanidine and other feldspars. *Zeitschift fur Kristallographie*, **85**: 425.

Telfer, D. J. and Walker, G. (1978). Ligand field bands of Mn^{2+} and Fe^{2+} luminescence centres and their site occupancy in plagioclase feldspars. *Modern Geology*, **6**: 199–210.

Thomas, B. and Houston, E. (1964). Correlation of optical absorption and thermoluminescence curves for single crystals of magnesium oxide. *British Journal of Applied Physics*, **15**: 953–958.

Thomas, D. G., Hopfield, J. J. and Augustyniak, W. M. (1965). Kinetics of radiative recombination at randomly distributed donors and acceptors. *Physical Review*, **140**(1A): A202–220.

Townsend, P. D., Jazmati, A. K., Karali, T., Maghrabi, M., Raymond, S. G. and Yang, B. (2001). Rare-earth-size effects on thermoluminescence and second-harmonic generation. *Journal of Physics: Condensed Matter*, **13**: 2211–2224.

Trautmann, T., Rieser, U. and Stolz, W. (1997). Activation energies of IRSL traps in feldspars. *Radiation Measurements*, **27**(2): 193–197.

Trautmann, T., Krbetschek, M. R., Dietrich, A. and Stolz, W. (1999). Feldspar radioluminescence: a new dating method and its physical background. *Journal of Luminescence*, **85**: 45–58.

van Heteren, S., Huntley, D. J., van de Plassche, O. and Lubberts, R. K. (2000). Optical dating of dune sand for the study of sea-level change. *Geology*, **28**: 411–414.

Visocekas, R. and Geoffroy (1977). Tunnelling afterglows and retrapping in calcite. *Physica Status Solidi (a)*, **41**: 499–503.

Visocekas, R. (1985). Tunnelling radiative recombination in labradorite: its association with anomalous fading of thermoluminescence. *Nuclear Tracks and Radiation Measurements*, **10**: 521–529.

Visocekas, R. (1993). Tunnelling radiative recombination in K-feldspar sanidine. *Nuclear Tracks and Radiation Measurements*, **21**(1): 175–178.

Visocekas, R., Spooner, N. A., Zink, A. and Blanc, P. (1994). Tunnel afterglow, fading and infrared emission in thermoluminescence of feldspars. *Radiation Measurements*, **23**(2/3): 377–385.

Visocekas, R. and Zink, A. (1999). Use of the far red TL emission band of alkali feldspars for dosimetry and dating. *Quaternary Geochronology*, **18**: 271–278.

Wang, Y. and Evans, M.E. (1997). Paleomagnetism of Canadian Arctic permafrost; Quaternary magnetostratigraphy of the Mackenzie Delta. *Canadian Journal of Earth Sciences*, **34**(2): 135–139.

Waters, M. R., Forman, S. L. and Pierson, J. M. (1999). Late Quaternary geology and geochronology of Diring Yuriakh, an early paleolithic site in central Siberia. *Quaternary Research*, **51**(2): 195–211.

Wolfe, S. A., Muhs, D. R., David, P. P. and McGeehin, J. P. (2000). Chronology and geochemistry of late Holocene eolian deposits in the Brandon Sand Hills, Manitoba, Canada. *Quaternary International*, **67**: 61–74.

Wolfe, S. A., Huntley, D. J., David, P. P., Ollerhead, J., Sauchyn, D. J. and MacDonald, G. M. (2001). Late 18th century drought-induced sand dune activity, Great Sand Hills, Saskatchewan. *Canadian Journal of Earth Sciences*, **38**: 105–117.

Xu, Yong-nian and Ching, W. Y. (1991). Electronic and optical properties of all polymorphic forms of silicon dioxide. *Physical Review B*, **44**(20): 11048–11059.

Zink, A., Visocekas, R. and Bos, A. J. (1995). Comparison of 'blue' and 'infrared' emission bands in thermoluminescence of alkali feldspars. *Radiation Measurements*, **24**(4): 513–518.